MOMENT METHOD ANALYSIS OF ARBITRARY SHAPED APERTURES IN WAVEGUIDES AND CONDUCTING SCREENS

A THESIS

Submitted in fulfilment of the
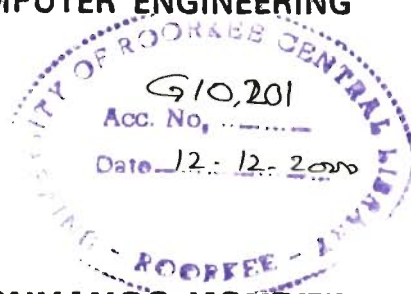*requirements for the award of the degree*
of

DOCTOR OF PHILOSOPHY

in

ELECTRONICS AND COMPUTER ENGINEERING

By

DOMINIC BERNARD ONYANGO KONDITI

DEPARTMENT OF ELECTRONICS AND COMPUTER ENGINEERING
UNIVERSITY OF ROORKEE
ROORKEE–247 667 (INDIA)

FEBRUARY, 2000

CANDIDATE'S DECLARATION

I hereby certify that the work which is being presented in the thesis entitled "**MOMENT METHOD ANALYSIS OF ARBITRARY SHAPED APERTURES IN WAVEGUIDES AND CONDUCTING SCREENS**" in fulfilment of the requirement for the award of the Degree of Doctor of Philosophy, submitted in the Department of Electronics and Computer Engineering of the University is an authentic record of my own work carried out during a period from February 1995 to February 2000 under the supervision of Dr. S.N. Sinha, Professor, Department of Electronics and Computer Engineering, University of Roorkee, Roorkee.

The matter presented in this thesis has not been submitted by me for the award of any other degree of this or any other University.

(D.B.O. KONDITI)

This is to certify that the above statement made by the candidate is correct to the best of my knowledge.
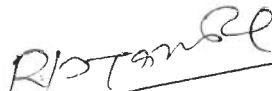
Date : 14.7.2000

(S.N. SINHA)
Professor
Deptt. of Electronics &
Computer Engineering
University of Roorkee
Roorkee - 247 667
India

The Ph.D. Viva-Voce examination of Mr. D.B.O. Konditi, Research Scholar, has been held on 25.10.2000

Signature of Supervisor   Signature of H.O.D.   Signature of External Examiner

ABSTRACT

Aperture coupling is an important boundary-value problem in electromagnetics. Practical applications of aperture coupling can be found in slotted antenna arrays, directional couplers, cavity resonators, radiating slots in screens, microstrip-patch antennas etc. Besides, undesirable coupling of electromagnetic energy may occur if there is an inadvertent crack/slit in the applicator/RF equipment leading to electromagnetic compatibility (EMC) and electromagnetic interference (EMI) problems.

In this study, we have developed a moment method solution procedure for the general problem of apertures of arbitrary shape coupling arbitrary regions. Appropriate modelling of the aperture surface has been carried out using triangular patch modelling, proposed by Rao et al. [82] for scattering from bodies of arbitrary shape. Suitably defined set of basis functions has been integrated into the formulation which is capable of accurately evaluating fields of apertures of arbitrary shape. The problem has been formulated by invoking equivalence theorem [46] and utilizing boundary conditions on the aperture to derive an integro-differential equation. This equation has been transformed into a matrix equation via the method of moments and solved numerically by simulation on a digital computer.

Easy-to-use expressions for numerical integration over a triangular domain have been developed. Further, careful treatment of singular integrals which arise due to the use of Green's function of free space has been performed. Explicit expressions for evaluating various matrices and parameters of interest have been developed.

Extensive computation of various parameters for apertures of various shapes, based on the preceding expressions, has been done and results presented. Also,

comparative studies for the various parameters of different aperture shapes have been undertaken.

Specifically, the four main classes of problems treated in this study comprise apertures of arbitrary shape coupling two half spaces via a conducting screen, waveguide-backed apertures of arbitrary shape in a ground plane radiating into half-space, apertures of arbitrary shape in the transverse cross-section of a uniform rectangular waveguide and broadwall radiating apertures and slots of arbitrary shape in a rectangular waveguide.

ACKNOWLEDGEMENTS

TABLE OF CONTENTS

LIST OF TABLES

LIST OF FIGURES

xiii

xiv

Chapter - 1

INTRODUCTION

Aperture coupling is an important boundary-value problem which has received considerable attention from many investigators over the years. With advancement in technology, the scale of utilization of microwave and millimeter-wave bands for communications, radar, industrial and domestic applications has increased. In many of these applications, apertures of various shapes are involved.

From a practical perspective, apertures have found applications in slotted antenna arrays, directional couplers, cavity resonators, radiating slots in screens, waveguide filters and power dividers and so on. Besides these applications, apertures can also cause undesirable electromagnetic coupling in some situations. For example, a crack/slit in the door of a microwave oven or in any other applicator or in any RF transmitting equipment may result in electromagnetic leakage leading to problems of Electromagnetic Compatibility (EMC) and Electromagnetic Interference (EMI).

Pioneering work in the area of aperture coupling dates back to 1944 when Bethe [11] developed his small aperture theory. Since then, concerted efforts have been made towards developing more elaborate techniques for solving aperture coupling problems. Majority of these techniques, however, deal with apertures of regular shapes and, in each case, only a particular problem has been solved. It is only with the development of numerical methods, such as the Method of Moments and Finite Element Method that it has become possible to treat irregularly shaped apertures.

1

Apertures having various shapes, such as rectangular, circular, elliptic, diamond, cross and H can be used to couple electromagnetic energy between two arbitrary regions.

In the following sections, we present a summary of the earlier work carried out in the field of aperture coupling followed by the statement of the problem and then the organization of material in this dissertation.

1.1 SURVEY OF EARLIER WORK

For several decades, a number of investigators have considered the problem of electromagnetic coupling through apertures. Aperture coupling problems can broadly be classified into three categories, i.e., apertures in the waveguide walls, as in the case of couplers, power dividers or radiating slots in the waveguide broad/narrow walls etc. or in the transverse cross-section of waveguides, as in the case of diaphragms and, lastly, apertures in conducting screens, causing coupling between two regions or radiating into half space. In this section, we have attempted to highlight the various representative contributions made by different researchers in each category.

Fig. 1.1(a)–(d) are typical examples of some aperture coupling problems in each category referred to above.
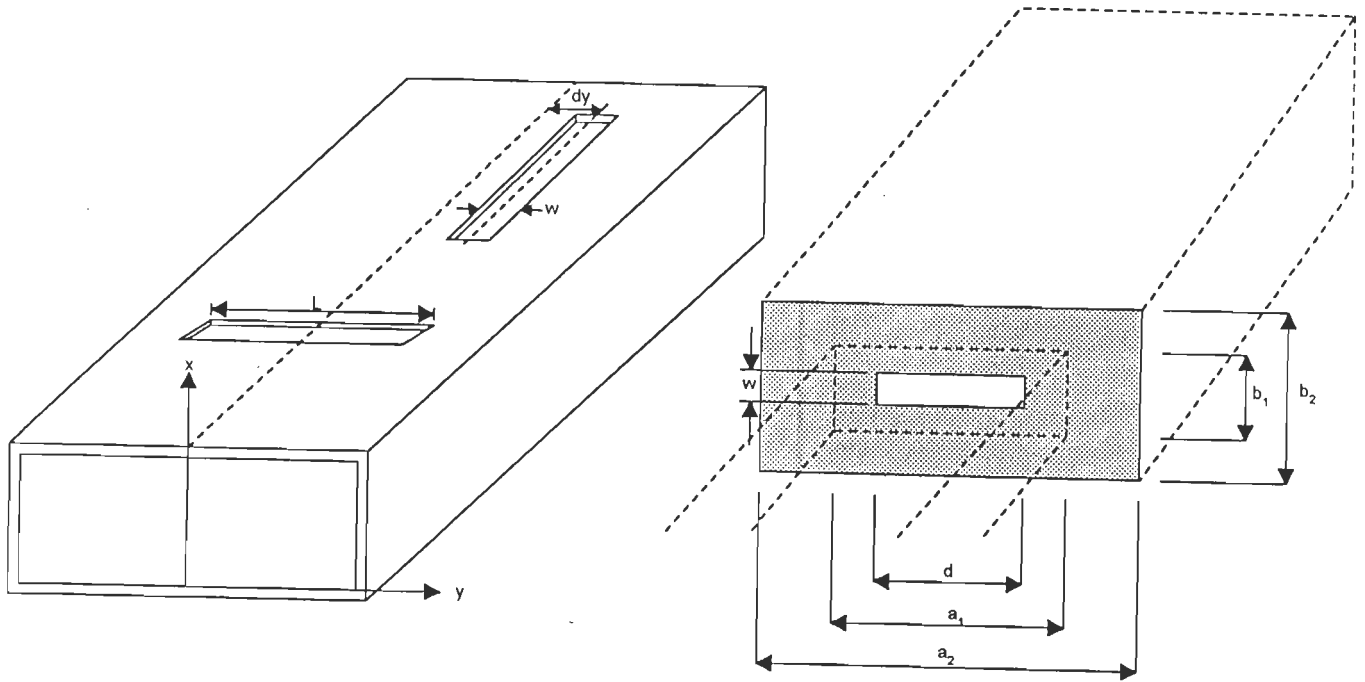
(a) Rectangular waveguide longitudinal
and transverse broadwall slots

(b) Aperture in the transverse cross-section
of dissimilar rectangular waveguides
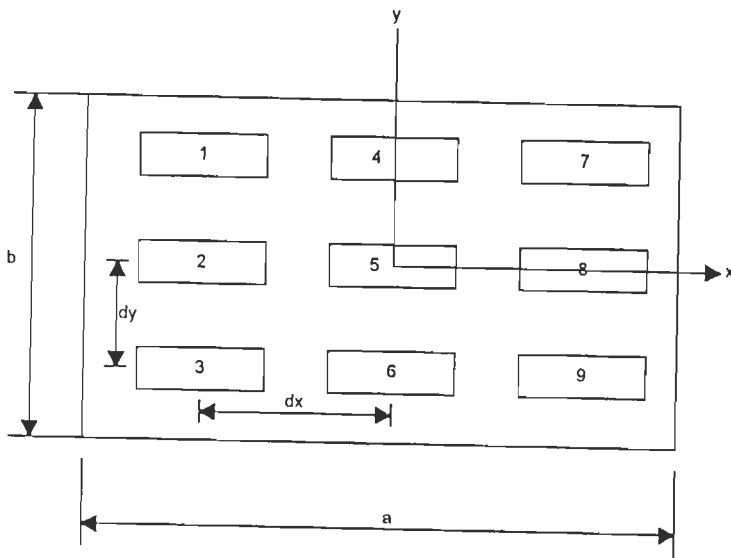
(c) Waveguide-backed slot arrays in a
perfect ground plane radiating
into half space
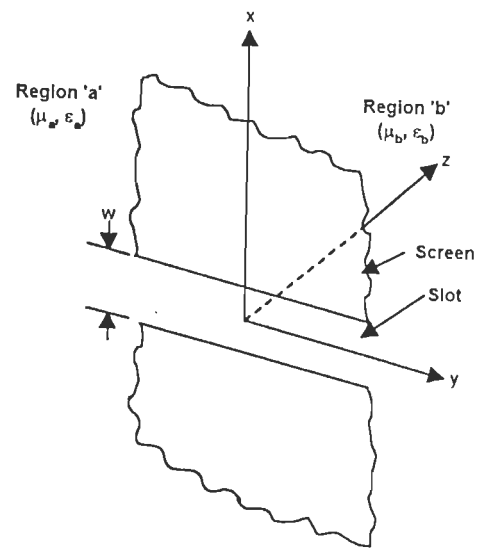
(d) Slot in an infinite conducting
screen coupling two different
regions

Fig. 1.1 : Typical examples of aperture coupling problems

3

1.1-1 Slots and Apertures in Waveguide Walls

The earliest treatment of slots in waveguides dates back to 1944, during the Second World War, when Bethe [11] developed his small aperture theory, which was later modified by Cohn [22], [23] to include large apertures of finite wall thickness. The modified Bethe-Cohn theory has been applied to the design of multi-aperture directional couplers by Levy [60]. The theory that forms the basis of the analysis and design of narrow slots and slot arrays in thin-walled waveguides, on the other hand, was developed by Stevenson [104]. The theory is well-explained in standard texts, such as [24] and [25]. In 1951, Stegen [102] experimentally investigated the characteristics of round-ended longitudinal shunt slots cut in the broadwall of X-band waveguides.

A variety of powerful methods for analysing discontinuities including apertures in the transverse cross-section or in the waveguide walls, which were developed during the Second World War, have been compiled by Marcuvitz [65] in the Waveguide Handbook. These techniques include the Variational Method, the Integral Transform Method and the Equivalent Static Method. Some of these techniques are well-explained by Collin [25] with the help of a number of examples. Lewin [61] has treated in full the Singular Integral Equation Method and its extensions by way of applying it to a number of examples. The method involves setting up an integral equation which is then solved by Weiner-Hopf technique to obtain various waveguide parameters. The method gives rigorous results for only a limited number of problems.

The Variational Method is a powerful tool for obtaining approximate solutions for problems formulated in terms of an integral equation. Oliner [75] has used the method to study the impedance properties of resonant and non-resonant narrow radiating rectangular slots in the broadwall of a rectangular waveguide.

Several investigators have also used variational method, notably Sangster [91] and Das et al. [28], [29], [30]. Although Variational Method can provide fairly accurate solutions to a variety of waveguide aperture problems, it requires a high level of mathematical ingenuity and for each problem, fresh calculations have to be done. Besides, the effects of finite wall thickness, sidewall proximity and higher-order mode coupling cannot easily be incorporated into the solution.

The Reaction Method was propounded by Das and Sanyal [27] as a means of analysing long slots (l > λ/2) on the broadwall of rectangular waveguides.

All in all, in each of the above methods, a specific formula has to be derived for a given type of discontinuity and often gross approximations have to be made. Further, a fresh mathematical problem has to be solved for each case and the effect of higher order modes is not properly accounted for.

The advent of digital computer has revolutionized the methodology for solving boundary-value problem. A number of powerful numerical techniques have been developed for analysing such problems. These include Modal Analysis, the Modified Residue Calculus Technique, the Principle of Conservation of Complex Power, the Field Expansion into Eigenmodes and the Method of Moments for solving aperture coupling problems.

Arndt et al. [5] have presented method for solving waveguide junctions and discontinuities by expanding the fields in terms of eigenmodes and setting up a matrix equation by matching the fields in the plane of the discontinuity. They have applied the method for the design of rectangular waveguide broadwall metal-insert slot couplers. The method gives directly the scattering matrix of the junction and takes into account the effect of evanescent modes.

However, amongst all these methods, the most powerful tool that has become popular with electromagnetic engineers is the method of Moments, MOM.

The MOM was proposed by Harrington [42] for solving differential and integral equations which appear in the computation of electromagnetic field problems. However, MOM has been applied mostly to integral equations. A succinct review on MOM for solving integral equations has been given by Wilton [111]. Briefly, MOM is based upon reducing integral, or integro-differential equations into a matrix equation which can be solved on a digital computer.

Vu Khac [107] has used the method of moments to solve problem of two waveguides coupled by an aperture in a common wall using pulse functions and point-matching technique. Later, Vu Khac and Carson [108] analysed impedance properties of broadwall radiating longitudinal slots in rectangular waveguide by the MOM, using pulse basis functions. They considered various slot offsets from guide centre-line. Lyon and Sangster [63] have also used MOM to investigate narrow rectangular slots in the broadwall of a rectangular waveguide by applying a sinusoidal Fourier set of basis functions. Both longitudinal and transverse rectangular slots were treated. Power radiated by the two type of slots were compared with those of Vu Khac and Carson [108], and Oliner's [75] based on variational method.

Similar studies on longitudinal and transverse rectangular slots and apertures in the broadwall/narrow wall can be found in [9], [34], [38], [50], [51], [52], [83], [90], [98], [101], [102], [103] and [114].

1.1-2 Diaphragms in Waveguides

Collin [25] has used variational method to obtain solutions for both thin and thick irises in a rectangular waveguide with dominant TE_{10} mode. Considerable contributions on the solution of inductive irises have been given by Rozzi et al. [84]-[87] using variational method.

The Modal Analysis was proposed by Wexler [109]. In this method, the electromagnetic field on either side of the discontinuity is first expanded into an infinite series of waveguide modes. Algebraic equations are obtained by matching the fields in each aperture which are then solved for the unknown amplitude coefficients. The method has been used by Luebbers and Munk [62]. However, the method involves a lot of numerical work.

Principle of Conservation of Complex Power has been used by Safavi-Naini and MacPhie [88] to solve the problems of scattering from a rectangular-to-rectangular waveguide junction and from a thick diaphragm with rectangular aperture in a rectangular waveguide. More recently, Omar and Schünemann [76] have given a general treatise of cascaded discontinuities in inhomogeneous waveguides as applied to finline circuits. Modified Residue Calculus Technique [105] has been applied to solve aperture problems in waveguides. The technique is useful in solving infinite set of equations which arise in dealing with double infinite summation over the waveguide fields. Above techniques have been applied to waveguide discontinuity problem by different workers, e.g., as can be found in [12] and [66].

Problems of diaphragms in a rectangular waveguide have been solved using Method of Moments. Some of the studies based on MOM can be found in [7], [8], [32], [99], [100] and [112].

It has been observed that MOM and Mode-matching method exhibit an inherent phenomenon known as the "relative convergence" when used to solve waveguide discontinuity problems. Lee et al. [56], Mittra et al. [71] and Aksun and Mittra [1] have reported a detailed study of the phenomenon and have proposed some useful guidelines in the use of method of moments solution procedure.

1.1-3 Apertures in a Conducting Screen

Apertures in conducting screens coupling two regions have also received considerable attention from many investigators. Butler and Umashankar [14] have studied the problem of a wire excited by an electromagnetic field penetrating an aperture-perforated infinite conducting screen. Harrington and Mautz [44] have presented a general formulation for aperture problems in terms of method of moments which can be applied to any two regions, isolated except for coupling through an aperture. With the help of equivalence theorem, the problem is divided into two separate regions and the aperture characteristics are expressed in terms of independent matrices, one for each region.

Using the above "generalized network formulation" for aperture problems [44]. Mautz and Harrington [67] have studied the problem of transmission through a rectangular aperture in a perfectly conducting plane. Computed parameters include magnetic surface current distribution over the aperture and transmission cross-sections for apertures of various lengths.

A similar approach has been used by Bozzetti et al. [13] to investigate coupling between an aperture and a biological body and, in a later work, by Harrington [45] to study the behaviour of an electrically small aperture in a conducting screen by a conducting body. Sarkar et al. [92] have considered the problem of electromagnetic transmission through mesh-covered apertures and arrays of apertures in a conducting screen.

Apertures situated in a perfect ground plane, backed by a rectangular waveguide, radiating into half-space have also been studied. Mautz and Harrington [68] utilized the "generalized network formulation" for aperture problems in moment method solution, with rooftop functions as basis and testing functions, to study electromagnetic transmission from a rectangular waveguide into

8

half-space through a rectangular aperture. Various parameters were computed including magnetic current distributions, aperture equivalent admittance seen by the dominant TE_{10} mode and antenna power gains.

Radiating aperture arrays, fed by a rectangular waveguide, in the ground plane have also been studied by various investigators. Such studies have been reported and can be found in [10], [35], [57], [58], [72], [96] and [97].

Cavity-backed apertures on a ground plane have also received attention in the literature. Typical reports on this class of apertures can be found in [2], [40], [47] and [94].

Another type of apertures/slots that has been reported in the literature consists of apertures in a conducting screen of finite thickness coupling two different media. This type of study was first conducted by Auckland and Harrington [6] in 1978 in order to develop a method for computing transmission characteristics of narrow slits. Typical examples of such studies are to be found in [43], [53] and [54].

1.2 STATEMENT OF THE PROBLEM

From the foregoing survey, it can be concluded that aperture problems form a very important class of boundary-value problems and a considerable effort has been directed towards solving these problems. In most of these studies, however, apertures of simple and regular shapes have been treated. Although Method of Moments can, in principle, be applied to apertures of arbitrary shape, its application also has been limited to apertures of simple shape since the popular rooftop and PWS functions are not suitable for modelling apertures of complex shapes.

In this study, we aim to develop a Method of Moments procedure, which is capable of analysing apertures of complex shapes. For modelling arbitrarily-shaped

apertures, triangular patch modelling, initially proposed by Rao et al. [82] for analysing scattering from object of arbitrary shape, seems appropriate because triangular patches can conform to surfaces of arbitrary shape. As such, triangular patches are to be used in discretizing the various aperture surfaces in conjunction with appropriately defined basis functions for evaluating the aperture fields.

The problem, as treated in this study, may be divided into five main parts :

(i)   General formulation for arbitrarily-shaped apertures coupling two arbitrary regions.

(ii)   Analysis of apertures of arbitrary shape, in a conducting screen, coupling two arbitrary regions.

(iii)   Analysis of waveguide-backed arbitrarily-shaped apertures in a ground plane.

(iv)   Analysis of arbitrarily-shaped apertures in the transverse cross-section of a rectangular waveguide.

(v)   Analysis of radiating broadwall slots of arbitrary shape in a rectangular waveguide.

1.3   ORGANIZATION OF THE THESIS

The work embodied in this dissertation has been arranged in Seven Chapters.

In Chapter 2, a Method of Moments procedure using the "generalized network formulation" for aperture problems has been developed for analysing apertures of arbitrary shape coupling two arbitrary regions. Various aspects have been considered, such as choice of basis functions and testing procedure and efficient evaluation of potential integrals over a triangular domain. Particular, attention has been given to the treatment of unbounded region integrals with singular kernels based on free space Green's function and closed region integrals with bounded kernels based on dyadic Green's function of the electric vector

potential. As a result, general expressions for various matrices and near- and far-field parameters have been developed.

In Chapter 3, the problem of an aperture of arbitrary shape in an infinite conducting screen coupling two half spaces with different electrical properties has been considered. Equations for evaluating various matrices and parameters have been derived. Parameters, such as surface magnetic current distribution, transmission coefficient and transmission cross-section have been computed. These results have been given in the last subsections of the chapter.

Chapter 4 deals with analysis of the problem of a waveguide-fed aperture of arbitrary shape on the ground plane radiating into half-space. Explicit expressions for evaluating various matrices and parameters have been developed. These expressions have been used to compute aperture surface magnetic current distribution, transmission coefficient, antenna power gain and equivalent aperture admittance seen by the dominant TE_{10} mode. The various computed results have been presented in the last subsections of the chapter.

In Chapter 5, we have investigated the problem of an arbitrarily-shaped aperture in the transverse cross-section of a uniform rectangular waveguide. Equations for evaluating various matrices and parameters have been derived. Computation of equivalent aperture shunt susceptance and surface magnetic current distribution has been done and results presented in the last section of the chapter.

In Chapter 6, the problem of broadwall slot/aperture of arbitrary shape radiating into half space has been considered. Expressions for evaluating various matrices and parameters have been developed. Computed parameters include aperture surface magnetic current distribution and power radiated by the aperture. The computed results have been presented in the last subsections of the chapter.

Chapter 7 concludes this dissertation by giving a review of the study in the preceding chapters and identifies some problems for future work in this area.

Chapter - 2

ELECTROMAGNETIC COUPLING VIA AN APERTURE OF ARBITRARY SHAPE

In this chapter, the general problem of electromagnetic coupling between two arbitrary regions via an aperture has been considered. The aperture is assumed to be located in a common conducting wall and can take arbitrary shape. The analysis is based upon the "generalised network formulation" for aperture problems [44]. Field equivalence principle is first used to divide the problem into two parts. Next, boundary conditions are invoked to obtain a magnetic field integral equation (MFIE) which is then solved using the method of moments (MOM). Triangular patches, with appropriately defined expansion functions, have been used to model the arbitrarily-shaped aperture. This leads to a matrix equation whose solution requires the evaluation of integrals with bounded and unbounded kernels over a triangular domain. A method for the evaluation of the integrals has been presented. Finally, various parameters, which can be used to characterize the aperture, have been derived.

2.1 GENERAL FORMULATION

Fig. 2.1 illustrates the general problem of an aperture coupling two dissimilar regions, called region 'a' and region 'b', which are bounded by perfect electrical conductors (PEC). Although region 'a' is shown to be closed and region 'b' open at infinity, both regions can be either closed or open. Further, the impressed sources $\bar{J}^i, \bar{M}^i$, have been shown to be present in region 'a' and region 'b' has been assumed to be source free. However, the more general case of
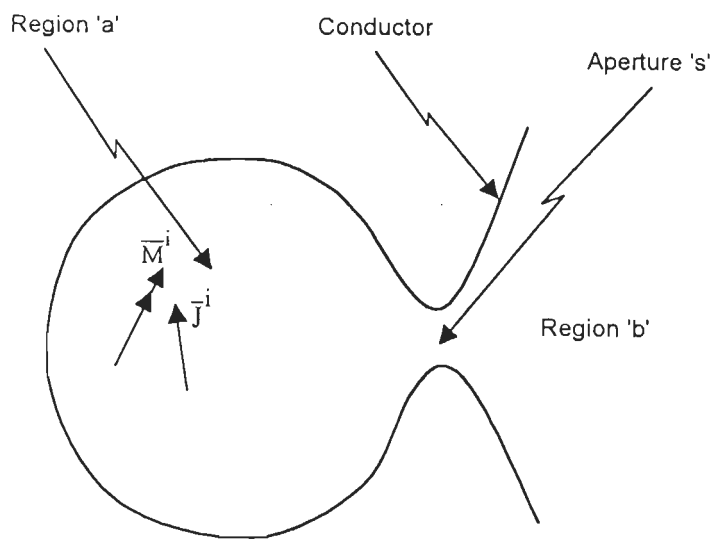
Fig. 2.1 : The general problem of two regions coupled by an aperture
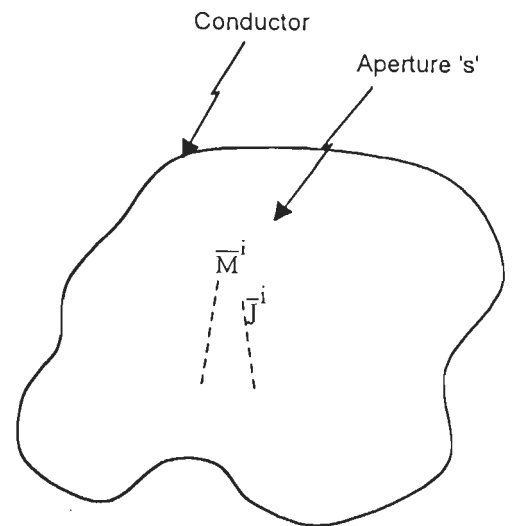
Fig. 2.2 : The planar view of the arbitrary-shaped aperture in Fig. 2.1.

sources in both regions can be treated as a superposition of two problems; one with sources in region 'a' only and the other with sources in region 'b' only.

As described in [46], field equivalence principle is first used to divide the problem into two separate parts. Aperture 's' is closed with a PEC and equivalent surface magnetic currents $\overline{M}$ and $-\overline{M}$ are placed over the aperture region on either side, as shown in Fig. 2.3. This enforces the continuity of tangential component of electric field across the aperture. The magnetic current $\overline{M}$ is given by

$$\overline{M} = \hat{n} \times \overline{E} \qquad\qquad (2.1)$$

where $\overline{E}$ is the electric field in the aperture of the original problem and $\hat{n}$ is the outward normal from region 'a'.

It is evident from Fig. 2.3 that the original problem has been divided into two equivalent problems, each of which can be formulated independent of each other. The field in region 'a' is due to the impressed sources $\overline{J}^i, \overline{M}^i$ and the equivalent surface magnetic current $\overline{M}$ over s with the aperture closed with a PEC, while the field in region 'b' is only due to the equivalent surface magnetic current $-\overline{M}$ over s in the presence of a complete conductor.

Enforcing the boundary condition that requires that tangential component of magnetic field should be continuous across the aperture, we obtain the operator equation

$$\overline{H}_t^a(\overline{M}) + \overline{H}_t^b(\overline{M}) = -\overline{H}_t^i \qquad\qquad (2.2)$$

where $\overline{H}_t^a(\overline{M})$ and $\overline{H}_t^b(\overline{M})$ respectively, denote the tangential (to s) components of magnetic field due to the current $\overline{M}$ in region 'a' and 'b' and $\overline{H}_t^i$ is the

tangential component due to the impressed sources $\overline{J}^i, \overline{M}^i$. It must be noted here that all the fields should be calculated with the aperture closed with a PEC.

The operator Eqn. (2.2) is an integro-differential equation which can only be solved approximately. We use the method of moments to obtain an approximate solution of (2.2).

Define a set of expansion functions $\{\overline{M}_n, n = 1, 2, \ldots, N\}$ over s

and let
$$\overline{M} = \sum_{n=1}^{N} V_n \overline{M}_n \tag{2.3}$$

where V_n are the complex coefficient vectors to be determined. Substituting (2.3) into (2.2) and using the linearity of the $\overline{H}_t$ operators gives

$$\sum_{n}^{N} V_n \overline{H}_t^a (\overline{M}_n) + \sum_{n}^{N} V_n \overline{H}_t^b (\overline{M}_n) = -\overline{H}_t^i \tag{2.4}$$

Next, define a symmetric product

$$<A, B> = \iint_{\text{over S}} \overline{A} \cdot \overline{B} \, dS \tag{2.5}$$

and a set of testing functions $\{\overline{W}_m, m = 1, 2, \ldots, N\}$ over s. Taking the symmetric product of (2.4) with each testing function $\overline{W}_m$, we obtain the set of algebraic equations

$$\sum_{n}^{N} V_n < W_m, H_t^a (\overline{M}_n)> + \sum_{n}^{N} V_n < W_m, H_t^b (\overline{M}_n)> = - <W_m, H_t^i>$$

$$m = 1, 2, \ldots, N \tag{2.6}$$

Eqn. (2.6) can be written in matrix form as

$$[Y^a + Y^b]\vec{V} = \vec{I}^i \tag{2.7}$$
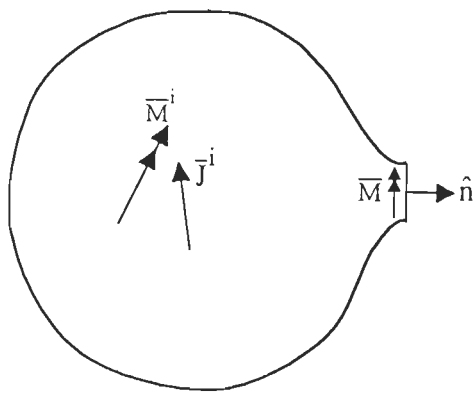
(a) Equivalent problem
(valid for region 'a')
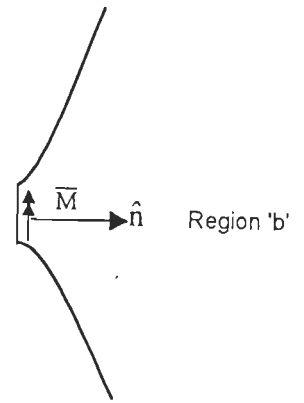
(b) Equivalent problem
(valid for region 'b')

Fig. 2.3 : Original problem divided into two equivalent problems

16

where $[Y^a]$ and $[Y^b]$ are, respectively, the aperture admittance matrices for region 'a' and region 'b' defined as

$$[Y^a] = [<W_m, H_t^a(\overline{M}_n)>]_{N \times N} \tag{2.8}$$

$$[Y^b] = [<W_m, H_t^b(\overline{M}_n)>]_{N \times N} \tag{2.9}$$

and $\overline{I}^i$ and $\vec{V}$ are, respectively, the source vector and measurement vector defined as

$$\overline{I}^i = [-<W_m, H_t^i>]_{N \times 1} \tag{2.10}$$

and $\quad \vec{V} = [V_n]_{N \times 1} \tag{2.11}$

2.2   CHOICE OF BASIS FUNCTIONS

The choice of basis functions in the MOM solution is critical because it determines the convergence and accuracy of results [1] and [111].

The commonly used basis functions can be broadly divided into two classes : whole domain functions and sub-domain functions. Whole-domain functions exist over the entire structure and are generally useful for problems with regular shape and where approximate distribution of the unknown quantity is known a priori. Sub-domain functions, on the other hand, offer greater flexibility in modelling complex structures. However, the most commonly used sub-domain functions such as rooftop and PWS functions, are not suitable for the present problem since an arbitrary-shaped surface cannot be approximated by rectangular patches. For an arbitrary-shaped aperture, triangular patch modelling as proposed by Rao [82] for scattering from bodies of arbitrary shape, is particularly appropriate as the shape of a triangle can conform easily to the

17

geometry of an arbitrary surface. Furthermore, a varying patch density can be incorporated in the discretization of regions where a higher resolution is desired.

Figure 2.4 depicts the triangulation of an aperture of irregular shape. A higher patch density has been taken around the edges where there is greater variation of contour gradient than elsewhere in the aperture in order to account for 'edge effect'.

Assuming that a proper triangulation scheme has been found for the aperture surface, let us consider a pair of triangle faces, denoted T_n^+ and T_n^-, having the nth edge (AB) as their common edge as shown in Fig. 2.5.

Figure 2.5 illustrates a triangle pair associated with the nth edge. Also shown are the local position vectors $\bar{\rho}_n^{\pm}$ and the global position vector $\bar{r}$. Any point in the triangles may either be located by its position vector $\bar{r}$ in a global coordinate system with respect to O or by its local position vectors $\bar{\rho}_n^{\pm}$ in $T_n^{\pm}$, defined with respect to free vertices F and F', respectively.

We define a vector basis function associated with the nth edge as

$$
\overline{M}_n = \begin{cases} \dfrac{l_n}{2A_n^+}\, \bar{\rho}_n^+, & \bar{r} \text{ in } T_n^+ \\[2mm] \dfrac{l_n}{2A_n^-}\, \bar{\rho}_n^-, & \bar{r} \text{ in } T_n^- \\[2mm] 0 & \text{otherwise} \end{cases} \tag{2.12}
$$

where l_n is the length of the edge and $A_n^{\pm}$ is the area of the triangle $T_n^{\pm}$. The designation T_n^+ or T_n^- is determined by choosing a positive current reference direction for the nth edge which is assumed to be from T_n^+ to T_n^-.
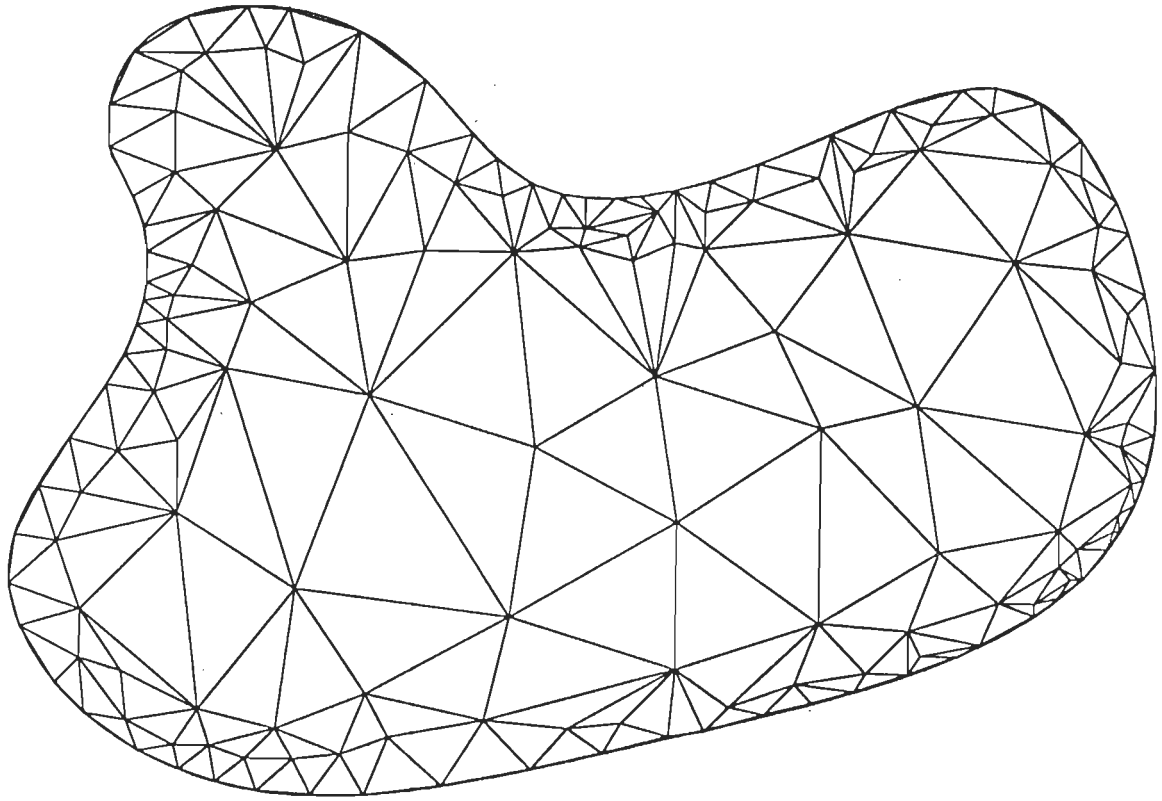
Fig. 2.4 : An irregularly-shaped aperture modelled by triangular patches
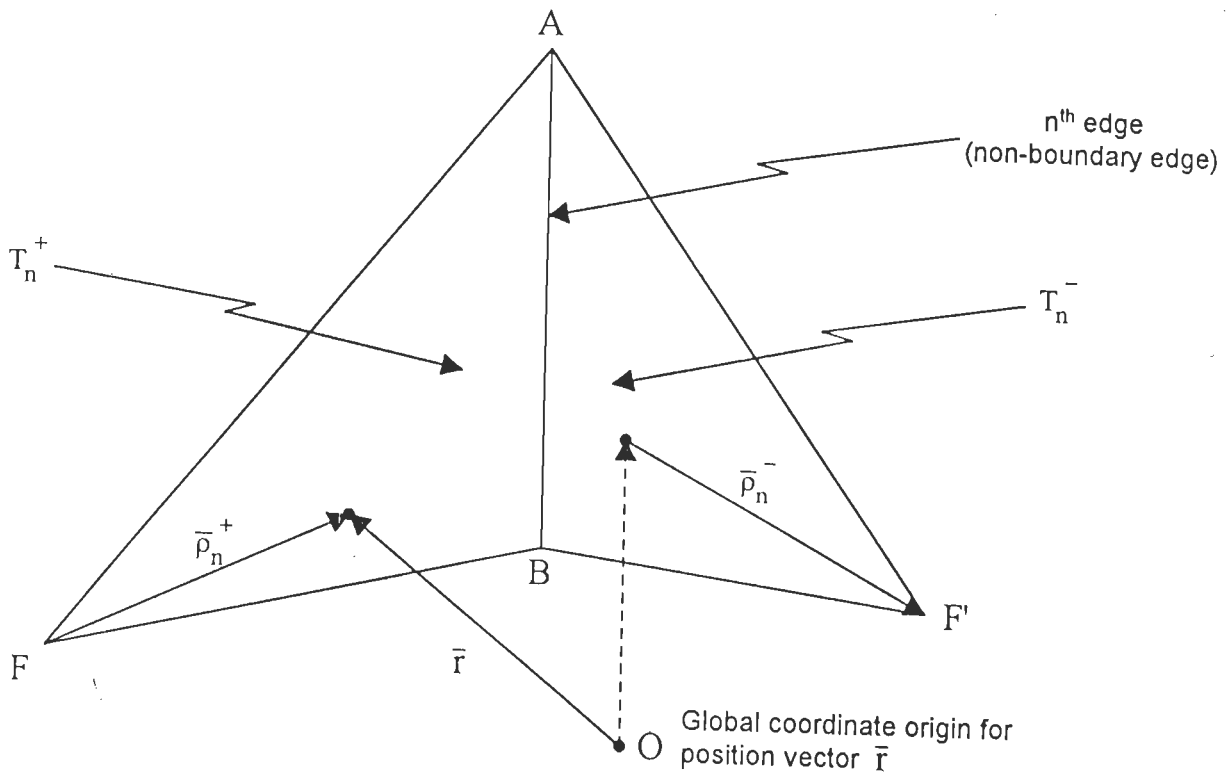
Fig. 2.5 : A triangle pair associated with the nth edge

Some of the unique properties of $\overline{M}_n$ which make it appropriate for the present problem are

(1) The current has no component normal to the boundary (which excludes the common edge) of the surface formed by the triangle pair T_n^+ and T_n^- and, as such, has no magnetic charge along this boundary. Thus, basis functions need not be defined on the edges which form the boundary of the aperture.

(2) From Fig. 2.6, since $\overline{\rho}_{n,normal}^+$ equals to $2A_n^+/l_n$ and $\overline{\rho}_{n,normal}^-$ to $2A_n^-/l_n$, from Eqn. (2.12), it is seen that the current at the edge is continuous and normalized to a value unity.

(3) Using the definition of $\overline{M}_n$ in (2.12), the associated magnetic charge density, m_n, is

$$m_n = -\frac{1}{j\omega} \nabla \cdot \overline{M}_n$$

$$= -\frac{1}{j\omega} \frac{\pm 1}{\rho_n^{\pm}} \frac{\partial(\rho_n^{\pm} M_n)}{\partial \rho_n^{\pm}}$$

$$= \begin{cases} \dfrac{-l_n}{j\omega A_n^+}, & \overline{r} \text{ in } T_n^+ \\[2mm] \dfrac{+l_n}{j\omega A_n^-}, & \overline{r} \text{ in } T_n^- \\[2mm] 0, & \text{otherwise} \end{cases} \qquad (2.13)$$

It is found that the charge density is constant in each triangle and the total charge associated with T_n^+ and T_n^- is zero.
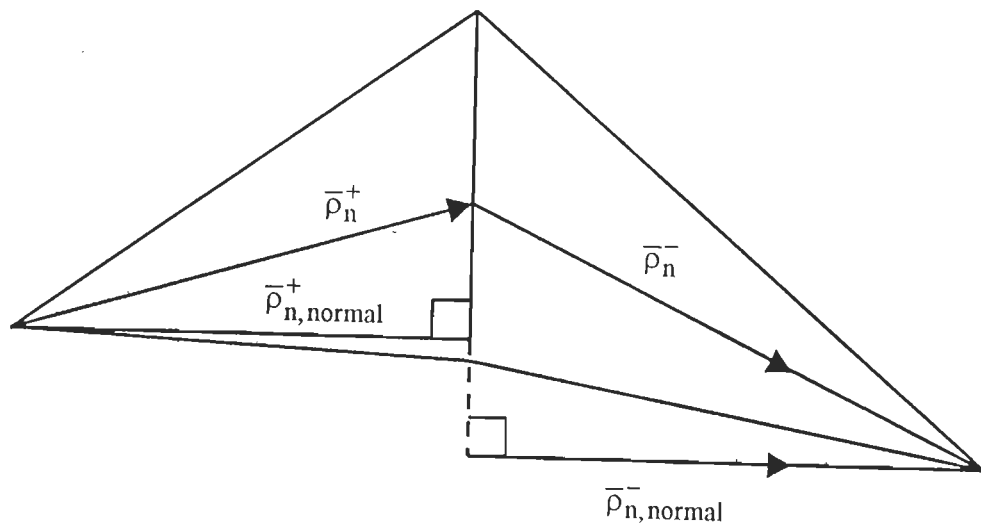
Fig. 2.6 : Normal components of the local position vectors

2.3   EVALUATION OF MATRIX ELEMENTS AND EXCITATION VECTOR

For computational simplicity, we follow Galerkin procedure with the weighting functions $\overline{W}_m = \overline{M}_m$.

From eqn. (2.8) or (2.9), a typical matrix element for the rth region is given by

$$Y_{mn}^r = <M_m, H_t^r(\overline{M}_n)> \tag{2.14}$$

$$= \iint\limits_{T_m^+} \overline{M}_m \bullet \overline{H}_t^r(\overline{M}_n)\,ds \;\; + \iint\limits_{T_m^-} \overline{M}_m \bullet \overline{H}_t^r(\overline{M}_n)\,ds$$

$$= \iint\limits_{T_m^\pm} \overline{M}_m \bullet \overline{H}_t^r(\overline{M}_n)\,ds \tag{2.15}$$

where the notation $\iint\limits_{T_m^+} (\qquad)\,ds$ has been introduced for compactness.

In terms of the electric vector potential $\overline{F}(\bar{r})$ and the magnetic scalar potential $\phi(\bar{r})$, the magnetic field $\overline{H}^r(\overline{M}_n)$ can be written as

$$\overline{H}^r(\overline{M}_n) = -j\omega \overline{F}_n(\bar{r}) - \nabla \phi_n(\bar{r}) \tag{2.16}$$

where $\overline{F}_n(\bar{r}) = \varepsilon \iint\limits_{T} \overline{\overline{G}}(\bar{r}/\bar{r}') \bullet \overline{M}_n(\bar{r}')\,ds' \tag{2.17}$

$$\phi_n(\bar{r}) = \frac{\nabla \bullet \overline{F}_n(\bar{r})}{-j\omega\mu\varepsilon} \tag{2.18}$$

In Eqn. (2.16), $\overline{\overline{G}}(\bar{r}/\bar{r}')$ denotes the dyadic Green's function of the region under consideration. It may also be noted here that the scalar product in Eqn. (2.15) automatically selects the component of $\overline{H}^r(\overline{M}_n)$ tangential to the aperture surface.

Using two-dimensional divergence theorem and the fact that there is no component of current expansion function normal to the boundary of the triangles $T_n^\pm$, substitution of Eqn. (2.16) in Eqn. (2.15) leads to

$$Y_{mn}^r = -j\omega \iint_{T_m^\pm} \overline{M}_m \bullet \overline{F}_n \, ds \ + \iint_{T_m^\pm} m_m \, \phi_n \, ds \qquad (2.19)$$

where $m_m = \dfrac{\nabla \bullet \overline{M}_m}{-j\omega}$ $\qquad\qquad (2.20)$

Eqn. (2.19) contains quadruple integrals; a double integral over the field triangles $T_m^\pm$ and a double integral over the source triangles $T_n^\pm$ involved in the computation of $\overline{F}_n(\overline{r})$ and $\phi_n(\overline{r})$. In order to reduce the numerical computations, the integrals over $T_m^\pm$ can be approximated by the values of integrals at the centroids of the triangles. This procedure yields

$$Y_{mn}^r = -l_m \left\{ j\omega \left[\overline{F}_n(\overline{r}_m^{c+}) \bullet \frac{\overline{\rho}_m^{c+}}{2} + \overline{F}_n(\overline{r}_m^{c-}) \bullet \frac{\overline{\rho}_m^{c-}}{2} \right] + \phi_n(\overline{r}_m^{c-}) - \phi_n(\overline{r}_m^{c+}) \right\} \quad (2.21)$$

where $\overline{F}_n(\overline{r}_m^{c\pm}) = \varepsilon \iint_{T_n^\pm} \overline{\overline{G}}(\overline{r}^{c\pm}|\overline{r}') \bullet \overline{M}_n(\overline{r}')ds'$ $\qquad (2.22)$

$$\phi_n(\overline{r}_m^{c\pm}) = \frac{-1}{j\omega\mu} \iint_{T_n^\pm} \left\{ \nabla \bullet \overline{\overline{G}}(\overline{r}^{c\pm}|\overline{r}') \right\} \bullet \overline{M}_n(\overline{r}')ds' \qquad (2.23)$$

In (2.21) to (2.23), $\overline{\rho}_m^{c\pm}$ are the local position vectors to the centroids of $T_m^\pm$ and $\overline{r}_m^{c\pm} = (\overline{r}_m^{1\pm} + \overline{r}_m^{2\pm} + \overline{r}_m^{3\pm})/3$ are the position vectors of centroids of $T_m^\pm$ with respect to the global coordinate system.

Similarly, using the centroid approximation in Eqn. (2.10), an element of excitation vector can be written as

$$I_m^i = -l_m \left\{ \overline{H}_t^i(\overline{r}_m^{c+}) \bullet \frac{\overline{\rho}_m^{c+}}{2} + \overline{H}_t^i(\overline{r}_m^{c-}) \bullet \frac{\overline{\rho}_m^{c-}}{2} \right\} \qquad (2.24)$$

2.4   EFFICIENT COMPUTATION OF INTEGRALS

Evaluation of each matrix element Y_{mn}^r involves the testing function associated with the mth edge and the basis function associated with the nth edge. However, the domain of integration is in triangle $T_n^{\pm}$ and the location of the observation points (r_m^{c+}, r_m^{c-}) are associated with the triangle faces attached to the mth edge. This implies that if edge-by-edge approach is used, integration over the same triangle face will be involved in the determination of several elements of Y_{mn}^r. A more efficient computation procedure would be to evaluate the integrals over all the triangular surfaces sequentially, store the results and use them in the computation of Y_{mn}^r after multiplication with appropriate factors.

Consider the evaluation of the vector potential and scalar potential integrals for a given source and observation face-pair. Figure 2.7 illustrates such a face-pair with the observation point in face p and with the source currents residing in face q. Each of the three basis functions which may possibly exist simultaneously in T^q is proportional to one of the vectors $\bar{\rho}_1, \bar{\rho}_2$ or $\bar{\rho}_3$ defined in the figure.

Each vector $\bar{\rho}_j$, $j = 1, 2, 3$ is shown directed away from its vertex but would be directed toward the vertex if the current reference direction from the associated edge was into the triangle. Consequently,

$$\bar{\rho}_j = \pm (\bar{r}' - \bar{r}_j) \tag{2.25}$$
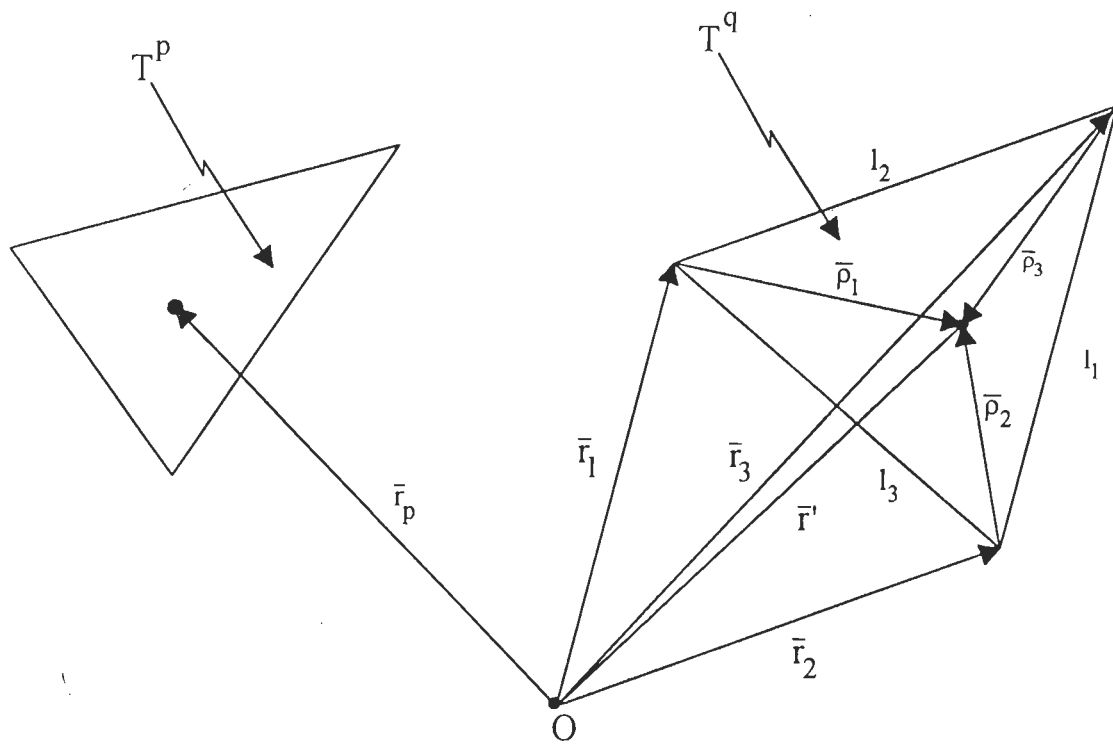
Fig. 2.7 : Local and global coordinates and edges of triangle T^q with observation point in triangle T^p

where the positive sign is used for the triangle T^{q+} and the negative sign for T^{q-}. $\bar{r}_p$ and $\bar{r}'$ are, respectively, position vectors of the field and source points.

If $\overline{F}_j^{pq}$ denotes the vector potential at $\bar{r}_p$ in T^p due to $\overline{M}_j$ $(j = 1, 2, 3)$ in T^q, it can be written as

$$\overline{F}_j^{pq} = \varepsilon \iint\limits_{T^q} \overline{\overline{G}}(\bar{r}_p / \bar{r}') \bullet \overline{M}_j(\bar{r}') \, ds' \tag{2.26}$$

and

$$\phi_j^{pq} = \frac{-\nabla \bullet \overline{F}_j^{pq}}{j\omega\mu\varepsilon} \tag{2.27}$$

The integrals encountered in this study can be classified into two categories : those pertaining to closed regions, e.g., waveguides and cavities and others pertaining to open regions, e.g., free space or half space. While the integrand of the former type is bounded at every point within the integration domain making numerical integration possible, the latter type of integrals have a singular kernel for coincident source and field points and require careful handling.

2.4-1 Integrals with a Singular Kernel

For the half space region, the dyadic Green's function $\overline{\overline{G}}(\bar{r}_p | \bar{r}')$ in Eqn. (2.26) is

$$\overline{\overline{G}}(\bar{r}_p | \bar{r}') = \overline{\overline{I}} \frac{e^{-jk|\bar{r}_p - \bar{r}'|}}{4\pi|\bar{r}_p - \bar{r}'|} \tag{2.28}$$

where $\overline{\overline{I}}$ is a unit dyad.

Substituting (2.28) in eqns. (2.26) and (2.27) gives

$$\overline{F}_j^{pq} = \frac{\varepsilon}{4\pi} \iint\limits_{T^q} \overline{M}_j(\overline{r}') \frac{e^{-jk|\overline{r}_p - \overline{r}'|}}{|\overline{r}_p - \overline{r}'|} ds' \tag{2.29}$$

$$\phi_j^{pq} = \frac{-1}{4\pi j\omega\mu} \iint\limits_{T^q} \nabla' \cdot \overline{M}_j(\overline{r}') \frac{e^{-jk|\overline{r}_p - \overline{r}'|}}{|\overline{r}_p - \overline{r}'|} ds' \tag{2.30}$$

Substitution of $\overline{M}_j(\overline{r}')$ from Eqn. (2.12) and $\nabla' \cdot \overline{M}_j(\overline{r}')$ from Eqn. (2.13) leads to

$$\overline{F}_j^{pq} = \frac{\varepsilon}{4\pi} \frac{l_j}{2A_q} \iint\limits_{T^q} \overline{\rho}_j \frac{e^{-jk|\overline{r}_p - \overline{r}'|}}{|\overline{r}_p - \overline{r}'|} ds' = \frac{\varepsilon}{4\pi} \frac{l_j}{2A_q} I_f \tag{2.31}$$

$$\phi_j^{pq} = \frac{\mp l_j}{4\pi j\omega\mu A_q} \iint\limits_{T^q} \frac{e^{-jk|\overline{r}_p - \overline{r}'|}}{|\overline{r}_p - \overline{r}'|} ds' = \frac{\mp l_j}{4\pi j\omega\mu A_q} I_p \tag{2.32}$$

where

$$I_f = \iint\limits_{T^q} \overline{\rho}_j \frac{e^{-jk|\overline{r}_p - \overline{r}'|}}{|\overline{r}_p - \overline{r}'|} ds' = \iint\limits_{T^q} \overline{\rho}_j \frac{e^{-jk|\overline{r}_p - \overline{r}'|} - 1}{|\overline{r}_p - \overline{r}'|} ds' + \iint\limits_{T^q} \overline{\rho}_j \frac{ds'}{|\overline{r}_p - \overline{r}'|}$$

$$= I_b + I_{s1} \tag{2.33}$$

$$I_p = \iint\limits_{T^q} \frac{e^{-jk|\overline{r}_p - \overline{r}'|}}{|\overline{r}_p - \overline{r}'|} ds' = \iint\limits_{T^q} \frac{e^{-jk|\overline{r}_p - \overline{r}'|} - 1}{|\overline{r}_p - \overline{r}'|} ds' + \iint\limits_{T^q} \frac{ds'}{|\overline{r}_p - \overline{r}'|}$$

$$= I_c + I_{s2} \tag{2.34}$$

$$I_b = \iint\limits_{T^q} \overline{\rho}_j \frac{e^{-jk|\overline{r}_p - \overline{r}'|} - 1}{|\overline{r}_p - \overline{r}'|} ds' \tag{2.35}$$

$$I_{s1} = \iint\limits_{T^q} \overline{\rho}_j \frac{ds'}{|\overline{r}_p - \overline{r}'|} \tag{2.36}$$

$$I_c = \iint\limits_{T^q} \frac{e^{-jk|\overline{r}_p - \overline{r}'|} - 1}{|\overline{r}_p - \overline{r}'|} ds' \tag{2.37}$$

$$I_{s2} = \iint_{T^q} \frac{ds'}{|\bar{r}_p - \bar{r}'|} \tag{2.38}$$

The integrals I_b and I_c have bounded kernels over the integration domain and can be evaluated using numerical integration techniques. However, the kernels of integrals I_{s1} and I_{s2} have a singularity for $\bar{r}_p = \bar{r}'$ and the integration domain is a plane triangle. Several workers have considered the evaluation of this type of integrals [110], [17] and [39]. We follow here the method proposed by Graglia [39].

Figure 2.8 depicts a plane triangle T^q with some of the parameters required for the evaluation of singular kernels. $\hat{t}_j$ and $\hat{n}_j$ are the unit tangent and unit normal, respectively, to the jth edge of T^q while L_j are the local area coordinates ($j = 1, 2, 3$).

Let $\bar{p}_j$ be the position vector of the jth vertex defined by

$$\bar{p}_j = (x_j, y_j) \qquad j = 1, 2, 3 \tag{2.39}$$

and l_j be the length of the side opposite the jth vertex expressed as

$$l_j = |\bar{p}_{m+j-1} - \bar{p}_{n+j+1}| \tag{2.40}$$

where m and n are dummy variables such that

$$m = \begin{cases} 3, & j = 1 \\ 0, & j = 2, 3 \end{cases}$$

and

$$n = \begin{cases} 0, & j = 1, 2 \\ -3, & j = 3 \end{cases}$$

The area of T^q denoted by Δ is given by

$$\Delta = |(\bar{p}_j - \bar{p}_{n+j+1}) \times (\bar{p}_{m+j-1} - \bar{p}_{n+j+1})| / l_2 \tag{2.41}$$
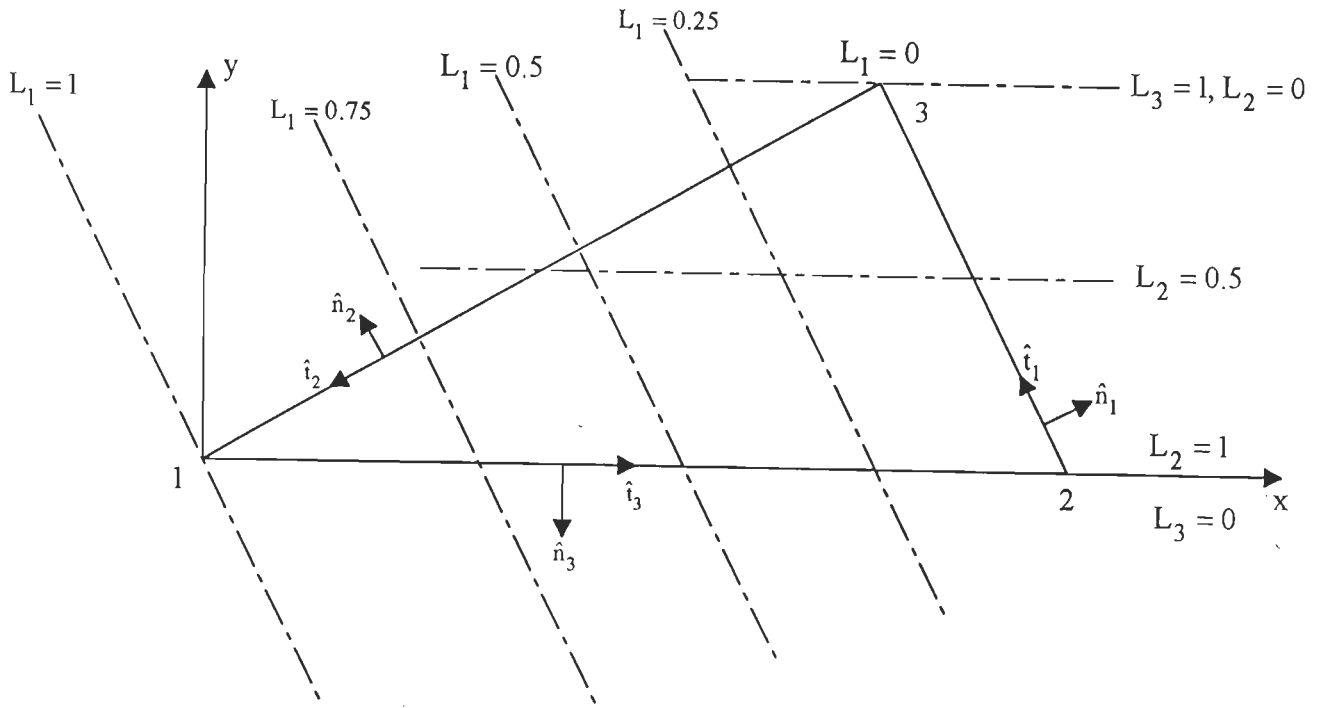
Fig. 2.8 : Unit tangent $\hat{t}_j$, unit normal $\hat{n}_j$ to the edges of T_q and area coordinate L_j (j = 1, 2, 3)

The unit outward normal, $\hat{n}$ on the plane of T^q is given by

$$\hat{n} = \frac{\{(\bar{p}_j - \bar{p}_{n+j+1}) \times (\bar{p}_{m+j-1} - \bar{p}_{n+j+1})\}}{2\Delta} \tag{2.42}$$

We define unit tangents $\hat{t}_j$ and unit normals $\hat{n}_j$ to the edges of T^q as

$$\hat{t}_j = (\bar{p}_{m+j-1} - \bar{p}_{n+j+1})/l_j \tag{2.43}$$

$$\hat{n}_j = \hat{t}_j \times \hat{n} \tag{2.44}$$

Cartesian coordinate system is not convenient for use with triangular shape. A convenient set of coordinates is the area coordinates L_1, L_2, L_3 [116] defined by the following linear relation between them and the Cartesian system :

$$\begin{aligned}
x' &= L_1 x_1 + L_2 x_2 + L_3 x_3 \\
y' &= L_1 y_1 + L_2 y_2 + L_3 y_3 \\
1 &= L_1 + L_2 + L_3
\end{aligned} \tag{2.45}$$

To every set L_1, L_2, L_3 (which are not independent but are related by the third equation above) corresponds a unique set of Cartesian coordinates. At vertex j, $L_j = 1$, $L_{j-1} = L_{j+1} = 0$. A linear relationship between these area coordinates and Cartesian coordinates implies that the contours of L_j are equally placed straight lines parallel to the side on which $L_j = 0$, etc. (Fig. 2.8).

Solving Eqn. (2.45) for x' and y'

$$\begin{aligned}
L_1 &= (a_1 + b_1 x' + c_1 y')/2\Delta \\
L_2 &= (a_2 + b_2 x' + c_2 y')/2\Delta \\
L_3 &= (a_3 + b_3 x' + c_3 y')/2\Delta
\end{aligned} \tag{2.46}$$

where

$$\begin{aligned}
a_1 &= x_2 y_3 - x_3 y_2 \\
b_1 &= y_2 - y_3 \\
c_1 &= x_3 - x_2
\end{aligned} \tag{2.47}$$

31

In a cyclic exchange of $1 \rightarrow 2 \rightarrow 3$,

$$a_2 = x_3 y_1 - x_1 y_3 \tag{2.48}$$

$$b_2 = y_3 - y_1$$

$$c_2 = x_1 - x_3$$

and

$$a_3 = x_1 y_2 - x_2 y_1 \tag{2.49}$$

$$b_3 = y_1 - y_2$$

$$c_3 = x_2 - x_1$$

For a simplex, such as a planar triangle, the shape functions denoted by N_1, N_2, N_3 are simply the area coordinates, i.e.

$$N_1 = L_1$$
$$N_2 = L_2 \tag{2.50}$$
$$N_3 = L_3$$

In Eqn. (2.45),

$$N_1 = 1 - N_2 - N_3 \tag{2.51}$$

which upon substituting in the first two equations in (2.45) gives

$$x' = x_1 + N_2 (x_2 - x_1) + N_3 (x_3 - x_1)$$
$$y' = y_1 + N_2 (y_2 - y_1) + N_3 (y_3 - y_1) \tag{2.52}$$

Also, in Eqn. (2.25), $\bar{r}'$ can be expressed as

$$\bar{r}' = \hat{x} x' + \hat{y} y'$$

$$= \hat{x} \{ x_1 + N_2 (x_2 - x_1) + N_3 (x_3 - x_1) \} + \hat{y} \{ y_1 + N_2 (y_2 - y_1) + N_3 (y_3 - y_1) \}$$

$$\tag{2.53a}$$

or

$$\bar{r}' = \bar{r}_1 + N_2 (\bar{r}_2 - \bar{r}_1) + N_3 (\bar{r}_3 - \bar{r}_1) \tag{2.53b}$$

Hence, $\bar{\rho}_j$ in Eqn. (2.25) can be written as

$$\bar{\rho}_j = \pm \left\{ (\bar{r}_1 - \bar{r}_j) + N_2 (\bar{r}_2 - \bar{r}_1) + N_3 (\bar{r}_3 - \bar{r}_1) \right\} \tag{2.54}$$

Substituting Eqn. (2.54) in Eqn. (2.36) gives

$$I_{s1} = \pm \left\{ (\bar{r}_1 - \bar{r}_j) \iint_{T^q} \frac{ds'}{|\bar{r}_p - \bar{r}'|} + (\bar{r}_2 - \bar{r}_1) \iint_{T^q} N_2 \frac{ds'}{|\bar{r}_p - \bar{r}'|} + (\bar{r}_3 - \bar{r}_1) \iint_{T^q} N_3 \frac{ds'}{|\bar{r}_p - \bar{r}'|} \right\} \quad (2.55)$$

I_{s2}, Eqn. (2.38) can be expressed in a similar manner as in [39, Eqn. 22], for

observation point lying on the plane of T^q, as

$$I_{s2} = \sum_{j=1}^{3} p_j^o \ln \left(\frac{t_j^+ + s_j^+}{t_j^- + s_j^-} \right) \quad (2.56)$$

where $p_j^o, t_j^{\pm}, s_j^{\pm}$ have been derived in Appendix-A and summarized as

$$s_j^{\pm} = |\bar{p}_j - \bar{p}_o| \quad (A-2)$$

$$\bar{p}_o = (x_p, y_p) \quad (2.57)$$

$$t_j^{\pm} = \bar{s}_j^{\pm} \bullet \hat{t}_j \quad (A-3)$$

$$p_j^o = \left| \left\{ (\bar{p}_{n+j+1} - \bar{p}_o) \times (\bar{p}_{n+j+1} - \bar{p}_{m+j-1}) / l_j \right\} \right| \quad (A-4)$$

or $\quad p_j^o = \left| (\bar{p}_{n+j+1} - \bar{p}_o) \times \hat{t}_j \right|$

In a similar manner as given in [39, Eqns. (23) and (24)], we can write

$$\iint_{T^q} \begin{bmatrix} N_1 \\ N_2 \\ N_3 \end{bmatrix} \frac{ds'}{|\bar{r}_p - \bar{r}'|} = \begin{bmatrix} N_1 \\ N_2 \\ N_3 \end{bmatrix} \sum_{j=1}^{3} p_j^o \ln \left(\frac{t_j^+ + s_j^+}{t_j^- + s_j^-} \right)$$

$$+ \frac{1}{2} \begin{bmatrix} \dfrac{-1}{l_3} & \dfrac{1}{y_3}\left(\dfrac{x_3}{l_3} - 1 \right) \\ \dfrac{1}{l_3} & \dfrac{-x_3}{l_3 y_3} \\ 0 & \dfrac{1}{y_3} \end{bmatrix} \begin{bmatrix} \hat{x} \\ \hat{y} \end{bmatrix} \bullet \sum_{j=1}^{3} \hat{n}_j f_{3j}^o \quad (2.58)$$

where $f_{3j}^o = \left(s_j^+ t_j^+ - s_j^- t_j^- \right) + (p_j^o)^2 \ln \left(\dfrac{t_j^+ + s_j^+}{t_j^- + s_j^-} \right)$ (2.59)

Eqns. (2.58) and (2.59) together with Eqn. (2.56) when substituted in Eqn. (2.55) give I_{sl}.

2.4-2 Integrals with Bounded Kernels

For the case of closed boundary regions, such as, waveguides and cavities, the potential integrals of eqns. (2.26) and (2.27) have kernels which are bounded over the integration domain T^q. Similarly, the integrals I_b and I_c of eqns. (2.35) and (2.37), respectively, have bounded kernels. These integrals can be integrated using numerical Gauss quadrature techniques. The integrals are conveniently evaluated in terms of area coordinates (L_1, L_2, L_3) following the procedure of Zienkiewicz [116].

Surface integrals in eqns. (2.26), (2.27), (2.35) and (2.37) can be transformed into integration over area coordinates (L_2, L_3) by the following transformation formula

$$\iint_{T^q} f(\bar{r}') ds' = 2A_q \int_0^1 \int_0^{1-L_2} f[\bar{r}_1 + (\bar{r}_2 - \bar{r}_1)L_2 + (\bar{r}_3 - \bar{r}_1)L_3] dL_2 \, dL_3$$ (2.60)

where $\bar{r}'$ is given by eqn. (2.53b) and a factor of $2A_q$ is derived in Appendix-B.

The right-hand side (RHS) of eqn. (2.60) and similar expressions developed for eqns. (2.26), (2.27), (2.35) and (2.37) are in a form amenable to numerical integration. For example, using Gauss-Legendre quadrature formula, the RHS of eqn. (2.60) can be evaluated as

34

$$2A_q \int_0^1 \int_0^{1-L_2} f\left[\bar{r}_1 + (\bar{r}_2 - \bar{r}_1)L_2 + (\bar{r}_3 - \bar{r}_1)L_3\right] dL_2 \, dL_3$$

$$= \sum_{k=1}^{kk} W(k) \, f\left[\bar{r}_1 + (\bar{r}_2 - \bar{r}_1)L_{2k} + (\bar{r}_3 - \bar{r}_1)L_{3k}\right] \qquad (2.61)$$

Where k denotes the kth sampling point in the domain of T^q, W(k) is the weighting factor for the kth sampling point, L_{2k} and L_{3k} are the L_2 and L_3 values at the kth sampling point. W(k), L_{2k}, L_{3k} are given in Table 2.1.

Table - 2.1

Gauss-Legendre Seven-Point Integration Formula

Sample	pt_1	pt_2	pt_3	pt_4	pt_5	pt_6	pt_7
L_2, L_3	V_1, V_1	V_2, V_2	V_2, V_3	V_3, V_2	V_4, V_4	V_4, V_5	V_5, V_7
Weight	W_a	W_b	W_b	W_b	W_c	W_c	W_c

$$V_1 = \frac{1}{3} \qquad\qquad W_a = \frac{9}{40}\Delta$$

$$V_2 = \frac{6 - \sqrt{15}}{21} \qquad\qquad W_b = \frac{155 - \sqrt{15}}{1200}\Delta$$

$$V_3 = \frac{9 + 2\sqrt{15}}{21} \qquad\qquad W_c = \frac{155 + \sqrt{15}}{1200}\Delta$$

$$V_4 = \frac{6 + \sqrt{15}}{21} \qquad\qquad \Delta = \text{Area of triangle}$$

$$V_5 = \frac{9 - 2\sqrt{15}}{21}$$

2.5 COMPUTATION OF APERTURE PARAMETERS

In the subsections that follow, we outline the computation of some important parameters that are used to characterize an aperture.

2.5-1 Magnetic Current Distribution over the Aperture

Since the aperture has been discretized into planar triangles, magnetic current distribution over each triangle, including that on its interior edge, is given by Eqn. (2.3) with $\overline{M}_j(\bar{r}')$ defined in Eqn. (2.12) as

$$\overline{M}_j(\bar{r}') = \frac{l_j}{2A_j} \begin{cases} \overline{\rho}_j, & \bar{r}' \text{ in } T_j^{\pm} \\ 0, & \text{otherwise} \end{cases}$$

in which $\overline{\rho}_j$ is given by Eqn. (2.25) as

$$\overline{\rho}_j = \pm (\bar{r}' - \bar{r}_j)$$

which can be written in terms of its components as

$$\overline{\rho}_j = \pm \left[\hat{x}(x'-x_j) + \hat{y}(y'-y_j) \right] \tag{2.62}$$

Therefore, x- and y-directed magnetic currents can be computed using eqns. (2.3), (2.12) and (2.62) as

$$M^x = \sum_{j=1}^{3} \frac{l_j}{2A_j} V_j (x'-x_j) \tag{2.63}$$

$$M^y = \sum_{j=1}^{3} \frac{l_j}{2A_j} V_j (y'-y_j) \tag{2.64}$$

where superscripts x and y, respectively, denote x-directed and y-directed magnetic currents.

2.5-2 Computation of Transmission Coefficient, T

The transmission coefficient T of an aperture is defined as the ratio of the time average power transmitted, denoted P_t, into region 'b' by the aperture to the time average incident power intercepted, denoted P_{inc}, by the aperture from region 'a'. Mathematically,

$$P_t = \text{Real} \iint_{apert} \overline{E}^t \times \overline{H}^{t*} \bullet d\overline{s} \tag{2.67}$$

Using Eqns. (2.9) and (2.11), P_t can be expressed as

$$P_t = \text{Real} \left\{ \widetilde{V}[y^b]^* \vec{V}^* \right\} \tag{2.68}$$

where tilde denotes transpose, asterisk complex conjugate and, E^t, H^t are the transmitted electric and magnetic fields, respectively.

P_{inc} is given by

$$P_{inc} = \text{Real} \iint_{apert} \overline{E}^i \times \overline{H}^{i*} \bullet d\overline{s} \tag{2.69}$$

where $\overline{E}^i$ and $\overline{H}^i$ are the electric and magnetic fields incident on the aperture. $\overline{E}^i$ and $\overline{H}^i$ depend on the type of excitation.

$$\text{Hence, } T = \frac{P_t}{P_{inc}} \tag{2.70}$$

It is to be noted that T depends on both the nature of source and the geometry of the aperture. A related quantity of interest is the transmission area TA, defined as the transmission coefficient times the area of the aperture. Thus,

$$TA = T * A_p \tag{2.71}$$

where A_p is the effective aperture area.

2.6 FAR-FIELD CALCULATIONS

The radiation field (far-field) may easily be calculated by making use of reciprocity theorem and the fact that the field of a magnetic current element is a known quantity [49].

Consider a magnetic dipole $\overline{K}$ at $\overline{r} = \overline{r}_m$, Fig. 2.9, with a current density given by

$$\overline{I}(\overline{r}) = \overline{K}\, \delta\, (\overline{r} - \overline{r}_m);$$

$$\delta\, (\overline{r} - \overline{r}_m) = \begin{cases} 1, \overline{r} = \overline{r}_m \\ 0, \text{ elsewhere} \end{cases} \tag{2.72}$$

Suppose the dipole produces a field $\overline{E}^m(\overline{r})$ and $\overline{H}^m(\overline{r})$ in free space. If $\overline{J}$ and $\overline{M}$ are the source currents, whether impressed or induced, whose field is to be found, then the dipole with its field and $\overline{J}, \overline{M}$ with their fields, comprise two source field pairs which must be related by reciprocity.

$$\iiint\limits_V (\overline{E}^a \bullet \overline{J}^b - \overline{H}^a \bullet \overline{M}^b)\, dv = \iiint\limits_V (\overline{E}^b \bullet \overline{J}^a - \overline{H}^b \bullet \overline{M}^a)\, dv \tag{2.73}$$

where $\overline{J}^a, \overline{M}^a$ and $\overline{J}^b, \overline{M}^b$ are two sets of sources in space at locations 'a' and 'b', respectively, and $\overline{E}^a, \overline{H}^a$ and $\overline{E}^b, \overline{H}^b$ are the fields at these locations. The integrations in Eqn. (2.73) include all space. Therefore, using Eqn. (2.72) in Eqn. (2.73) we may write

$$\overline{K} \bullet \overline{H}_m\, (\overline{r}_m) = \iiint\limits_V (\overline{J} \bullet \overline{E}^m - \overline{M} \bullet \overline{H}^m)\, dv \tag{2.74}$$

where $\overline{H}_m\, (\overline{r}_m)$ is the magnetic field due to $\overline{J}, \overline{M}$ at $\overline{r}_m$ and $\overline{E}^m, \overline{H}^m$ are the fields at location of $\overline{J}, \overline{M}$ due to the magnetic dipole. It is noted here that the various components of the far-field $\overline{H}_m\, (\overline{r}_m)$ may be obtained by orientating the magnetic dipole accordingly.
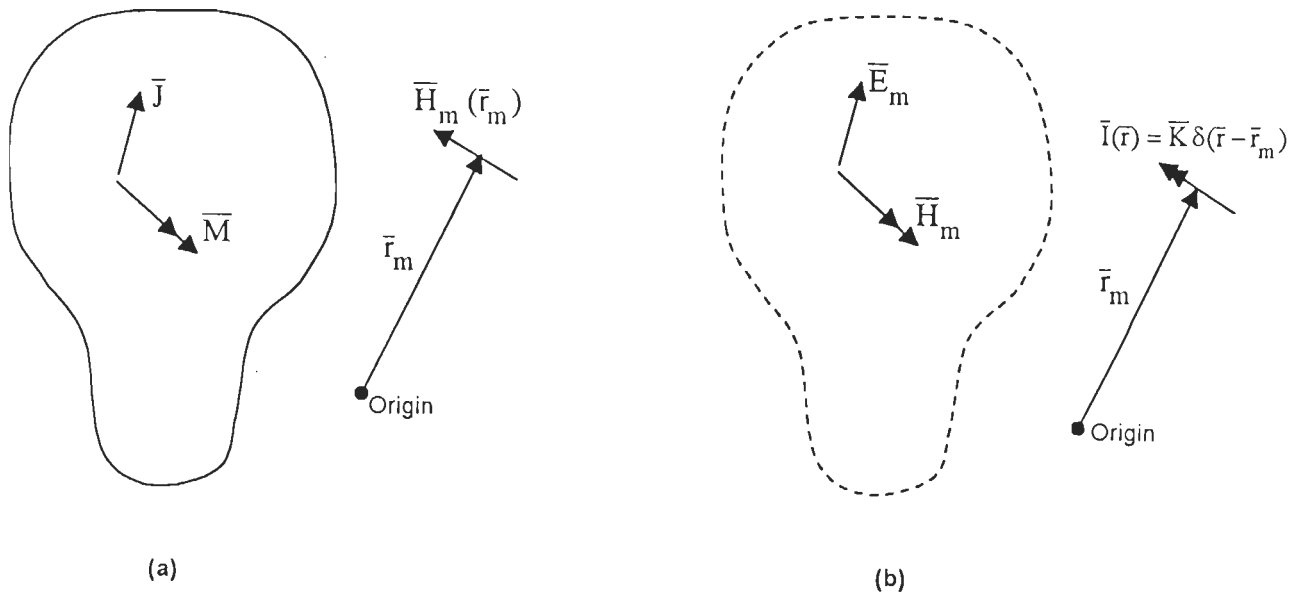
Fig. 2.9 : Source-field pairs for the evaluation of the radiation field of current sources $\bar{J}$ and $\overline{M}$.

2.6-1 Determination of Far-field Measurement Vector

For the general problem illustrated in Fig. 2.11, measurement of magnetic field $\overline{H}_m$ at an arbitrary point $\overline{r}_m$ in region 'b' depends linearly on magnetic current $-\overline{M}$ on 's'. As discussed earlier, this measurement may be done by placing a magnetic dipole $\overline{K} \, \delta \, (\overline{r} - \overline{r}_m)$ at $\overline{r}_m$ and applying the reciprocity theorem to its field and to the field of the original problem, in Fig. 2.3b. Now the set of sources comprises the dipole at $\overline{r}_m$ and the magnetic current $\overline{M}$ on 's' radiating in the presence of a continuous PEC at $z = 0$. The problem involving the magnetic dipole is called the adjoint problem and is shown in Fig. 2.10.
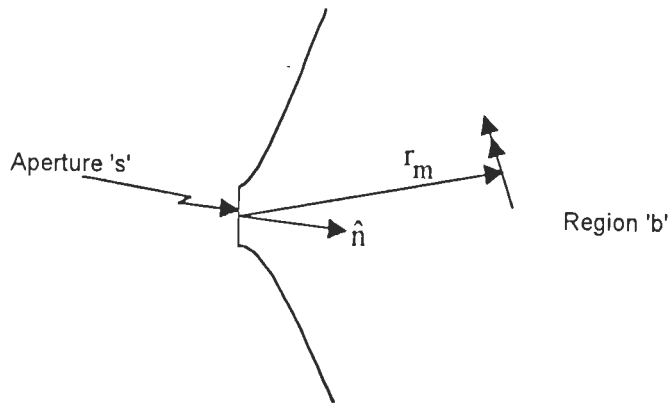
Fig. 2.10 : Adjoint problem for determining $\overline{\overline{H}}_m$

Both measurements of the fields are made in the presence of PEC. Application of the reciprocity theorem to these two fields yields

$$H_m K = - < M, H^m >$$

(2.75)

where H_m^1 is the magnetic field component in the direction of $\overline{K}$ at r_m due to $-\overline{M}$ in the presence of a PEC and $\overline{H}^m$ is the magnetic field from K in the presence of a PEC. To evaluate Eqn. (2.75) we substitute for $\overline{M}$, according to Eqn. (2.3), giving

$$H_m K = \sum_n V_n < -M_n, H^m >$$

$$= -\sum_n V_n \iint_{apert} \overline{M}_n \bullet \overline{H}^m \, ds \tag{2.76}$$

Since the scalar product in the integrand of Eqn. (2.76) would involve only the tangential component of the fields, we may write

$$H_m K = -\sum_n V_n < M_n, H_t^m > \tag{2.77}$$

or $\quad \overline{K} H_m = \left[\vec{P}^m \right] \vec{V} \tag{2.78}$

where $\vec{P}^m = -[< M_n, H_t^m >]_{N \times 1} \tag{2.79}$

In order to obtain a component of $\overline{H}_m$ on the radiation sphere, we orient the dipole $\overline{K}$ perpendicular to $\bar{r}_m$ and let r_m tend to infinity. At the same time, we adjust $\overline{K}$ so that it produces a unit plane wave in the vicinity of the origin. The required dipole moment is given by

$$\frac{1}{K} = \frac{-j \, \omega \, \varepsilon}{4 \, \pi \, r_m} \, e^{-j \bar{k}_0 \bullet \bar{r}_m} \tag{2.80}$$

where $k_0 = \dfrac{2 \pi}{\lambda} \tag{2.81}$

and the plane wave produced by it in the vicinity of the origin is

$$\overline{H}_m = \hat{u}_m \, e^{-j \bar{k}_m \bullet \bar{r}} \tag{2.82}$$

41

where $\hat{u}_m$ is the unit vector specifying the polarization of the wave, $\bar{k}_m$ is the wavenumber vector pointing in the direction of wave travel, and $\bar{r}$ is the position vector to an arbitrary point on s. Substituting Eqn. (2.80) in Eqn. (2.78), gives

$$H_m = \frac{-j\,\omega\,\varepsilon}{4\,\pi\,r_m}\, e^{-j\overline{K}_0 \cdot \overline{r}_m} \left[\overline{P}^m\right]^\Gamma \tag{2.83}$$

Once the measurement vector $\vec{P}^m$ is determined, the far-zone magnetic field can readily be calculated from (2.83). The procedure for determining $\vec{P}^m$ is outlined below.

Fig. 2.11 illustrates the cross-sectional view of the aperture (Fig. 2.2) and the geometry and parameters of the measurement vector.
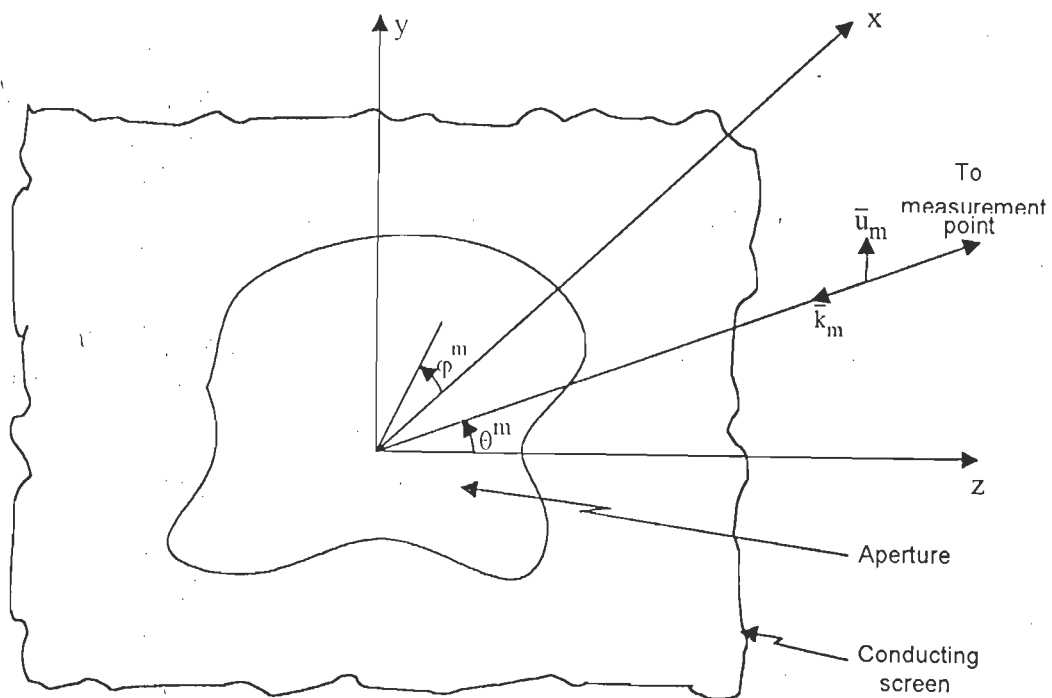
Fig. 2.11 : Cross-sectional view of aperture 's' and measurement vector in region 'b'

In the expression for $\vec{P}^m$ (Eqn. 2.79), $\overline{H}_t^m$ is the tangential component of the magnetic field at any point $\overline{r}$ on s which can be obtained, using the following

$$\overline{r} = \hat{x}\,x + \hat{y}\,y \tag{2.84}$$

$$\overline{k}_m = -k_0\,\overline{r}_m = -k_0\,(\hat{x}\sin\theta^m\cos\varphi^m + \hat{y}\sin\theta^m\sin\varphi^m + \hat{z}\cos\varphi^m) \tag{2.85}$$

$\overline{H}_t^m$ in Eqn. (2.79) can be written as

$$\overline{H}_t^m = 2H_{tx}^{mo}\,\hat{x} + 2H_{ty}^{mo}\,\hat{y} \tag{2.86}$$

where H_t^{mo} is the tangential component of the magnetic field when the dipole $\overline{K}$ is radiating into free space.

First we express Eqn. (2.25) in terms of its x and y components as

$$\overline{\rho}_n = \hat{x}\,\rho_{nx}^{\pm} + \hat{y}\,\rho_{ny}^{\pm} \tag{2.87}$$

which upon substituting in Eqn. (2.79) gives a component of $\overline{P}^m$ as

$$P_n^m = \frac{l_n}{A_n}\left\{ \iint_{A_q} H_{tx}^{mo}\,\rho_{nx}^{\pm}\,ds + \iint_{A_q} H_{ty}^{mo}\,\rho_{ny}^{\pm}\,ds \right\} \tag{2.88}$$

By applying Galerkin method and centroid approximation to (2.88), P_n^m may be written as

$$P_n^m = l_n\left\{ H_{tx}^{mo}(\overline{r}_n^{c+})\rho_{nx}^{c+} + H_{ty}^{mo}(\overline{r}_n^{c+})\rho_{ny}^{c+} + H_{tx}^{mo}(\overline{r}_n^{c-})\rho_{nx}^{c-} + H_{ty}^{mo}(\overline{r}_n^{c-})\rho_{ny}^{c-} \right\} \tag{2.89}$$

where $\overline{H}_t^{mo}(\overline{r}_n^{c\pm}) = (\hat{\theta}H_{\theta^m}^m + \hat{\varphi}H_{\varphi^m}^m)\,e^{j\overline{k}_m^- \cdot \overline{r}_m^{c\pm}} \tag{2.90}$

and from the definition of $\overline{r}_m^{c\pm}$ following Eqn. (2.23), we have

$$\overline{K}_m' \cdot \overline{r}_m^{c\pm} = \frac{-k_0}{3}\left[\left(x_n^{1\pm} + x_n^{2\pm} + x_n^{3\pm}\right)\sin\theta^m\cos\varphi^m + \left(y_n^{1\pm} + y_n^{2\pm} + y_n^{3\pm}\right)\sin\theta^m\cos\varphi^m\right. \tag{2.91}$$

43

The antenna power gain may be specialized to four principal planes given by

$$G_{yy}(\hat{u}_m = \hat{y}, \varphi^m = 0^o) \text{ for } y\text{-polarisation measurement in the}$$

$$y = 0 \text{ plane} \tag{2.92a}$$

$$G_{\theta y}(\hat{u}_m = \hat{\theta}, \varphi^m = 0^o) \text{ for } \theta\text{-polarisation measurement in the}$$

$$y = 0 \text{ plane} \tag{2.92b}$$

$$G_{\theta x}(\hat{u}_m = \hat{\theta}, \varphi^m = 90^o) \text{ for } \theta\text{-polarisation measurement in the}$$

$$x = 0 \text{ plane} \tag{2.92c}$$

and
$$G_{xx}(\hat{u}_m = \hat{x}, \varphi^{III} = 90^o) \text{ for } \theta\text{-polarisation measurement in the}$$

$$x = 0 \text{ plane} \tag{2.92d}$$

The magnetic fields in these four principal planes can be obtained as follows after substituting (2.91) in (2.90) :

$$(\overline{H}_t^{mo})_{yy}(\overline{r}_n^{c\pm}) = \hat{y}\, e^{\frac{jk_m}{3}(x_n^{1\pm}+x_n^{2\pm}+x_n^{3\pm})\sin\theta^m} \qquad \left(\frac{\pi}{2} \geq \theta^m \geq -\frac{\pi}{2}\right) \tag{2.93a}$$

$$(\overline{H}_t^{mo})_{\theta y}(\overline{r}_n^{c\pm}) = \hat{\theta}\, e^{\frac{jk_m}{3}(x_n^{1\pm}+x_n^{2\pm}+x_n^{3\pm})\sin\theta^m} \qquad \left(\frac{\pi}{2} \geq \theta^m \geq -\frac{\pi}{2}\right) \tag{2.93b}$$

$$(\overline{H}_t^{mo})_{\theta x}(\overline{r}_n^{c\pm}) = \hat{\theta}\, e^{\frac{jk_{III}}{3}(y_n^{1\pm}+y_n^{2\pm}+y_n^{3\pm})\sin\theta^{III}} \qquad \left(\frac{\pi}{2} \geq \theta^m \geq -\frac{\pi}{2}\right) \tag{2.93c}$$

$$(\overline{H}_t^{mo})_{xx}(\overline{r}_n^{c\pm}) = \hat{x}\, e^{\frac{jk_m}{3}(y_n^{1\pm}+y_n^{2\pm}+y_n^{3\pm})\sin\theta^m} \qquad \left(\frac{\pi}{2} \geq \theta^m \geq -\frac{\pi}{2}\right) \tag{2.93d}$$

2.6-2 Transmission Cross-section

Transmission cross-section τ is defined as that area in which the incident wave contains sufficient power to produce the radiation field $\overline{H}_m$ by omnidirectional radiation over half space.

Let the intrinsic impedances of region 'a' and region 'b' be η_a and η_b, respectively. Power incident, P_{inc}, on the aperture is given as

44

$$P_{inc} = \eta_a \, | \, H^{io} \, |^2 \tag{2.94}$$

and power transmitted, P_t, by the aperture as

$$P_t = \eta_b \, | \, H_m \, |^2 \tag{2.95}$$

τ is then determined by the ratio of P_t/P_{inc} over half space S (where area of $S = 2\pi r_m^2$).

Thus, $\tau = 2\pi r_m^2 \eta_b \, | \, H_m \, |^2 \, / \, \eta_a \, | \, H^{io} \, |^2$ \hfill (2.96)

where $\overline{H}^{io}$ is the magnetic field over the aperture de to sources $\overline{J}^i$, $\overline{M}^i$ in free space.
$\overline{H}^{io}$ components have been derived in Sec. 3.2. The far-zone magnetic field $\overline{H}_m$ has been expressed in the four principal planes by eqns. 2.93(a)-(d), η_a and η_b are the intrinsic impedances of region 'a' and region 'b', respectively..

2.6-3 Determination of Power Gain Pattern

Antenna power gain $G(\theta,\phi)$ is the ratio of the radiation intensity in a given direction to the radiation intensity which would exist if the total power were radiated uniformly in half space. That is

$$G(\theta,\phi) = \frac{\psi(\theta,\phi)}{\psi_{av}} \tag{2.97}$$

If P_t is the total complex power radiated into half space the average radiated power is

$$\psi_{av} = Real(P_t)/2\pi \tag{2.98}$$

Also, the radiation intensity in a given direction [49] is

$$\psi(\theta,\phi) = r_m^2 | H_m |^2 /\eta \tag{2.99}$$

where $\overline{H}_m$ is the magnetic field intensity at the measurement point and r_m is the distance of this point from the origin of coordinates.

Substituting (2.98) and (2.99) in (2.97), we obtain

$$G(\theta,\phi) = \frac{k_o^2 \eta}{8\pi \, \mathrm{Re}(P_t)} \, |[\vec{p}^m]^T \vec{V}|^2 \tag{2.100}$$

The complex power P_t transmitted through the aperture in Eqn. (2.67) is

$$P_t = \iint\limits_{\mathrm{apert}} \overline{E} \times \overline{H}^* \cdot \hat{z} \, ds \tag{2.101}$$

Using Eqn. (2.1), P_t may be written as

$$P_t = \iint\limits_{\mathrm{apert}} \overline{M} \cdot \overline{H}^* \, ds \tag{2.102}$$

Since the transmitted power is dependent only on the tangential component of $\overline{H}$ at

$z = 0$, using Eqn. (2.3) and the tangential component of $\overline{H}^*$ yields

$$[\overline{H}_t^b]^* = \sum_{n=1}^{N} V_n^* \, [H_t^b(-\overline{M}_n)]^* \tag{2.103}$$

which upon substituting in (2.102) together with substitution for $\overline{M}$ according to (2.103) gives P_t as

$$P_t = -\sum_{m=1}^{M} V_m V_n^* \iint\limits_{\mathrm{apert}} \overline{M}_m \cdot [\overline{H}_t^b(\overline{M}_n)]^* \, ds \tag{2.104}$$

Using (2.9) and (2.11), P_t may be expressed in a matrix form as

$$P_t = [\vec{V}]^T [Y^b]^* \vec{V}^* \tag{2.105}$$

Substituting (2.104) and (2.105) in (2.103), the expression for the power gain becomes

$$G(\theta,\phi) = \frac{k_o^2 \eta}{8\pi} \frac{|[\vec{p}^m]^T [Y]^{-1} \vec{I}|^2}{\mathrm{Re}\left\{[Y]^{-1} \vec{I}\right\}^T [Y^b]^* \left\{[Y]^{-1} \vec{I}^*\right\}} \tag{2.106}$$

where $[Y]^{-1} = [Y^a + Y^b]^{-1}$

46

2.7 SUMMARY

In this chapter, a general formulation for the boundary value problem of an aperture of arbitrary shape coupling two arbitrary regions has been developed. General equations for solving the various matrices, aperture surface magnetic current distributions, transmission coefficient, transmission area and antenna gain patterns have been derived.

Chapter - 3

ELECTROMAGNETIC TRANSMISSION THROUGH AN APERTURE IN A CONDUCTING SCREEN

In this chapter, the problem of two dissimilar regions, both open at infinity, coupled via an arbitrarily-shaped aperture in a conducting screen is considered. The problem is a special case of the general problem discussed in Chapter 2.

3.1 FORMULATION

The geometry of the problem under investigation is shown in Fig. 3.1. The $z = 0$ plane is covered by a perfectly conducting screen except for an aperture, which can be of any shape. The regions on either side of the screen are assumed to be different dielectric media with electrical parameters (μ_a, ε_a) and (μ_b, ε_b), respectively. The excitation is due to a plane wave, which is obliquely incident on the aperture.

As discussed in Chapter 2 and depicted in Fig. 3.2, equivalence principle is utilized to divide the problem into two separate regions, namely, region 'a' $(z < 0)$ and region 'b' $(z > 0)$.
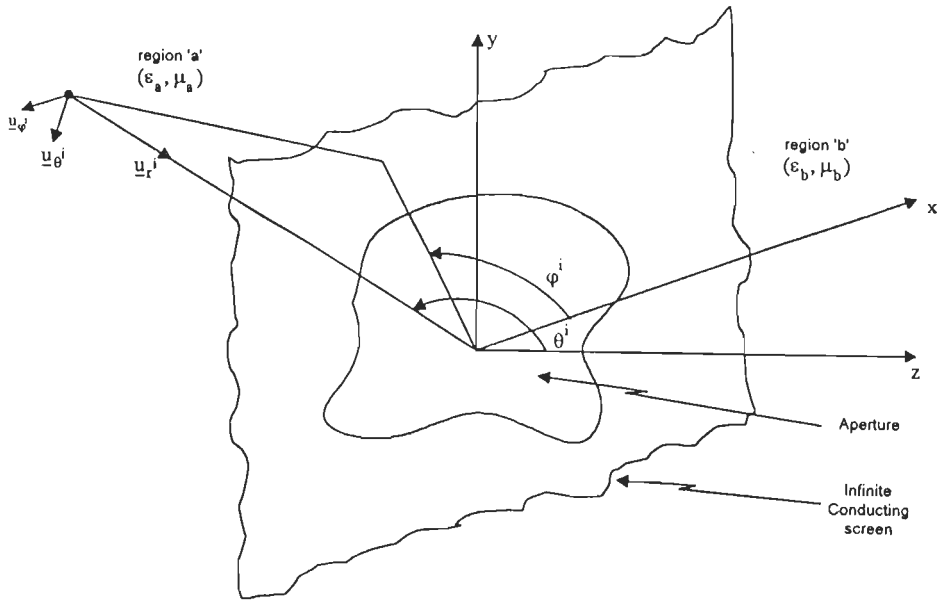
Fig. 3.1 : An Arbitrarily-shaped Aperture in an Infinite Conducting Screen
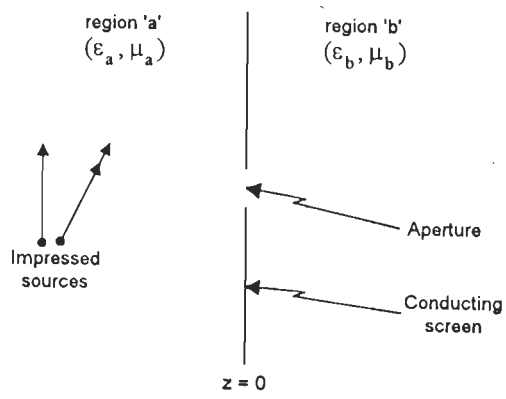
(a) Original Problem
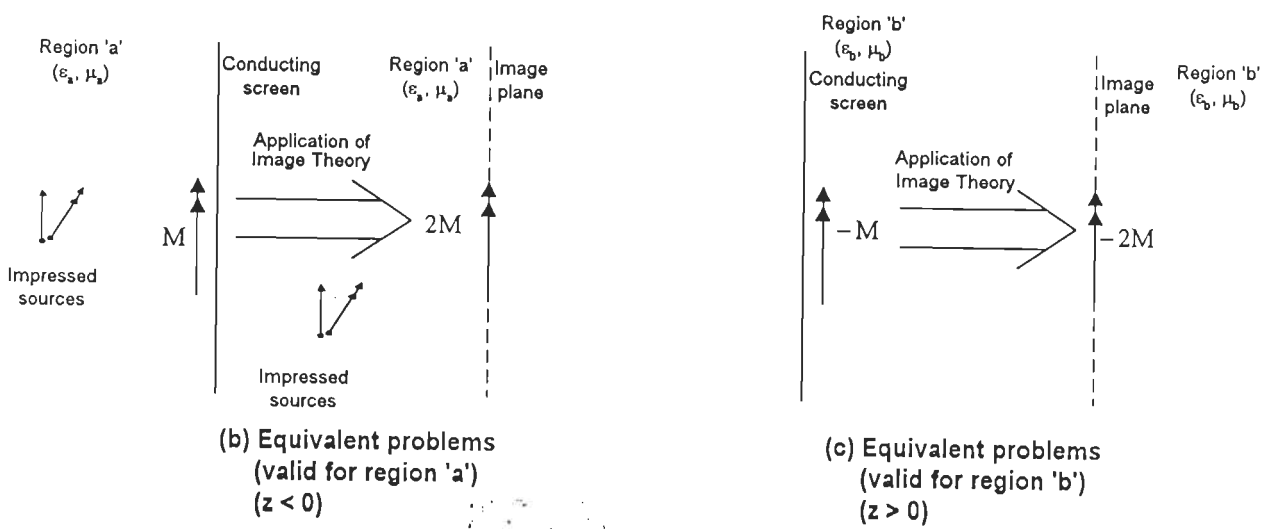
(b) Equivalent problems (valid for region 'a') (z < 0)

(c) Equivalent problems (valid for region 'b') (z > 0)

Fig. 3.2 : Original Problem and its Equivalent Models

The problem is now described by matrix equation

$$[Y^a + Y^b]\vec{V} = \vec{I}^i \tag{3.1}$$

where the aperture admittance matrices for region 'a' and region 'b' are given by

$$[Y^a] = [<M_m, H_t^a(2\overline{M}_n)>]_{NxN} \tag{3.2}$$

$$[Y^b] = [<M_m, H_t^b(2\overline{M}_n)>]_{NxN} \tag{3.3}$$

and $\vec{I}$ and $\vec{V}$ are, respectively, the source vector and unknown coefficient vector defined as

$$\vec{I}^i = [- <M_m, H_t^i>]_{Nx1} \tag{3.4}$$

$$\vec{V} = [V_n]_{Nx1} \tag{3.5}$$

3.2 EVALUATION OF MATRIX ELEMENTS AND EXCITATION VECTOR

Using the centroid approximation discussed in sec. 2.3 the elements of the aperture admittance matrices can be written as

$$Y_{mn}^a = -2l_m \left\{ j\omega \left[\overline{F}_n^a(r_m^{c+}) \cdot \frac{\overline{\rho}_m^{c+}}{2} + \overline{F}_n^a(\overline{r}_m^{c-}) \cdot \frac{\overline{\rho}_m^{c-}}{2} + \phi_n^a(\overline{r}_m^{c-}) - \phi_n^a(\overline{r}_m^{c+}) \right] \right\} \tag{3.6}$$

$$Y_{mn}^b = -2l_m \left\{ j\omega \left[\overline{F}_n^b(r_m^{c+}) \cdot \frac{\overline{\rho}_m^{c+}}{2} + \overline{F}_n^b(\overline{r}_m^{c-}) \cdot \frac{\overline{\rho}_m^{c-}}{2} + \phi_n^b(\overline{r}_m^{c-}) - \phi_n^b(\overline{r}_m^{c+}) \right] \right\} \tag{3.7}$$

where $\overline{F}_n^r(\overline{r}_m^{c\pm}) = \varepsilon_r \iint\limits_{T_n^{\pm}} \overline{\overline{G}}^r(\overline{r}^{c\pm}|\overline{r}') \cdot \overline{M}_n(\overline{r}')ds' \tag{3.8}$

$$\phi_n^r(\overline{r}_m^{c\pm}) = \frac{-1}{j\omega\mu_r} \iint\limits_{T_n^{\pm}} \left\{ \nabla' \cdot \overline{\overline{G}}^r(\overline{r}^{c\pm}|\overline{r}') \right\} \cdot \overline{M}_n(\overline{r}')ds' \tag{3.9}$$

In eqns. (3.8) and (3.9), superscript r (either a or b) denotes the region and $\overline{\overline{G}}^r(\overline{r}^{c\pm}/\overline{r}')$ is the dyadic Green's function.

G10, 201

Evaluation of matrices Y_{mn}^{a} and Y_{mn}^{b} given by eqns (3.6) and (3.7), respectively, involves a number of integrals given by eqns. (2.35) to (2.38), which are repeated here for the sake of completeness.

$$I_b = \iint_{T^q} \bar{\rho}_j \frac{(e^{-jk|\bar{r}_p - \bar{r}'|} - 1)}{|\bar{r}_p - \bar{r}'|} \, ds' \tag{3.10}$$

$$I_{s1} = \iint_{T^q} \bar{\rho}_j \frac{ds'}{|\bar{r}_p - \bar{r}'|} \tag{3.11}$$

$$I_c = \iint_{T^q} \frac{(e^{-jk|\bar{r}_p - \bar{r}'|} - 1)}{|\bar{r}_p - \bar{r}'|} \, ds' \tag{3.12}$$

$$I_{s2} = \iint_{T^q} \frac{ds'}{|\bar{r}_p - \bar{r}'|} \tag{3.13}$$

Eqns. (3.11) and (3.13) are evaluated as per procedure in sub-section 2.4.1. The remaining two integrals can be evaluated as described below.

Using eqn. (2.60) in conjunction with eqn. (2.54), eqns. (3.10) and (3.12) can be written as

$$
I_b = 2A_q \left\{ (\bar{r}_i - \bar{r}_j) \int_0^1 \int_0^{1-L_2} \frac{(e^{-jk|\bar{r}_p - \bar{r}'|} - 1)}{|\bar{r}_p - \bar{r}'|} \, dL_2 \, dL_3 \right.
$$

$$
+ (\bar{r}_2 - \bar{r}_1) \int_0^1 \int_0^{1-L_2} L_2 \frac{(e^{-jk|\bar{r}_p - \bar{r}'|} - 1)}{|\bar{r}_p - \bar{r}'|} \, dL_2 \, dL_3
$$

$$
\left. + (\bar{r}_3 - \bar{r}_1) \int_0^1 \int_0^{1-L_2} L_3 \frac{(e^{-jk|\bar{r}_p - \bar{r}'|} - 1)}{|\bar{r}_p - \bar{r}'|} \, dL_2 \, dL_3 \right\} \tag{3.14}
$$

$$
I_c = 2A_q \int_0^1 \int_0^{1-L_2} \frac{(e^{-jk|\bar{r}_p - \bar{r}'|} - 1)}{|\bar{r}_p - \bar{r}'|} \, dL_2 \, dL_3 \tag{3.15}
$$

where $|\bar{r}_p - \bar{r}'| = |(\bar{r}_p - \bar{r}_1) - ((\bar{r}_2 - \bar{r}_1)L_2 + (\bar{r}_3 - \bar{r}_1)L_3)|$ (3.16)

Applying Gauss-Legendre quadrature formula given by eqn. (2.61) to eqns. (3.14) and (3.15), we can write

$$I_b = A_q \sum_{s=1}^{kk} W(s) \left\{ (\bar{r}_i - \bar{r}_j) \frac{(e^{-jk|\bar{r}_p - \bar{r}'|} - 1)}{|\bar{r}_p - \bar{r}'|} \right.$$

$$\left. + (\bar{r}_2 - \bar{r}_1) \frac{(e^{-jk|\bar{r}_p - \bar{r}'|} - 1)}{|\bar{r}_p - \bar{r}'|} L_{2s} + (\bar{r}_3 - \bar{r}_1) \frac{(e^{-jk|\bar{r}_p - \bar{r}'|} - 1)}{|\bar{r}_p - \bar{r}'|} L_{3s} \right\}$$ (3.17)

$$I_c = A_q \sum_{s=1}^{kk} W(s) \left\{ \frac{(e^{-jk|\bar{r}_p - \bar{r}'|} - 1)}{|\bar{r}_p - \bar{r}'|} \right\}$$ (3.18)

in which $|\bar{r}_p - \bar{r}'|$ in eqn. (3.16) is now given by

$$|\bar{r}_p - \bar{r}'| = |(\bar{r}_p - \bar{r}_1) - ((\bar{r}_2 - \bar{r}_1)L_{2s} + (\bar{r}_3 - \bar{r}_1)L_{3s})|$$ (3.19)

3.2-1 Evaluation of Excitation Vector

Excitation vector $\bar{I}^i$ is given by eqn. (3.4) as

$$\bar{I}^i = [- <M_m, H_t^i>]_{Nx1}$$ (3.20)

For the present case, when the aperture is closed with a conductor, we have

$$\overline{H}_t^i = 2\overline{H}_t^{io}$$ (3.21)

where $\overline{H}_t^{io}$ is the tangential component of the magnetic field over the aperture region for a plane wave travelling in free space, which can be written as

$$\overline{H}_t^{io} = \left(\hat{u}_{\theta^i} H_\theta^i + \hat{u}_{\varphi^i} H_\varphi^i \right) e^{-j\bar{k}^i \cdot \bar{r}_m}$$ (3.22)

$$\bar{k}^i = \hat{u}_{r^i} k^i = k^i \left(\hat{x} \sin\theta^i \cos\varphi^i + \hat{y} \sin\theta^i \sin\varphi^i + \hat{z}\cos\theta^i \right)$$ (3.23)

where $\hat{u}_{r^i}$ is a unit vector specifying the direction of the incident wave and $\overline{k}^i$ is the propagation vector.

Substituting eqn. (3.21) in eqn. (2.24) gives an element of excitation vector as

$$I_m^i = -2l_m \left\{ \overline{H}_t^{io}(\overline{r}_m^{c+}) \bullet \frac{\overline{\rho}_m^{c+}}{2} + \overline{H}_t^{io}(\overline{r}_m^{c-}) \bullet \frac{\overline{\rho}_m^{c-}}{2} \right\} \tag{3.24}$$

where $\overline{H}_t^{io}(\overline{r}_m^{c\pm})$ can be broken up into its x- and y- components as :

$$\overline{H}_t^{io}(\overline{r}_m^{c\pm}) = \hat{x}\, H_{tx}^{io}(\overline{r}_m^{c\pm}) + \hat{y}\, H_{ty}^{io}(\overline{r}_m^{c\pm}) \tag{3.25}$$

Further, using eqn. (3.22), $H_{tx}^{io}(\overline{r}_m^{c\pm})$ and $H_{ty}^{io}(\overline{r}_m^{c\pm})$ can be expressed as

$$H_{tx}^{io}(\overline{r}_m^{c\pm}) = \left[H_\theta^i \cos\theta^i \cos\varphi^i - H_\varphi^i \sin\varphi^i \right] e^{-j\overline{k}^i \bullet \overline{r}_m^{c\pm}} \tag{3.26}$$

$$H_{ty}^{io}(\overline{r}_m^{c\pm}) = \left[H_\theta^i \cos\theta^i \sin\varphi^i + H_\varphi^i \cos\varphi^i \right] e^{-j\overline{k}^i \bullet \overline{r}_m^{c\pm}} \tag{3.27}$$

Using expression for $\overline{r}_m^{c\pm}$ in eqn. (2.23), $\overline{k}^i \bullet \overline{r}_m^{c\pm}$ can be expressed as

$$\overline{k}^i \bullet \overline{r}_m^{c\pm} = \frac{k^i}{3}\left[\left(x_m^{1\pm} + x_m^{2\pm} + x_m^{3\pm} \right) \sin\theta^i \cos\varphi^i \right.$$

$$\left. + \left(y_m^{1\pm} + y_m^{2\pm} + y_m^{3\pm} \right) \sin\theta^i \sin\varphi^i \right] \tag{3.28}$$

3.3   RESULTS AND DISCUSSION

Based on the preceding formulation, a general computer program has been developed which can be used to analyse apertures of arbitrary shape in an infinite conducting screen separating two dissimilar regions. The formulation has been validated by considering a rectangular aperture for which results are available in the literature [67]. Thereafter a number of aperture shapes have been studied which include rectangular, circular, elliptical, diamond, cross and H.

For each aperture shape, different discretization schemes were considered before arriving at the optimum one. Similarly, convergence studies were made in each case to determine the number of expansion functions that should be used.

In this section, we present some representative results for different aperture shapes. For simplicity, the regions on either side of the screen are considered to be free space and a y-polarised plane wave (H_x) of unit amplitude has been assumed to be incident normally on the aperture.

3.3-1 Rectangular Slot

The first example is a narrow slot of width $\lambda/20$ with its length along x-direction. Fig. 3.3 shows the triangulation scheme for the slot. The slot surface is discretized into 56 triangular patches resulting in 68 non-boundary edges (68 expansion functions). The associated nodes, edges and current directions in triangle edges are also shown.

The edges are ordered according to the directions of the arrows. This ensures the continuity of magnetic current across each edge (excluding the boundary edge, on which current is zero). The + and − signs denote T^+ and T^- triangles, respectively, associated with an edge.
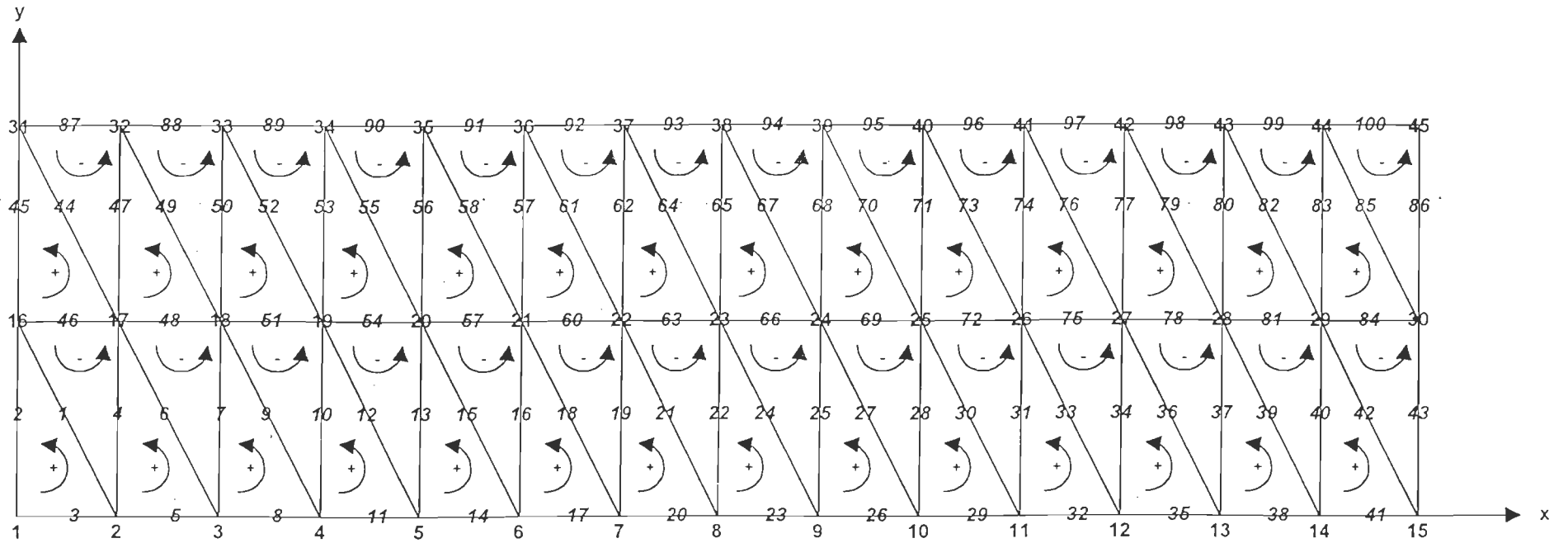
Fig. 3.3 : Rectangular Slot Discretization Showing Nodes, Edges and Current Directions

55

Table 3.1 shows the results for convergence study on transmission coefficient as a function of the number of expansion functions generated by varying triangular patch density over the slot surface.

Table - 3.1

Convergence of Transmission Coefficient

Slot Length L	No. of Expansion Functions N	Transmission Coefficient T	% Change in T
λ/4	38	0.1719670	
	48	0.1795997	4.44
	53	0.1825320	1.63
	68	0.1839750	0.80
λ/2	38	8.340040	
	48	8.169690	-2.11
	53	8.028399	-1.79
	68	7.956730	-0.89
3λ/4	48	2.141330	
	53	2.126040	-0.7
	68	2.122330	-0.2
λ	38	1.547793	
	48	1.521988	-1.67
	53	1.520760	-0.80
	68	1.519995	-0.15

From the table, it is noted that 48 expansion functions are quite sufficient to yield converged results.

Fig. 3.4 and Fig. 3.5 show the magnetic current distributions and the transmission cross-sections, respectively, for slots of various lengths, which were obtained using 68 expansion functions resulting from the discretization shown in Fig. 3.3. For comparison, we have also plotted the results obtained by Mautz and Harrington [67] using rooftop functions (RTF). It is found that our results are in good agreement with their results for slots of length λ/2, 3λ/4 and λ.
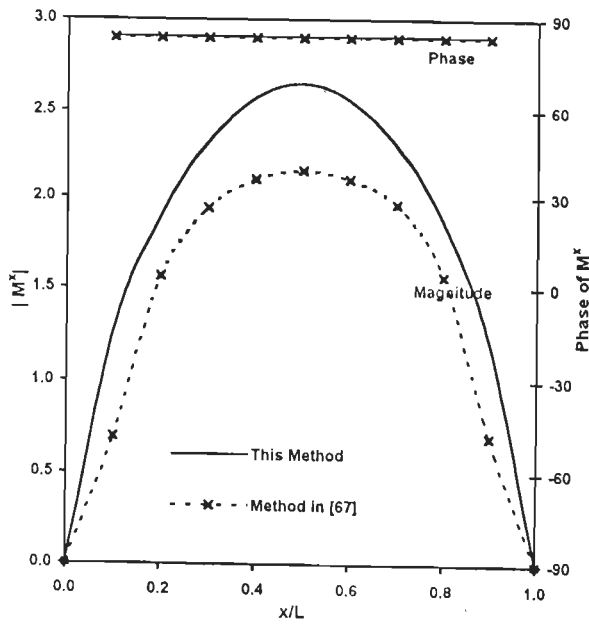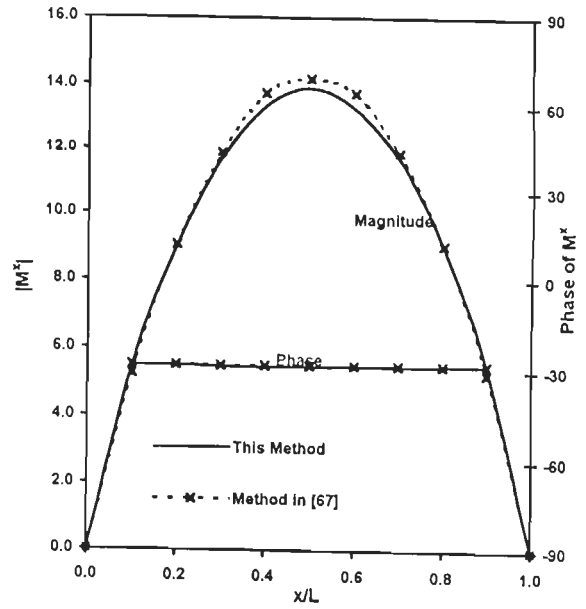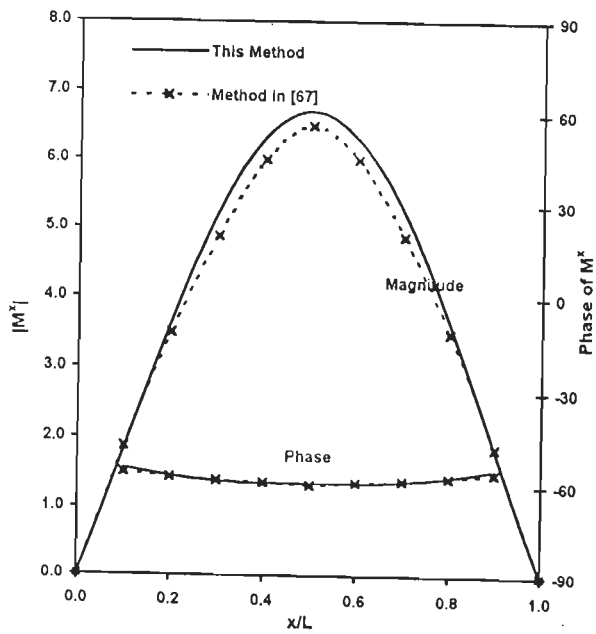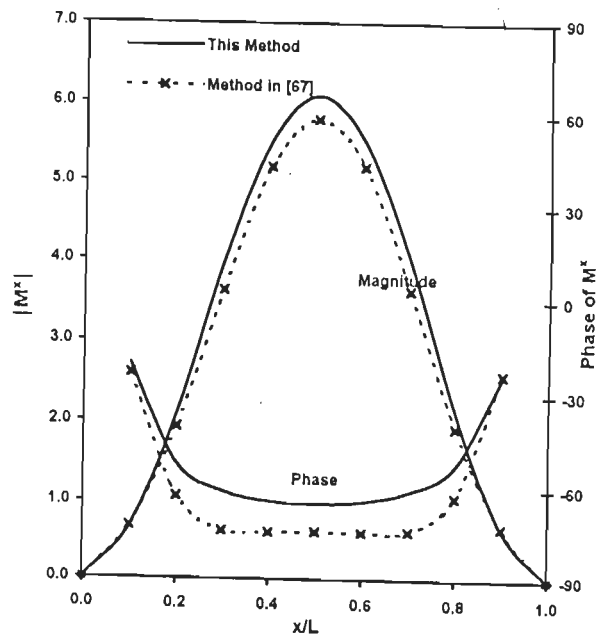
Fig. 3.4 : x-directed Surface Magnetic Current Distributions for λ/20-wide Rectangular Slots in a Conducting Screen.
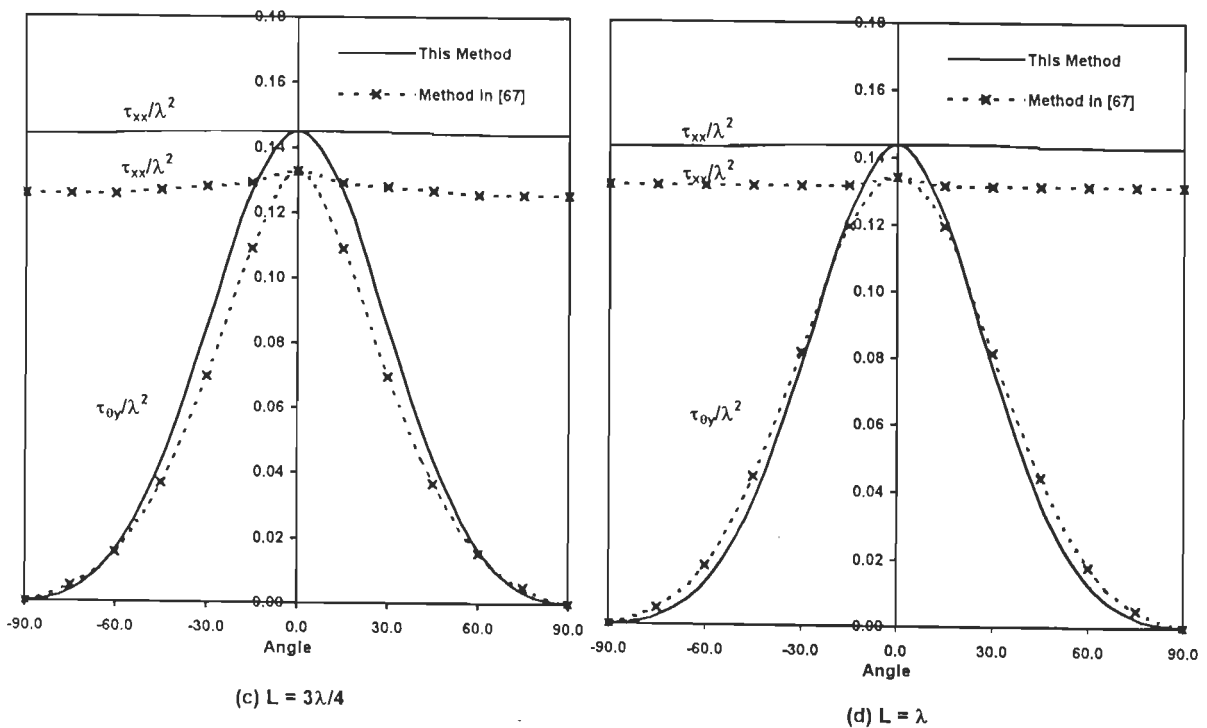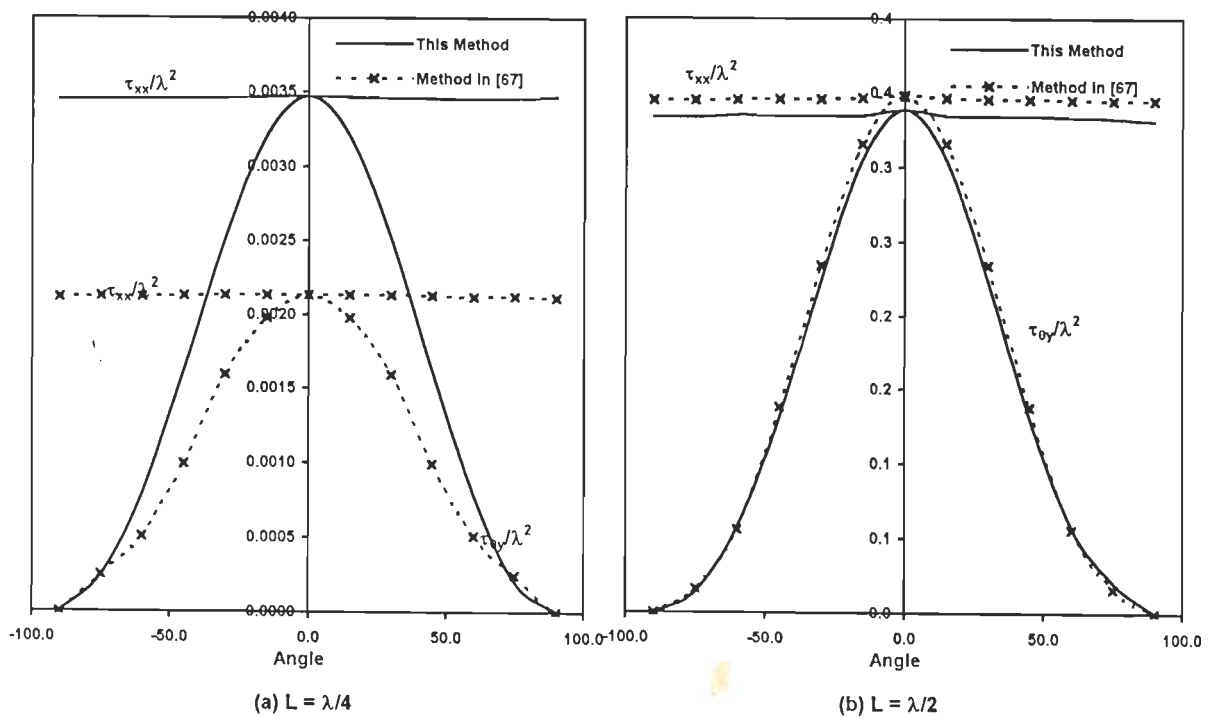
Fig. 3.5 : Transmission Cross-sections τ_{0y}/λ^2 and τ_{xx}/λ^2 for $\lambda/20$-wide Rectangular Slots

58

However, for $\lambda/4$-long slot, a large discrepancy between our results and those published in ref. [67] was observed. Since we had already tested our procedure for convergence and were reasonably sure of the accuracy of our results, we undertook a detailed study of the method in [67] to identify the cause of this discrepancy. A computer program was written based upon the equations derived in [67] and its results for a $\lambda/4$ slot are shown in Fig. 3.6. It was found that the data presented in [67] for the $\lambda/4$ slot was obtained with only 5 sub sections (4 RTF) along the x-direction. Fig. 3.6(a), on the other hand, shows that about 40 subsections are required to obtain convergence. Fig. 3.6(b) and (c) show our results with 56 triangular patches and the results of Mautz and Harrington [67] using 4 RTF and 47 RTF; it is found that, in the latter case, the agreement between our results and those obtained using rooftop functions is good. Thus, the reason for the apparent discrepancy was that the results in [67] were obtained using insufficient number of expansion functions. Further, it was found that for the other slot lengths also, the agreement improved if the number of rooftop functions was increased.
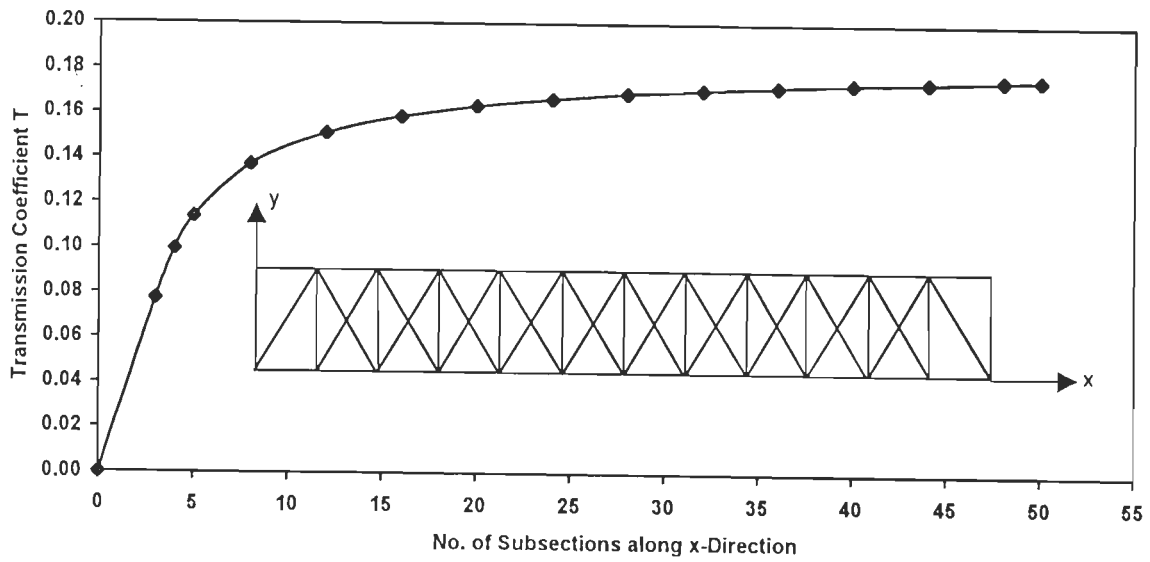
(a)
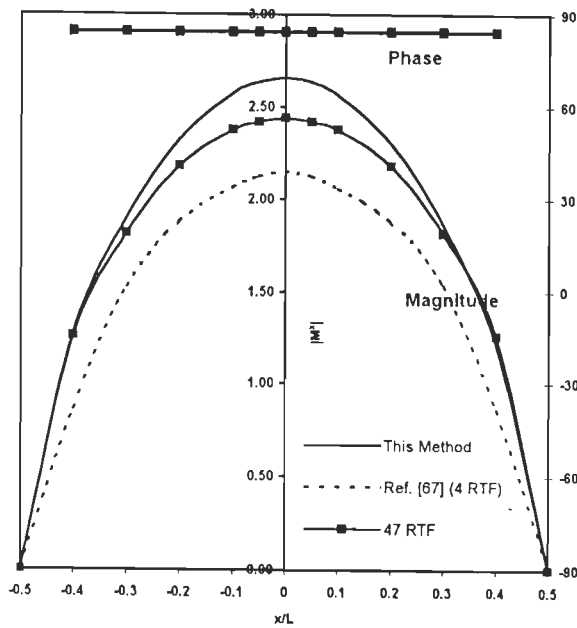
(b)
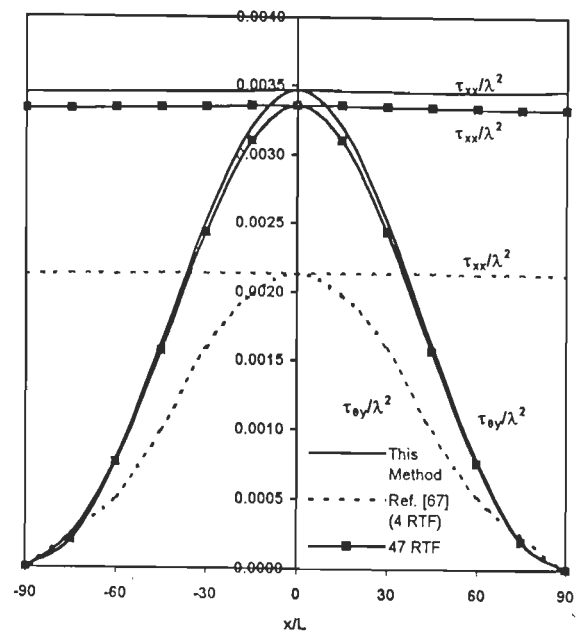
(c)

Fig. 3.6 : Transmission properties of a $\lambda/4 \times \lambda/20$ rectangular slot (a) convergence of transmission coefficient as a function of the number of rooftop functions (RTF), (b) x-directed surface magnetic current distribution and (c) transmission cross-sections τ_{0y}/λ^2 and τ_{xx}/λ^2.

Fig. 3.7 shows the transmission coefficient as a function of slot length for slots of different widths. It is seen that as slot width is decreased, the transmission coefficient progressively increases accompanied by a slight increase in the resonant length of the slot. This can be attributed to the presence of a relatively high electric field within the narrow slot compared with the field in the broad slot for the same time average input power. As a result, computed parameters, such as transmission coefficient, transmission cross-sections and surface magnetic currents for the narrower slot are higher.
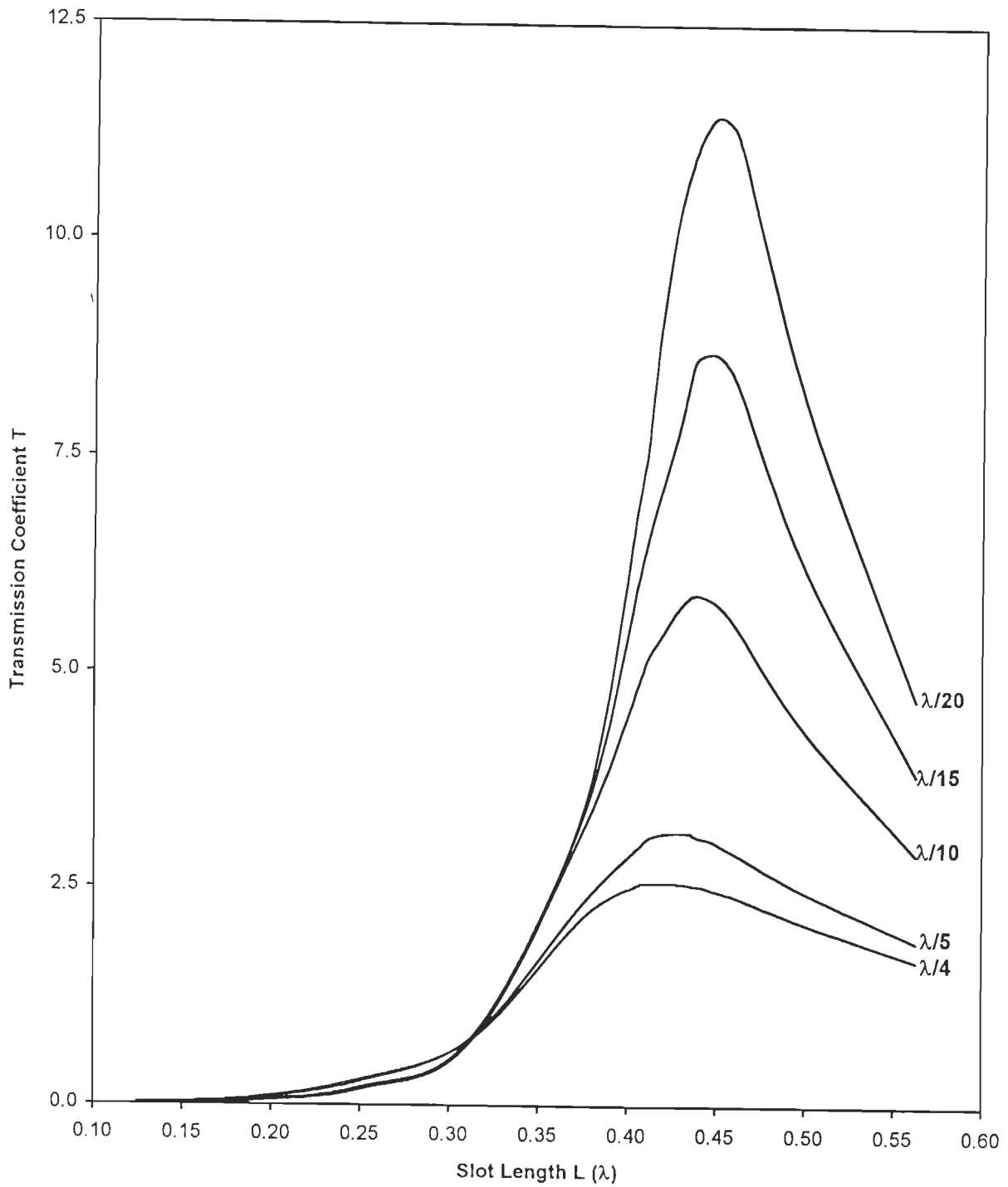
Fig. 3.7 : Transmission Coefficient as a Function of Slot Length for
Slots of Different Widths in a Conducting Screen

3.3-2 Square Aperture

The discretization used for a square aperture is shown in Fig. 3.8. It consists of 96 non-boundary edges. Apertures of the size $\lambda/4 \times \lambda/4$ and $\lambda/2 \times \lambda/2$ were considered.
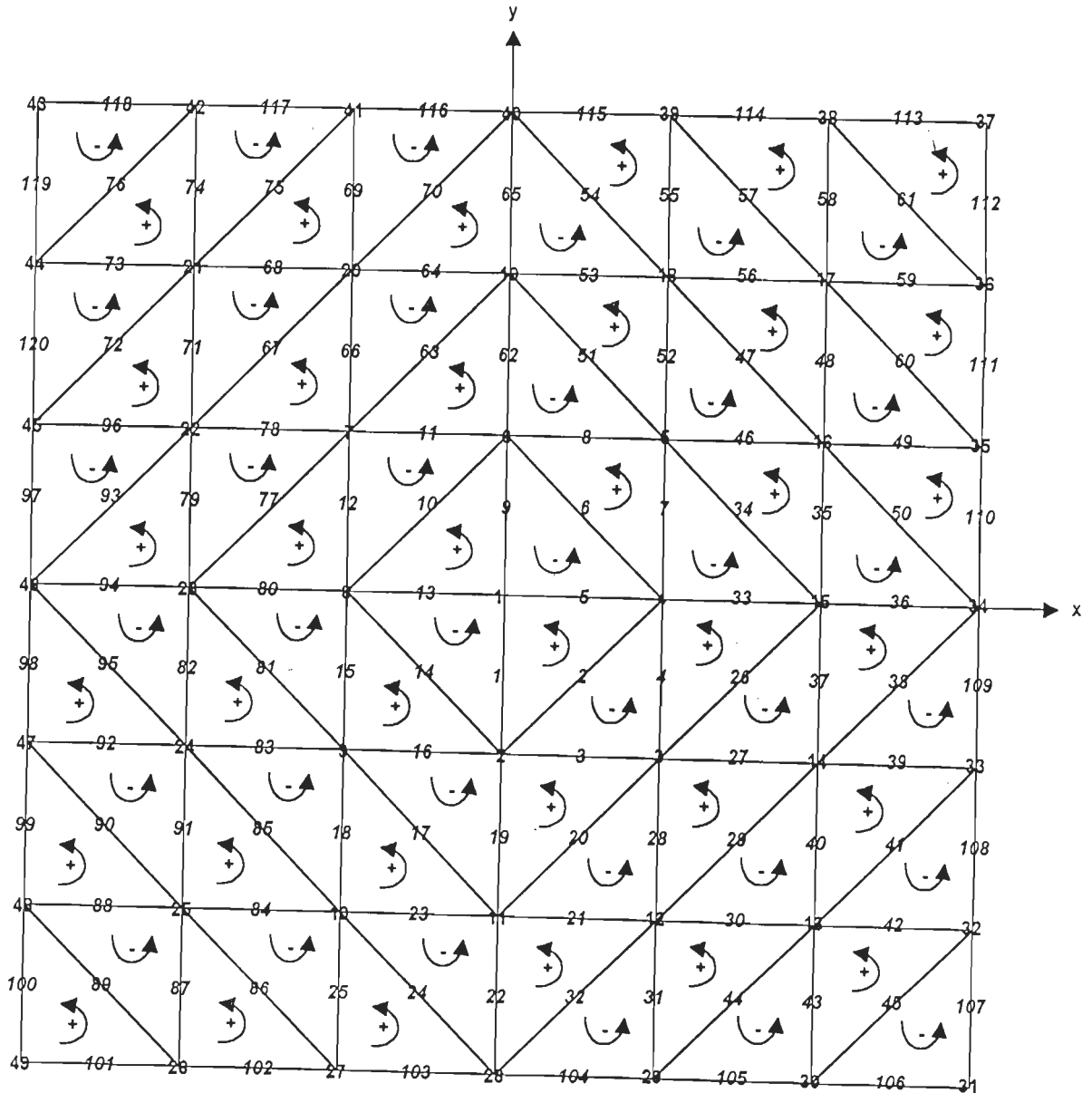
Fig. 3.8 : A Square Aperture Surface Discretized by Triangular Patches Showing Edges, Nodes and Current Directions

The results for convergence test on the transmission coefficients of the square apertures are given in Table 3.2.

Table - 3.2

Convergence of Transmission Coefficient for a Square Aperture in a Conducting Screen

Aperture Size L x L	No. of Expansion Functions N	Transmission Coefficient T	% Change
λ/4 x λ/4	21	0.19036490	
	40	0.22355000	+17.4
	65	0.25096036	+12.3
	96	0.26784400	+6.73
	133	0.27105720	+1.1996
λ/2 x λ/2	21	1.55473200	
	40	1.58751400	+2.11
	65	1.60130600	+0.87
	96	1.60794300	+0.41
	133	1.61799500	+0.38

From the table, it is noted that at least 96 expansion functions are required for the smaller aperture to attain convergence while only about 65 expansion functions are sufficient for the larger aperture.

Figs. 3.9(a)-(b) and 3.10(a)-(b) show the distribution of the surface magnetic current M^x as a function of x and y. It is found that for both λ/4 x λ/4 and λ/2 x λ/2 apertures, the magnitude of the current has a similar nature. M^x vs x curves exhibit a "shoulder" as one moves away from the centre before falling off sharply near the aperture edges. However, while the phase of M^x is constant along the x direction for the λ/4 aperture, the phase distribution of the λ/2 aperture is sharply tapered near the edges. The M^x vs y curves have similar nature and exhibit edge conditions near the aperture boundary.

Fig. 3.11 and 3.12 compare the computed transmission cross-sections τ_{oy}/λ^2 and τ_{xx}/λ^2 with those obtained by Mautz and Harrington [67]. A good agreement between the two results can be seen.
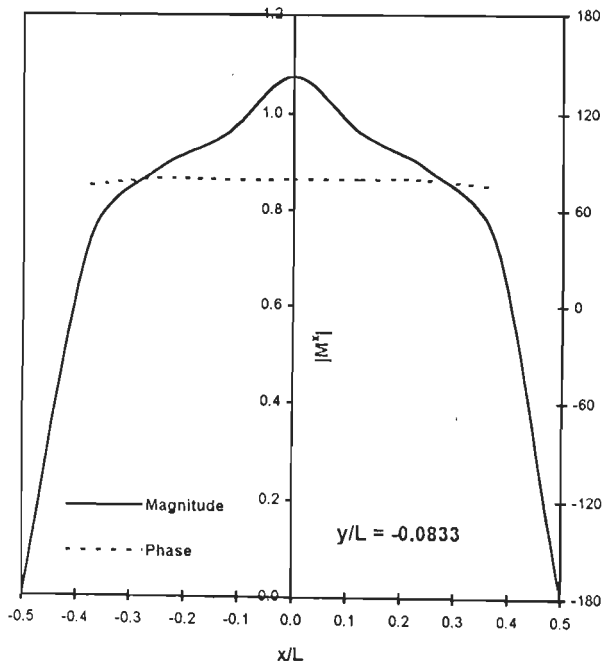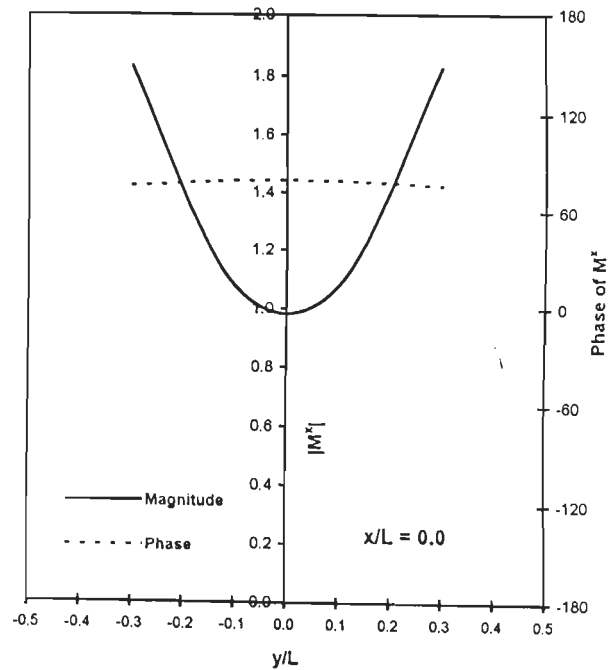
Fig. 3.9 : Equivalent Surface Magnetic Current Distributions for λ/4-Square Aperture in a Conducting Screen.

Fig. 3.10 : Equivalent Surface Magnetic Current Distributions for λ/2-Square Apertures in a Conducting Screen.
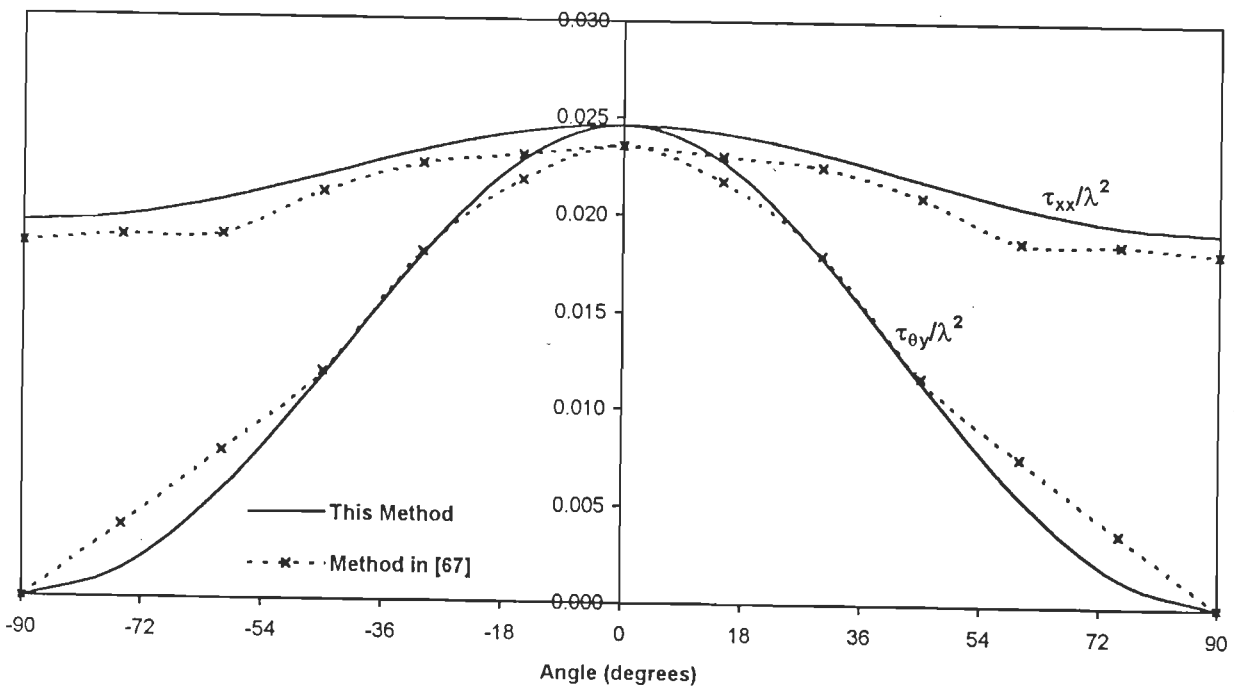
Fig. 3.11 : Transmission Cross-sections for $\lambda/4$-Square Aperture in a Conducting Screen.
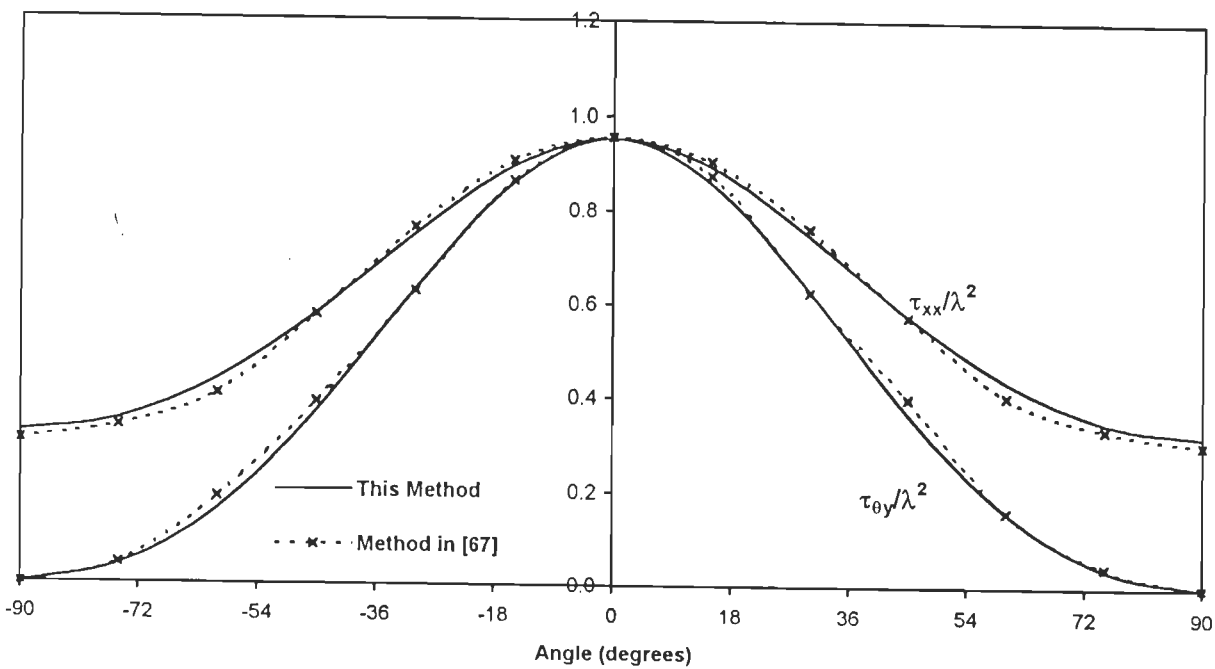
Fig. 3.12 : Transmission Cross-sections for $\lambda/2$-Square Aperture in a Conducting Screen.

3.3-3 Circular Aperture

Fig. 3.13 shows the triangulation scheme for a circular aperture. The surface comprises 56 faces, 33 nodes and 76 interior edges.

The figure illustrates clearly the advantages of triangular patches for modelling the curved boundary regions. The orientation and density of the patches can be varied appropriately to conform to the physical boundary of the aperture.
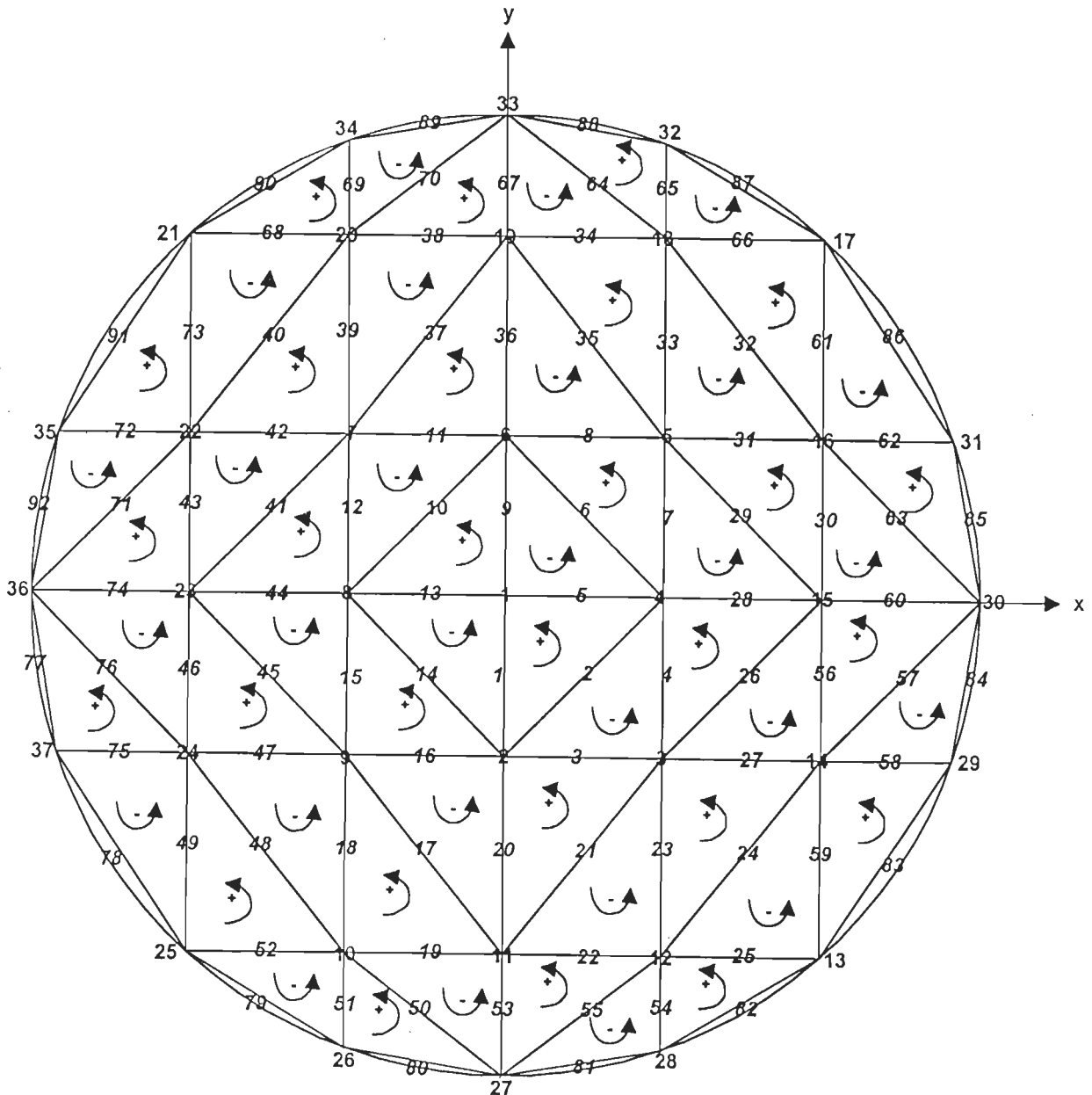
Fig. 3.13: Discretization Scheme for a Circular Aperture Showing Edges, Nodes and Current Directions

Table 3.3 shows the results of a study on transmission coefficient as a function of the number of expansion functions for various aperture diameters. It is evident that about 48 expansion functions are sufficient to obtain converged results.

Table - 3.3

Convergence of Transmission Coefficient for a Circular Aperture in a Conducting Screen.

Normalized Diameter d/λ	No. of expansion Functions N	Transmission Coefficient T	% Change in T
0.2	20	0.0352500	
	48	0.0420340	19.25
	76	0.0429959	2.29
0.3	20	0.2511654	
	48	0.2548490	1.49
	76	0.2552010	0.138
0.4	20	0.9374096	
	48	1.0139820	8.17
	76	1.0694360	5.47
	128	1.1257500	5.27
0.5	20	1.498541	
	48	1.634501	9.07
	76	1.646438	0.73
	128	1.649220	0.17
0.6	48	1.544001	
	76	1.523680	-1.32
	128	1.522670	-0.07
0.7	48	1.328800	
	76	1.339980	0.84
	128	1.340477	0.04
0.8	48	1.230142	
	76	1.235578	0.44
	128	1.240382	0.39

Fig. 3.14 and 3.15 show, respectively, equivalent surface magnetic current M^x at $y/d = -0.0833$ and at $x/d = 0.0$ for circular apertures having 128 non-boundary edges. As expected, the peak value of the current increases with the size of the aperture. In Fig. 3.14, as one moves away from the current peaks, it is seen that there is a uniform decrease for the largest aperture current until at $x/d = \pm\ 0.25$ from the centre when the curve exhibits a "shoulder". For smaller aperture, the magnitude of the current is nearly constant over a small region around the centre and the phase distribution is almost uniform over the entire length of the aperture. The current distributions along the y-direction (Fig. 3.15) exhibit minima at the centre and maxima at $x/d = \pm\ 0.167$.

Fig. 3.16 shows transmission coefficient T as a function of aperture diameter, d. It is noted that T reaches its maximum value at d/λ slightly greater than 0.5, suggesting that resonance occurs at this point.

Fig. 3.17 shows transmission cross-sections $\tau_{\theta y}/\lambda^2$ and τ_{xx}/λ^2 for different aperture diameters. Transmission cross-sections are noted to be a function of aperture diameter.
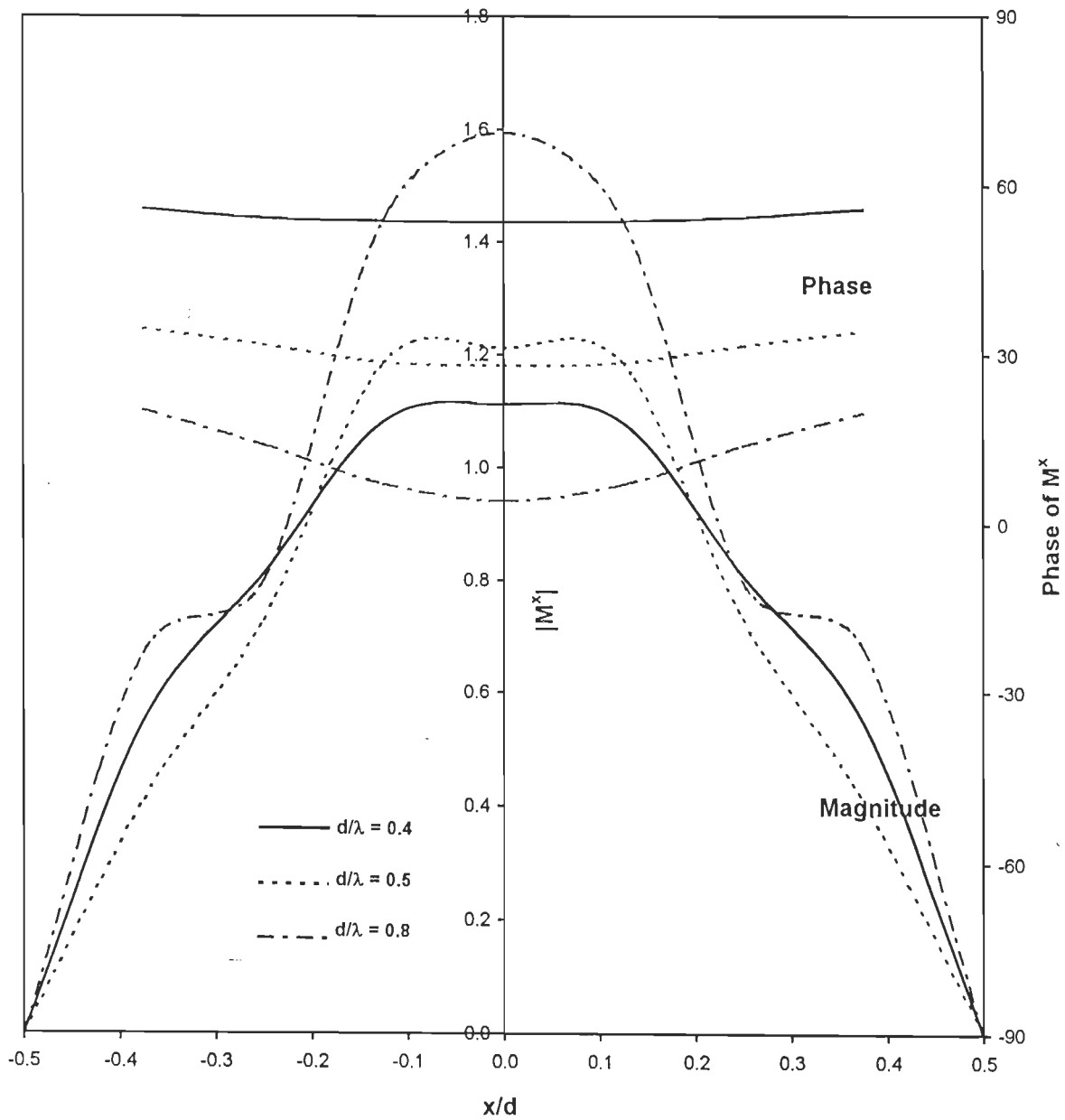
Fig. 3.14 : Equivalent Surface Magnetic Current Distributions M^x at y/d = -0.0833 for Circular Apertures in a Conducting Screen.
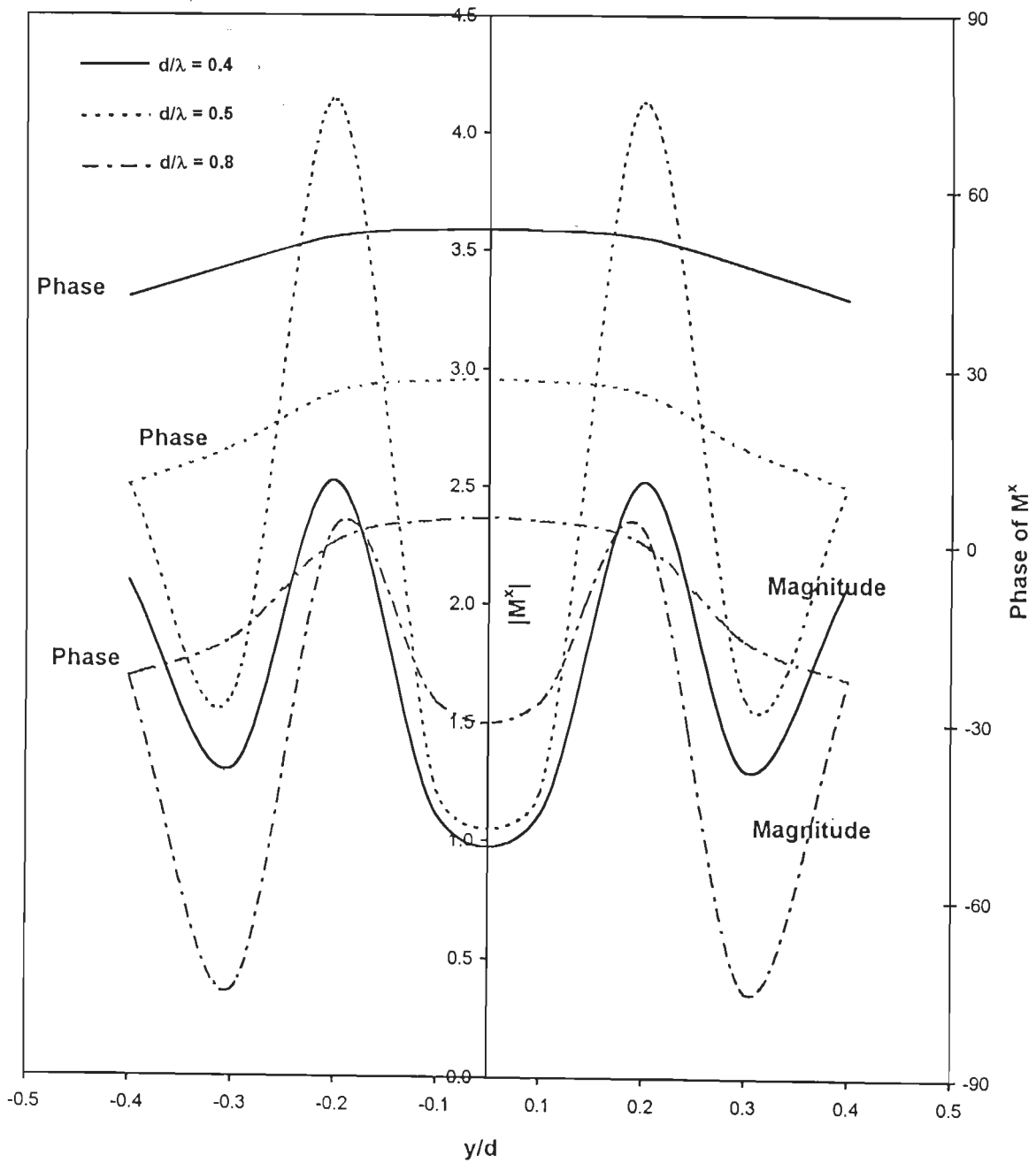
Fig. 3.15 : Equivalent Surface Magnetic Current Distributions M^x at x/d = 0.0 for Circular Apertures in a Conducting Screen.
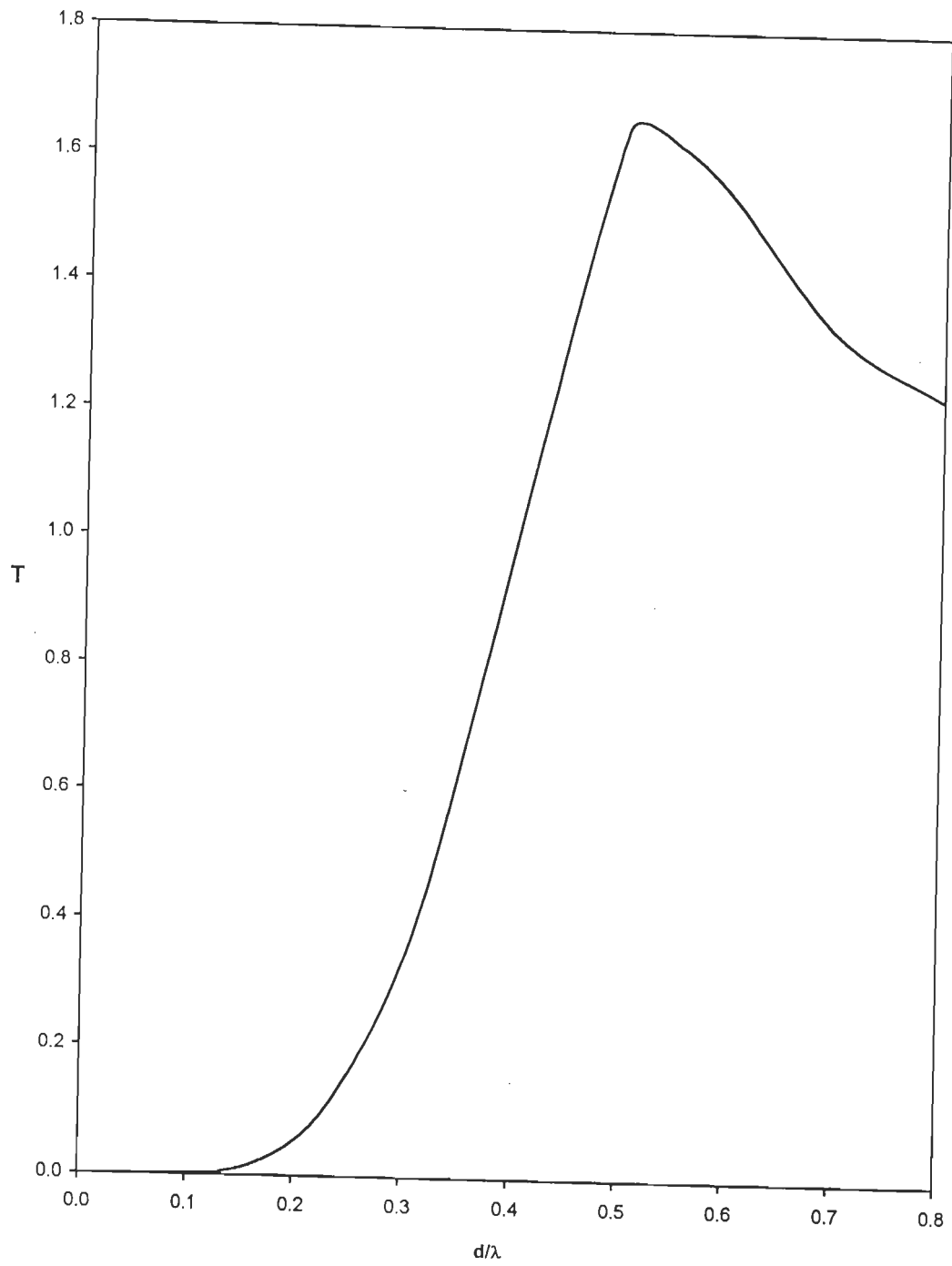
Fig. 3.16 : Transmission Coefficient, T, of Circular Aperture as a Function of Diameter.
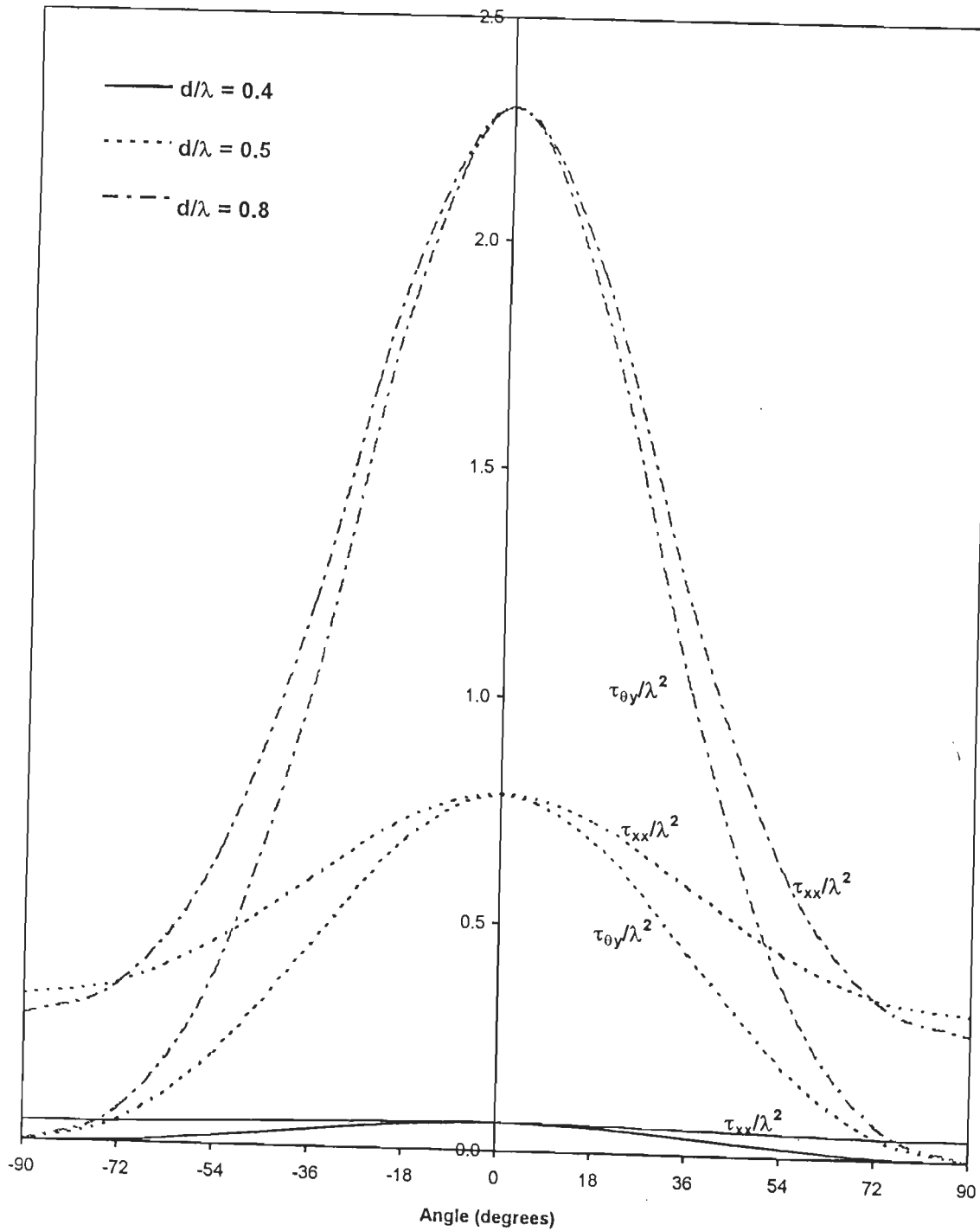
Fig. 3.17 : Transmission Cross-sections τ_{0y}/λ^2 and τ_{xx}/λ^2 for Circular Aperture for Various Diameters in a Conducting Screen.

3.3-4 Elliptical Aperture

Fig. 3.18 shows the triangulation scheme for an elliptical aperture. The aperture surface is discretised into 36 triangular patches, resulting in 48 non-boundary edges. It is emphasized again that the use of triangular patches has made it easier to model the surface quite accurately by incorporating a higher density of patches in regions where it is desirable, especially the boundary regions.
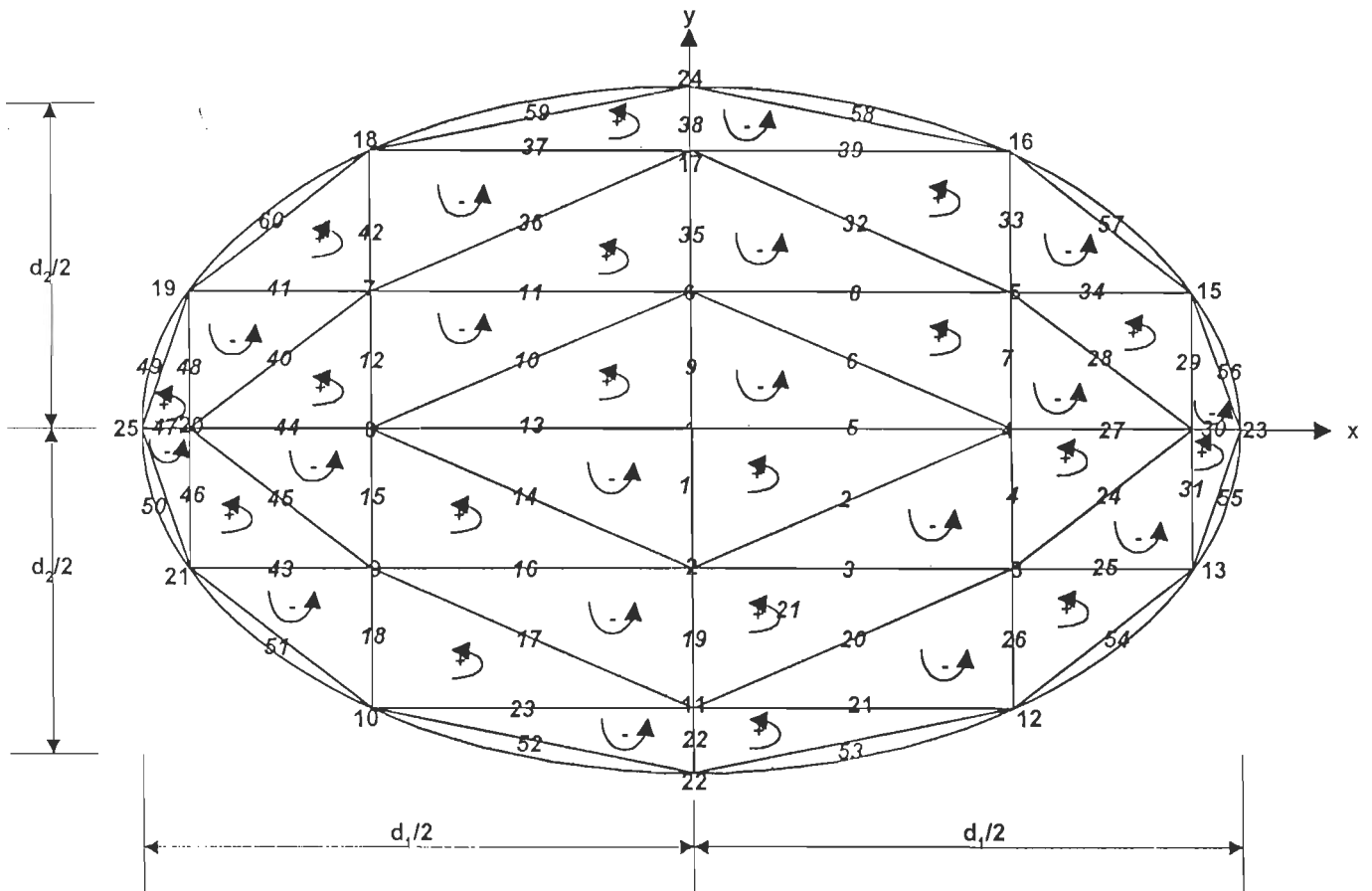
Fig. 3.18 : Discretization of Elliptical Aperture Showing Nodes, Edges and Current Directions

Elliptic apertures of different eccentricities were considered, where eccentricity, e, is given by

$$e = \sqrt{1 - (d_2 / d_1)^2} \qquad (3.29)$$

in which d_1 = major axis

             d_2 = minor axis

Fig. 3.19(a) and (b) show surface magnetic current distributions M^x as a function of x and y at $y/d_2 = -0.0833$ and at $x/d_1 = 0.0$, respectively, for elliptical apertures of eccentricity, e = 0.5 and e = 0.8. Both apertures have a major axis $d_1 = 0.8\lambda$. The magnitude distributions have almost equal peak values but for e = 0.8, the current falls more sharply as one moves away from the centre. The distribution of M^x along the y-direction exhibits widely different behaviour for the two cases (Fig. 3.19(b)). While the current distribution is almost uniform for smaller eccentricity (e = 0.5), it exhibits a nature similar to that of a circular aperture for e = 0.8.

Fig. 3.20 shows the transmission cross-sections $\tau_{\theta y}/\lambda^2$ and τ_{xx}/λ^2 for elliptical apertures for e = 0.3, 0.5 and 0.8. The patterns are seen to become more directive for smaller eccentricities.

The elliptic aperture was studied in more detail by considering two different orientations shown in the inset of Fig. 3.21(a). In one case the major axis of the ellipse is along the x-direction (ellipse 1) and in the other, along y-direction (ellipse 2). In both cases, the aperture area is same. It is observed that when the major axis is along the y-direction (ellipse 2), the $|M^x|$ vs x curve is very nearly flat over a large part of the aperture and $|M^x|$ falls only near the aperture edges. On the other hand, for ellipse 1, the current distribution is tapered along the x-direction. Further, while $|M^x|$ vs y curve for ellipse 1 (major axis along x-direction) exhibits a minima at the centre, the curve for ellipse 2 exhibits a maxima (Fig. 3.21(b)). Ellipse 1 curve is similar to that of $\lambda/2$-square aperture in Fig. 3.10(b).

Fig. 3.22 shows the transmission cross-sections $\tau_{\theta y}/\lambda^2$ and τ_{xx}/λ^2 for the aperture in the two orientations. It is noted that vertical orientation (ellipse 2) gives a higher transmission cross-section than that obtained with horizontal orientation (ellipse 1) for E-polarization in the y-direction.

(a) $y/d_2 = -0.0833$

(b) $x/d_1 = 0.0$
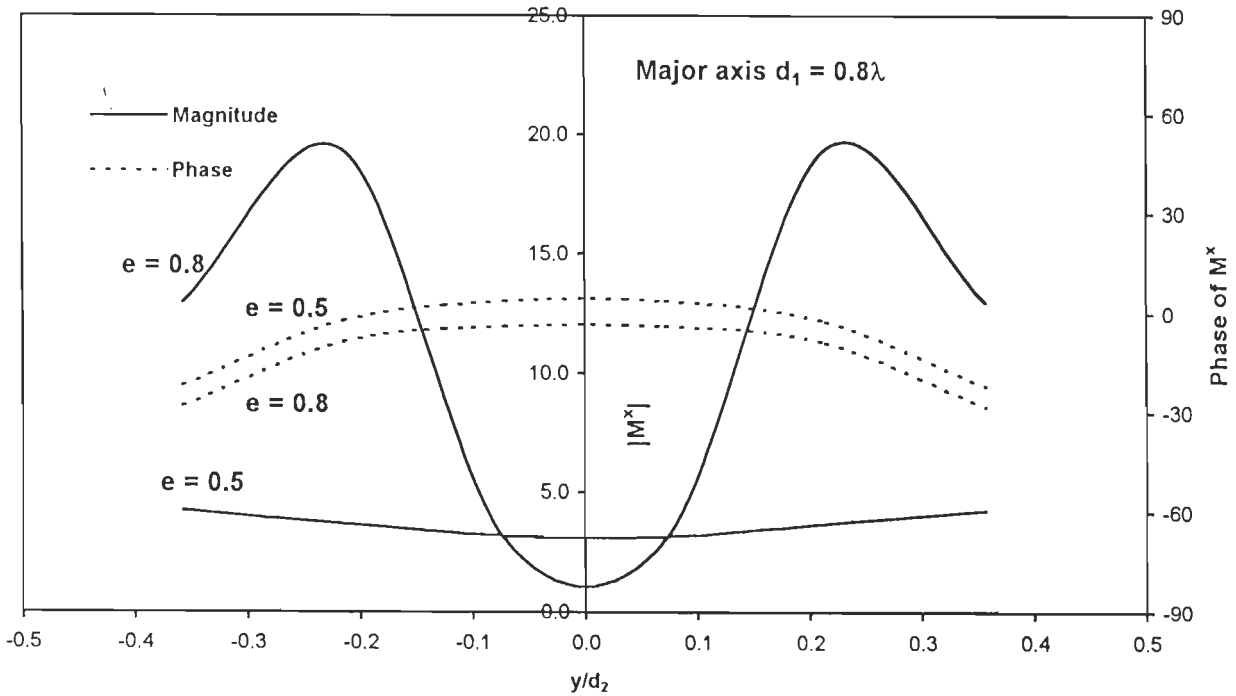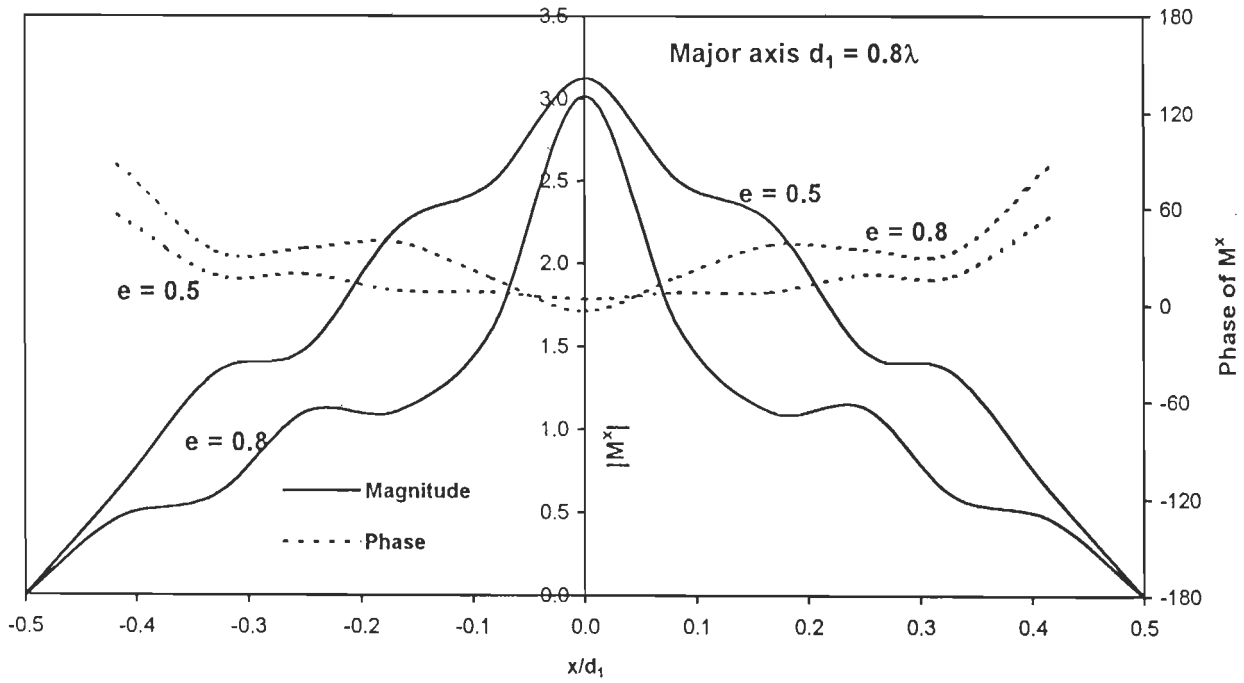
Fig. 3.19 : Equivalent Surface Magnetic Current Distributions M^x for Elliptic Apertures at Different Eccentricities e in a Conducting Screen.

76
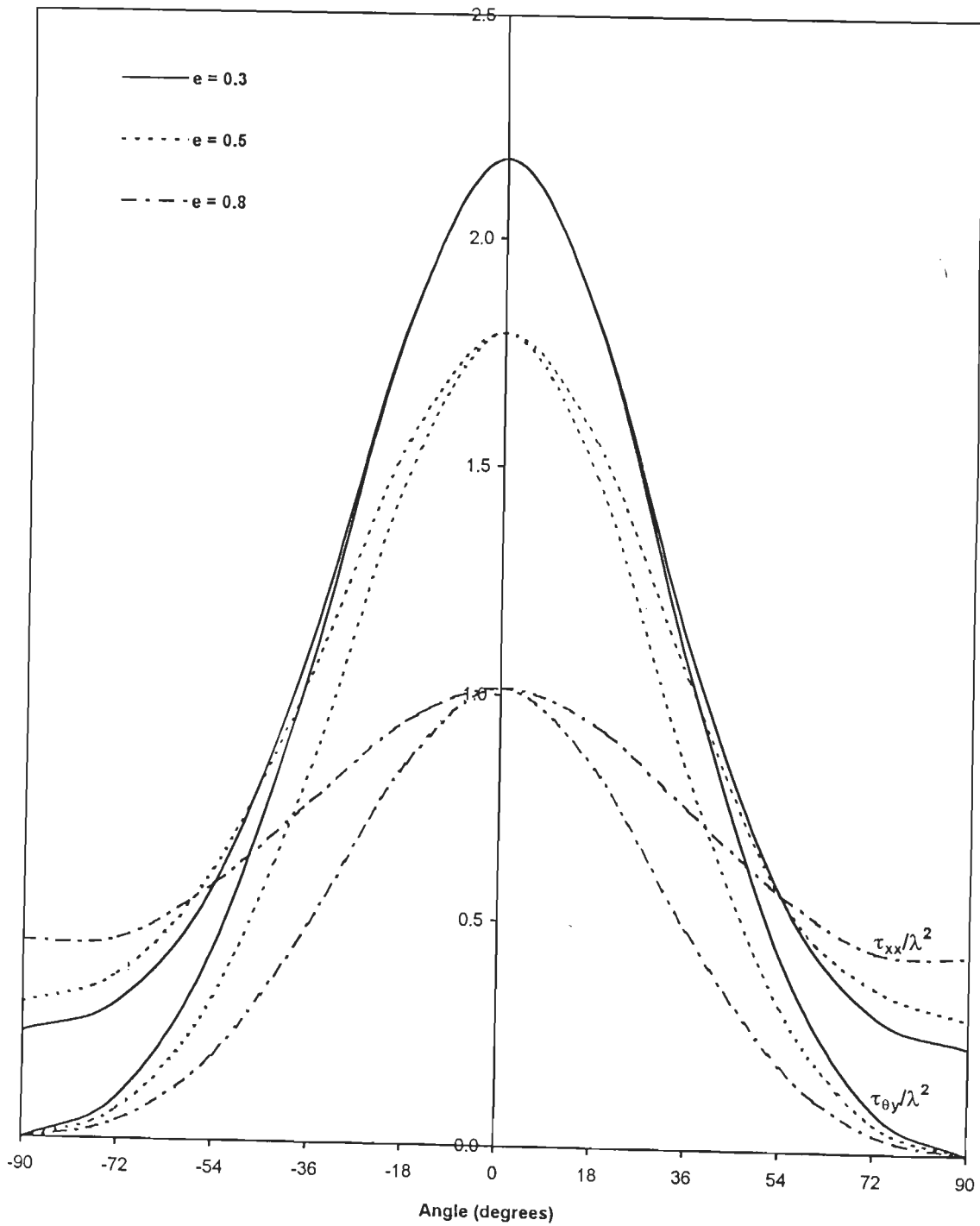
Fig. 3.20 : Transmission Cross-sections τ_{0y}/λ^2 and τ_{xx}/λ^2 for Elliptic Aperture for Various Eccentricities in a Conducting Screen.
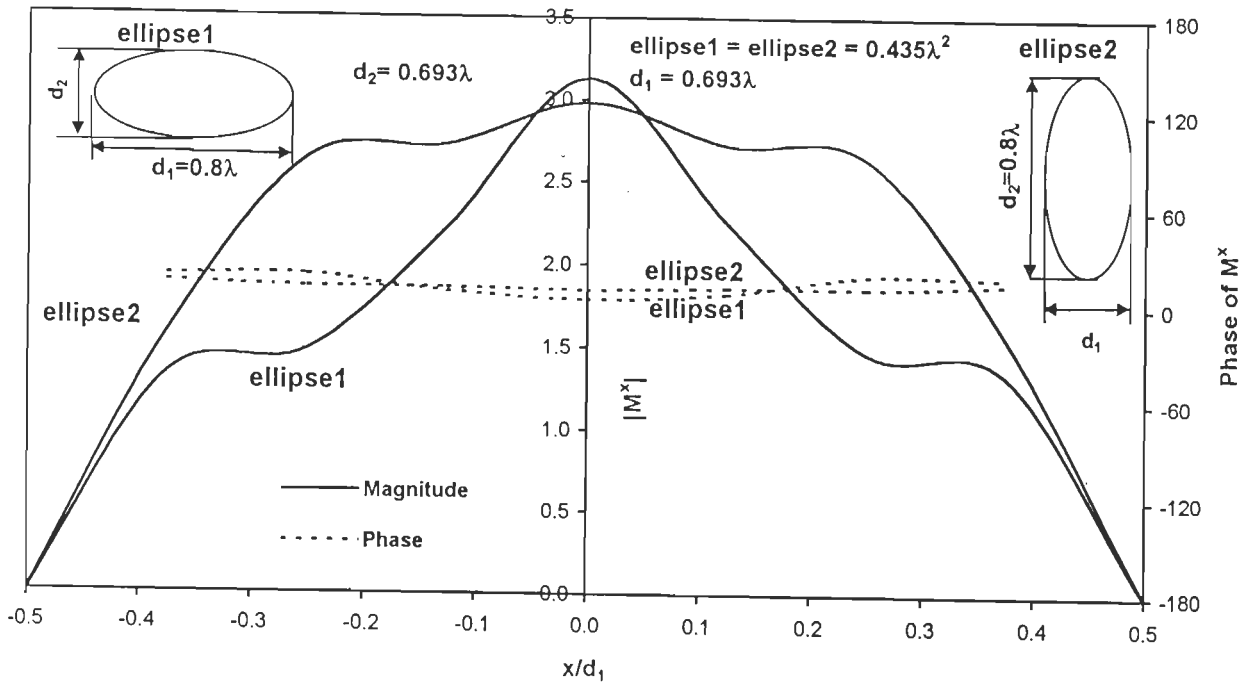
(a) $y/d_2 = -0.0833$
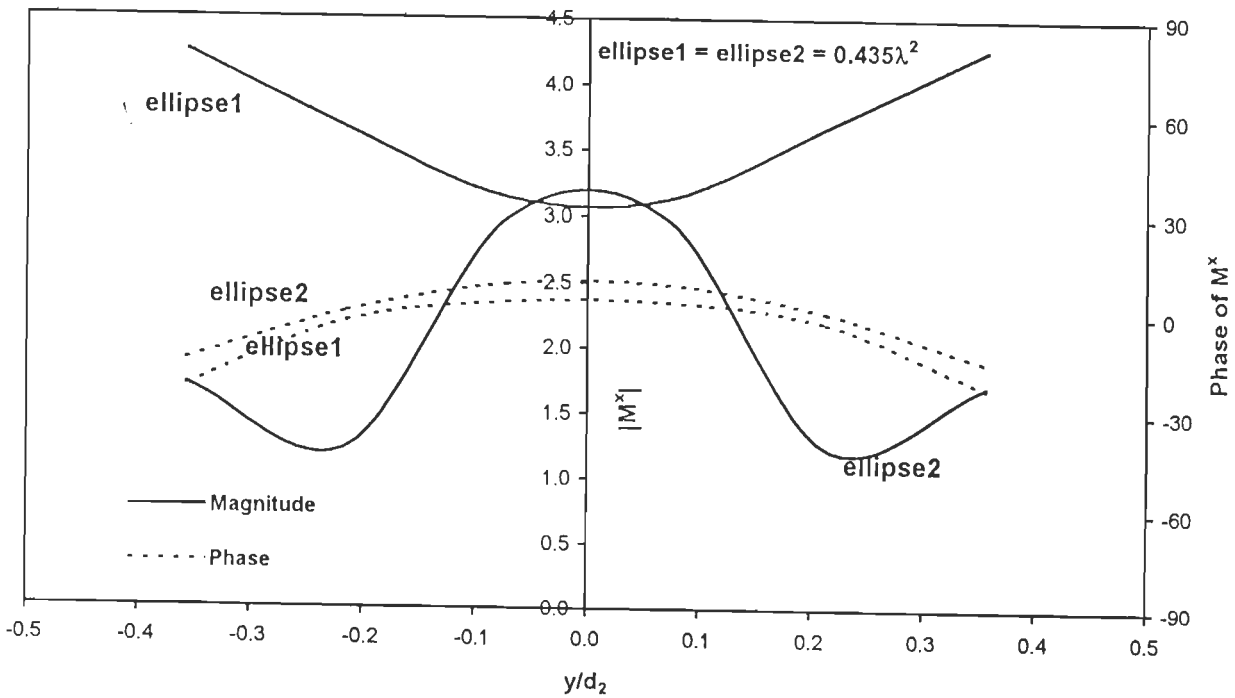
(b) $x/d_1 = 0.0$

Fig. 3.21 : Effect of Orientation on Equivalent Surface Magnetic Current Distributions for Elliptic Apertures in a Conducting Screen.
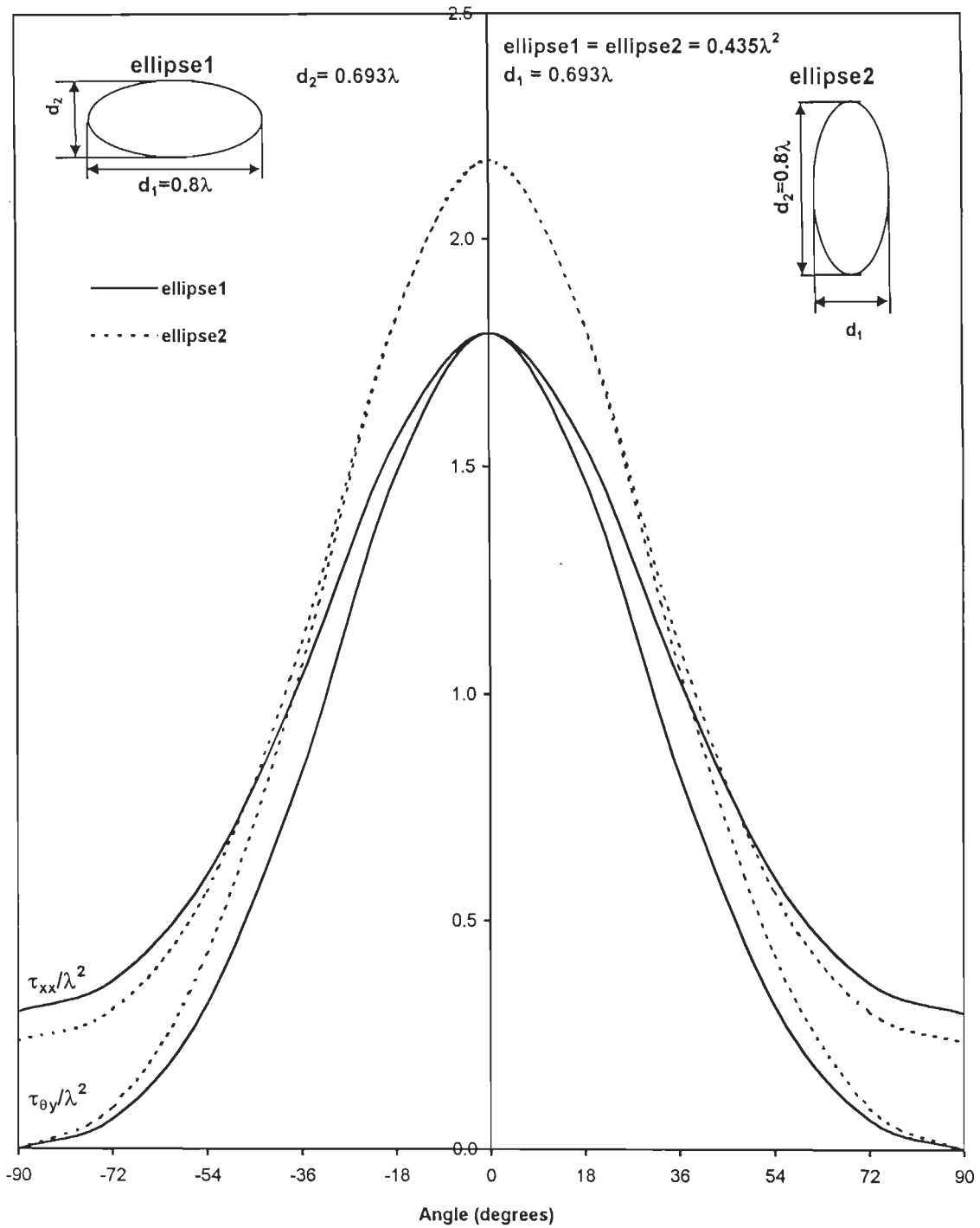
Fig. 3.22 : Effect of Orientation on Transmission Cross-sections $\tau_{\theta y}/\lambda^2$ and τ_{xx}/λ^2 for Elliptic Aperture in a Conducting Screen.

Effect of increasing aperture size for a constant d_2 was also studied. Fig. 3.23(a) and (b) show magnetic current distributions. It is observed that the larger ellipse (ellipse 2) has a higher peak value. However, both apertures exhibit very little change in phase of M^x along the aperture axes.

Fig. 3.24 shows the corresponding transmission cross-sections. Here also, it is noted that ellipse 2 has higher peak values.

From the above results, it can be concluded that for a y-polarized incident plane wave, an elliptical aperture with its major axis oriented along y-direction exhibits a higher transmission cross-section.
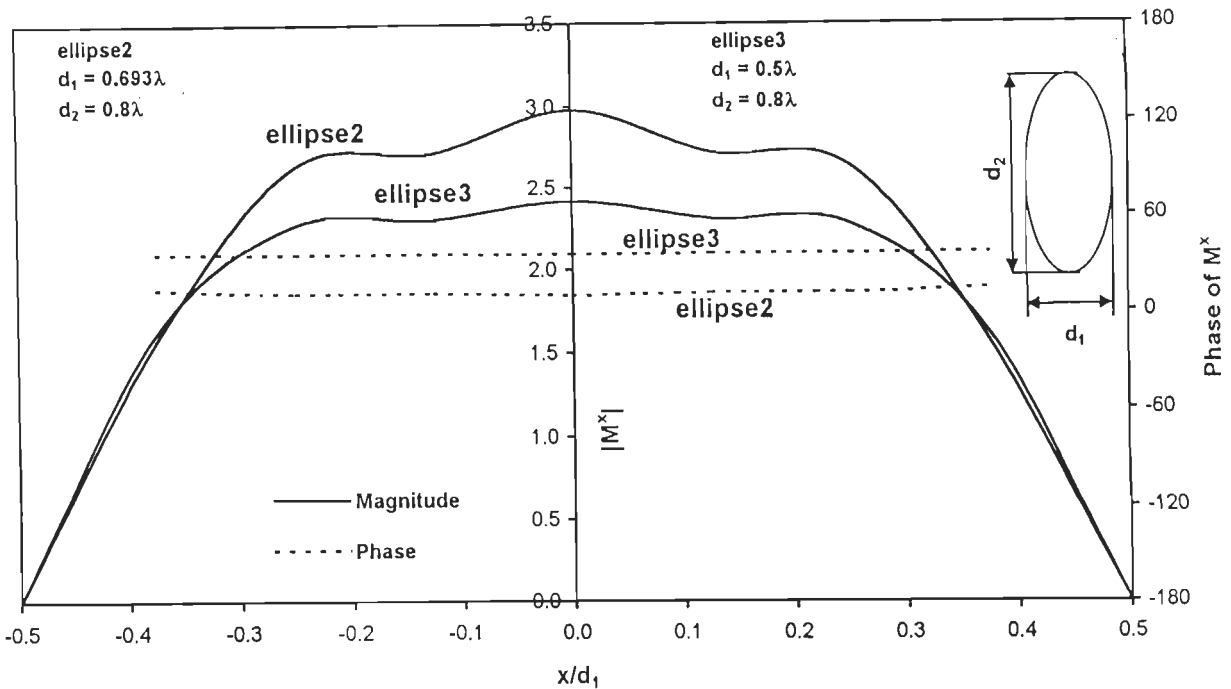
(a) $y/d_2 = -0.0833$
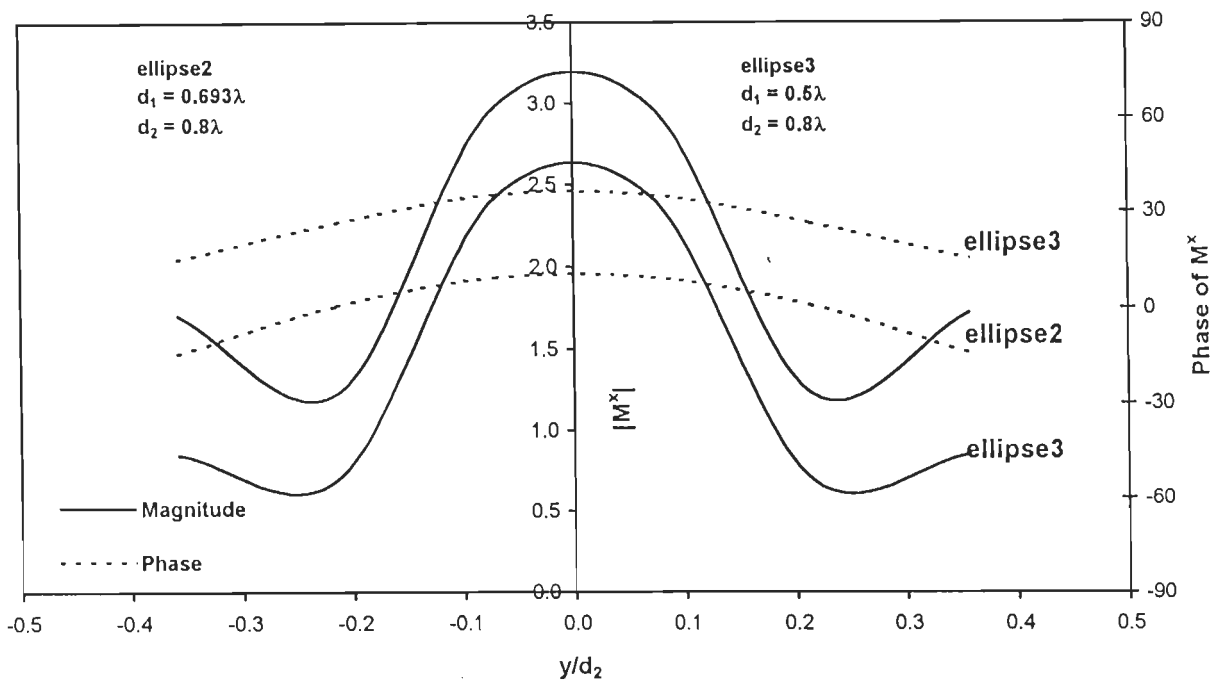
(b) $x/d_1 = 0.0$

Fig. 3.23 : Effect of Varying d_1 on Equivalent Surface Magnetic Current Distributions for Elliptic Apertures in a Conducting Screen.

81
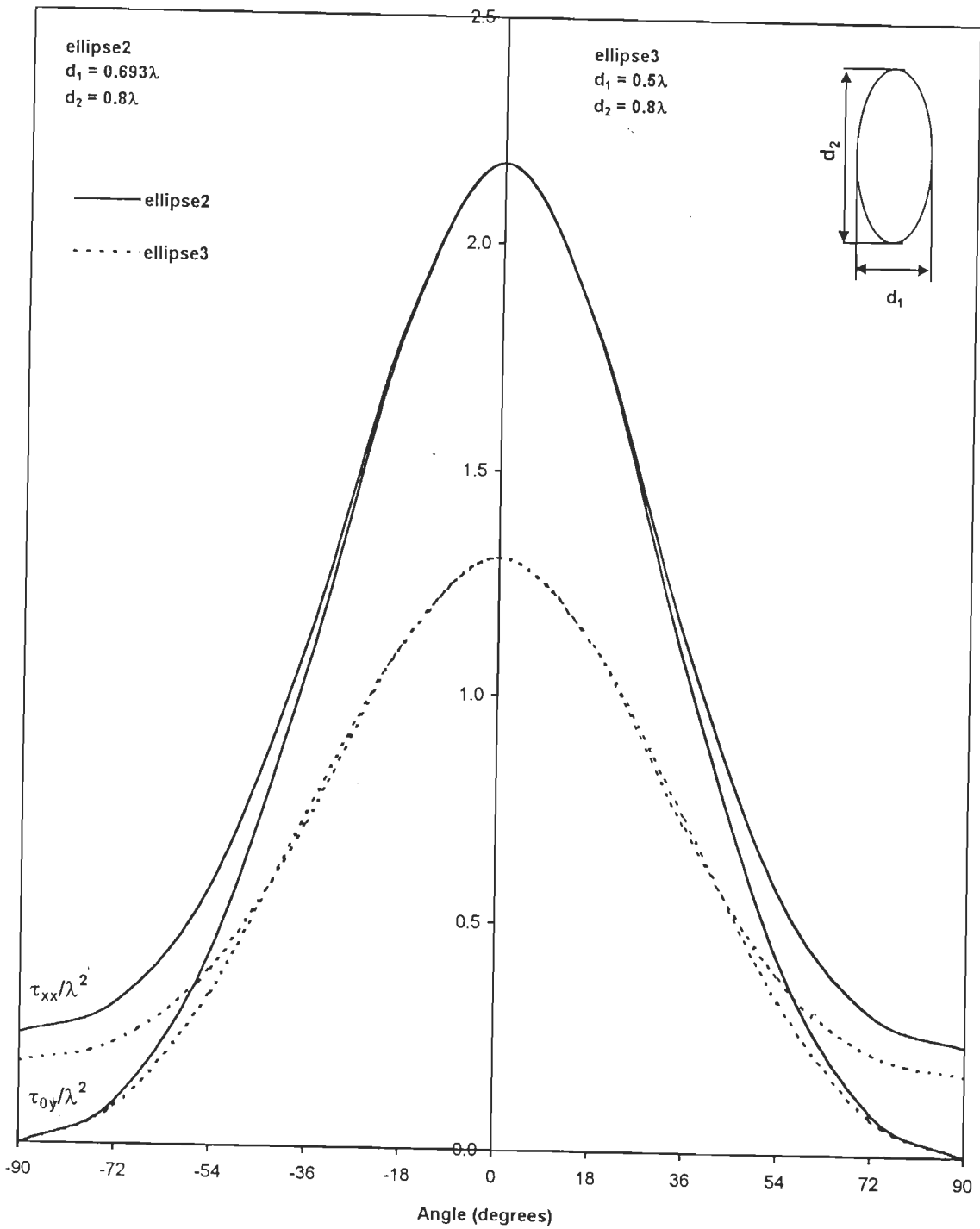
Fig. 3.24 : Effect of d_1 on Transmission Cross-sections τ_{0y}/λ^2 and τ_{xx}/λ^2 for Elliptic Aperture in a Conducting Screen.

3.3-5 Diamond-shaped Aperture

Fig. 3.25 illustrates the surface of a typical diamond-shaped aperture discretized by triangular patches. The surface consists of 41 nodes, 64 triangular faces and 88 non-boundary edges.
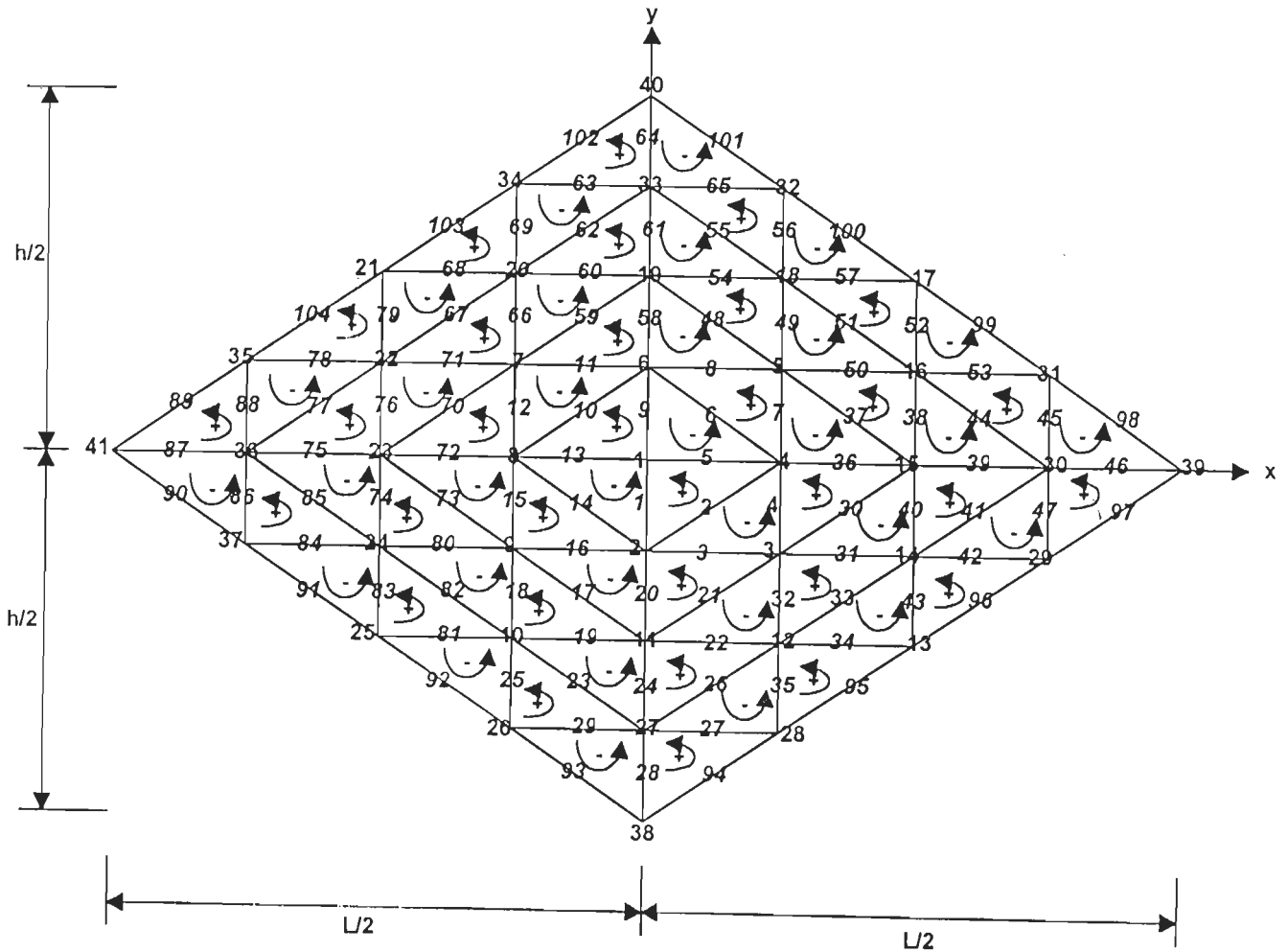
Fig. 3.25 : Discretization of a Diamond-shaped Aperture Surface Showing Nodes, Edges and Current Directions

Owing to the influence of the four corners in the diamond-shaped aperture structure, current distribution and transmission cross-sections are very much different in this case when compared to those of circular and elliptical apertures. Fig. 3.26(a) shows surface magnetic current distribution M^x as a function of x for $L/\lambda = 0.4$, 0.6 and 0.8 and $h/\lambda = 0.3556$. It is seen that the peak magnitude of M^x is considerably higher in this case and the current distribution is highly tapered near the centre. $|M^x|$ versus y curves shown in Fig. 3.26(b) exhibit a maxima at the centre of the aperture as opposed to the minima exhibited by circular apertures of Fig. 3.15 and ellipse 1 of Fig. 3.21.

Transmission cross-sections for diamond-shaped apertures are shown in Fig. 3.27. It is observed that the pattern peak value is a function of the aperture size; the larger the aperture the higher the peak value.

It appears that, for a fixed aperture height (in this case, $h/\lambda = 0.3556$), the angles formed by the edges have an effect on the current distributions. For instance, under conditions where the angles formed on the x-axis are acute, such as for $L/\lambda = 0.6$ and $L/\lambda = 0.8$, the current distributions are sharply tapered, attaining much higher peak values at the centre than for the case where these angles are obtuse. For $L/\lambda = 0.4$, it is found that the current peaks are lower and the curves are flatter. The peak values of corresponding transmission cross-sections are also lower.
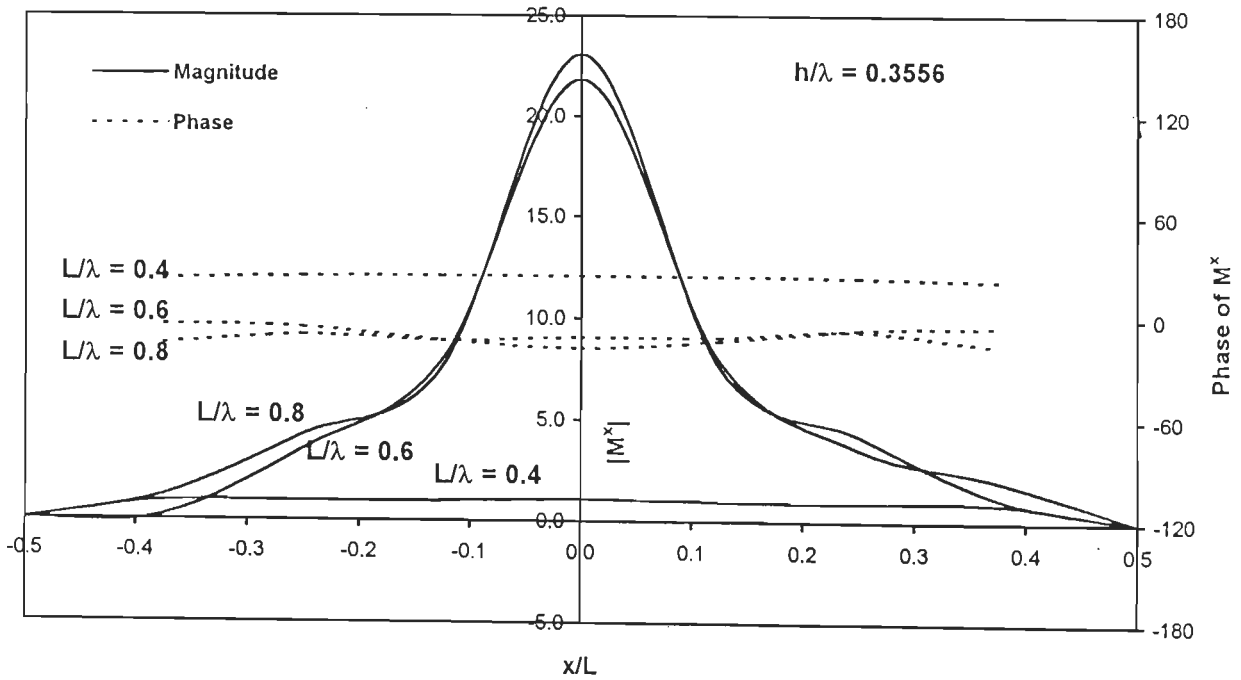
(a) y/h = - 0.0833
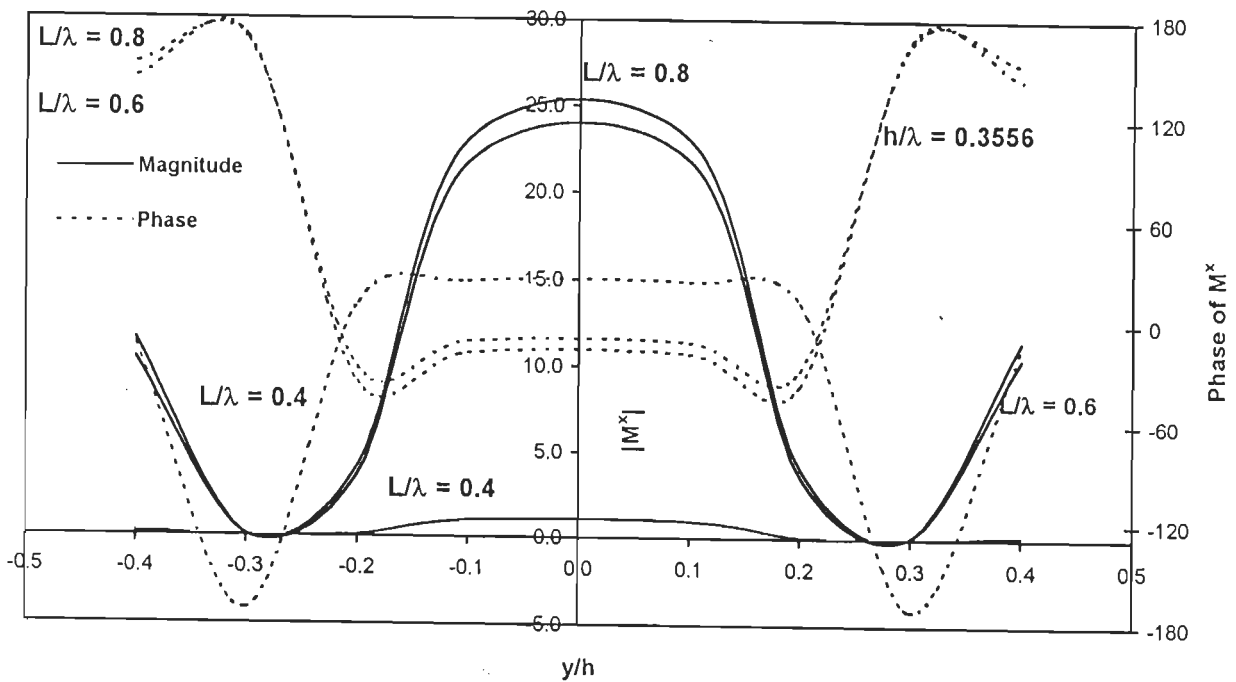
(b) x/L = 0.0

Fig. 3.26 : Equivalent surface magnetic current distributions for diamond-shaped apertures in a conductng screen
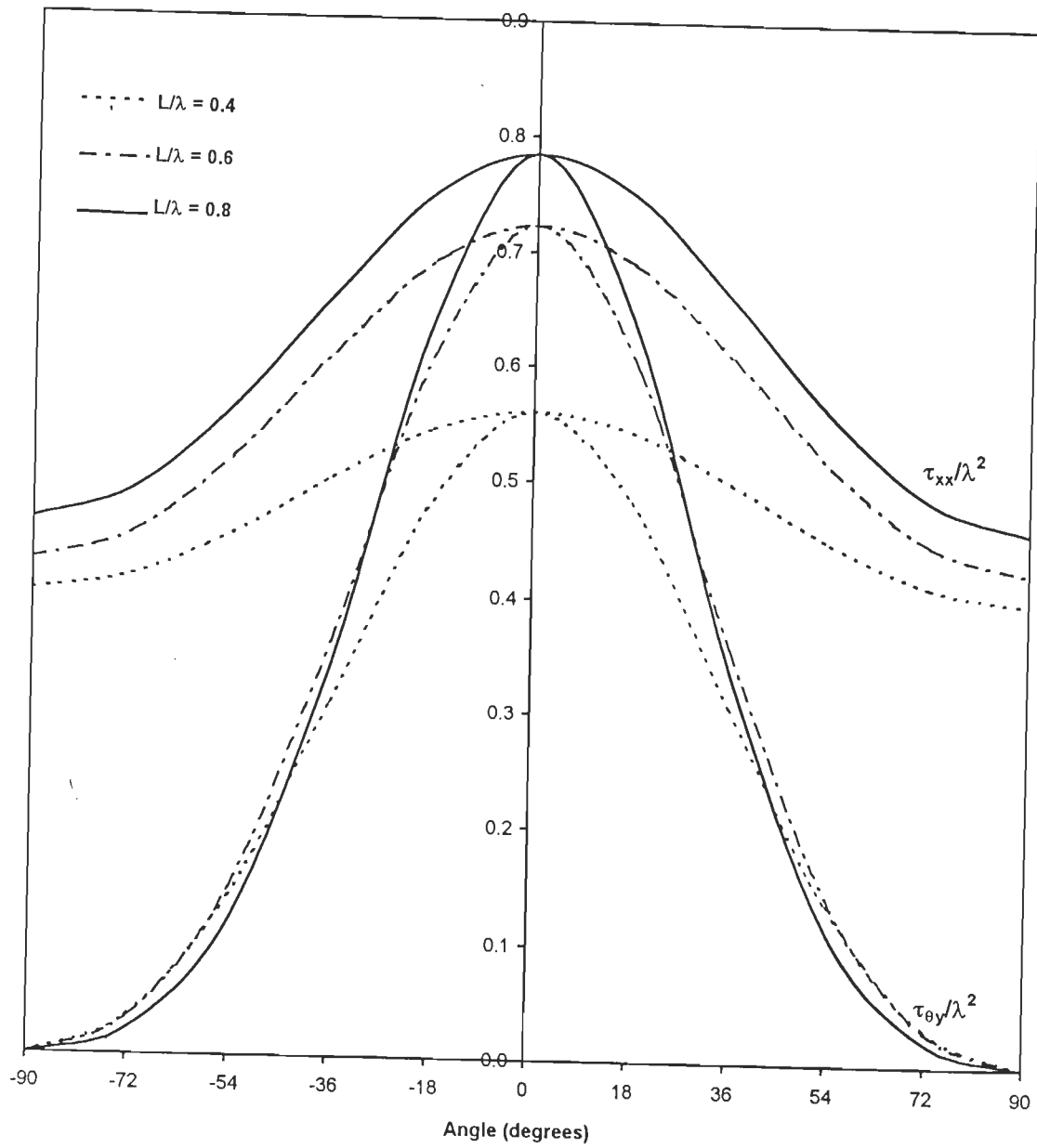
Fig. 3.27 : Transmission cross-sections $\tau_{\theta y}/\lambda^2$ and τ_{xx}/λ^2 for diamond-shaped aperture for various lengths in a conducting screen.

3.3-6 Cross-shaped Slot

The discretization of a cross-shaped slot surface using triangular patches is illustrated in Fig. 3.28. The slot surface consists of 45 nodes, 56 triangular surfaces and 68 non-boundary edges.
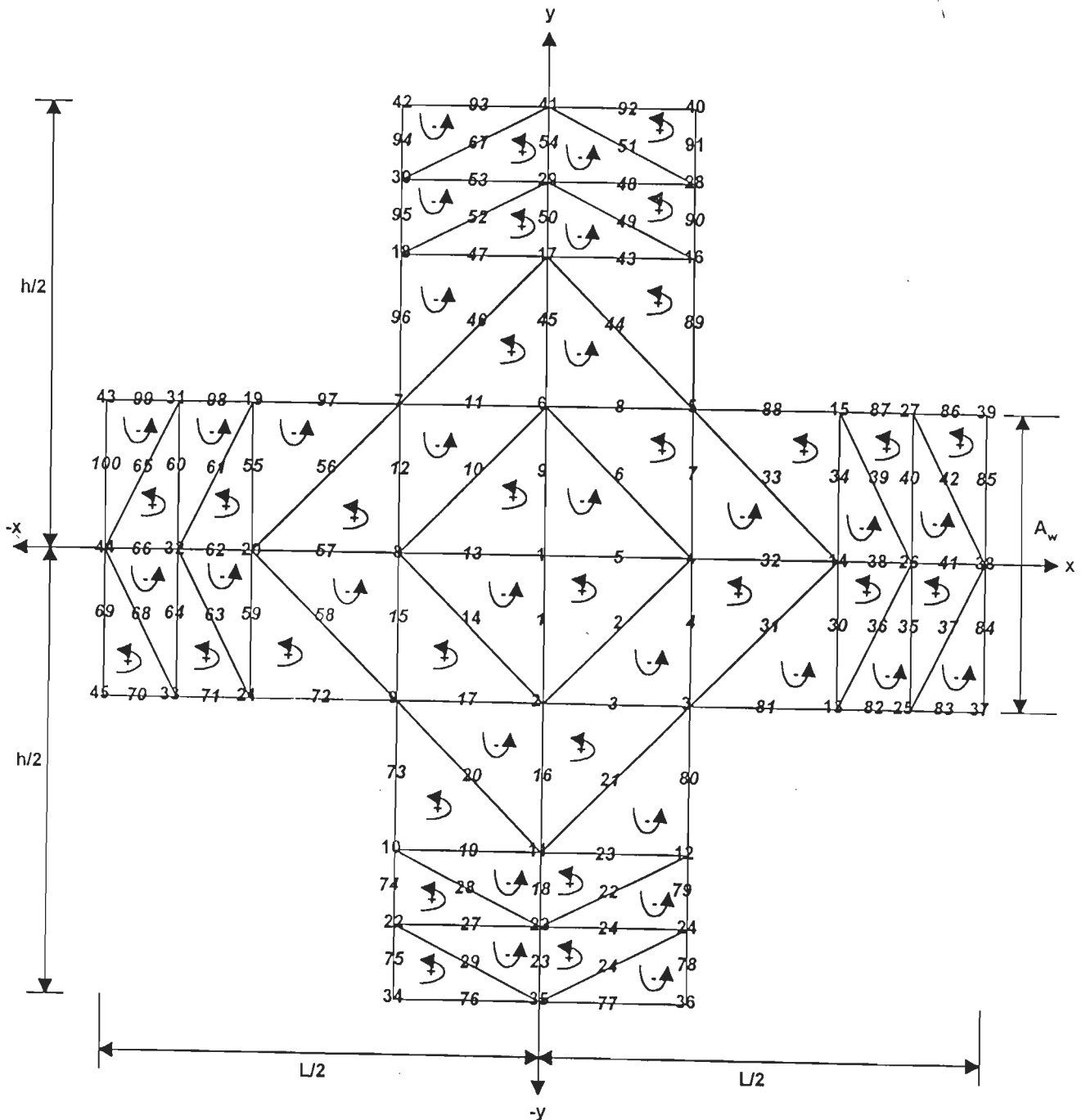
Fig. 3.28 : Discretization of Cross-shaped Slot Showing Nodes, Edges and Current Directions

Fig. 3.29(a) and (b) show the current distributions M^x at y/h = -0.0625, -0.0833, -0.1667 and x/L = 0.0, respectively, for slot arm widths A_w = L/4, L/3 and 2L/3. Since cross-shaped slot is in fact a combination of two rectangular slots bisecting each other perpendicularly, it is expected that the nature of its current distributions and associated parameters should have some similarities with those of a rectangular slot or a square slot depending on the size of A_w. This is indeed apparent when one observes the shape of the current curve corresponding to A_w = 2L/3 which nearly approaches that for a square aperture of Fig. 3.9. It can also be anticipated that a further reduction of A_w beyond L/4 will lower the current minima in 3.29(a) to almost zero, thus contributing to half sinusoids, one on each side of the aperture centre, each similar to the rectangular slot current curves in Fig. 3.4 either (a) or (b).

However, the current distributions in Fig. 3.29(b) are similar to those of elliptical apertures of Fig. 3.23.

Fig. 3.30 shows transmission cross-sections for the slot. It is observed that increasing A_w produces a large increase in the peak value of the transmission cross-sections.
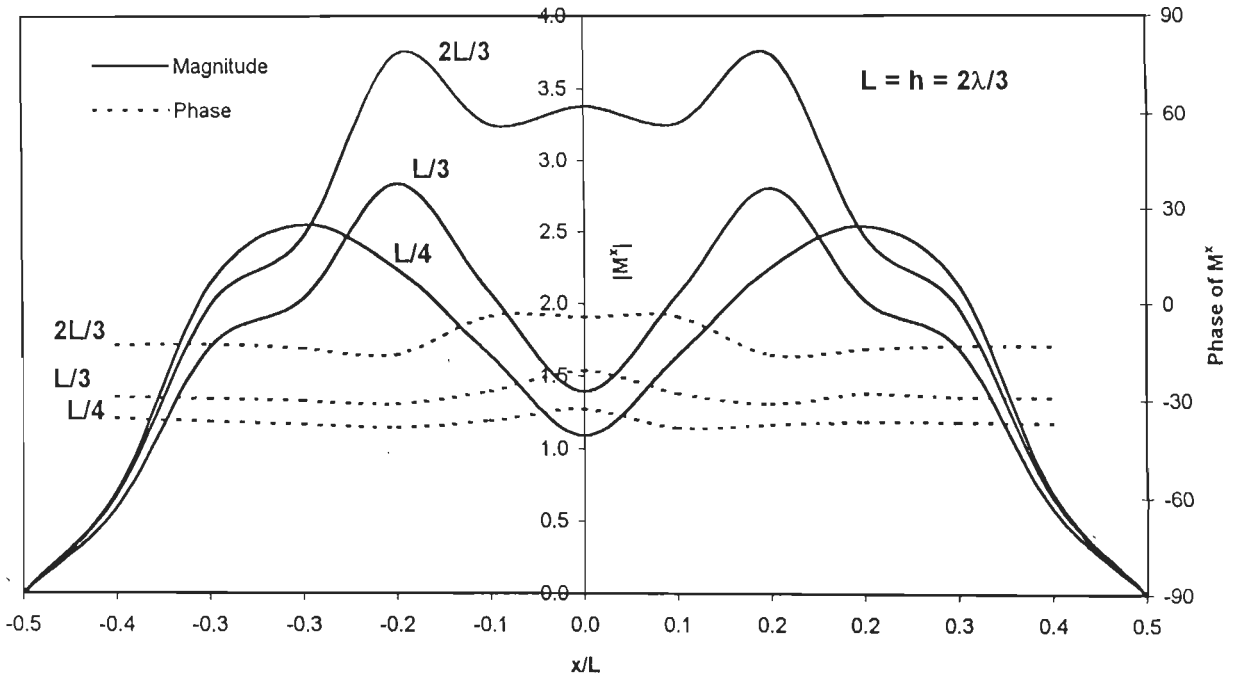
(a) y/h = -0.0625, -0.0833, -0.1667 for A_w = L/4, L/3 and 2L/3, respectively
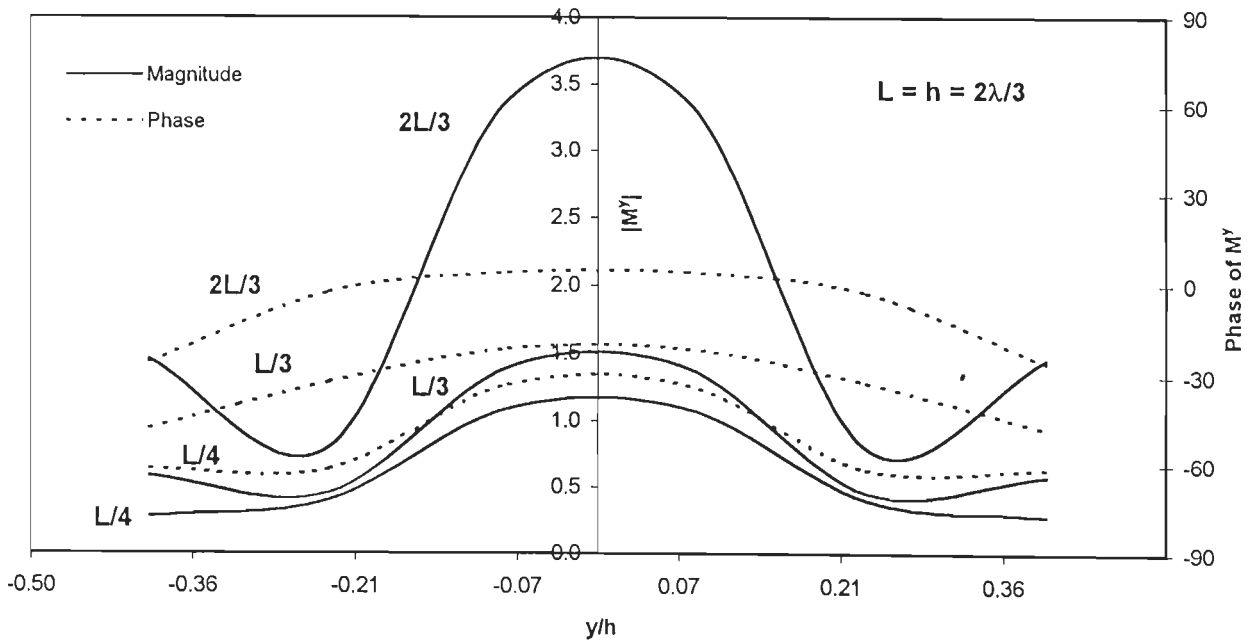
(b) x = 0.0

Fig. 3.29 : Equivalent surface magnetic current distributions for cross-shaped slots for different arm widths in a conducting screen
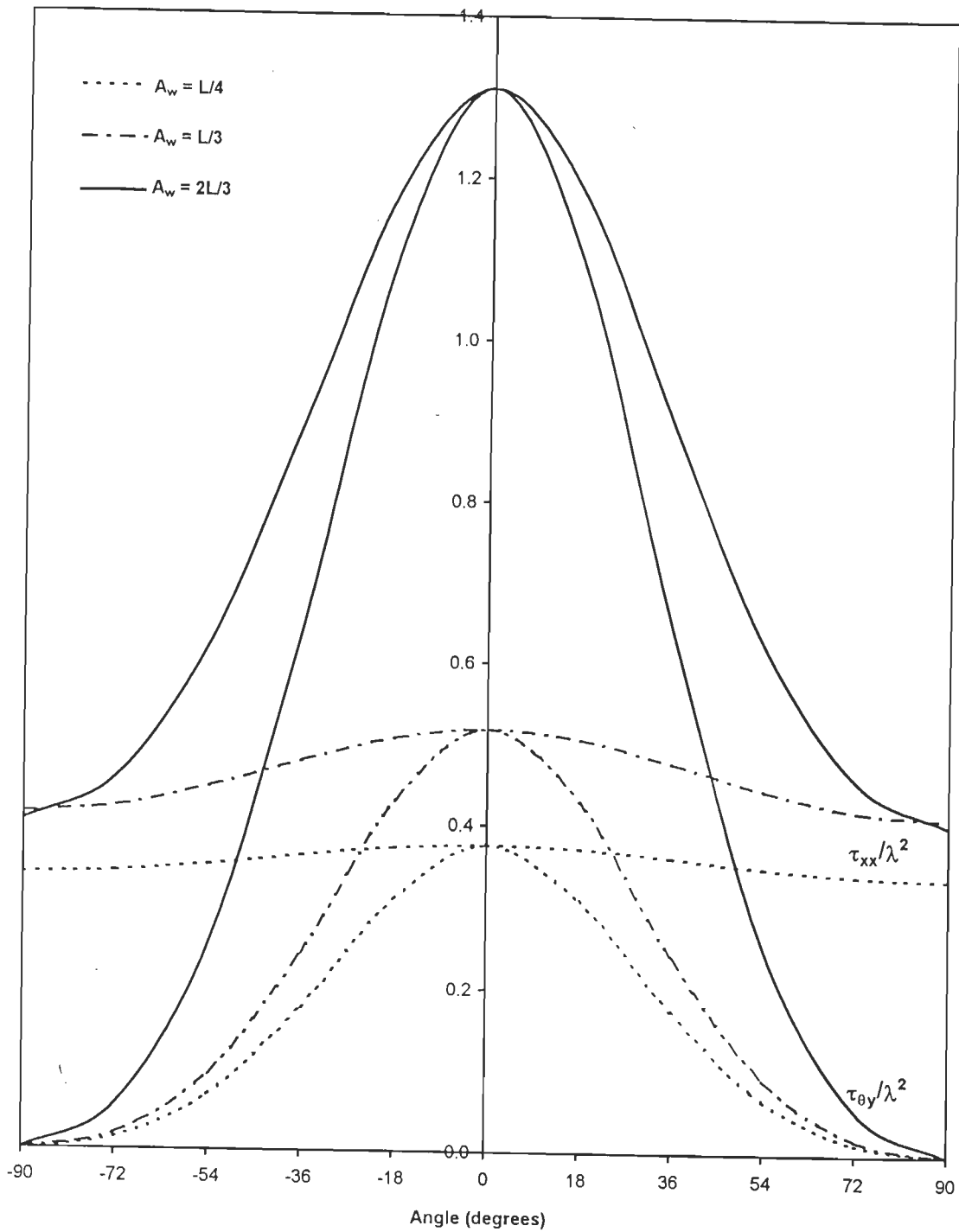
Fig. 3.30 : Transmission cross-sections τ_{0y}/λ^2 and τ_{xx}/λ^2 for cross-shaped slots for different arm widths in a conducting screen.

3.3-7 H-shaped Slot

The discretization used for H-shaped slot is shown in Fig. 3.31. The slot surface consists of 45 nodes, 68 interior edges and 56 triangular faces.
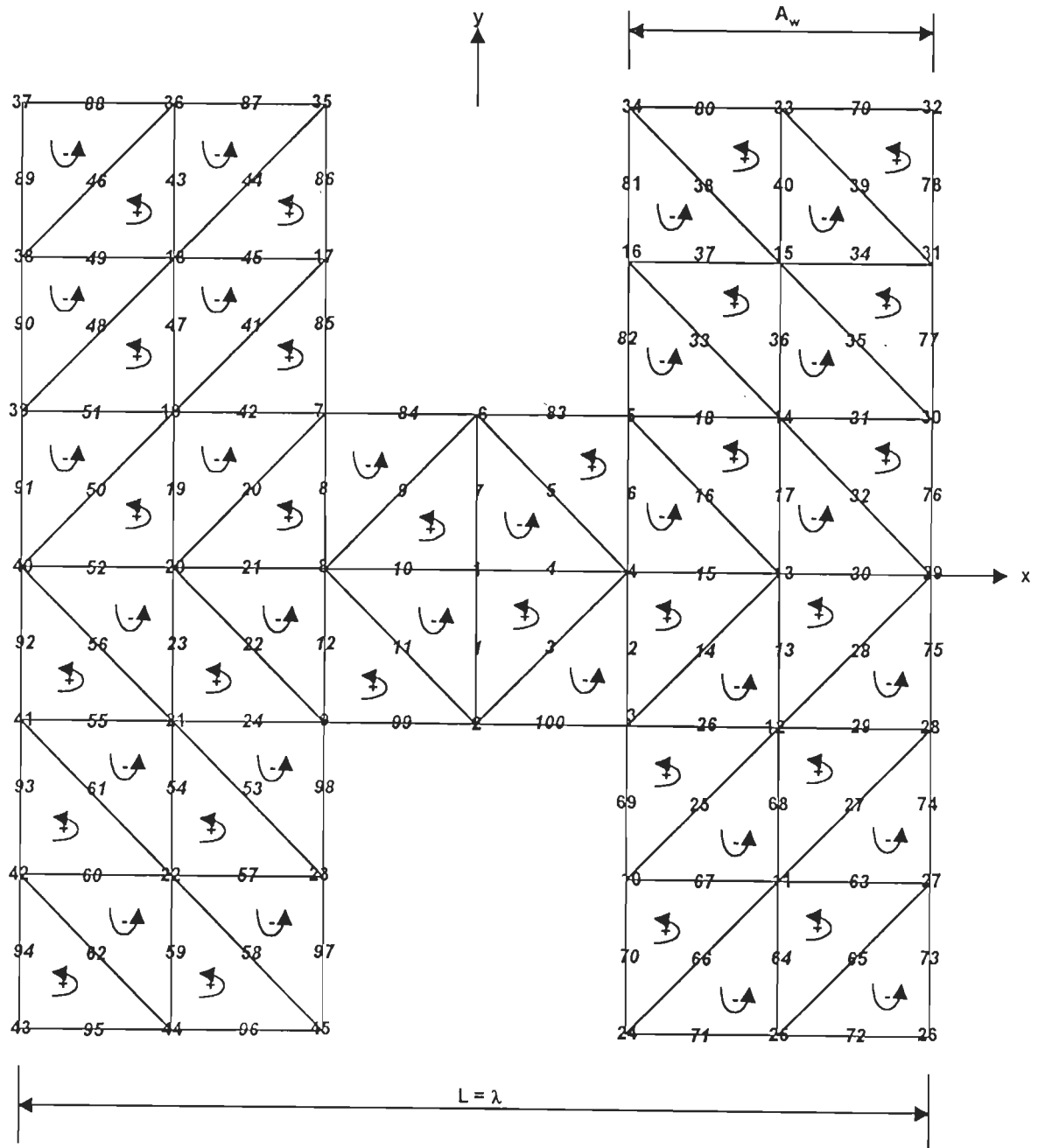
Fig. 3.31: Discretization of an H-shaped Slot Surface Showing Nodes, Edges and Current Directions

We considered two types of H-shaped slots, namely, small slots for which $L = h = \lambda/4$ and large slots for which $L = h = \lambda$. For each slot, the effect of varying arm width A_w on its near- and far-field parameters was considered. Fig. 3.32(a) shows magnetic current distributions at $y/h = -0.025$ and -0.0333, respectively, corresponding to slots with $A_w = \lambda/20$ and $A_w = \lambda/15$. The current distribution is relatively uniform around the aperture centre and in this case also, the magnitude of peak current is much greater than that obtained for circular and elliptic apertures. Fig. 3.32(b) shows current distributions at $x/L = 0.4875$ and 0.4833, respectively, for slots with $A_w = \lambda/20$ and $A_w = \lambda/15$. It is found that along the y-direction, the magnitude and phase distributions of M^x are nearly uniform.

Fig. 3.33 shows the corresponding transmission cross-sections of the slots with $A_w = \lambda/20$ and $A_w = \lambda/15$. It is seen that the transmission cross-section for slot with $A_w = \lambda/20$ is higher.

Fig. 3.34 shows magnetic current distributions at $y/h = -0.03125$, -0.0625, -0.09375 and -0.1, respectively, for slots of arm widths $A_w = 0.125\lambda$, 0.25λ, 0.375λ and 0.4λ. It is observed that as A_w is increased the current peak value decreases. Conversely, as A_w decreases, the current peak increases and the shape of its curve tapers towards the peak. Fig. 3.35 shows M^x distributions at $x/L = 0.4375$, 0.375, 0.3125 and 0.3 for slots of $A_w = 0.125\lambda$, 0.25λ, 0.375λ and 0.4λ, respectively.

Fig. 3.36 shows the corresponding transmission cross-sections for the slots. It is noted that transmission cross-section peak value increases with A_w as opposed to that in Fig. 3.33.
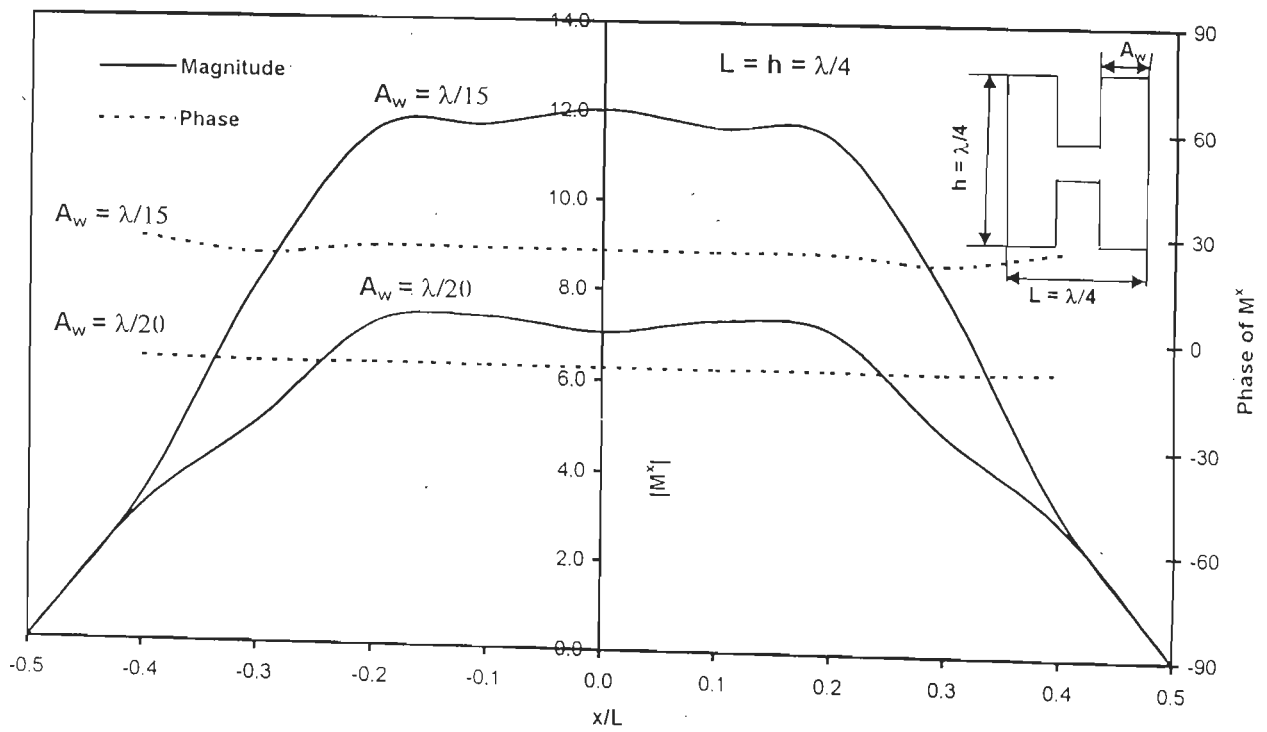
(a) y/h = - 0.025, - 0.0333, respectively
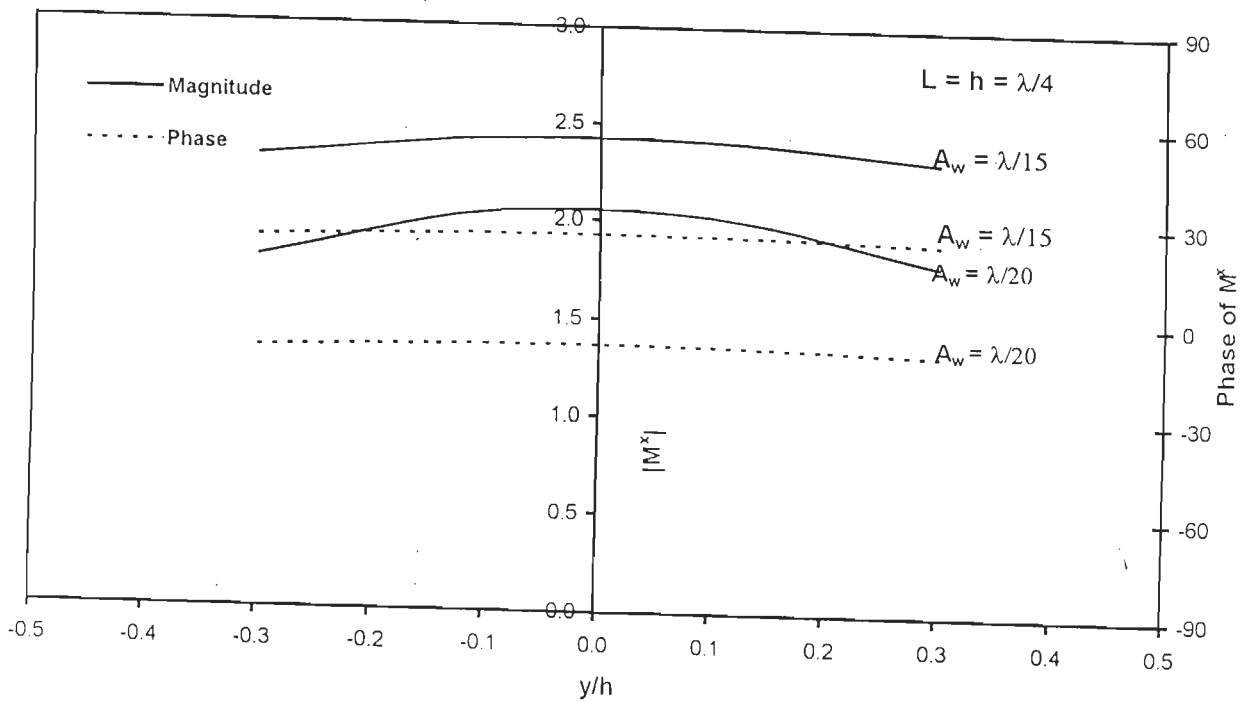
(b) x/L = 0.4875, 0.4833, respectively

Fig. 3.32 : Equivalent surface magnetic current distributions for
H-shaped slot in a conducting screen
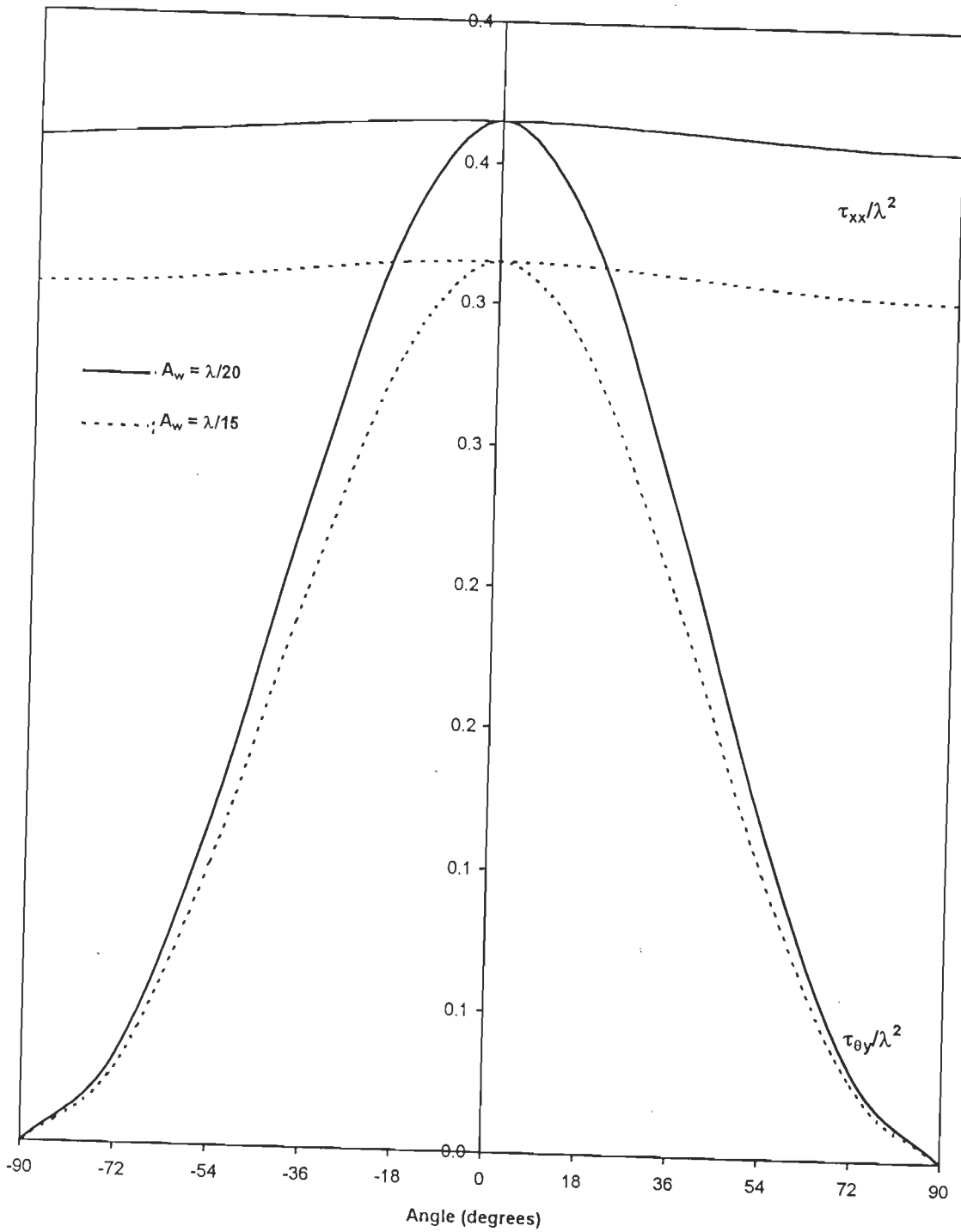
Fig. 3.33 : Transmission cross-sections for λ/4-long H-shaped slots for different arm widths in a conducting screen.
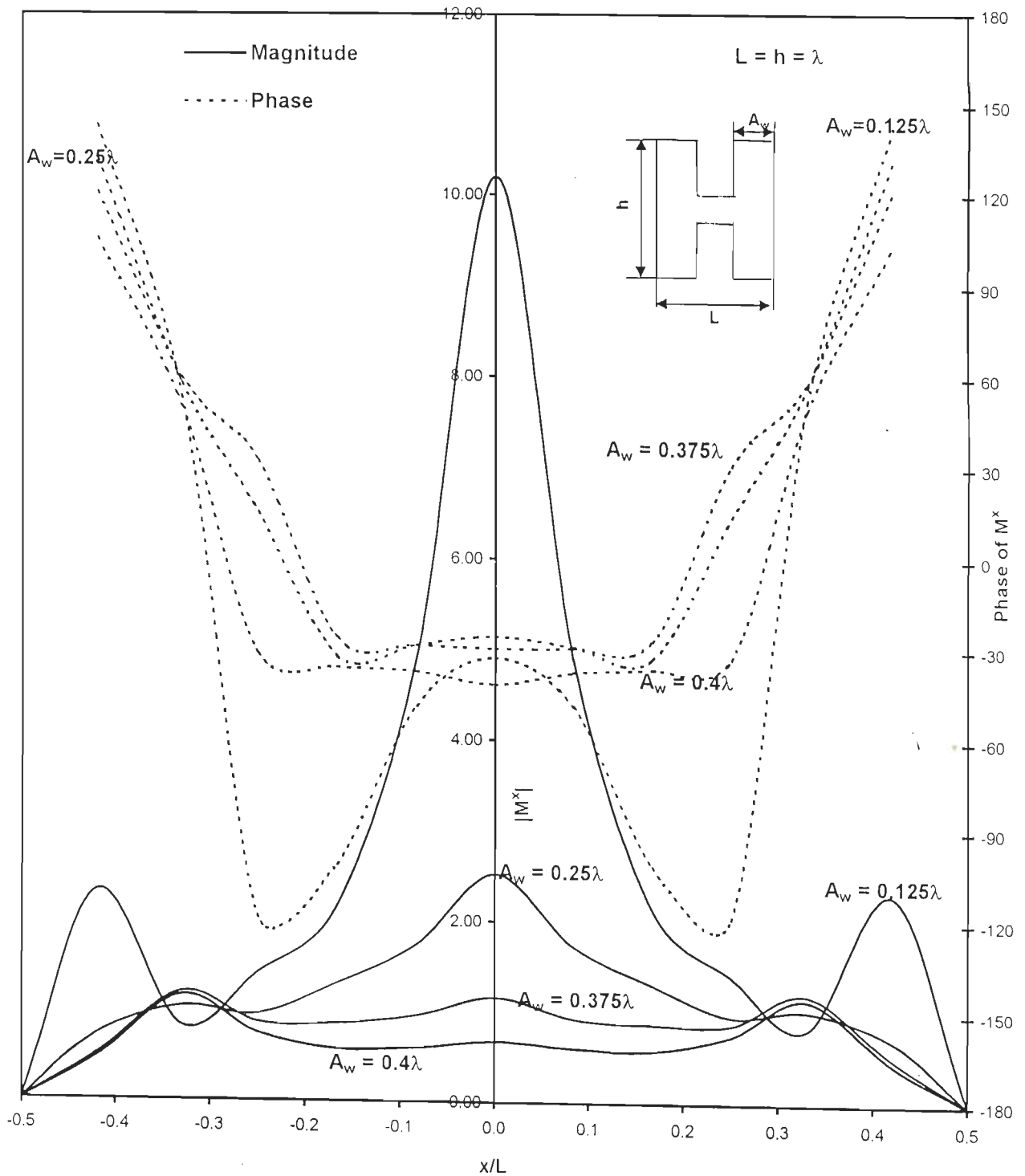
Fig. 3.34 : Equivalent surface magnetic current distributions for H-shaped slots at y/h = -0.03125, -0.0625, -0.09375 and -0.1, respectively, in a conducting screen
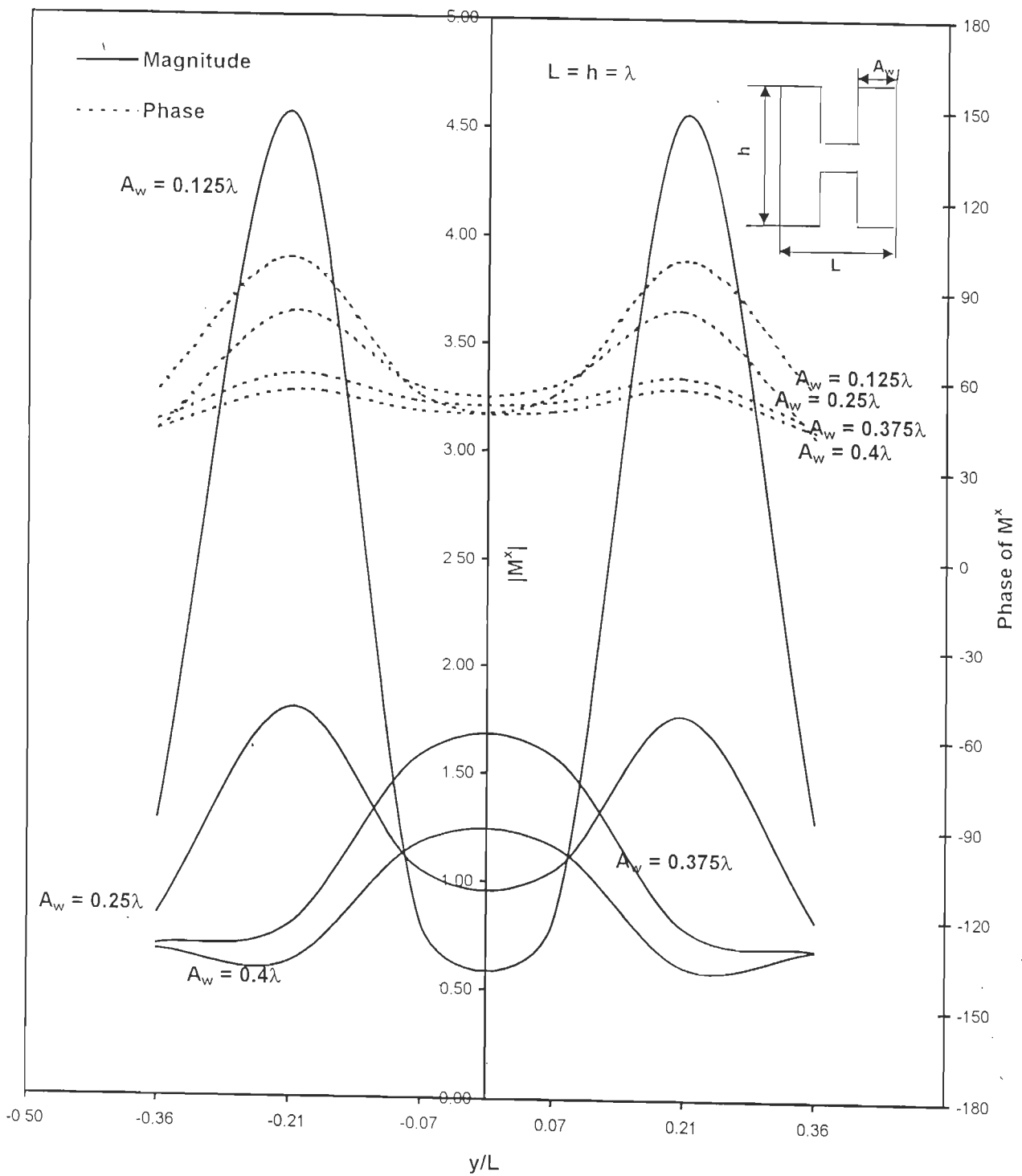
Fig. 3.35 : Equivalent surface magnetic current distributions along vertical arm of H-shaped slots for various arm widths at x/L = 0.4375, 0.375, 0.315 and 0.3, respectively, in a conducting screen
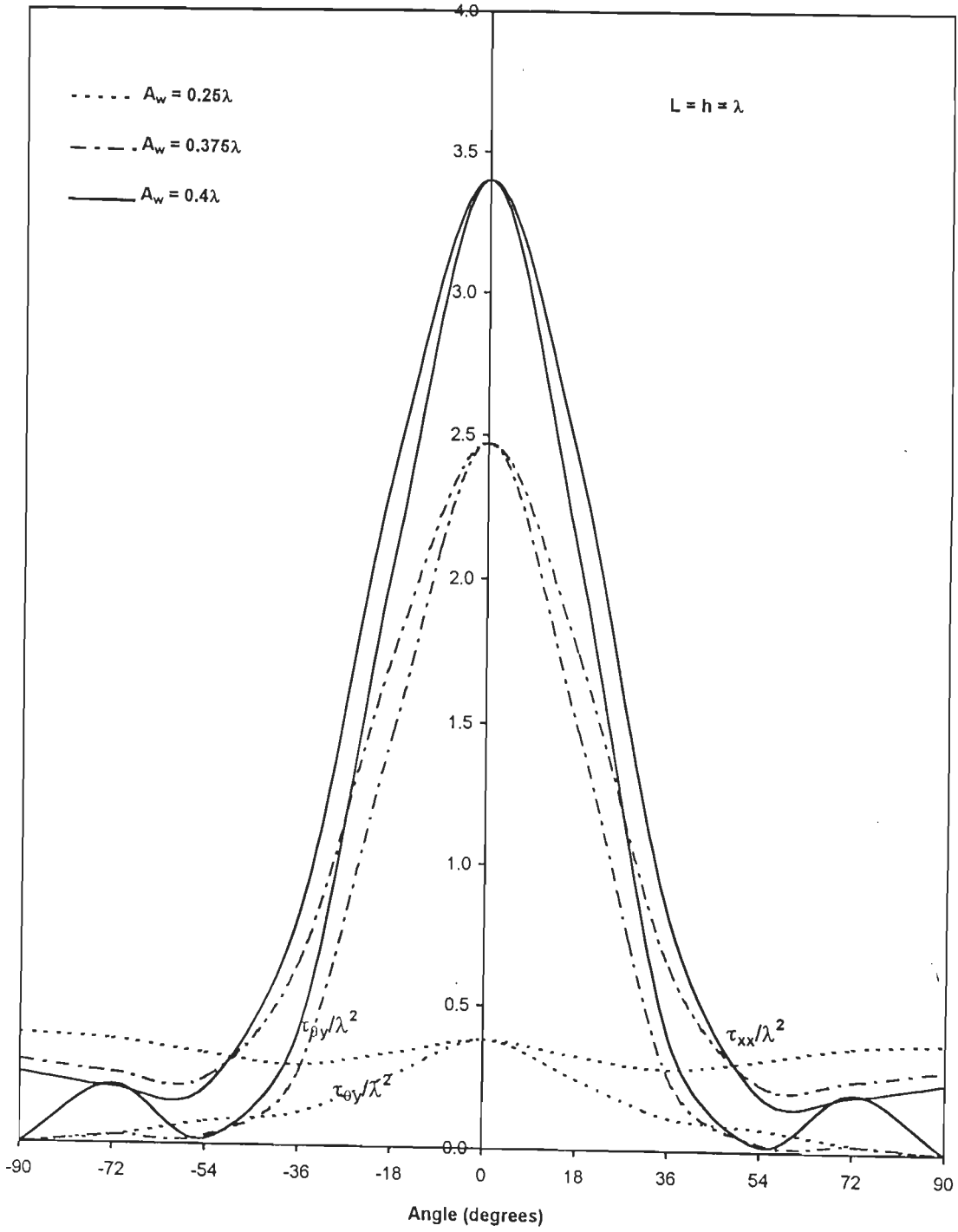
Fig. 3.36 : Transmission cross-sections for λ long H-shaped slots for different arm widths in a conducting screen.

3.3-8 A Comparative Study of Transmission Cross-sections for Various Aperture Shapes

We consider here a comparison of the transmission cross-sections for the apertures of various shapes. Two cases have been considered : small apertures having an area of $0.0325\lambda^2$ and relatively large apertures with an area of $0.1632\lambda^2$.

Fig. 3.37 compares transmission cross-sections τ_{0y}/λ^2 and τ_{xx}/λ^2 for smaller apertures of same area but different shapes. It is seen that the pattern for a H-shaped slot of $L = h = \lambda/4$ of arm width $\lambda/20$ exhibits the largest peak value. It is further observed that elliptic aperture gives a larger peak value than that of a rectangular slot of the same area. The peak values of transmission cross-section for circular and diamond-shaped apertures seem to be negligibly low for relatively small apertures. The τ_{xx}/λ^2 patterns for H-shaped slot, rectangular slot and elliptical apertures are similar with equally wide beamwidths. However, $\tau_{\theta y}/\lambda^2$ pattern for elliptic aperture has the narrowest beamwidth followed by that of H-shaped slot.

Fig. 3.38 shows the transmission cross-sections $\tau_{\theta y}/\lambda^2$ and τ_{xx}/λ^2 for relatively large apertures of various shapes. It is noted that diamond-shaped aperture has the highest peak value and the smallest τ_{xx}/λ^2 pattern beamwidth. Cross-shaped slot has the lowest peak value and the largest τ_{xx}/λ^2 pattern beamwidth. Elliptic aperture and rectangular slot, on the other hand, exhibit similar τ_{xx}/λ^2 patterns but the former has more directive τ_{0y}/λ^2 pattern of all the four cases studied here.
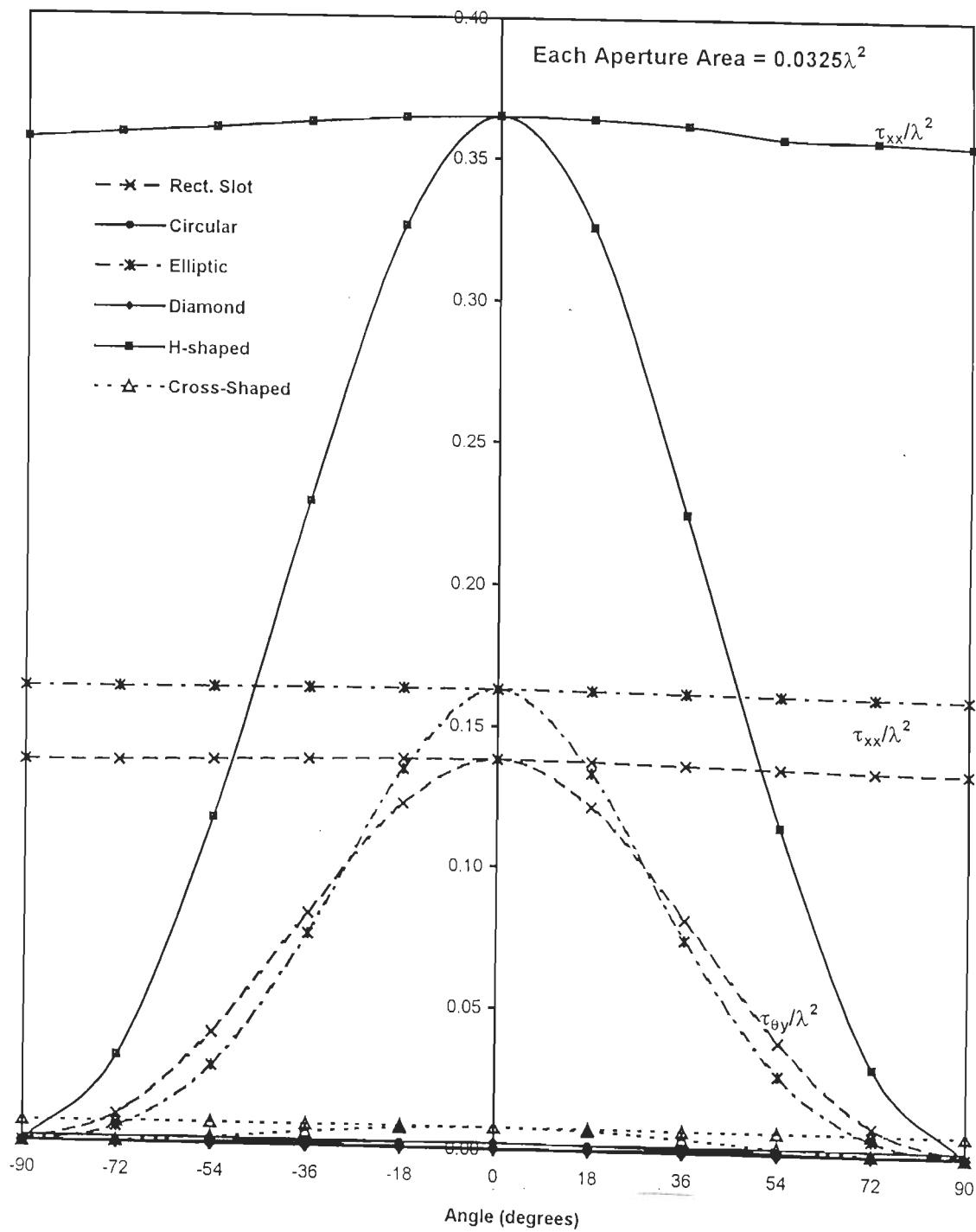
Fig. 3.37 : Transmission cross-sections $\tau_{\theta y}/\lambda^2$ and τ_{xx}/λ^2 for various small apertures in a conducting screen
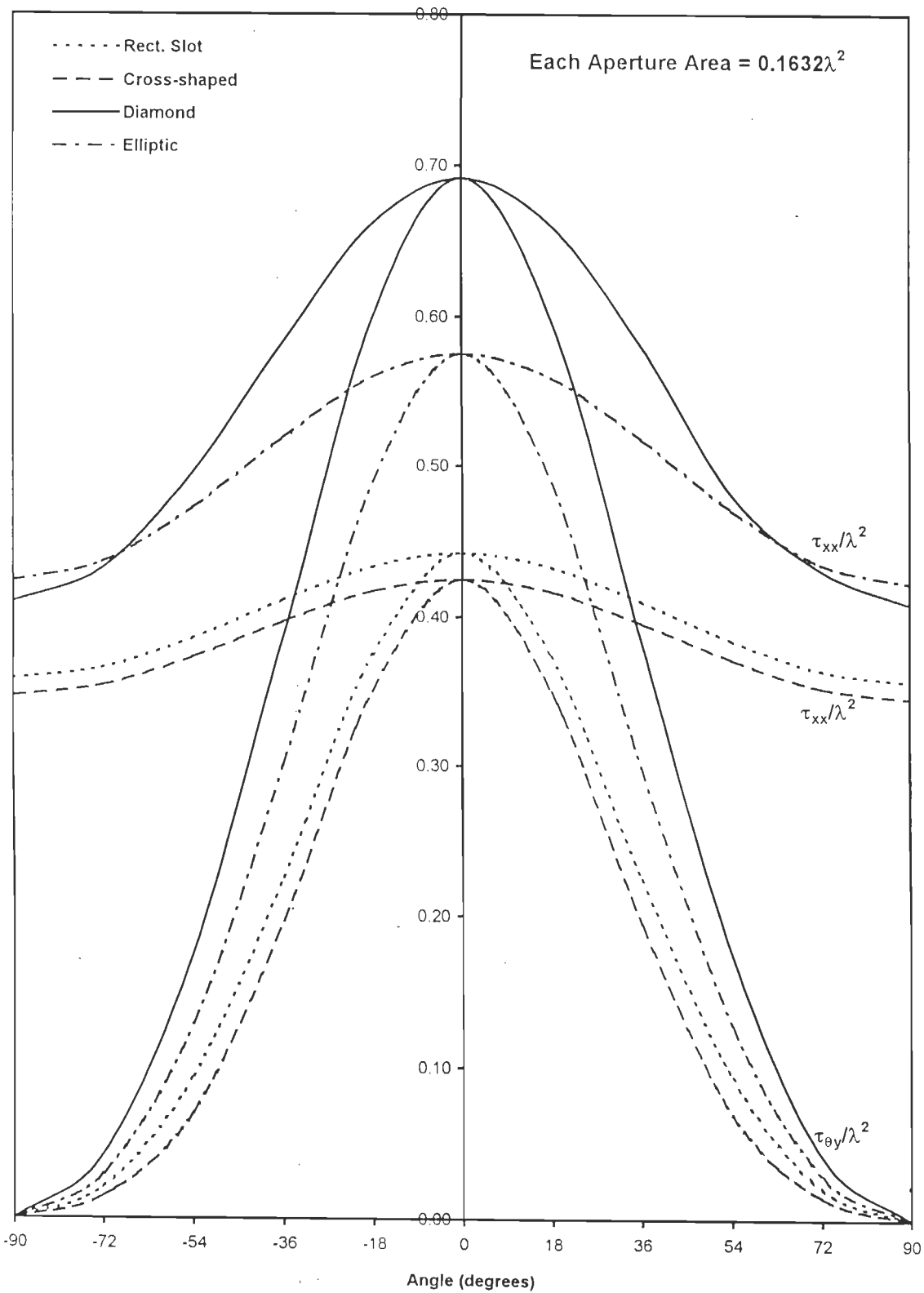
Fig. 3.38 : Transmission cross-sections $\tau_{\theta y}/\lambda^2$ and τ_{xx}/λ^2 for various large apertures in a conducting screen

3.4 SUMMARY

In this chapter, an extensive numerical study has been carried out on apertures of various shapes in an infinitesimally thin, perfectly conducting screen. The computer code has been validated by considering rectangular slots and square apertures for which results are available in the literature. All the results have been tested for convergence by utilizing sufficient number of triangular patches to discretise the aperture surfaces.

Results have been presented for magnetic current distribution, transmission coefficient and transmission cross-sections for rectangular, square, circular, elliptic, diamond-shaped, cross-shaped and H-shaped apertures.

A comparative study has been made on the transmission cross-sections of various apertures.

Chapter - 4

WAVEGUIDE BACKED APERTURES IN A CONDUCTING PLANE

Waveguide backed apertures radiating into half space, either singly or as an array, have been studied by many investigators, notably, Cohen et al. [21], Mautz and Harrington [68], Fenn et al. [35], Sinha et al. [97], Leong et al [57], [58] and Butler et al. [16]. However, all these studies have been restricted to rectangular apertures because of the difficulty in handling the apertures of other shapes.

We utilize the general formulation of Chapter 2 to study the radiation properties of waveguide backed apertures of different shapes, such as rectangular, circular, elliptical, diamond and H.

4.1 FORMULATION

Fig. 4.1 depicts the problem under investigation and defines the coordinates and parameters used. The waveguide-fed aperture is located in $z = 0$ plane which is occupied by a PEC except for the aperture. The conductor is considered to be infinitesimally thin and the aperture can take any shape.

As described in Chapter 2, we use equivalence principle to divide the problem into two separate regions, namely, a waveguide region ($z < 0$) and a half space region ($z > 0$), hereafter, called region 'a' and region 'b', respectively.

The original problem and equivalent problems are shown in Fig. 4.2. Region 'a' is now a semi-infinite waveguide short-circuited at $z = 0$, in which the total field is the superposition of the field due to the impressed sources and that due to equivalent magnetic surface current $\overline{M}$ over the aperture region. Region

102
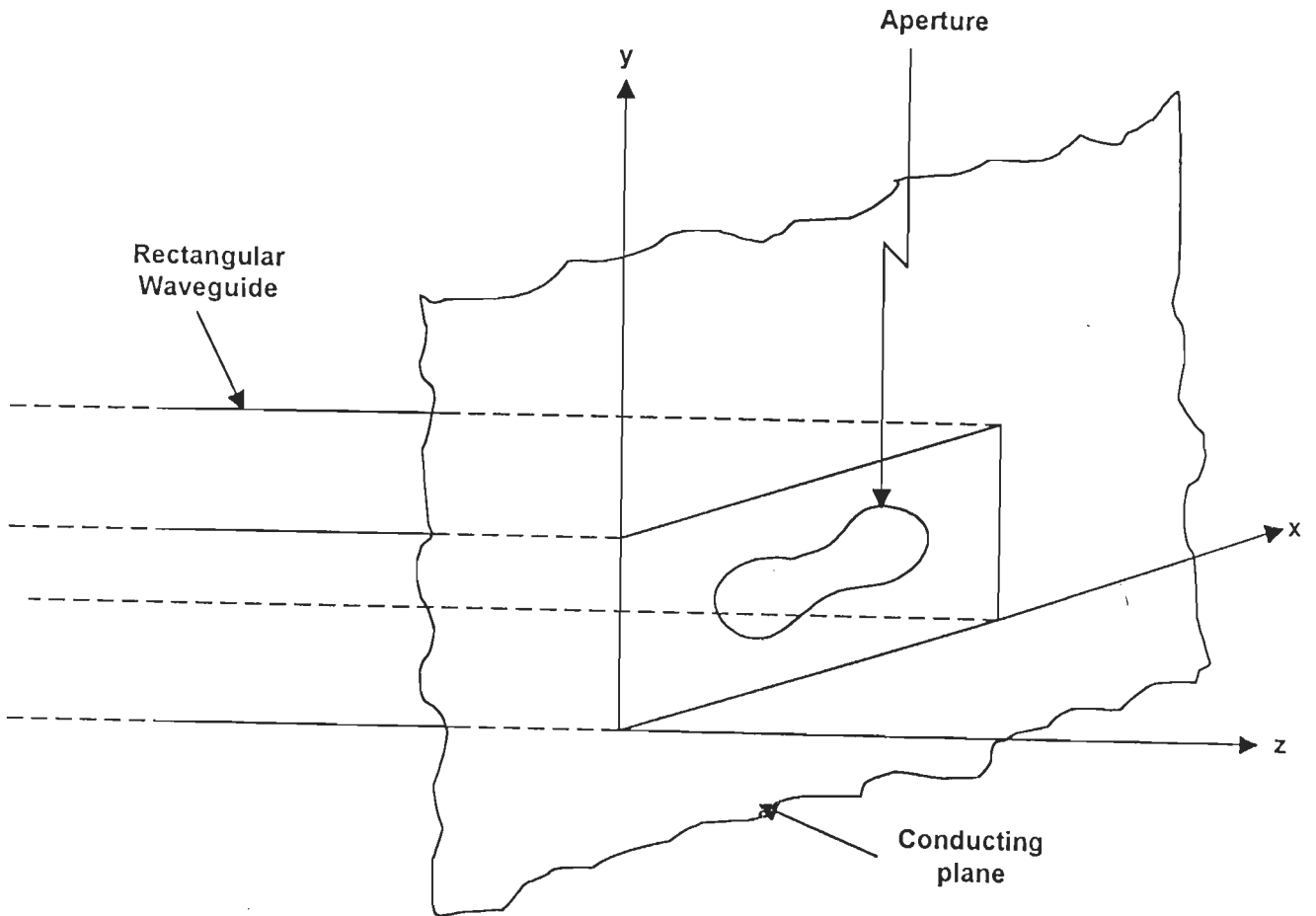
Fig. 4.1 : Waveguide-backed Aperture Radiating into Half Space
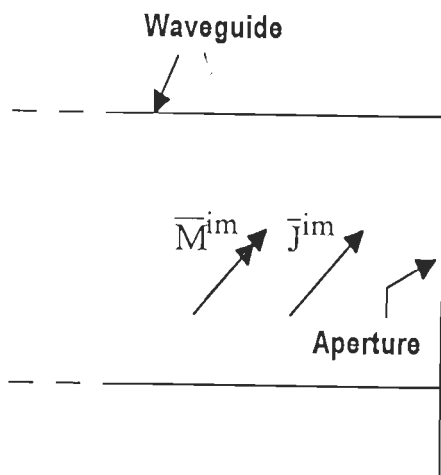
(a) Original problem
(Valid everywhere)
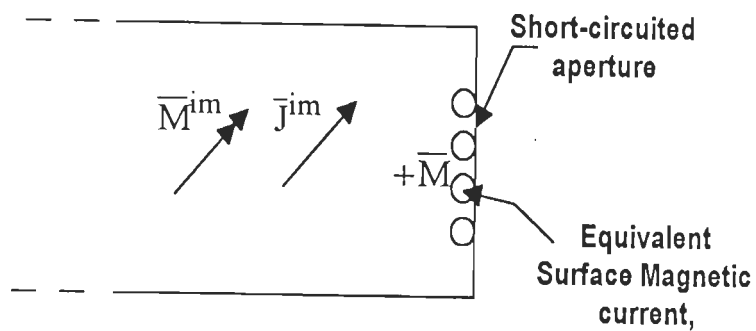
(b) Equivalent problem for region 'a'
(Valid at z < 0)
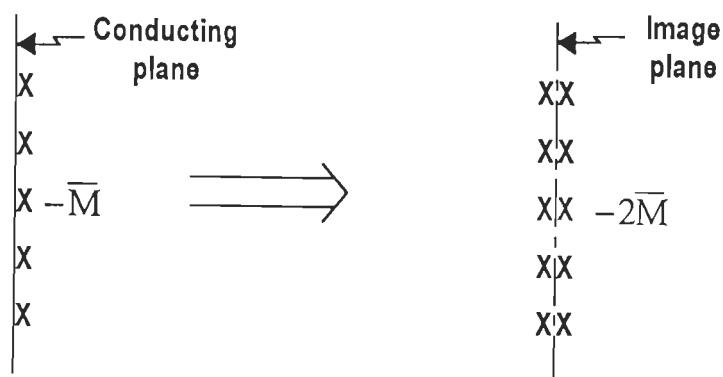
(c) Equivalent problem for region 'b'
(Valid at z > 0)

Fig. 4.2 : Original Problem and its Equivalent Models

'b' is a half space in which the field is due to current $-\overline{M}$ over the aperture region radiating in the presence of a continuous conducting plane. Using the image theory, it reduces to the problem of a current $-2\overline{M}$ over the aperture region radiating into free space (Fig. 4.2(c)).

From eqns. (2.8) and (2.9), the aperture admittance matrices for region 'a' and region 'b' can be written as

$$[Y^a] = [Y^{wg}] = [<M_m, H_t^a(\overline{M}_n)>]_{N \times N} \tag{4.1}$$

$$[Y^b] = [Y^{hs}] = [<M_m, H_t^b(\overline{M}_n)>]_{N \times N} \tag{4.2}$$

The elements of admittance matrices and the excitation vector have been derived in Chapter 2 (eqns (2.21) and (2.24), respectively) and are repeated here for the sake of completeness :

$$Y_{mn}^{wg} = -l_m \left\{ j\omega \left[\overline{F}_n^a(\overline{r}_m^{c+}) \bullet \frac{\overline{\rho}_m^{c+}}{2} + \overline{F}_n^a(\overline{r}_m^{c-}) \bullet \frac{\overline{\rho}_m^{c-}}{2} \right] + \phi_n^a(\overline{r}_m^{c-}) - \phi_n^a(\overline{r}_m^{c+}) \right\} \tag{4.3}$$

$$Y_{mn}^{hs} = -2l_m \left\{ j\omega \left[\overline{F}_n^b(\overline{r}_m^{c+}) \bullet \frac{\overline{\rho}_m^{c+}}{2} + \overline{F}_n^b(\overline{r}_m^{c-}) \bullet \frac{\overline{\rho}_m^{c-}}{2} \right] + \phi_n^b(\overline{r}_m^{c-}) - \phi_n^b(\overline{r}_m^{c+}) \right\} \tag{4.4}$$

$$I_m^i = -l_m \left\{ \overline{H}_t^i(\overline{r}_m^{c+}) \bullet \frac{\overline{\rho}_m^{c+}}{2} + \overline{H}_t^i(\overline{r}_m^{c-}) \bullet \frac{\overline{\rho}_m^{c-}}{2} \right\} \tag{4.5}$$

Evaluation of the half-space admittance matrix, eqn. (4.4), has already been carried out in sections 2.4.1 and 2.4.2. In the next section, we discuss the evaluation of potential functions ϕ and $\overline{F}$ which appear in eqn. (4.3).

4.2   EVALUATION OF $\overline{F}$ AND ϕ FOR THE WAVEGUIDE REGION

Equation (2.16) gives the magnetic field $\overline{H}^a(\overline{M}_n)$ due to the nth expansion function at any point inside region 'a' in terms of $\overline{F}_n^a(\overline{r}')$ and $\phi_n^a(\overline{r}')$. Further, $\overline{F}_n^a(\overline{r}')$ and $\phi_n^a(\overline{r}')$ are given by Eqns. (2.22) and (2.23), respectively,

$$\overline{F}_n^a(\overline{r}') = \varepsilon \iint_{T_n^{\pm}} \overline{\overline{G}}(\overline{r}\,|\overline{r}') \bullet \overline{M}_n(\overline{r}')ds' \tag{4.6}$$

$$\phi_n^a(\overline{r}') = \frac{-1}{j\omega\mu} \iint_{T_n^{\pm}} \left\{\nabla\bullet\overline{\overline{G}}(\overline{r}\,|\,\overline{r}')\right\}\bullet\overline{M}_n(\overline{r}')ds' \tag{4.7}$$

where $\overline{\overline{G}}(\overline{r}\,|\overline{r}')$, in this problem, is dyadic Green's function pertaining to the electric vector potential in a waveguide short-circuited at one end, which is given by [106]

$$\overline{\overline{G}}(\overline{r}\,|\overline{r}') = \sum_{r=0}^{\infty}\sum_{s=0}^{\infty} \frac{\varepsilon_r\varepsilon_s}{ab\gamma_{rs}} \left[\left\{ \hat{x}\hat{x}\sin\left(\frac{r\pi x}{a}\right)\sin\left(\frac{r\pi x'}{a}\right)\cos\left(\frac{s\pi y}{b}\right)\cos\left(\frac{s\pi y'}{b}\right) \right.\right.$$

$$\left. +\hat{y}\hat{y}\cos\left(\frac{r\pi x}{a}\right)\cos\left(\frac{r\pi x'}{a}\right)\sin\left(\frac{s\pi y}{b}\right)\sin\left(\frac{s\pi y'}{b}\right)\right\}$$

$$\times \begin{cases} e^{-\gamma_{rs}z}\cosh(\gamma_{rs}z') & , \quad z > z' \\ e^{-\gamma_{rs}z'}\cosh(\gamma_{rs}z) & , \quad z < z' \end{cases}$$

$$+ \hat{z}\hat{z}\cos\left(\frac{r\pi x}{a}\right)\cos\left(\frac{r\pi x'}{a}\right)\cos\left(\frac{s\pi y}{b}\right)\cos\left(\frac{s\pi y'}{b}\right)$$

$$\left.\times \begin{cases} e^{-\gamma_{rs}z}\sinh(\gamma_{rs}z') & , \quad z > z' \\ e^{-\gamma_{rs}z'}\sinh(\gamma_{rs}z) & , \quad z < z' \end{cases}\right] \tag{4.8}$$

where ε_l and γ_{rs} are, respectively, the Neumann's constant and the waveguide propagation constant which are given by

$$\varepsilon_l = \begin{cases} 1, & l = 0 \\ 2, & l > 0 \end{cases} \tag{4.9}$$

$$\gamma_{rs}^2 = \left(\frac{r\pi}{a}\right)^2 + \left(\frac{s\pi}{b}\right)^2 - k^2 \tag{4.10}$$

where r and s are modal indices and

$$k = \omega\sqrt{\mu\varepsilon} \tag{4.11}$$

Substituting eqns. (4.9), (2.12) and (2.13), accordingly, in eqns. (4.6) and (4.7), we get

$$\overline{F}_n^a(\overline{r}') = \frac{\pm\varepsilon}{ab}\frac{l_n}{2A_q}\sum_{r=0}^{\infty}\sum_{s=0}^{\infty}\frac{\varepsilon_r\varepsilon_s}{\gamma_{rs}}\iint_{T_n^\pm}\left\{\hat{x}\,(x'-x_n)\sin\left(\frac{r\pi x}{a}\right)\sin\left(\frac{r\pi x'}{a}\right)\cos\left(\frac{s\pi y}{b}\right)\cos\left(\frac{s\pi y'}{b}\right)\right.$$
$$\left. +\hat{y}(y'-y_n)\cos\left(\frac{r\pi x}{a}\right)\cos\left(\frac{r\pi x'}{a}\right)\sin\left(\frac{s\pi y}{b}\right)\sin\left(\frac{s\pi y'}{b}\right)\right\}dx'dy' \tag{4.12}$$

$$\phi_n^a(\overline{r}') = \frac{\mp l_n}{j\omega\mu ab}\frac{1}{2A_q}\sum_{r=0}^{\infty}\sum_{s=0}^{\infty}\frac{\varepsilon_r\varepsilon_s}{\gamma_{rs}}\iint_{T_n^\pm}\left\{\frac{r\pi}{a}(x'-x_n)\cos\left(\frac{r\pi x}{a}\right)\sin\left(\frac{r\pi x'}{a}\right)\cos\left(\frac{s\pi y}{b}\right)\cos\left(\frac{s\pi y'}{b}\right)\right.$$
$$\left. +\frac{s\pi}{b}(y'-y_n)\cos\left(\frac{r\pi x}{a}\right)\cos\left(\frac{r\pi x'}{a}\right)\cos\left(\frac{s\pi y}{b}\right)\sin\left(\frac{s\pi y'}{b}\right)\right\}dx'dy' \tag{4.13}$$

As discussed in chapter 2, we utilize Galerkin method and centroid approximation to evaluate the integrals in eqns. (4.12) and (4.13) for observation point in triangle p and source currents residing in triangle q.

Thus, according to eqns. (2.26) and (2.27), eqns. (4.12) and (4.13) can be written as :

$$\overline{F}_j^{pq} = \frac{\varepsilon l_j}{2abA_q}\sum_{r=0}^{\infty}\sum_{s=0}^{\infty}\frac{\varepsilon_r\varepsilon_s}{\gamma_{rs}}\iint_{A_q}\left\{\hat{x}\,(x'-x_j)\sin\left(\frac{r\pi x}{a}\right)\sin\left(\frac{r\pi x'}{a}\right)\cos\left(\frac{s\pi y}{b}\right)\cos\left(\frac{s\pi y'}{b}\right)\right.$$
$$\left. +\hat{y}(y'-y_j)\cos\left(\frac{r\pi x}{a}\right)\cos\left(\frac{r\pi x'}{a}\right)\sin\left(\frac{s\pi y}{b}\right)\sin\left(\frac{s\pi y'}{b}\right)\right\}dx'dy' \tag{4.14}$$

$$\phi_j^{pq} = \frac{\mp 1_j}{2j\omega\mu abA_q} \sum_{r=0}^{\infty}\sum_{s=0}^{\infty} \frac{\varepsilon_r\varepsilon_s}{\gamma_{rs}} \iint_{A_q} \left\{ \frac{r\pi}{a}(x'-x_j)\cos\left(\frac{r\pi x}{a}\right)\sin\left(\frac{r\pi x'}{a}\right)\cos\left(\frac{s\pi y}{b}\right)\cos\left(\frac{s\pi y'}{b}\right) \right.$$

$$\left. + \frac{s\pi}{b}(y'-y_j)\cos\left(\frac{r\pi x}{a}\right)\cos\left(\frac{r\pi x'}{a}\right)\cos\left(\frac{s\pi y}{b}\right)\sin\left(\frac{s\pi y'}{b}\right) \right\} dx'dy' \qquad (4.15)$$

Integrals in eqns. (4.14) and (4.15) can be evaluated conveniently, after transformation into area coordinates. Thus, according to eqn. (2.60), $\overline{F}_j^{pq}$ and ϕ_j^{pq} can be expressed as :

$$\overline{F}_j^{pq} = \frac{\varepsilon 1_j}{2abA_q} \sum_{r=0}^{\infty}\sum_{s=0}^{\infty} \frac{\varepsilon_r\varepsilon_s}{\gamma_{rs}} 2A_q \int_0^1 \int_0^{1-L_2} \left\{ \hat{x}\left((x_1-x_j)+(x_2-x_1)L_2 \right.\right.$$

$$+(x_3-x_1)L_3)\sin\left(\frac{r\pi x}{a}\right)\sin\left(\frac{r\pi}{a}(x_1+(x_2-x_1)L_2+(x_3-x_1)L_3)\right)$$

$$\times \cos\left(\frac{s\pi y}{b}\right)\cos\left(\frac{s\pi}{b}(y_1+(y_2-y_1)L_2+(y_3-y_1)L_3)\right)$$

$$+ \hat{y}((y_1-y_j)+(y_2-y_1)L_2+(y_3-y_1)L_3)\cos\left(\frac{r\pi x}{a}\right)$$

$$\times \cos\left(\frac{r\pi}{a}(x_1+(x_2-x_1)L_2+(x_3-x_1)L_3)\right)\sin\left(\frac{s\pi y}{b}\right)$$

$$\left.\times \sin\left(\frac{s\pi}{b}(y_1+(y_2-y_1)L_2+(y_3-y_1)L_3)\right)\right\} dL_2 dL_3 \qquad (4.16)$$

$$\phi_j^{pq} = \frac{\mp 1_j}{2abj\omega\mu A_q} \sum_{r=0}^{\infty}\sum_{s=0}^{\infty} \frac{\varepsilon_r\varepsilon_s}{\gamma_{rs}} 2A_q \int_0^1 \int_0^{1-L_2} \left\{ \frac{r\pi}{a}((x_1-x_j)+(x_2-x_1)L_2 \right.$$

$$+(x_3-x_1)L_3)\cos\left(\frac{r\pi x}{a}\right)\sin\left(\frac{r\pi}{a}(x_1+(x_2-x_1)L_2+(x_3-x_1)L_3)\right)$$

$$\times \cos\left(\frac{s\pi y}{b}\right)\cos\left(\frac{s\pi}{b}(y_1+(y_2-y_1)L_2+(y_3-y_1)L_3)\right)$$

$$+ \frac{s\pi}{b}((y_1-y_j)+(y_2-y_1)L_2+(y_3-y_1)L_3)\cos\left(\frac{r\pi x}{a}\right)$$

$$\times \cos\left(\frac{r\pi}{a}(x_1+(x_2-x_1)L_2+(x_3-x_1)L_3)\right)\cos\left(\frac{s\pi y}{b}\right)$$

$$\left.\times \sin\left(\frac{s\pi}{b}(y_1+(y_2-y_1)L_2+(y_3-y_1)L_3)\right)\right\} dL_2 dL_3 \qquad (4.17)$$

For seven point numerical integration, the equations reduce to

$$\overline{F}_j^{pq} = \frac{\varepsilon l_j}{2abA_q} \sum_{r=0}^{\infty}\sum_{s=0}^{\infty} \frac{\varepsilon_r\varepsilon_s}{\gamma_{rs}} A_q \sum_{m=1}^{7} W(m)\Big\{ \hat{x}\,((x_1 - x_j) + (x_2 - x_1)L_{2m}$$

$$+(x_3 - x_1)L_{3m})\sin\left(\frac{r\pi x}{a}\right)\sin\left(\frac{r\pi}{a}(x_1 + (x_2 - x_1)L_{2m} + (x_3 - x_1)L_{3m})\right)$$

$$\cos\left(\frac{s\pi y}{b}\right)\cos\left(\frac{s\pi}{b}(y_1 + (y_2 - y_1)L_{2m} + (y_3 - y_1)L_{3m})\right)$$

$$+\hat{y}((y_1 - y_j) + (y_2 - y_1)L_{2m} + (y_3 - y_1)L_{3m})\cos\left(\frac{r\pi x}{a}\right)$$

$$\times \cos\left(\frac{r\pi}{a}(x_1 + (x_2 - x_1)L_{2m} + (x_3 - x_1)L_{3m})\right)\sin\left(\frac{s\pi y}{b}\right)$$

$$\times \sin\left(\frac{s\pi}{b}(y_1 + (y_2 - y_1)L_{2m} + (y_3 - y_1)L_{3m})\right)\Big\} \tag{4.18}$$

$$\phi_j^{pq} = \frac{\mp l_j}{2abj\omega\mu A_q}\sum_{r=0}^{\infty}\sum_{s=0}^{\infty}\frac{\varepsilon_r\varepsilon_s}{\gamma_{rs}} A_q \sum_{m=1}^{7} W(m)\Big\{ \frac{r\pi}{a}((x_1 - x_j) + (x_2 - x_1)L_{2m}$$

$$+(x_3 - x_1)L_{3m})\cos\left(\frac{r\pi x}{a}\right)\sin\left(\frac{r\pi}{a}(x_1 + (x_2 - x_1)L_{2m} + (x_3 - x_1)L_{3m})\right)$$

$$\cos\left(\frac{s\pi y}{b}\right)\cos\left(\frac{s\pi}{b}(y_1 + (y_2 - y_1)L_{2m} + (y_3 - y_1)L_{3m})\right)$$

$$+\frac{s\pi}{b}((y_1 - y_j) + (y_2 - y_1)L_{2m} + (y_3 - y_1)L_{3m})\cos\left(\frac{r\pi x}{a}\right)$$

$$\times \cos\left(\frac{r\pi}{a}(x_1 + (x_2 - x_1)L_{2m} + (x_3 - x_1)L_{3m})\right)\cos\left(\frac{s\pi y}{b}\right)$$

$$\times \sin\left(\frac{s\pi}{b}(y_1 + (y_2 - y_1)L_{2m} + (y_3 - y_1)L_{3m})\right)\Big\} \tag{4.19}$$

where m denotes the mth sampling point in the domain of T^q, $W(m)$ is the weighting factor for the mth sampling point, L_{2m} and L_{3m} are the values of L_2 and L_3 at the mth sampling point. $W(m)$, L_{2m} and L_{3m} are given in Table 2.1.

4.3   EVALUATION OF EXCITATION VECTOR

Assuming that only the dominant TE_{10} mode of unit amplitude is incident in region 'a', tangential (to the aperture) components of the electric and magnetic fields in the incident wave can be written as

$$\overline{E}_t^{io} = \overline{e}_o e^{-\gamma_o z}$$

(4.20)

$$\overline{H}_t^{io} = Y_o e^{-\gamma_o z} \hat{z} \times \overline{e}_o$$

(4.21)

where Y_o and γ_o are, respectively, the characteristic admittance and the propagation constant for the dominant mode and are given by

$$Y_o = \frac{\gamma_o}{j\omega\mu}$$

(4.22)

$$\gamma_o = \begin{cases} jk_o\sqrt{1-(f_c/f)^2}, & f > f_c \\ \dfrac{2\pi}{\lambda_e}\sqrt{1-(f/f_c)^2}, & f < f_c \end{cases}$$

(4.23)

where f_c is the cut-off frequency of the dominant mode. The normalized modal vector $\overline{e}_o$ for the dominant mode can be written as

$$\overline{e}_o = -\hat{y}\sin\frac{\pi x}{a}$$

(4.24)

When the aperture is covered by a conductor, the waveguide is terminated in a short-circuit and tangential magnetic field at $z = 0$ is now twice that in the wave. That is,

$$\overline{H}_t^i = 2\overline{H}_t^{io}$$

(4.25)

where $\overline{H}_t^{io}$ denotes the magnetic field incident on the short-circuit. Therefore, an element of excitation vector, in eqn. (4.5) becomes

$$I_m^i = -2l_m\left\{ H_{tx}^{io}(\overline{r}_m^{c+})\frac{\rho_{mx}^{c+}}{2} + H_{tx}^{io}(\overline{r}_m^{c-})\frac{\rho_{mx}^{c-}}{2} \right\}$$

(4.26)

110

4.4   EVALUATION OF EQUIVALENT APERTURE ADMITTANCE

To evaluate the aperture admittance seen by the dominant TE_{10} mode, we first evaluate the dominant mode reflection coefficient. Since the excitation of the waveguide is by the dominant TE_{10} mode of unit amplitude, the electric field transverse to the z-direction can be expressed in modal form as

$$\overline{E}_t = e^{-\gamma_o z} \overline{e}_o + \sum_{i=0}^{\infty} \Gamma_i e^{\gamma_i z} \overline{e}_i \qquad (4.27)$$

where the subscript 'o' denotes the dominant TE_{10} mode and Γ_i are the complex amplitudes of the $-z$ travelling wave of the ith mode. The $\overline{e}_i$ are normalized modal vectors, such that;

$$\iint_s \overline{e}_i \bullet \overline{e}_j \, ds = \begin{cases} 0, & i \neq j \\ 1, & i = j \end{cases} \qquad (4.28)$$

where the integration is over the waveguide cross-section. The magnetic current $\overline{M}$ over the aperture region is given by eqn. (2.1) as

$$\overline{M} = \hat{z} \times \overline{E}_t = \hat{z} \times \overline{e}_o + \sum_i \Gamma_i \hat{z} \times \overline{e}_i \qquad (4.29)$$

Now multiplying each side of eqn. (4.29) scalarly by $\hat{z} \times \overline{e}_j$, integrating over the waveguide cross-section and using orthogonality property of eqn. (4.28), we obtain

$$\iint_{\text{aperture}} \overline{M} \bullet \hat{z} \times \overline{e}_i \, . \, ds = \begin{cases} 1 + \Gamma_o, & i = 0 \\ \Gamma_i, & i \neq 0 \end{cases} \qquad (4.30)$$

where Γ_o is the reflection coefficient for the dominant TE_{10} mode and the integration is over the aperture region, since $\overline{M} = 0$ elsewhere.

Substituting for $\overline{M}$ from eqn. (2.3) and using the fact that only Γ_o is of interest in this case, leads to

$$\sum_n V_n \iint_{T_n^{\pm}} \overline{M}_n \bullet \hat{z} \times \overline{e}_o \ ds \ = \ 1 + \Gamma_o$$

or

$$\Gamma_o \ = \ -1 + \sum_n V_n \iint_{T_n^{\pm}} \overline{M}_n \bullet \hat{z} \times \overline{e}_o \ ds \qquad (4.31)$$

in which substituting $\overline{e}_o$ and using eqns. (2.12) and (2.62) in eqn. (4.31) we get

$$\Gamma_o \ = \ -1 + \frac{1}{2A_q} \sum_{n=1}^{N} l_n V_n \iint_{T_n^{\pm}} (x - x_n) \sin\frac{\pi}{a} \ dx\, dy \qquad (4.32)$$

The integration in eqn. (4.32) can be transformed into an integration over area coordinates to obtain

$$\Gamma_o \ = \ -1 + \sum_{q=1}^{Q} \Gamma_{oq} \qquad (4.33)$$

where $\Gamma_{oq} = \dfrac{1}{2A_q} \sum_{j=1}^{3} l_j V_j \ 2A_q \displaystyle\int_o^1 \int_o^{1-L_2} \{ \hat{x} \ ((x_1 - x_j) + (x_2 - x_1)L_2$

$$+ (x_3 - x_1)L_3) \sin\left(\frac{\pi}{a}(x_1 + (x_2 - x_1)L_2 + (x_3 - x_1)L_3)\right) \} \, dL_2 \, dL_3 \qquad (4.34)$$

Using Gauss quadrature technique, eqn. (4.34) can be written as

$$\Gamma_{oq} = \frac{1}{2A_q} \sum_{j=1}^{3} l_j V_j \ A_q \sum_{m=1}^{M} W(m) \{ (x_1 - x_j) + (x_2 - x_1)L_{2m}$$

$$+ (x_3 - x_1)L_{3m}) \sin\left(\frac{\pi}{a}(x_1 + (x_2 - x_1)L_{2m} + (x_3 - x_1)L_{3m})\right) \qquad (4.35)$$

Aperture equivalent admittance seen by the dominant mode is computed, according to [68], as

$$Y_{ap} \ = \ \frac{1 - \Gamma_o}{1 + \Gamma_o} Y_o \qquad (4.36)$$

where Y_o is given by eqn. (4.22).

4.5   RESULTS AND DISCUSSION

Based on the preceding formulation, a computer program has been developed which can be used to analyse waveguide-backed apertures of arbitrary shape radiating into half space. The computer code has been validated by considering a rectangular aperture for which results are available in the literature [21], [68].

Apertures of various shapes, such as rectangular, circular, elliptical, diamond, cross and H have been investigated. Results for each aperture has been tested for convergence by increasing the density of triangulation (i.e., number of expansion functions) and the value of each modal index for the waveguide field. It has been established that a value between 5 and 15 for each modal index is sufficient for all the problems treated in this section.

Table 4.1 lists the change in equivalent surface magnetic current M^x about the centre of open-ended square waveguides as a function of the number of expansion functions. It is found that about 40 expansion functions are required to obtain converged results.

Table - 4.1

Convergence test on open-ended square waveguides radiating into half space.

a/λ	No. of expansion functions	Magnitude of $M^x(x)$	Phase of $M^x(x)$	% change of $\|M^x(x)\|$
0.6	8	0.11	-104	
	21	1.139	7.1	935.5
	40	1.171	4.2	2.81
	96	1.183	3.0	1.02
0.8	8	0.26	102	
	21	0.931	6.6	258.1
	40	1.346	6.0	2.74
	96	1.352	4.5	0.45

4.5-1 Rectangular Aperture

In order to validate our program, we first considered rectangular apertures for which results are available in the literature. The first problem considered was that of a narrow ($\lambda \times \lambda/10$) waveguide-fed rectangular slot radiating into half space. The quantities computed were the x-directed surface magnetic currents over the aperture and the power gain pattern shown in Fig. 4.3 and Fig. 4.4, respectively. The results obtained by Harrington and Mautz [68] using rooftop functions are also shown for comparison. It can be observed that there is an excellent agreement between the two results.

Next, we considered the problems of open-ended rectangular and square waveguides radiating into half space. Fig. 4.5 to 4.8 show some representative computations for these problems. The problem of open-ended rectangular waveguide has earlier been solved by Cohen et al. [21] using classical methods, Harrington and Mautz [68] using rooftop functions and by Mongiardo and Rozzi [72] using singular integral formulation. It can be observed that our results are in good agreement with those of previous workers. Figs. 4.9 and 4.10 show the corresponding results for a square waveguide which are again found to be in good agreement with those in [68].
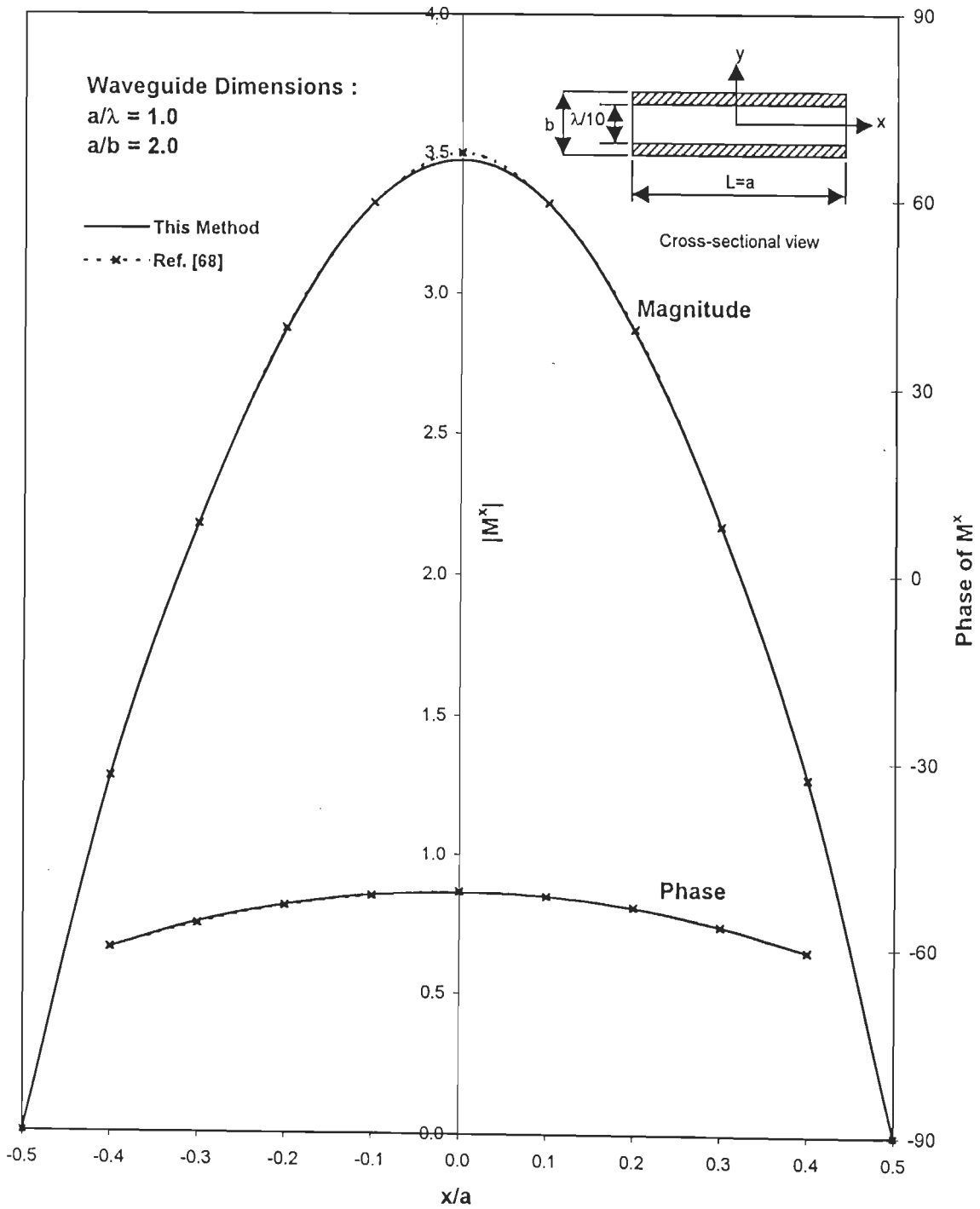
Fig. 4.3 : Equivalent surface magnetic current M^x at $y/b = 0.1$ for a waveguide-fed λ x $\lambda/10$ rectangular slot radiating into half space.
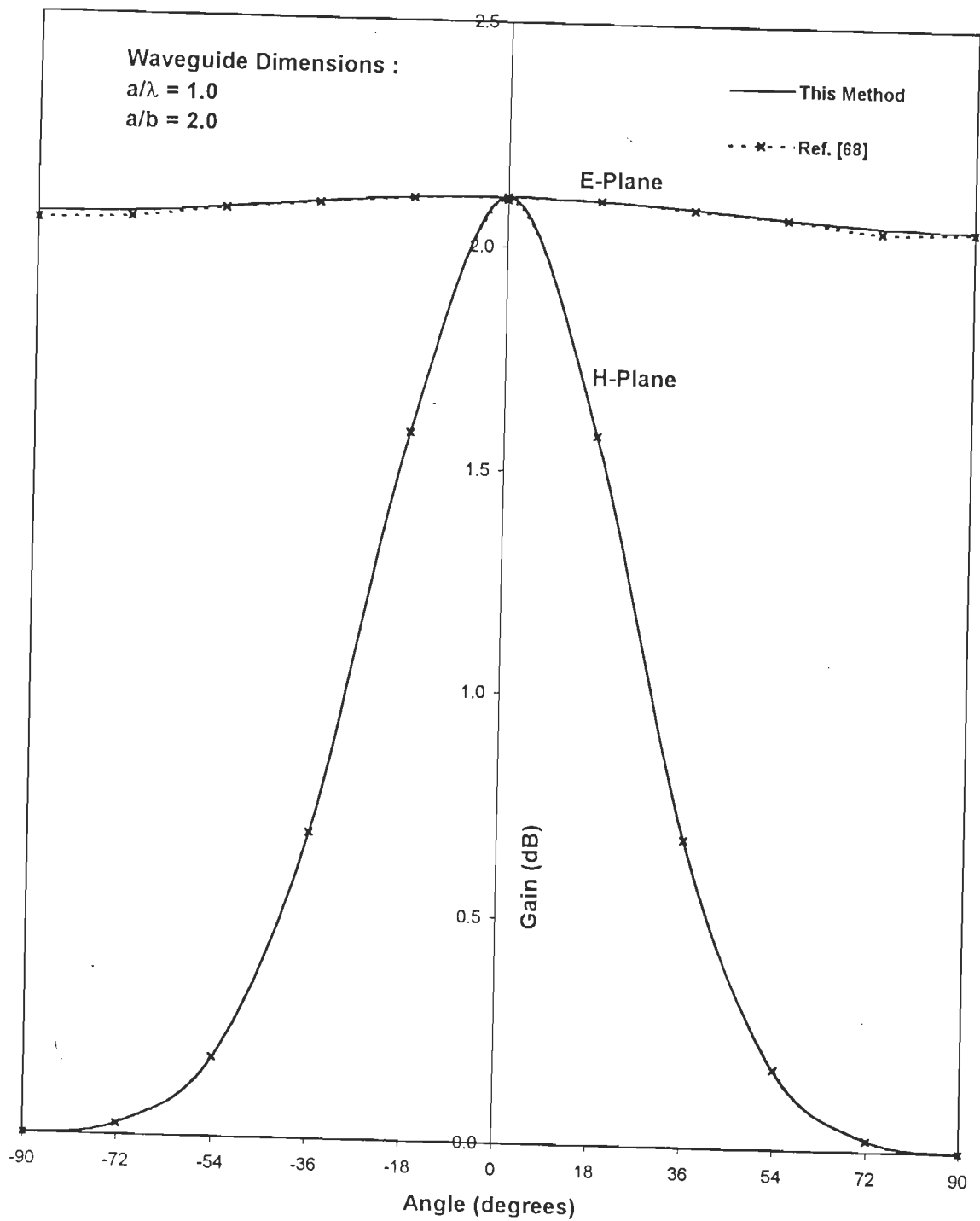
Fig. 4.4 :   Power gain patterns for a waveguide-fed λ x λ/10
rectangular slot radiating into half space.
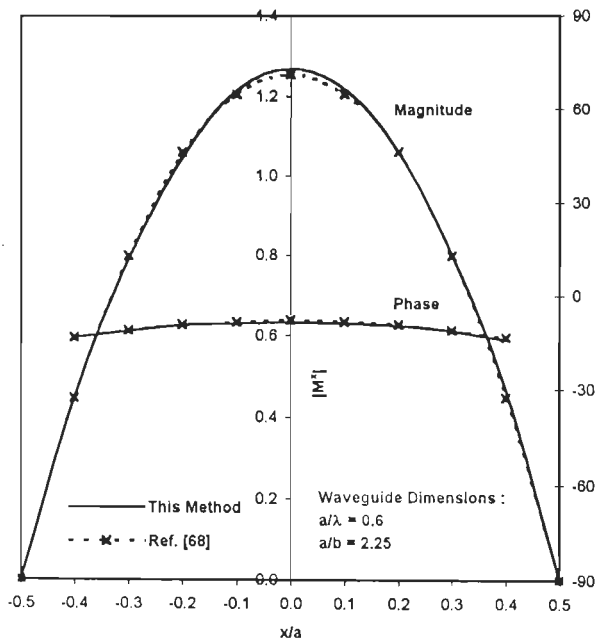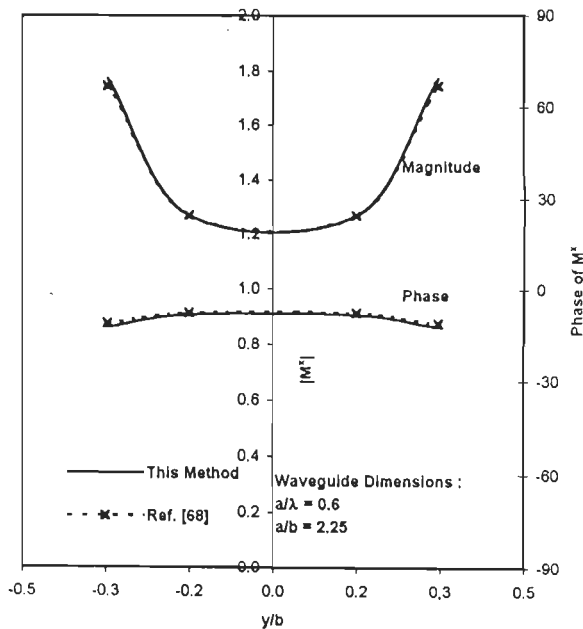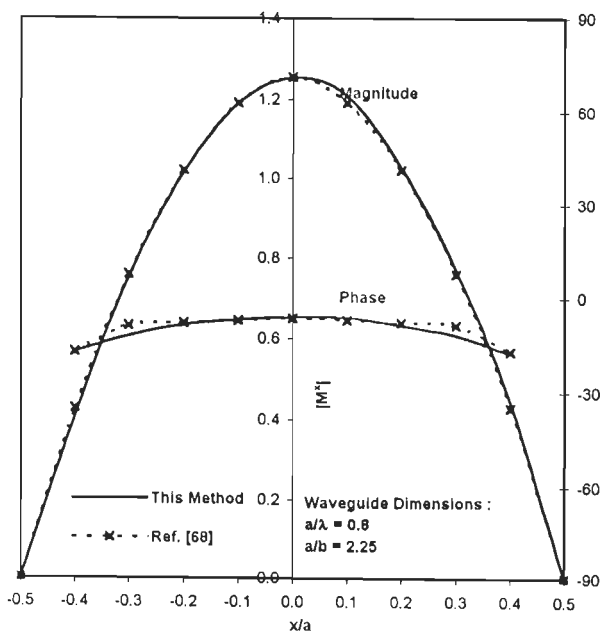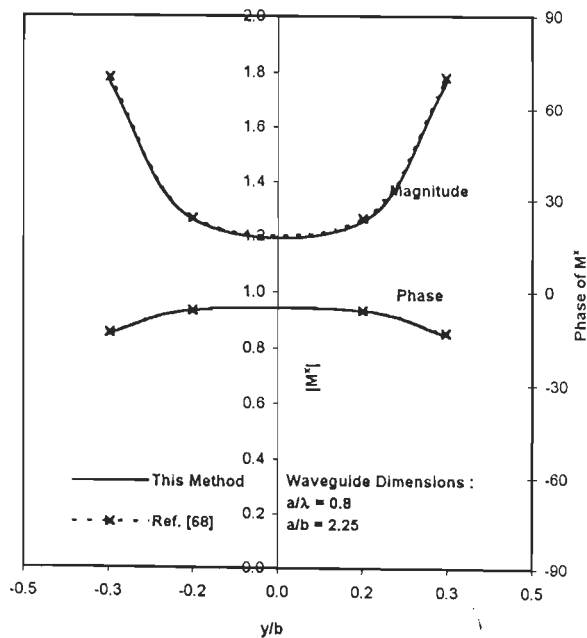
Fig. 4.5 : Equivalent surface magnetic current for open ended rectangular waveguide radiating into half space.

117

(a) a/λ = 0.6
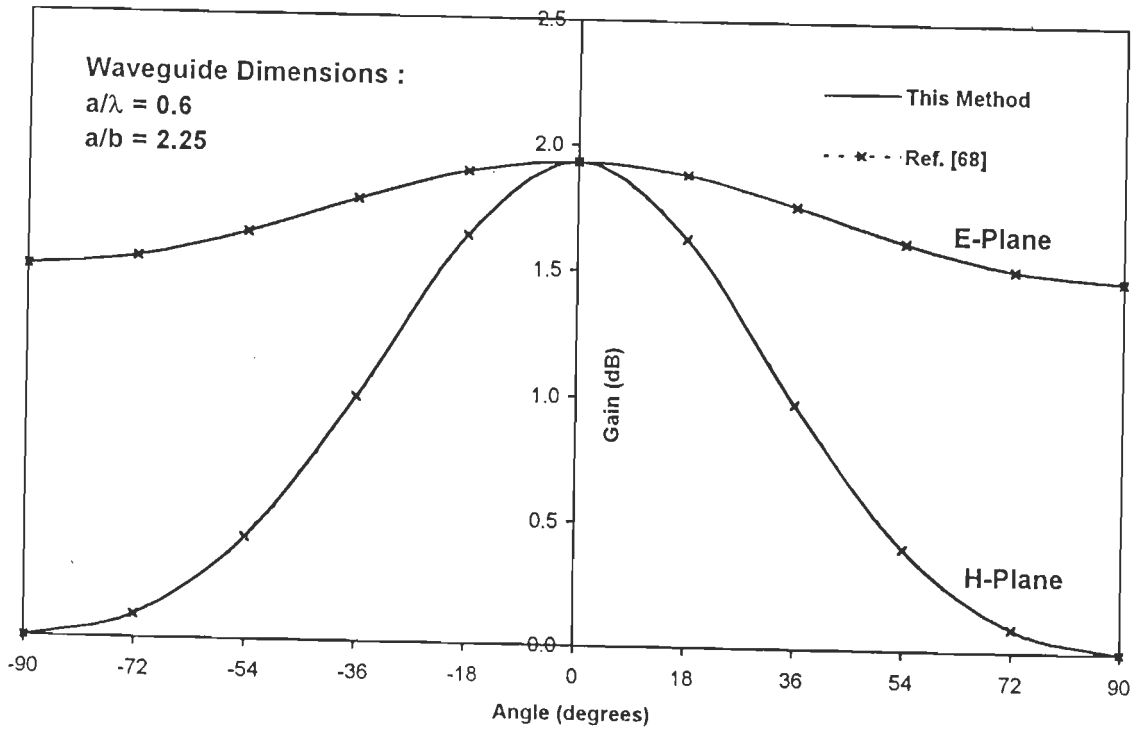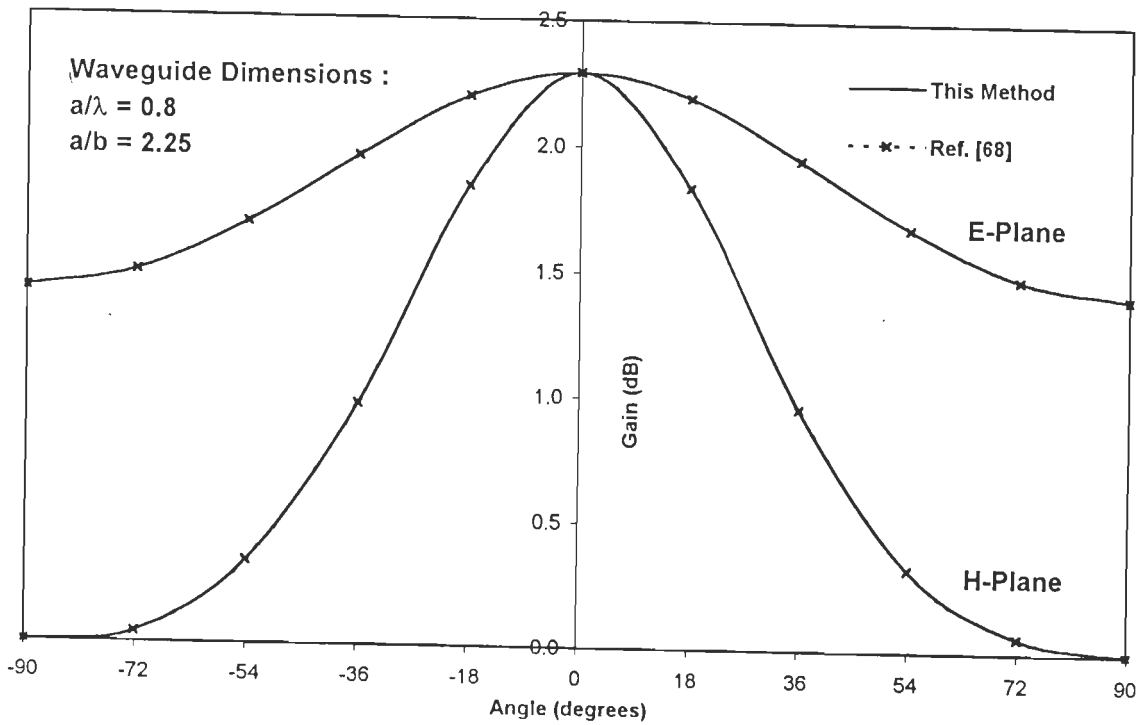
(b) a/λ = 0.8

Fig. 4.6 : Power gain patterns for an open ended rectangular waveguide radiating into half space.

118
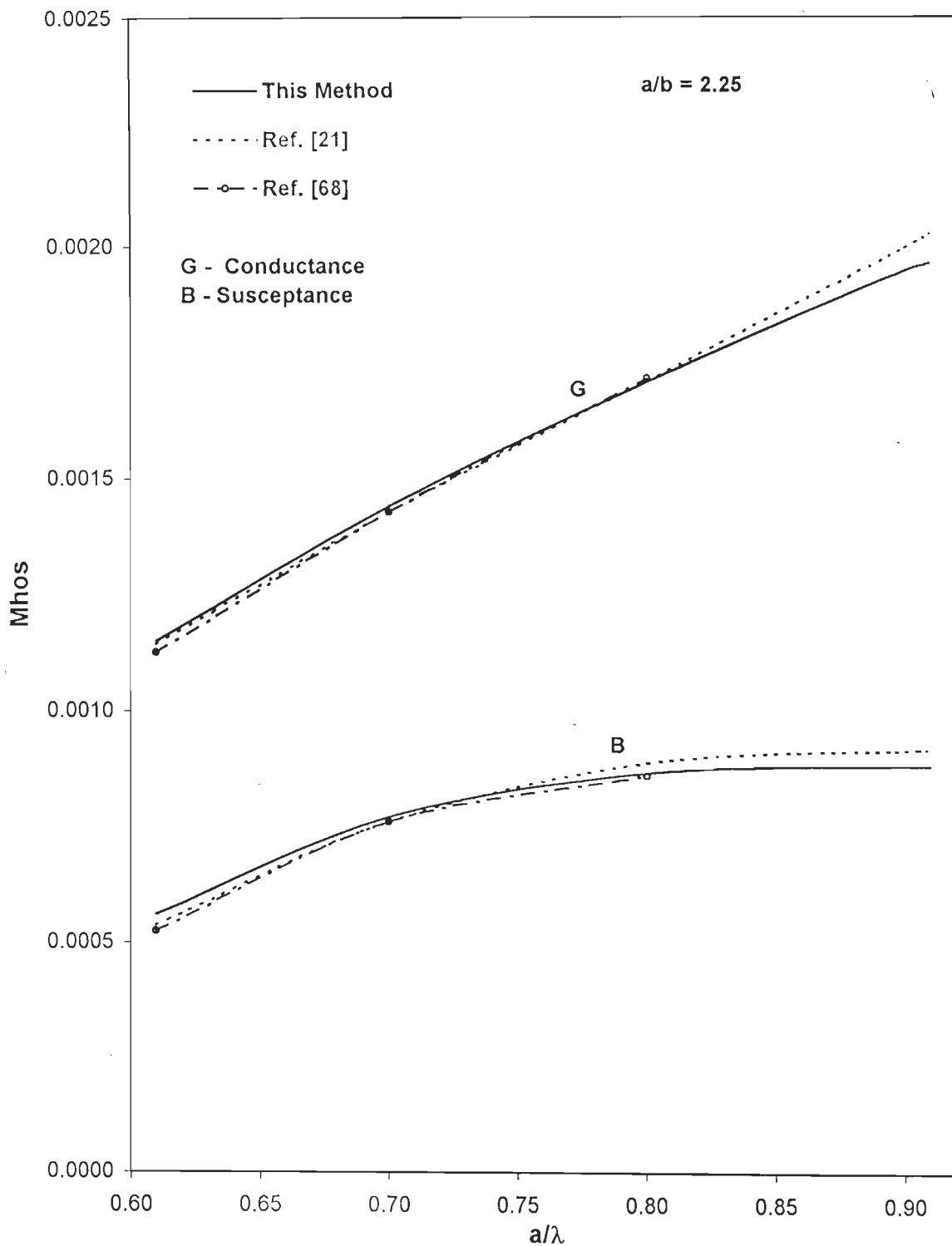
Fig. 4.7 : Equivalent aperture admittance seen by the dominant TE$_{10}$ mode for an open ended rectangular waveguide.
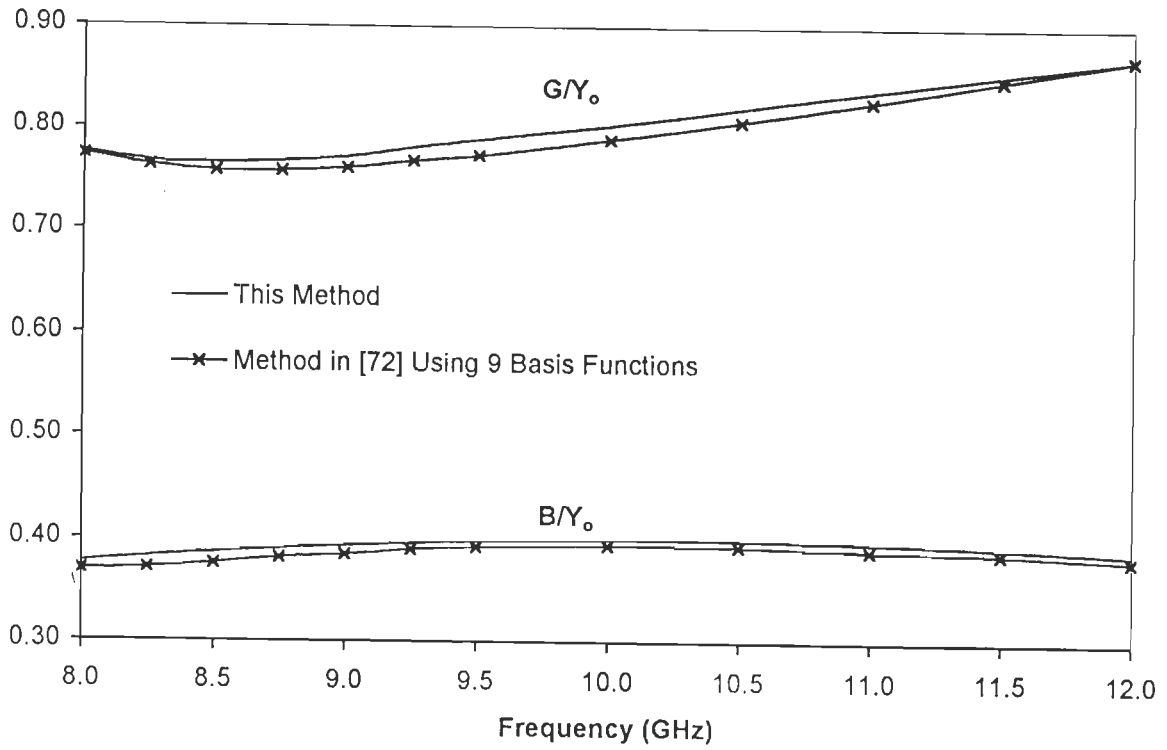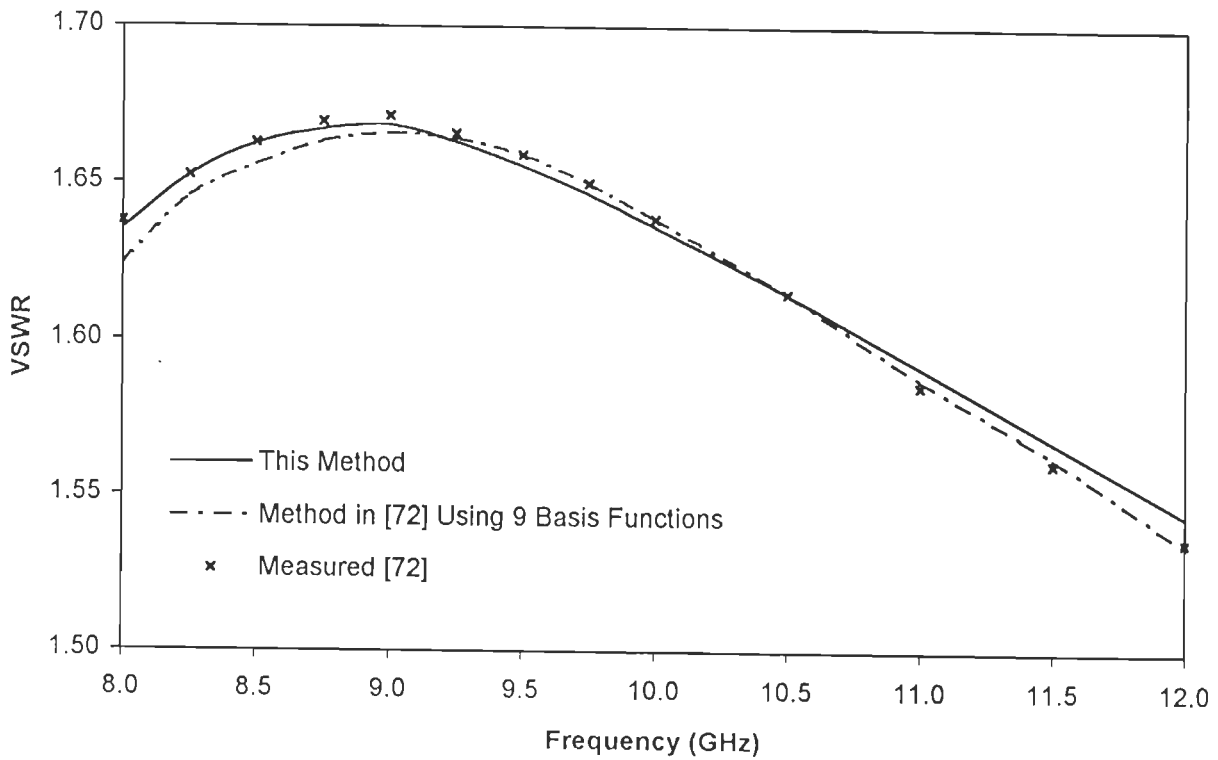
Fig. 4.8 : (a) Normalized input admittance and (b) VSWR as a function of frequency of a standard WR90 waveguide
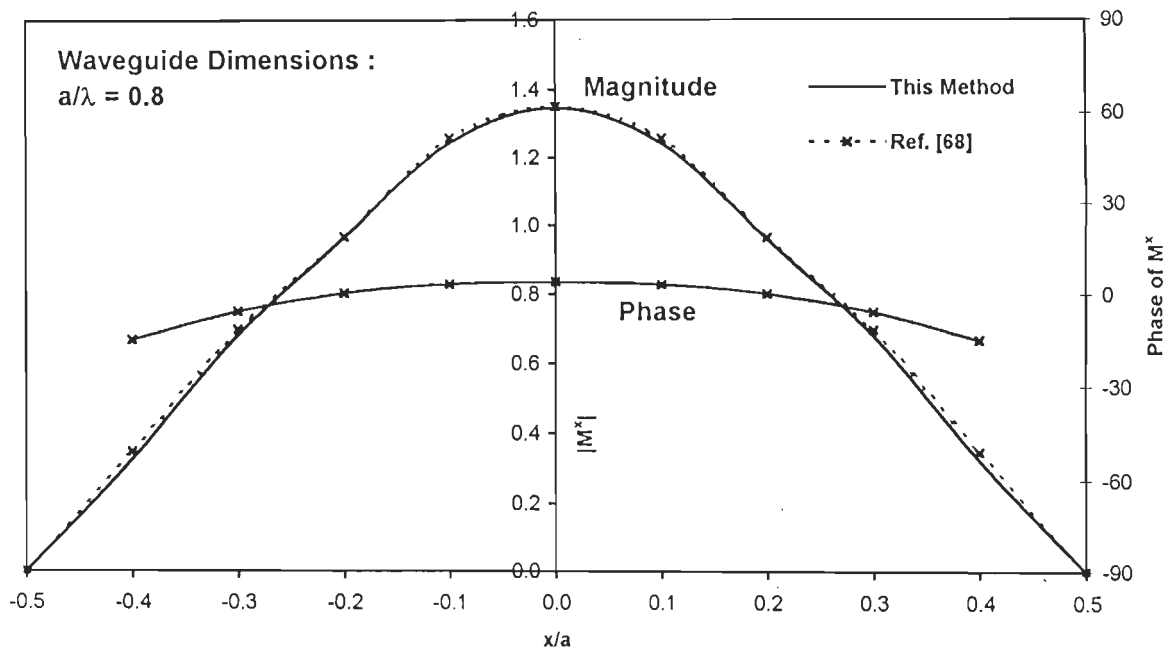
(a) $a/\lambda = 0.8$, $y/b = -0.125$
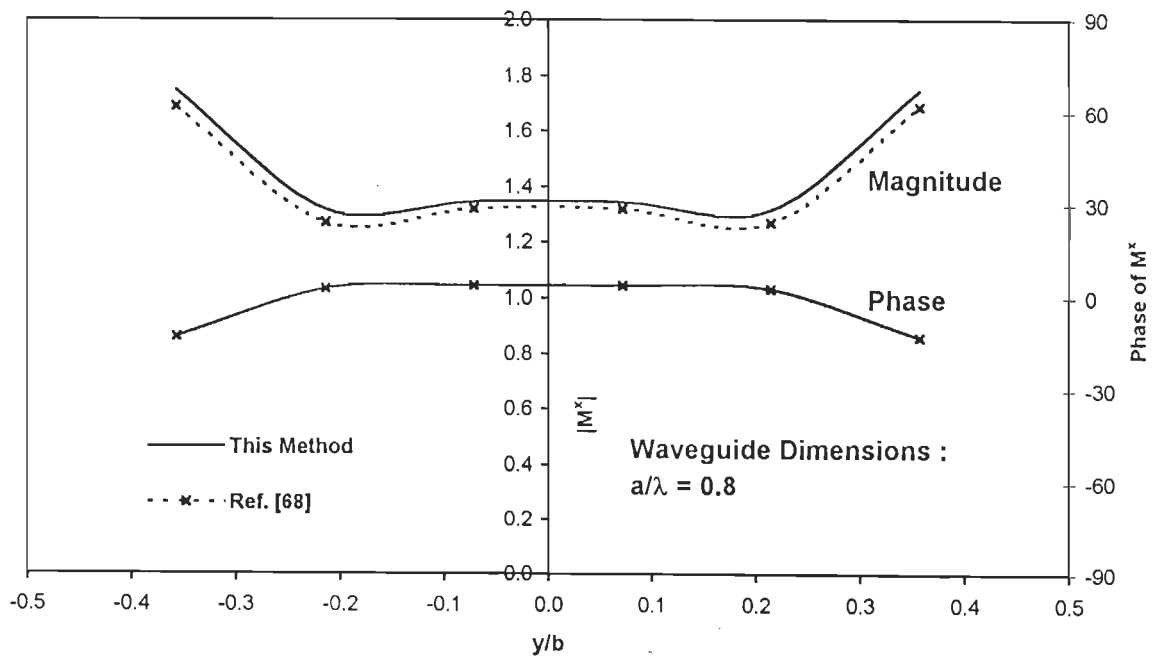
(b) $a/\lambda = 0.8$, $x/a = 0.0$

Fig. 4.9 : Equivalent surface magnetic current distributions for open ended square waveguide of width 'a' radiating into half space.

121
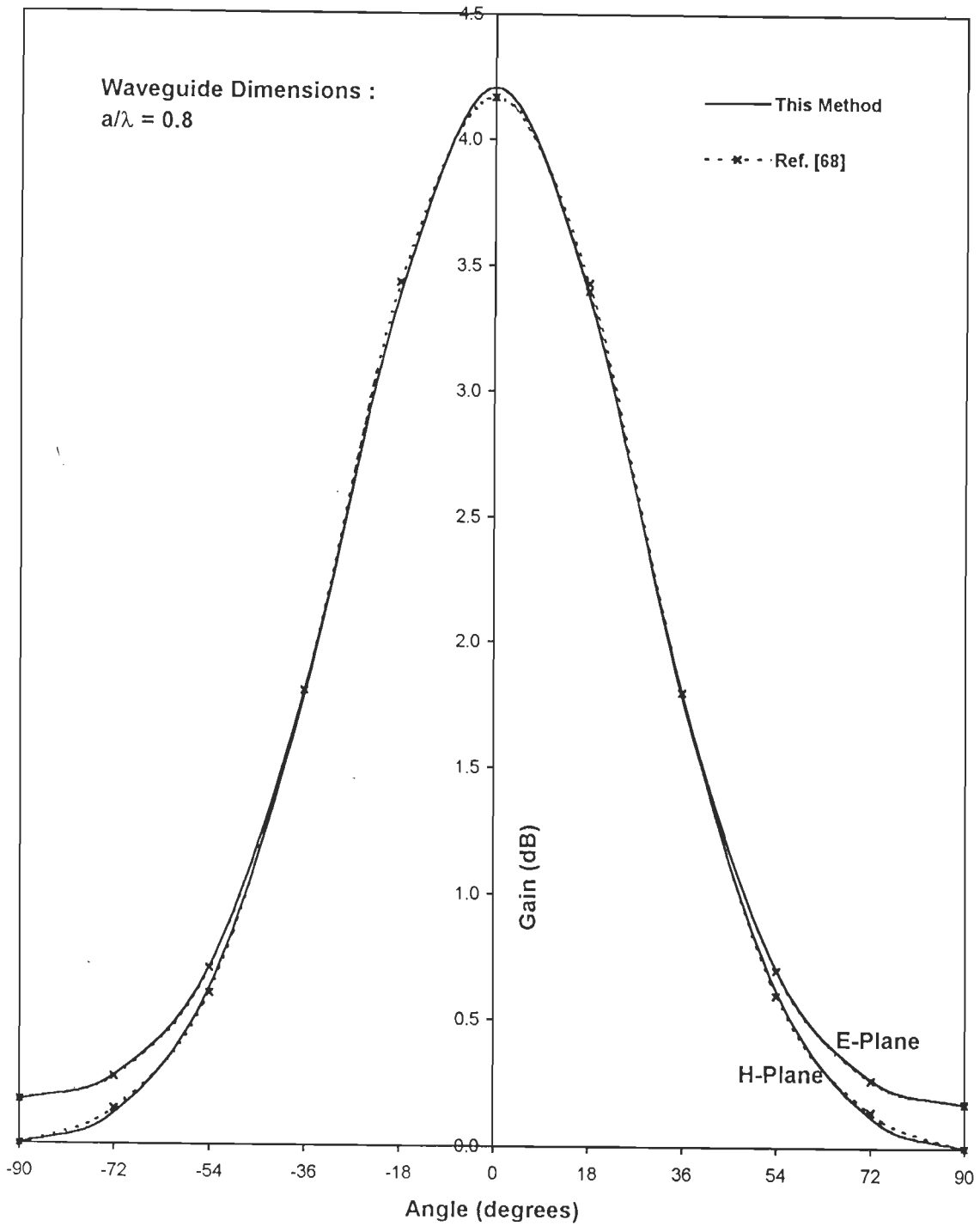
Fig. 4.10 : Power gain patterns for an open ended square
waveguide of width 'a' radiating into half space.

4.5-2 Circular Aperture

Convergence studies on circular aperture established that 76 expansion functions are sufficient to yield converged results. The triangulation scheme used is shown in Fig. 3.13.

Fig. 4.11 shows equivalent surface magnetic current distributions. The $|M^x|$ curve at $y/d = -0.125$ in (a) for $d/a = 0.4$ exhibits "shoulders", which are symmetrically located at $x/d = \pm 0.4$ on either side of the centre, while the curve for $d/a = 0.2$ is relatively flat and its peak value is much lower. The nature of the curve is similar to those of rectangular slots shown in Fig. 4.3. The phase distribution is uniform for both the apertures. In Fig. 4.11(b), the distribution of M^x as a function of y is shown at the aperture centre. Here, it is noted that the magnitude curve for $d/a = 0.4$ exhibits a maxima at the centre but falls rapidly as one moves away until at $y/d = \pm 0.25$ when it rises again. Similar pattern is imitated by the curve for $d/a = 0.2$ which rises at $y/d = \pm 0.3$ and its peak value is much lower and therefore, the current appears to be uniformly distributed. Both curves exhibit the "edge effect". These curves show only a slight similarity to those of open-ended square waveguides of Fig. 4.9.

Fig. 4.12 shows the antenna power gain patterns for waveguide-backed circular aperture. It is observed that the power gain depends on the size of the aperture; the larger the diameter, the higher the power gain.

Fig. 4.13 shows equivalent admittance seen by the dominant TE_{10} mode. In these apertures, conductances G are relatively high compared to those of open-ended rectangular- and square- waveguides and their susceptances B are inductive instead of capacitive. The susceptance is relatively high for $d/a < 0.3$ but reduces to a much lower value for $d/a > 0.3$. G, on the other hand, is constant for the two cases considered.
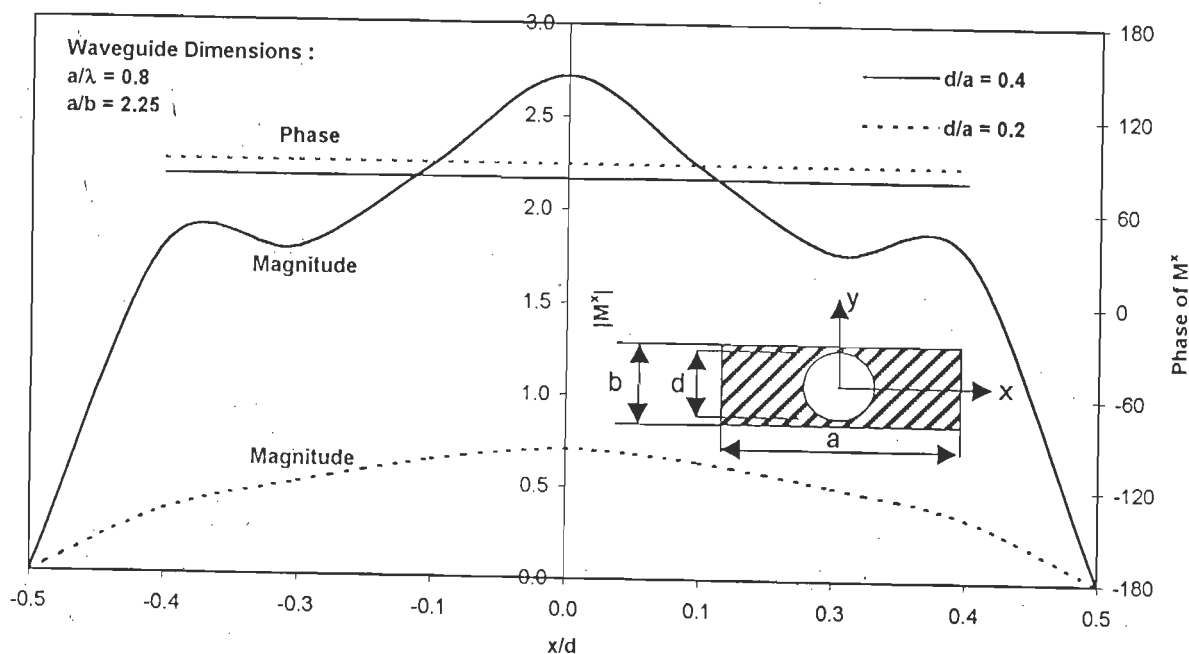
(a) $a/\lambda = 0.8$, $y/d = -0.125$
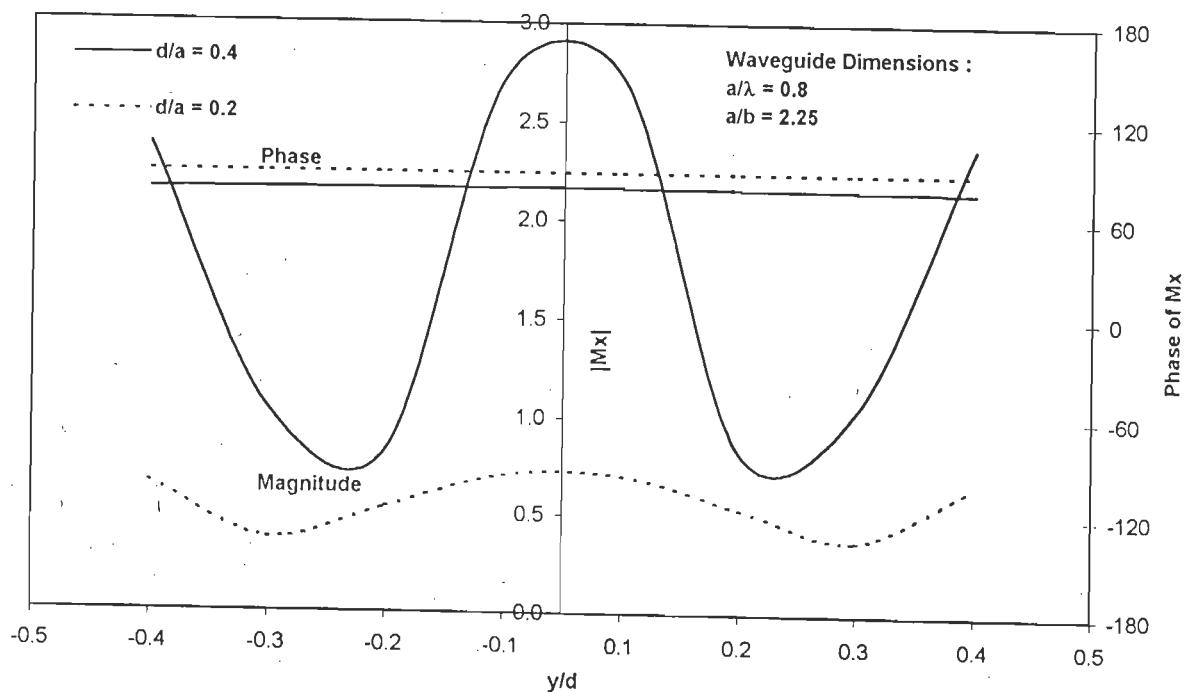
(b) $a/\lambda = 0.8$, $x/d = 0.0$

Fig. 4.11 : Equivalent surface magnetic current distributions for waveguide backed circular aperture of different diameters radiating into half space.
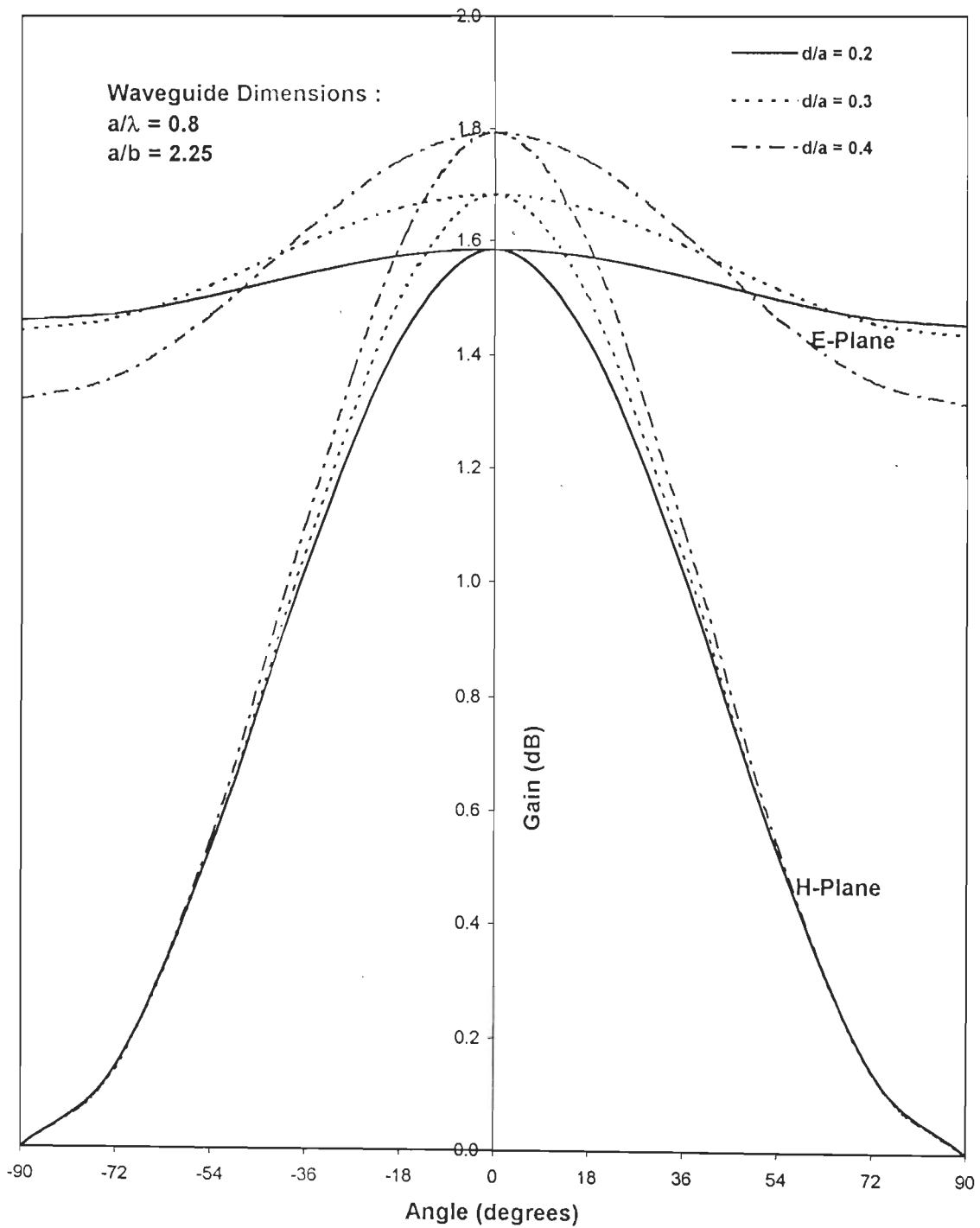
Fig. 4.12 : Power gain patterns for waveguide backed circular
aperture radiating into half space.

125
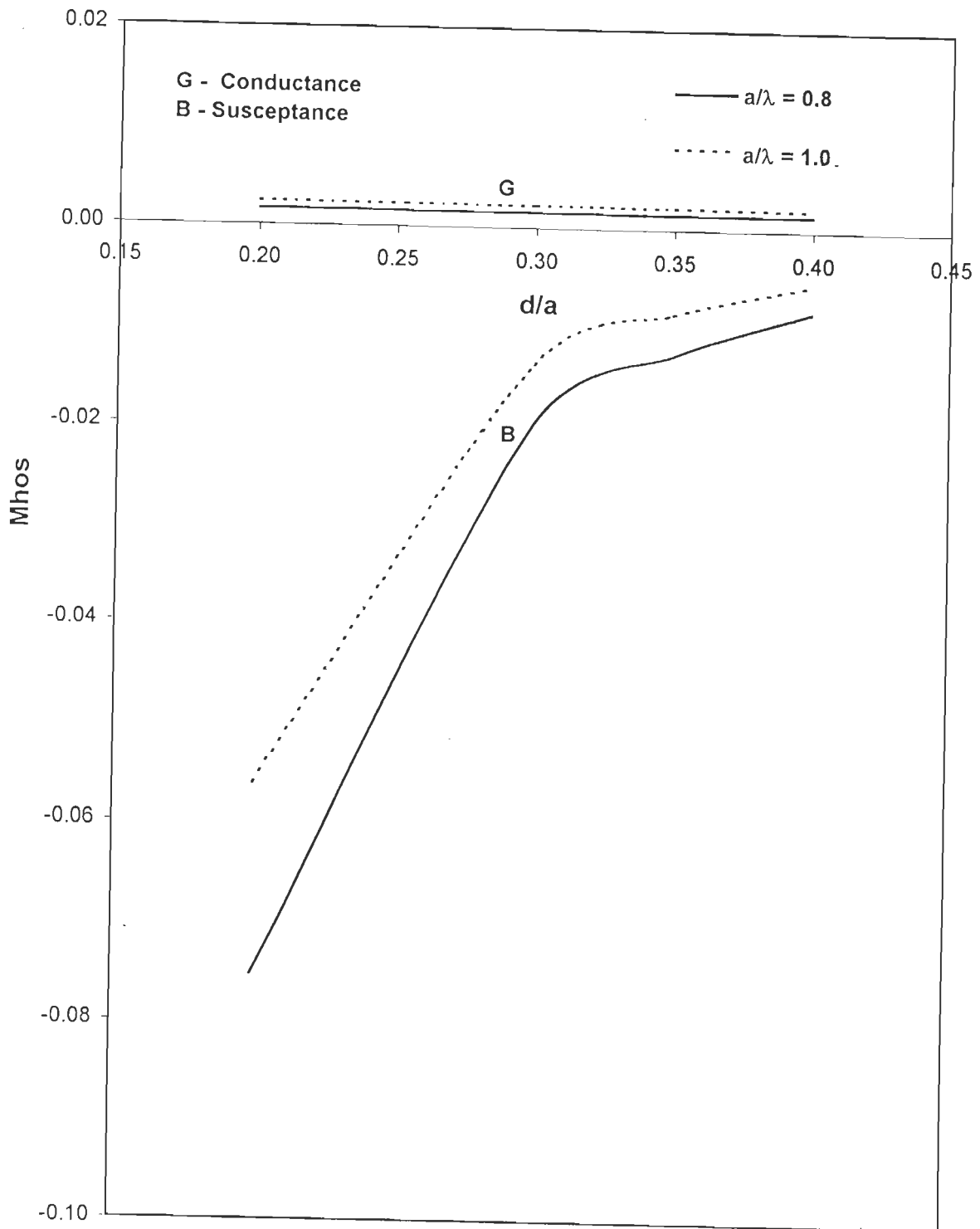
Fig. 4.13 : Equivalent aperture admittance seen by the dominant TE_{10} Mode as a function of normalized circular aperture diameter d .

4.5-3 Elliptic Aperture

Convergence test on elliptic aperture has revealed that 76 expansion functions are sufficient to produce converged results. The triangulation scheme used to discretize the aperture surface is shown in Fig. 3.18.

Fig. 4.14(a) shows equivalent surface magnetic current distributions M^x at $y/d_2 = -0.125$ for two different major-to-minor axes ratio d_1/d_2. While $|M^x|$ has a tapered distribution for $d_1/d_2 = 2$, the distribution for $d_1/d_2 = 4.5$ is nearly uniform over a large part of the aperture. On the other hand, the phase distribution for $d_1/d_2 = 2$ is nearly uniform while that for $d_1/d_2 = 4.5$ is sharply tapered near the aperture edges. Fig. 4.14(b) shows the distribution of M^x at $x = 0.0$. It is observed that the magnitude curve corresponding to $d_1/d_2 = 4.5$ has a nature similar to that for open-ended rectangular waveguides of Fig. 4.5(b) and (d). The nature of the magnitude curve corresponding to $d_1/d_2 = 2.0$, on the other hand, is entirely different. The phase distributions are very similar to those for open-ended square waveguide of Fig. 4.7(b).

Fig. 4.15 shows antenna power gain patterns in both E- and H-planes. It is observed that antenna gain increases with aperture size. Further, the larger the major axis d_1, the narrower the pattern beam-width.

Fig. 4.16(a) shows the equivalent admittance seen by the dominant TE_{10} mode as a function of d_1/a. It is noted that the aperture has an inductive susceptance B which is large for $d/a < 0.3$ but reduces to a very small value for $d/a > 0.3$. Fig. 4.16(b) shows aperture equivalent admittance as a function of eccentricity e (according to eqn. (3.29)). It is observed that as the aperture size becomes smaller, for a fixed value of d_1/a, inductive susceptance becomes larger. However, in this case, the increase of B is gradual for $0.2 \le e \le 0.8$ and thereafter it increases rapidly. In both the cases, the conductance G is quite small.
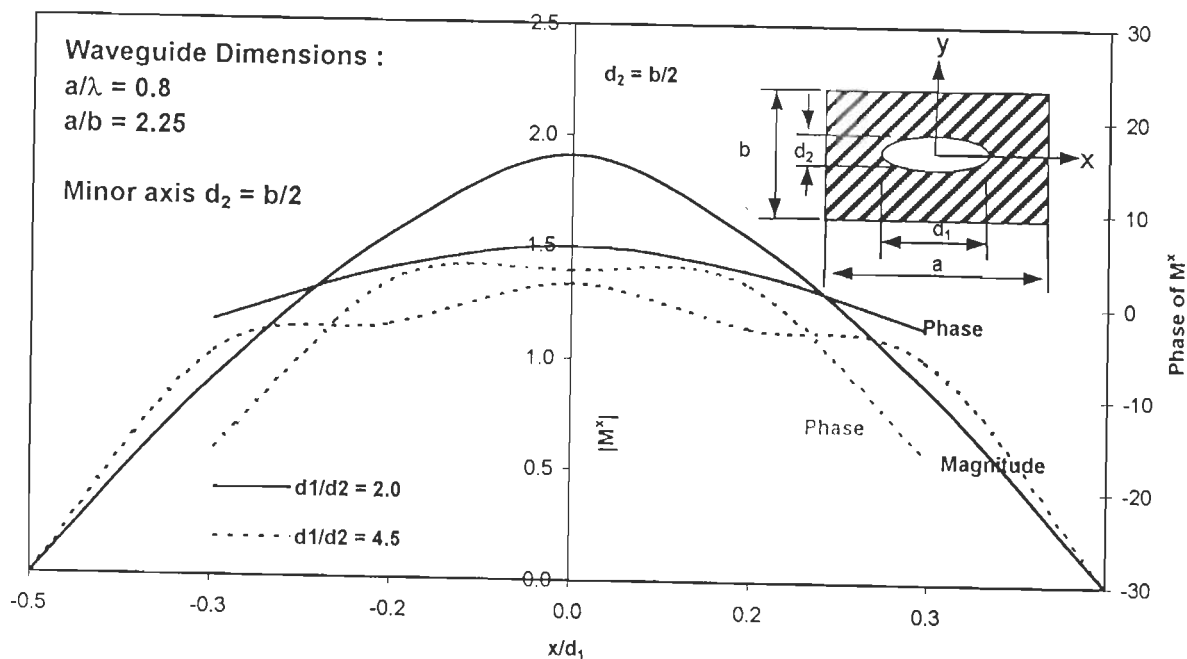
(a) y/d2 = -0.125
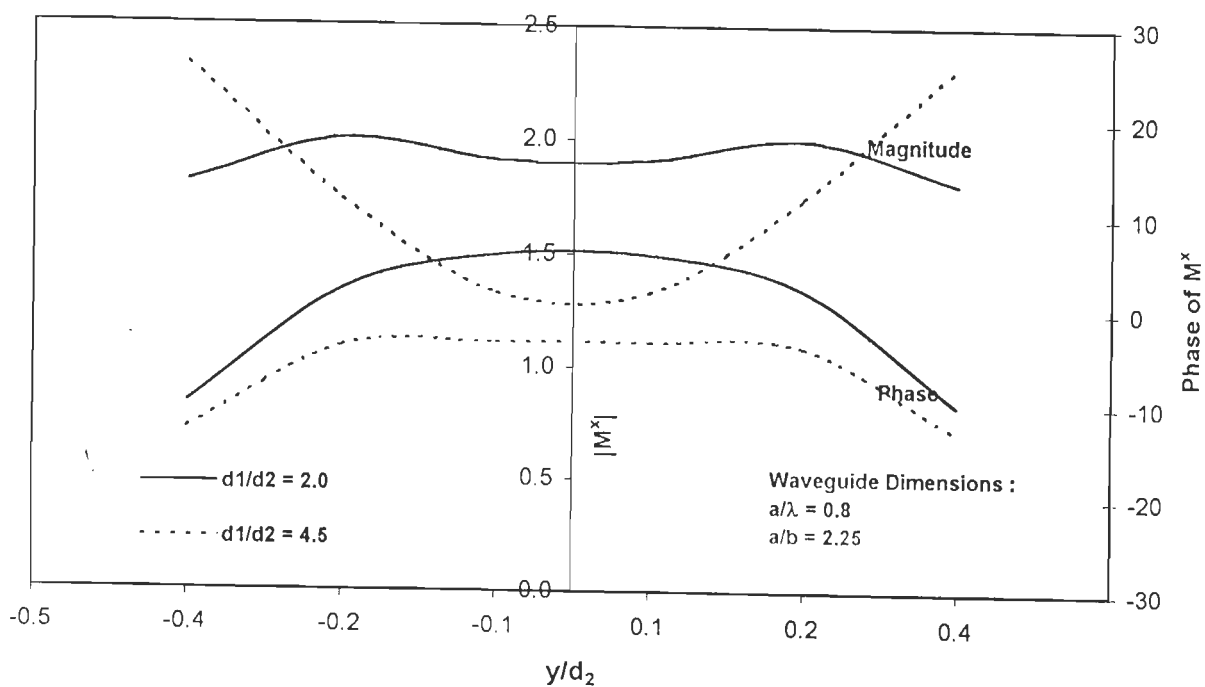
(b) x/d₁ = 0.0

Fig. 4.14 : Equivalent surface magnetic current distributions for waveguide backed elliptical apertures radiating into half space.

128
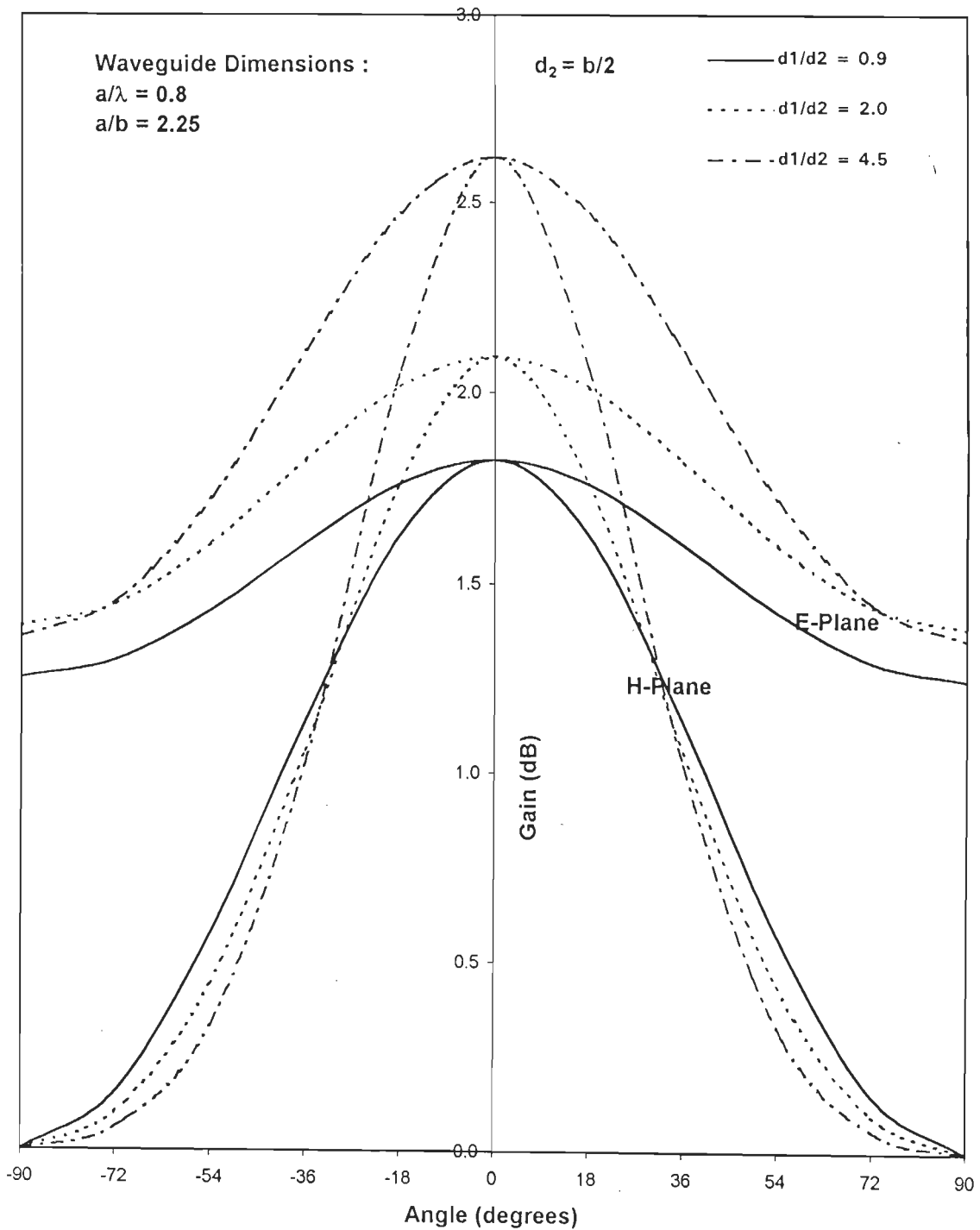
Fig. 4.15 : Power gain patterns for waveguide backed elliptical aperture radiating into half space.
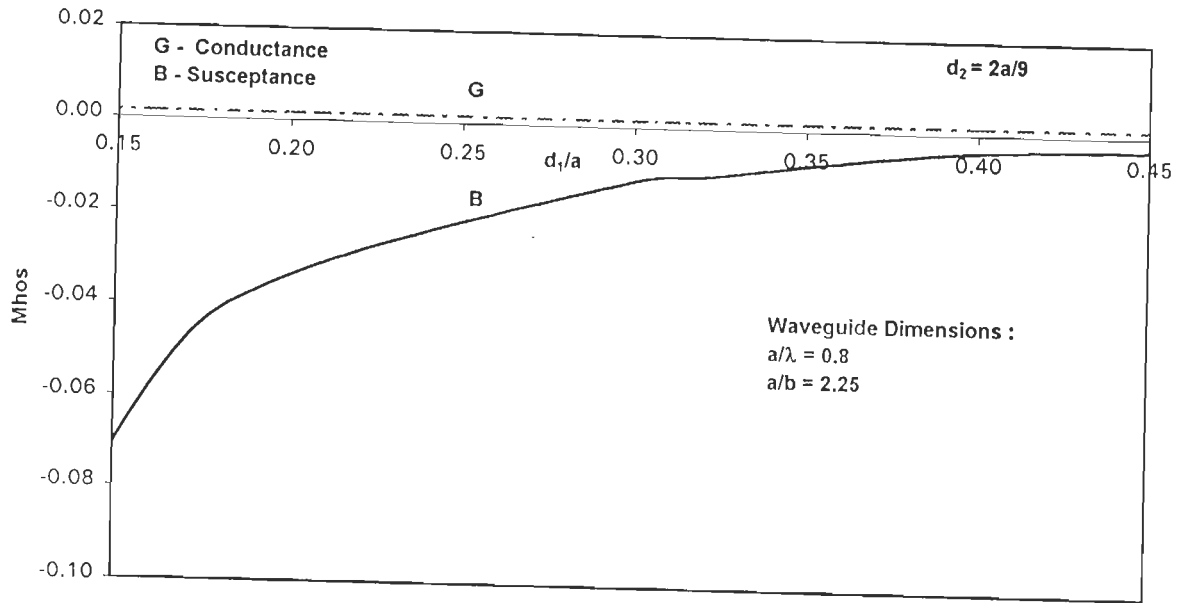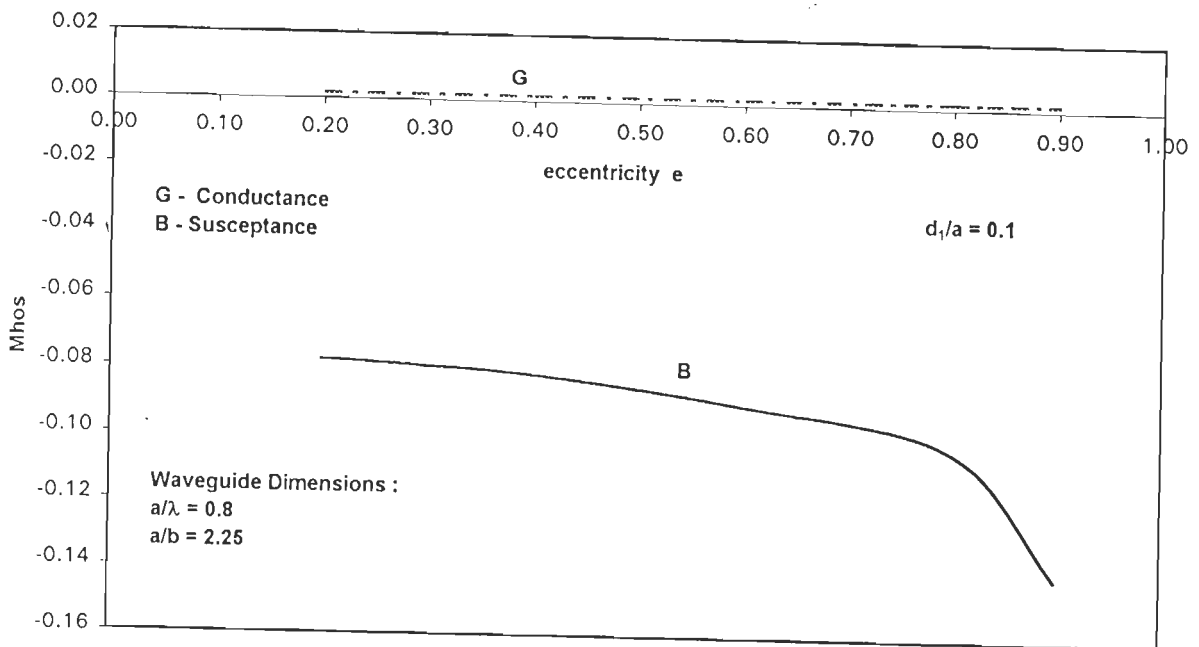
Fig. 4.16 : Equivalent aperture admittance for elliptic apertures fed by rectangular waveguide as a function of (a) d_1/a and (b) eccentricity

130

Further, we studied the radiation characteristics of an elliptical aperture backed by WR-90 waveguide as a function of frequency. Figs. 4.17(a) and (b) show input admittance and VSWR, respectively, as a function of frequency for three different values of major axes with minor axis $d_2 = 0.5b$. Figure 4.17(a) shows that G/Y_o is fairly small and almost constant over the entire $8.0 - 12.0$ GHz band in all the three cases considered. However, while B/Y_o corresponding to $d_1/b = 1.5$ and 1.75 are inductive over the entire frequency range, B/Y_o corresponding to $d_1/b = 2.0$ exhibits capacitive susceptance over almost the whole frequency range except for $8.0 - 8.25$ GHz where it is inductive. Thus, only the aperture corresponding to $d_1/b = 2.0$ exhibits a resonance. Figure 4.17(b) shows the corresponding VSWR curves, which exhibits the expected behaviour. It is observed that the lowest VSWR is obtained over the entire band for the aperture with $d_1/b = 2.0$.

Figure 4.18(a) and (b) show the results of a similar study for fixed dimensions of major axis with minor axis dimensions as a parameter. Of the three cases considered, resonance occurs only for $d_2/b = 0.5$. At resonance, the VSWR curve nearly exhibits a minimum.
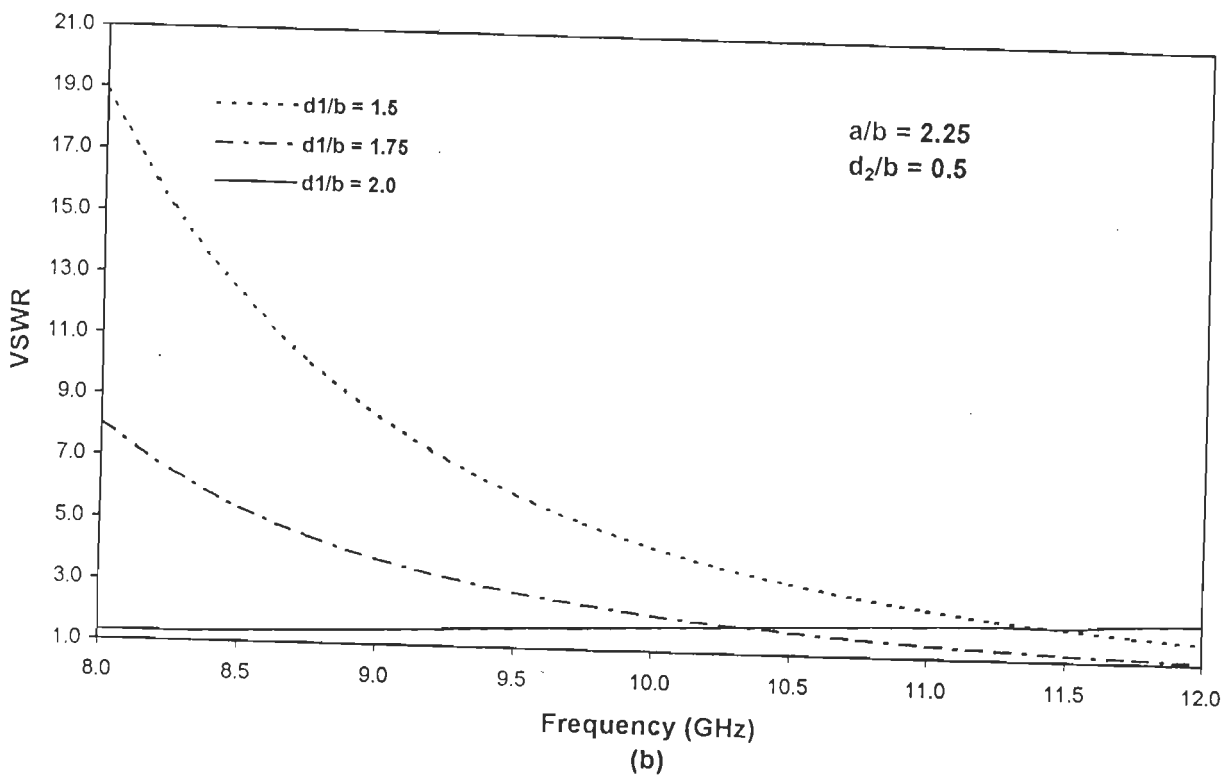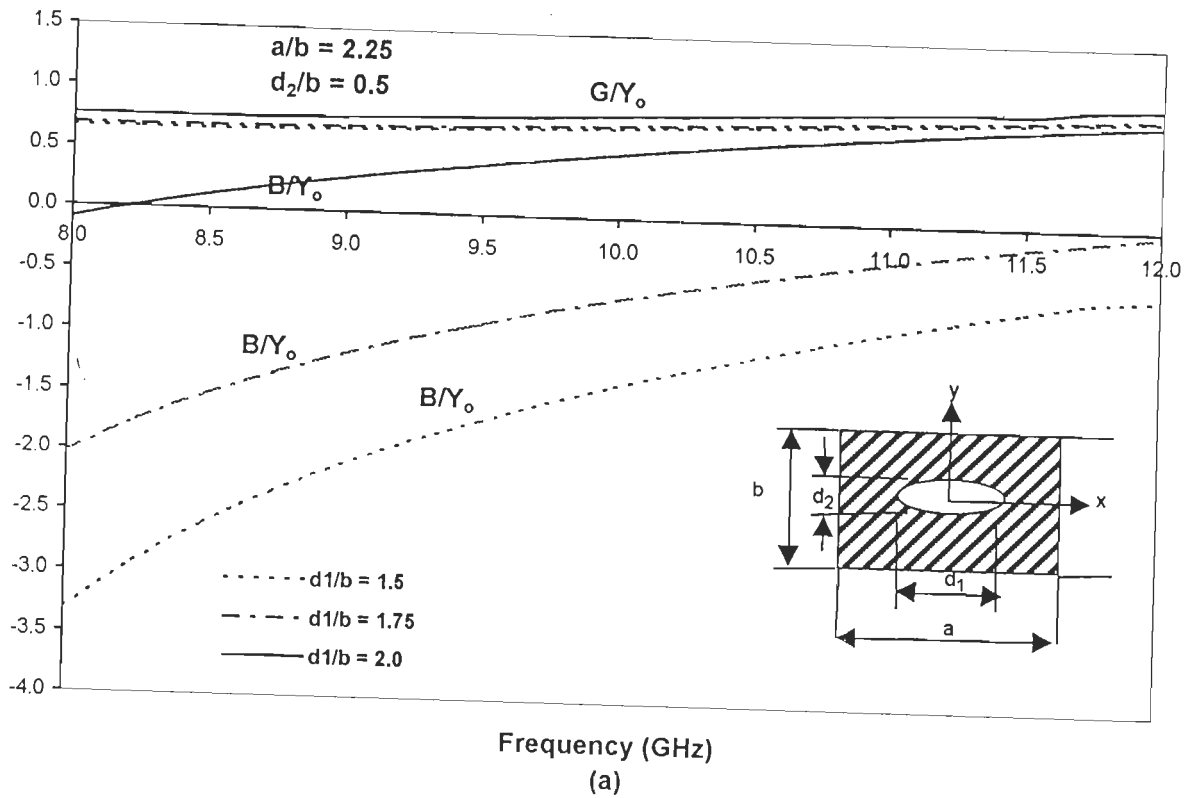
Fig. 4.17 : (a) Normalized input admittance and (b) VSWR as a function of frequency of a waveguide backed elliptical aperture with constant minor axis radiating into half space

132
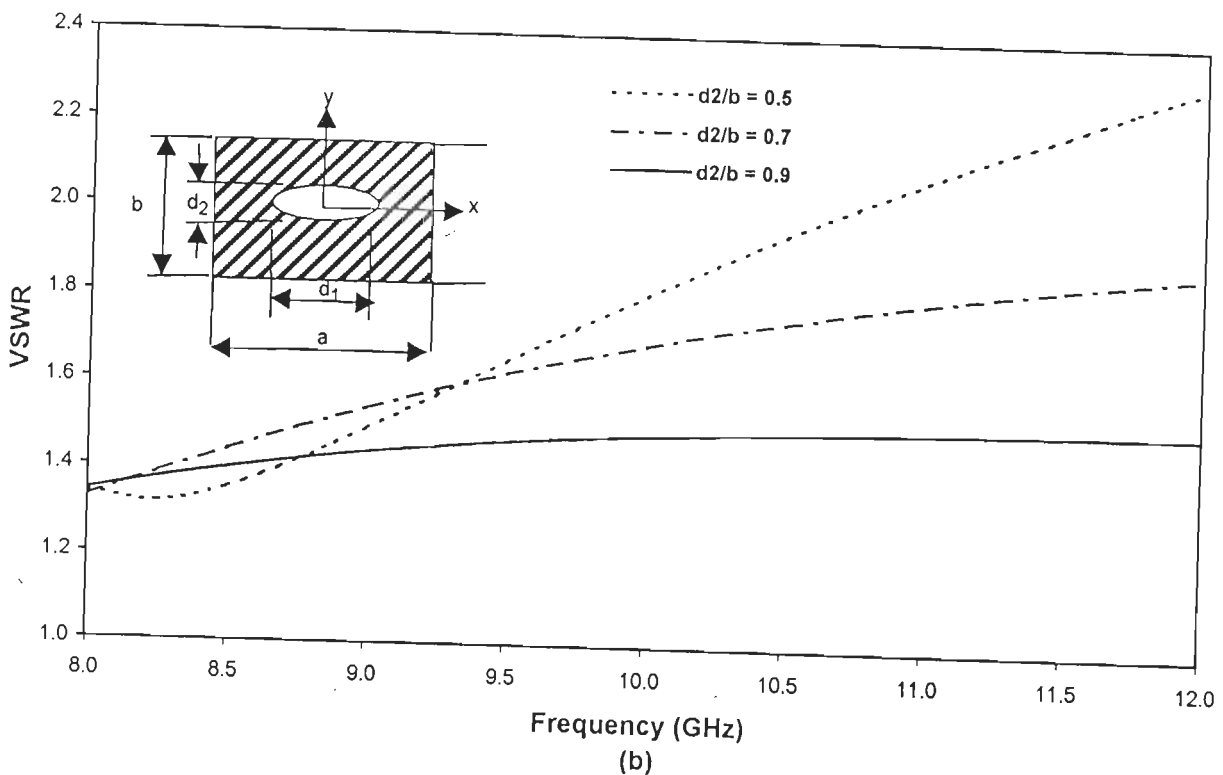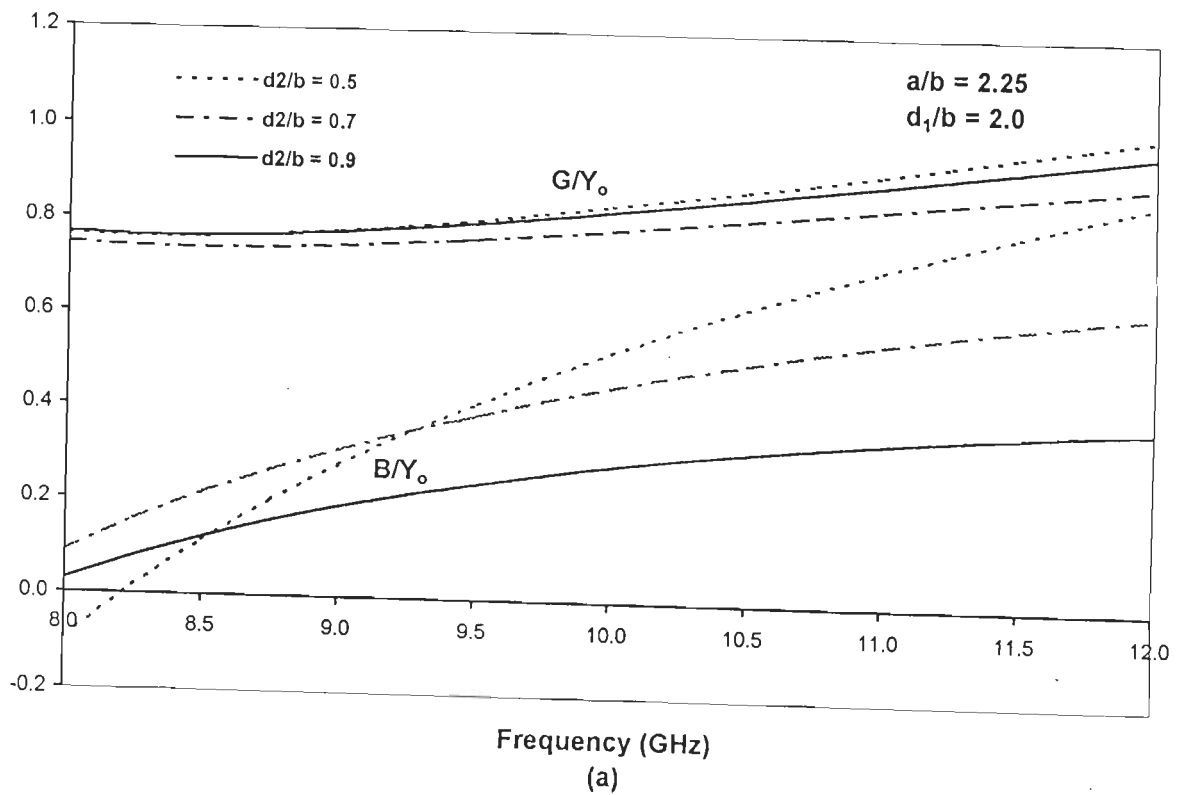
Fig. 4.18 : Transmission properties of a waveguide backed elliptic aperture as a function of frequency for a constant major axis (a) normalized input admittance and (b) VSWR radiating into half space

133

4.5-4 Diamond-shaped Aperture

It was established, through convergence studies, that 88 expansion functions were sufficient to yield correct results for a diamond-shaped aperture, the triangulation scheme for which is shown in Fig. 3.25.

Fig. 4.19(a) and (b) show the equivalent surface magnetic current distributions for various aperture lengths L/λ. In Fig. 4.19(a), it is seen that the interior angles of the diamond formed on the x-axis have a great influence on the nature of distribution and peak values of M^x, which are plotted at $y/b = -0.125$: If the angles are acute, as for $L/\lambda = 0.6$ and 0.8, the current curve taper sharply towards their peaks. However, if the angles formed are obtuse, as for $L/\lambda = 0.2$, the variation of $|M^x|$ is gradual. However, the phase distributions corresponding to obtuse angles are fairly constant but vary greatly if the angles are acute. The curve corresponding to $L/\lambda = 0.2$ is similar to that of elliptical aperture shown in Fig. 4.14(a). However, the curves corresponding to $L/\lambda = 0.6$ and 0.8 are entirely different from the previous ones.

Fig. 4.19(b) shows the current distributions at $x/h = 0.0$. The magnitude curves are very nearly of the same nature. However, the phase distributions corresponding to $L/\lambda = 0.2$ varies considerably, while for $L/\lambda = 0.6$ and 0.8, it is relatively uniform along the aperture.

Fig. 4.20 shows antenna power gain patterns for diamond-shaped apertures. It is noted that the patterns in both E- and H-planes become more directive as the aperture length is increased (i.e., as the interior angle formed on

the x-axis becomes more acute). Also, gain increases with the increase in aperture length.

Fig. 4.21 shows equivalent aperture admittance seen by the dominant TE_{10} mode as a function of aperture length L/λ. The dominant mode equivalent susceptance B is inductive for $L/\lambda < 0.52$ but changes to capacitive for $L/\lambda > 0.52$. This behaviour distinguishes diamond-shaped aperture from other apertures studied so far. It is also noted that as L is reduced from 0.5λ, the magnitude of susceptance increases at a very fast rate.

Conductance G of diamond-shaped aperture however, is comparable to those of elliptical apertures in Fig. 4.16(a) and (b).
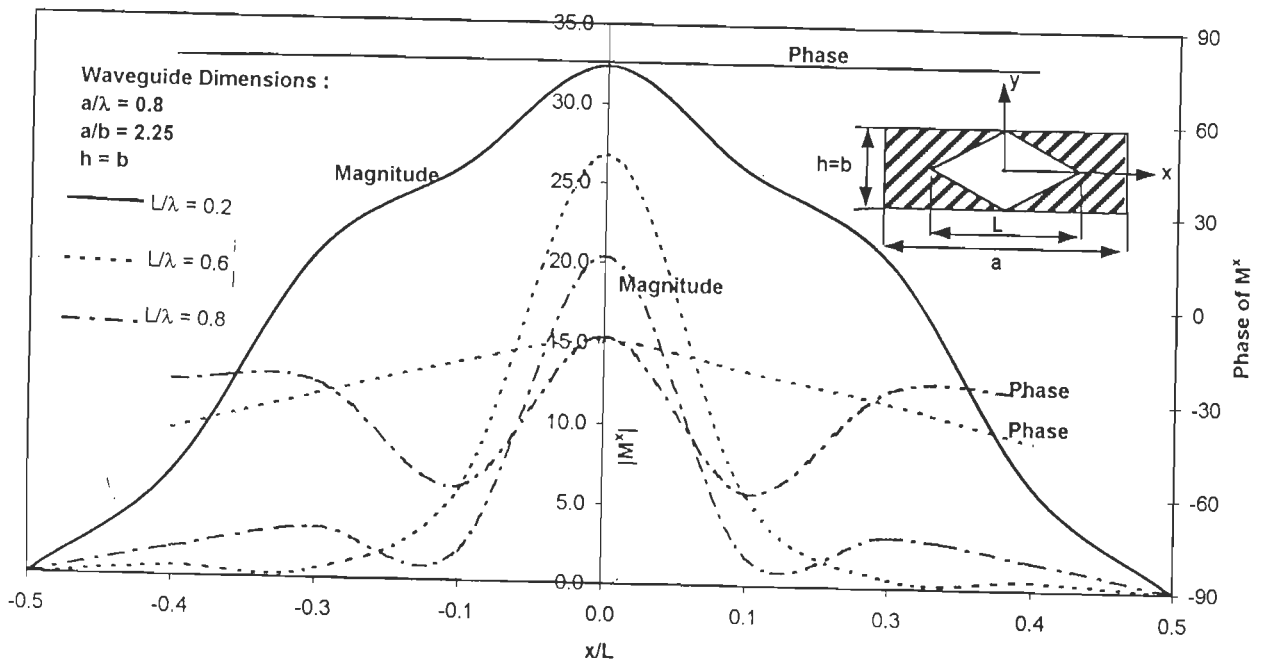
(a) y/h = -0.125
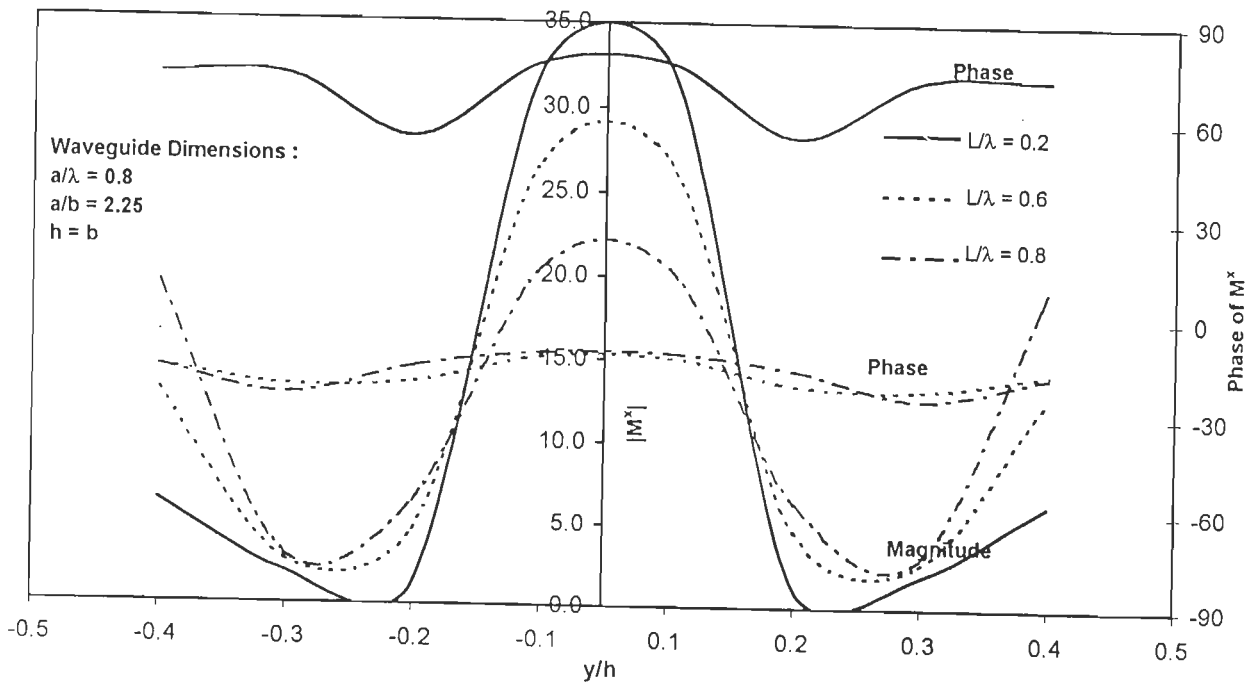
(b) x/d = 0.0

Fig. 4.19 : Equivalent surface magnetic current distributions for waveguide backed diamond-shaped aperture of different lengths L/λ radiating into half space.
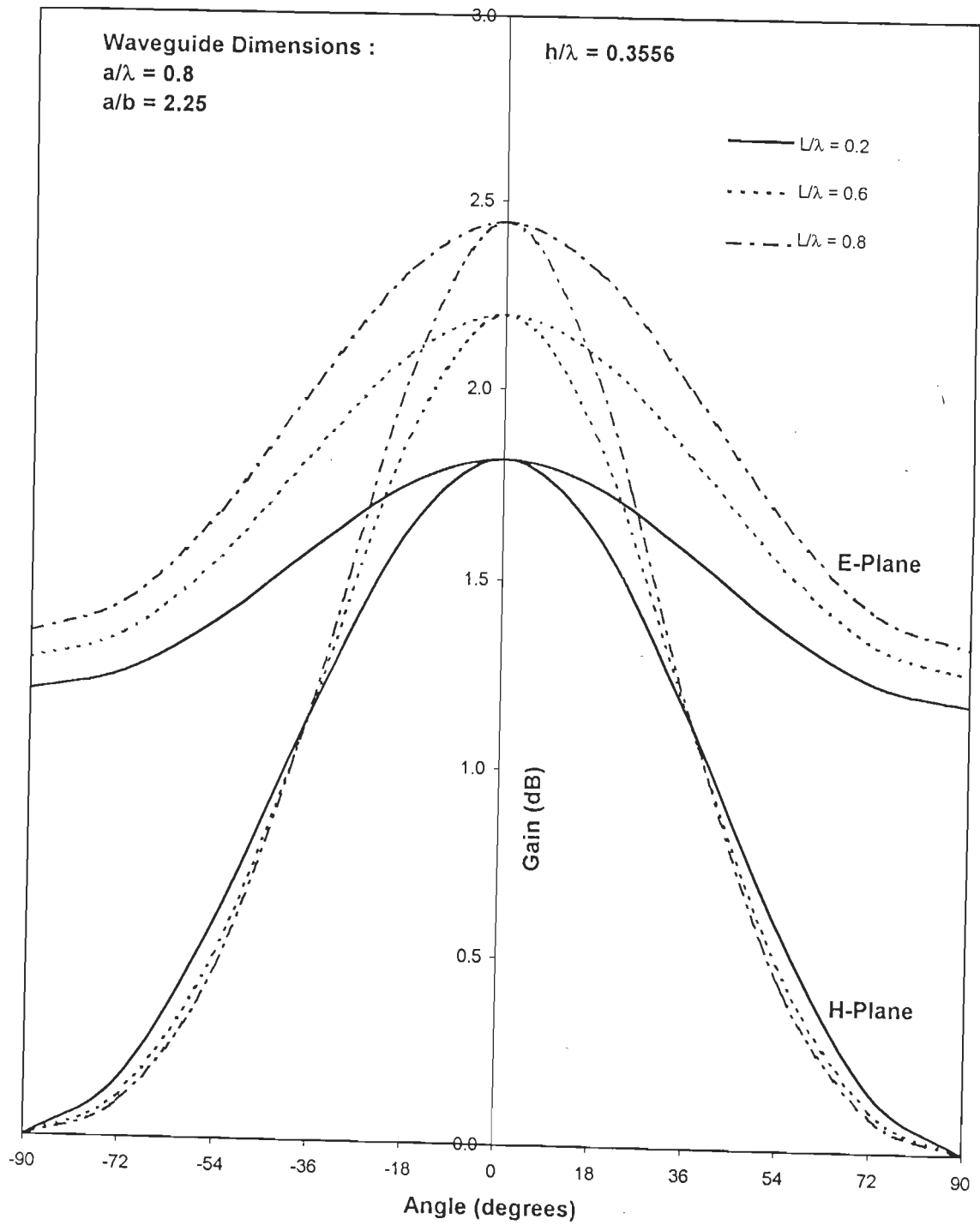
Fig. 4.20 : Power gain patterns for waveguide backed diamond-shaped apertures radiating into half space.
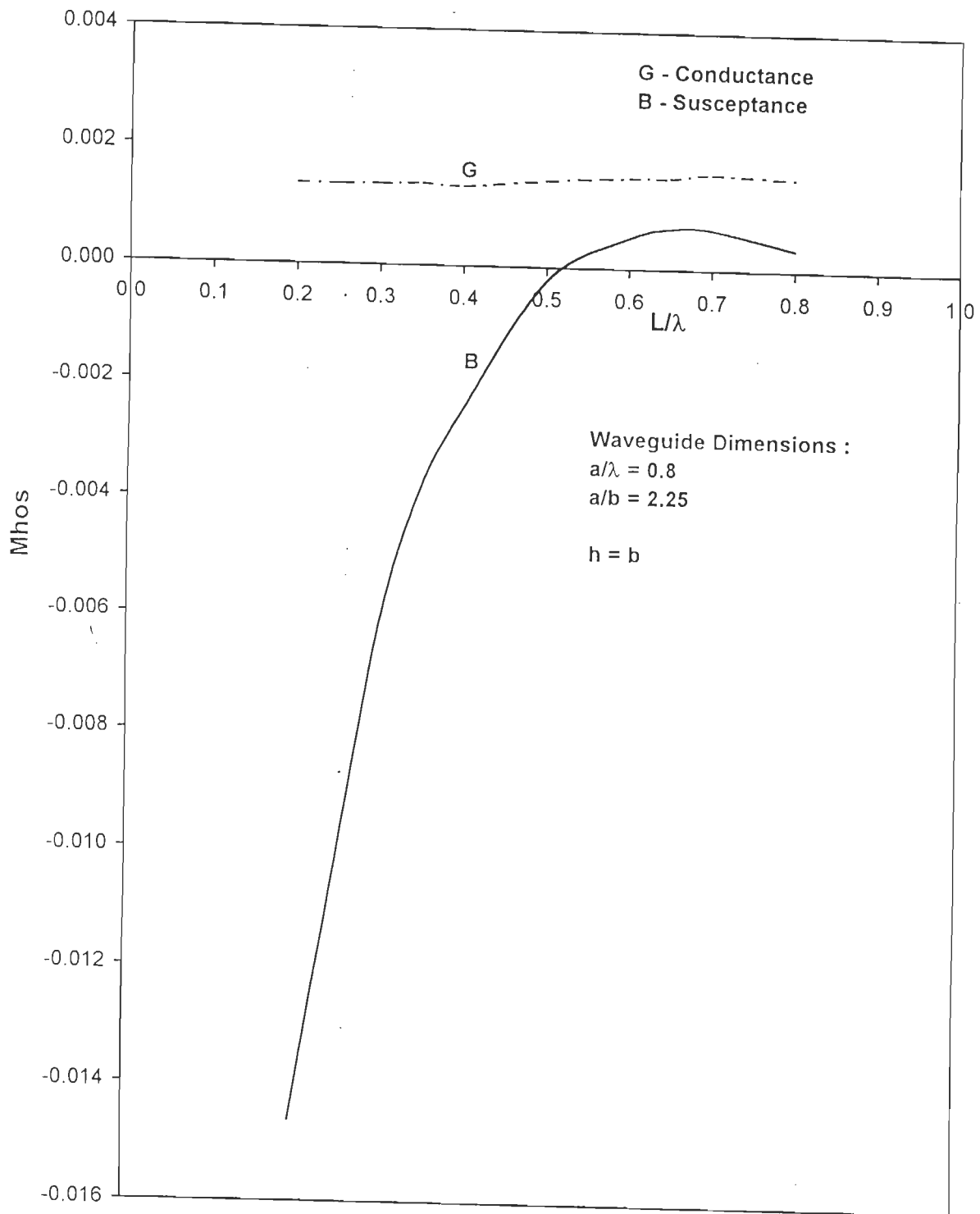
Fig. 4.21 : Equivalent aperture admittance for diamond-shaped apertures fed by a rectangular waveguide as a function of L/λ .

138

4.5-5 Cross-shaped Slot

In order to achieve convergence for cross-shaped slot, 68 expansion functions were used. The triangulation scheme used for the slot is shown in Fig. 3.28.

Fig. 4.22 shows equivalent surface magnetic current distributions for different slot arm-width, A_w. In Fig. 4.22(a) curves for A_w = L/8, L/4 and L/3 are plotted at y/h = -0.03125, - 0.0625 and −0.0833, respectively. All the curves exhibit a minima at the centre with symmetrically placed maxima on either side. The curve with the highest peak corresponds to the slot with smallest A_w (i.e., A_w = L/8) and the peak value of current decreases as A_w is increased. The nature of these curves is entirely different from the corresponding curves for other apertures studied so far. The current distributions shown in Fig. 4.22(b) exhibit peaks at the centre of the slot for A_w = L/3 and L/4 but the curve corresponding to A_w = L/8 exhibits a minima at this point. In all the cases, phase distribution is uniform.

Fig. 4.23 shows antenna gain patterns for slots of various arm widths A_w. It is observed that variation in A_w causes very small change in antenna gains and beam widths.
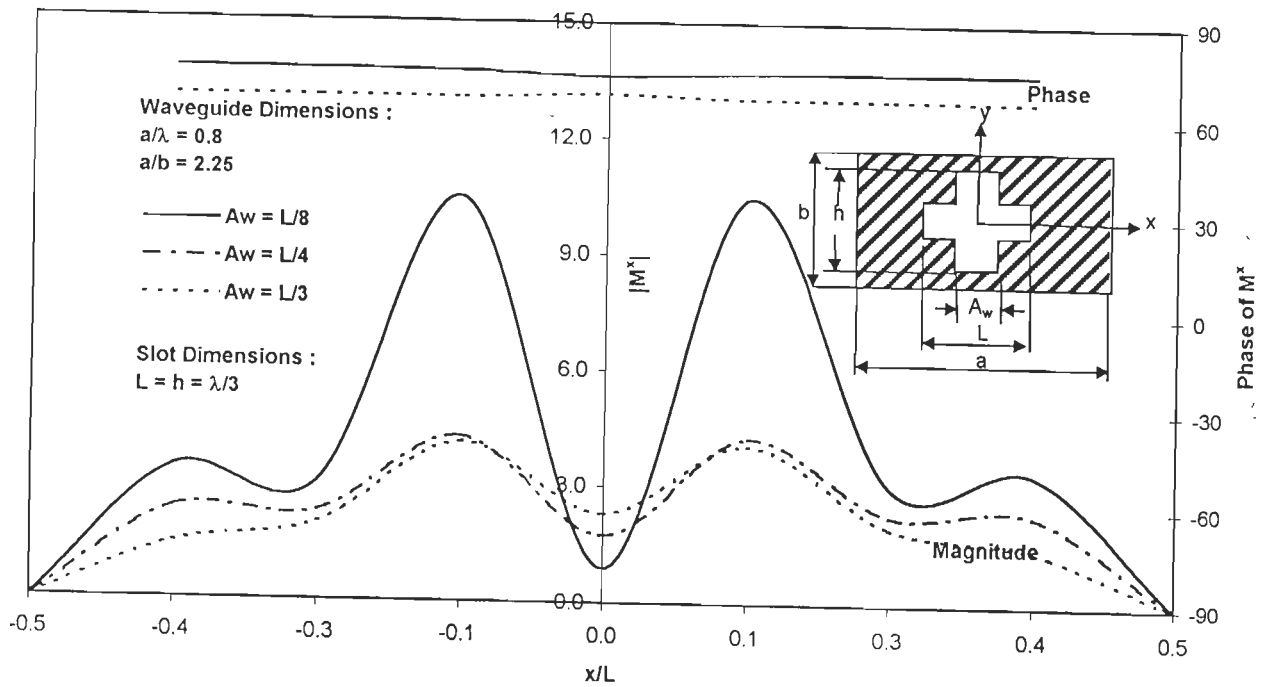
(a) y/h = -0.03125, -0.0625, -0.0833, respectively, corresponding to
A_w = L/8, L/4 and L/3
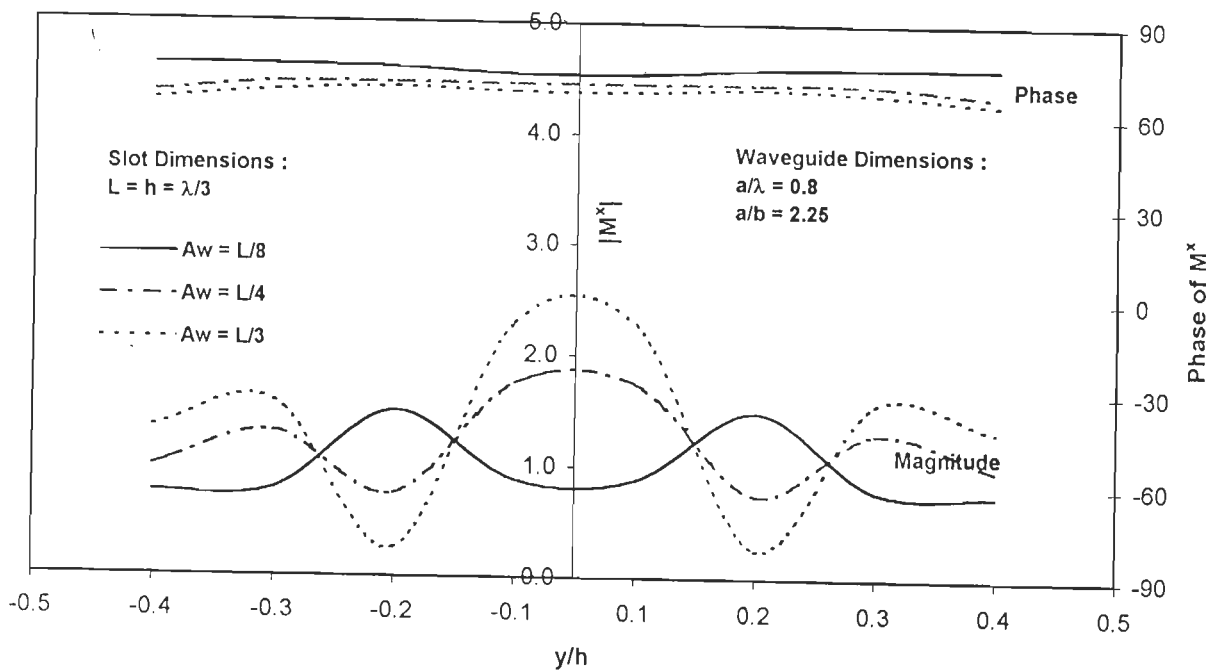
(b) x/L = 0.0

Fig. 4.22 : Equivalent surface magnetic current distribution for waveguide
backed cross-shaped slots for various arm widths A_w
radiating into half space.
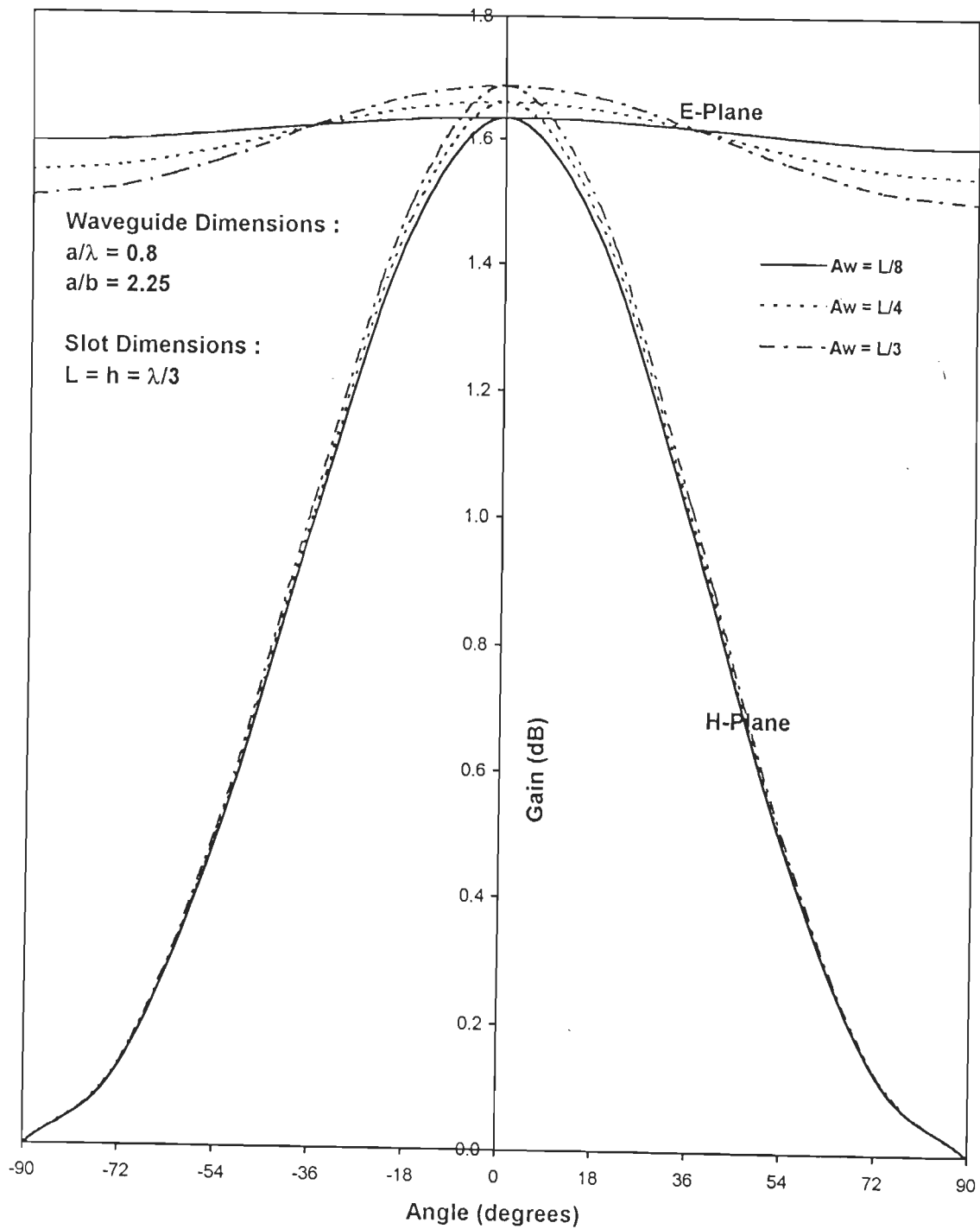
Fig. 4.23 : Power gain patterns for waveguide backed cross-shaped slots of various arm widths A_w radiating into half space.

141

4.5-6 H-shaped Slot

For the computation of various quantities for H-shaped slot, 68 expansion functions were found to yield converged results. The triangulation scheme is shown in Fig. 3.31.

Fig. 4.24 shows equivalent surface magnetic current M^x for various aperture lengths L/λ with $h = \lambda/4$ and arm width $A_w = \lambda/20$. In Fig. 4.24(a) curves corresponding to $L = \lambda/5$, $\lambda/4$ and $2\lambda/5$ plotted at $y/h = -0.0125$ are shown. The magnitude curves have broad peaks and the phase distributions are constant for $L = \lambda/5$ and $2\lambda/5$ but for $L = \lambda/4$, phase is constant only for $-0.3 \leq x/L \leq +0.3$ and thereafter, it increases sharply to a very high value towards the edges of the slot. In Fig. 4.24(b), distribution of $|M^x|$ for $L = \lambda/5$, $\lambda/4$ and $2\lambda/5$ along either arm at $x/\lambda = \pm 0.0875$, ± 0.1125 and ± 0.1875, respectively, are shown. The magnitude curves are similar to those of open-ended rectangular waveguides in Fig. 4.5(b) and (d). The phase distributions for $L = \lambda/5$ and $\lambda/4$ are uniform but for $L = 2\lambda/5$, the phase distribution is highly tapered.

Fig. 4.25 shows the power gain patterns for the H-shaped slots. It is observed that there is not much significant change in the gain patterns when the slot length is increased.

Fig. 4.26 shows equivalent aperture admittance seen by the dominant TE_{10} mode as a function of H-slot length L/λ. The slot has an inductive susceptance for $L/\lambda \leq 0.25$ which becomes capacitive for $L/\lambda > 0.25$. In this respect, H-shaped slot behaviour is similar to that of diamond-shaped aperture of Fig. 4.21. However, H-shaped slot exhibits a much higher magnitude of capacitive susceptance but its conductance G is comparable to that of diamond-shaped aperture.

142
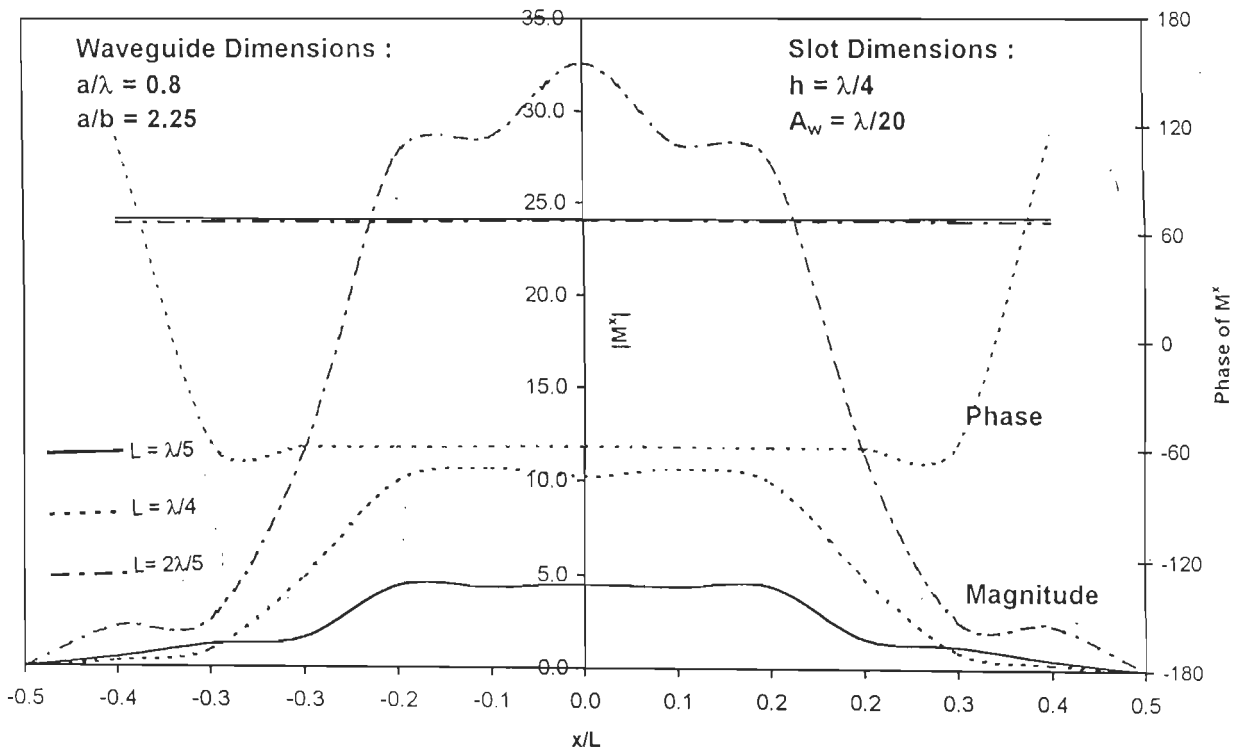
(a) y/h = - 0.0125
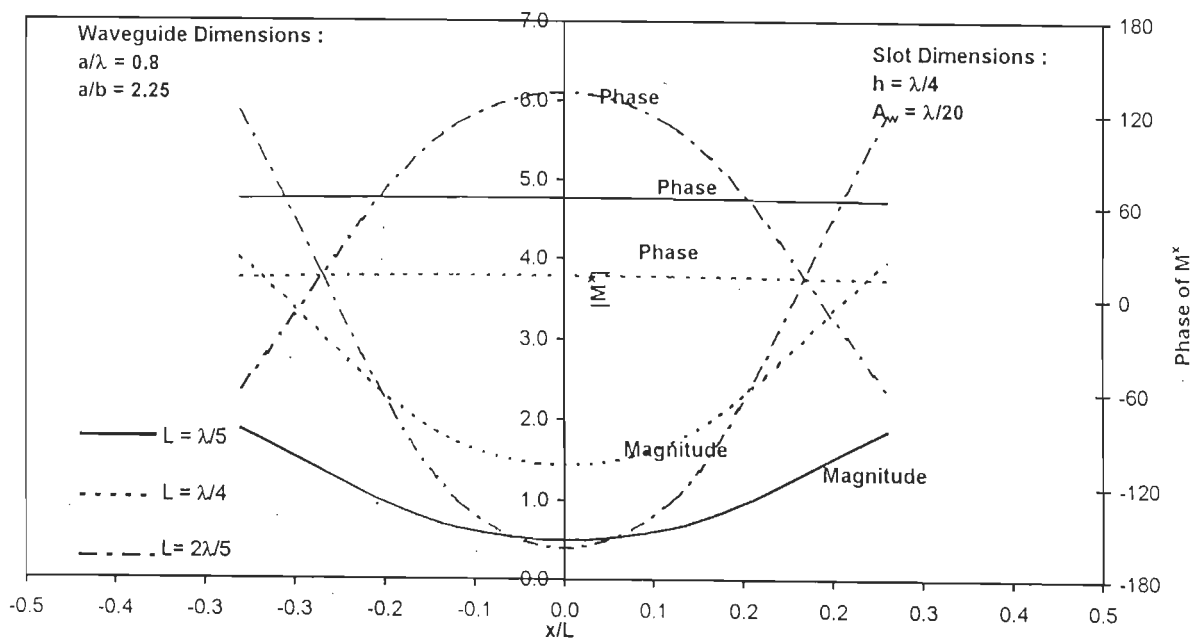
(b) x/λ = 0.0875, 0.1125 and 0.1875 respectively corresponding to
L = λ/5, λ/4 and 2λ/5.

Fig. 4.24 : Equivalent surface magnetic current distributions for waveguide
backed H-shaped slots for various lengths L/λ
radiating into half space.
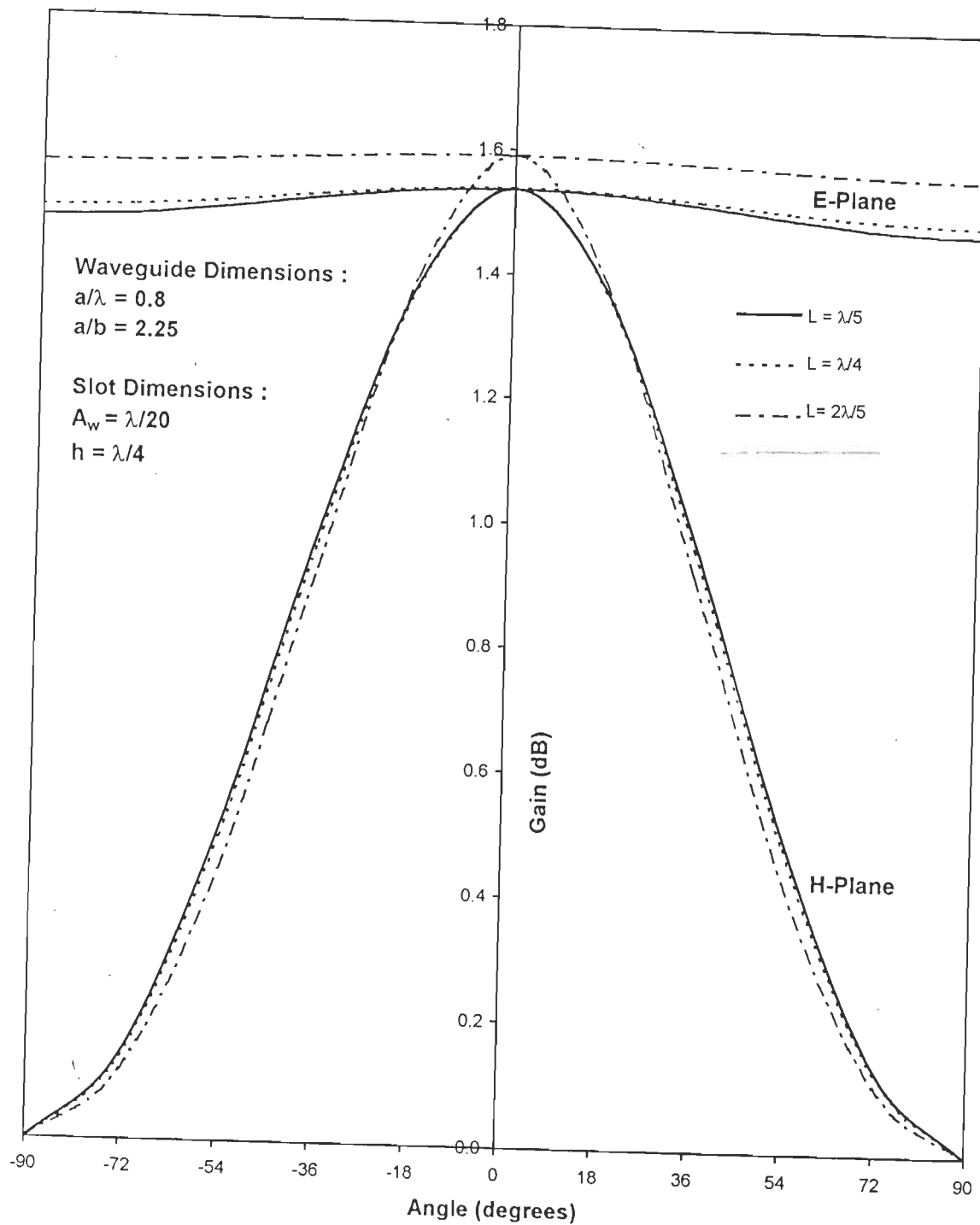
Fig. 4.25 : Power gain patterns for waveguide backed H-shaped slots of different lengths L/λ radiating into half space.
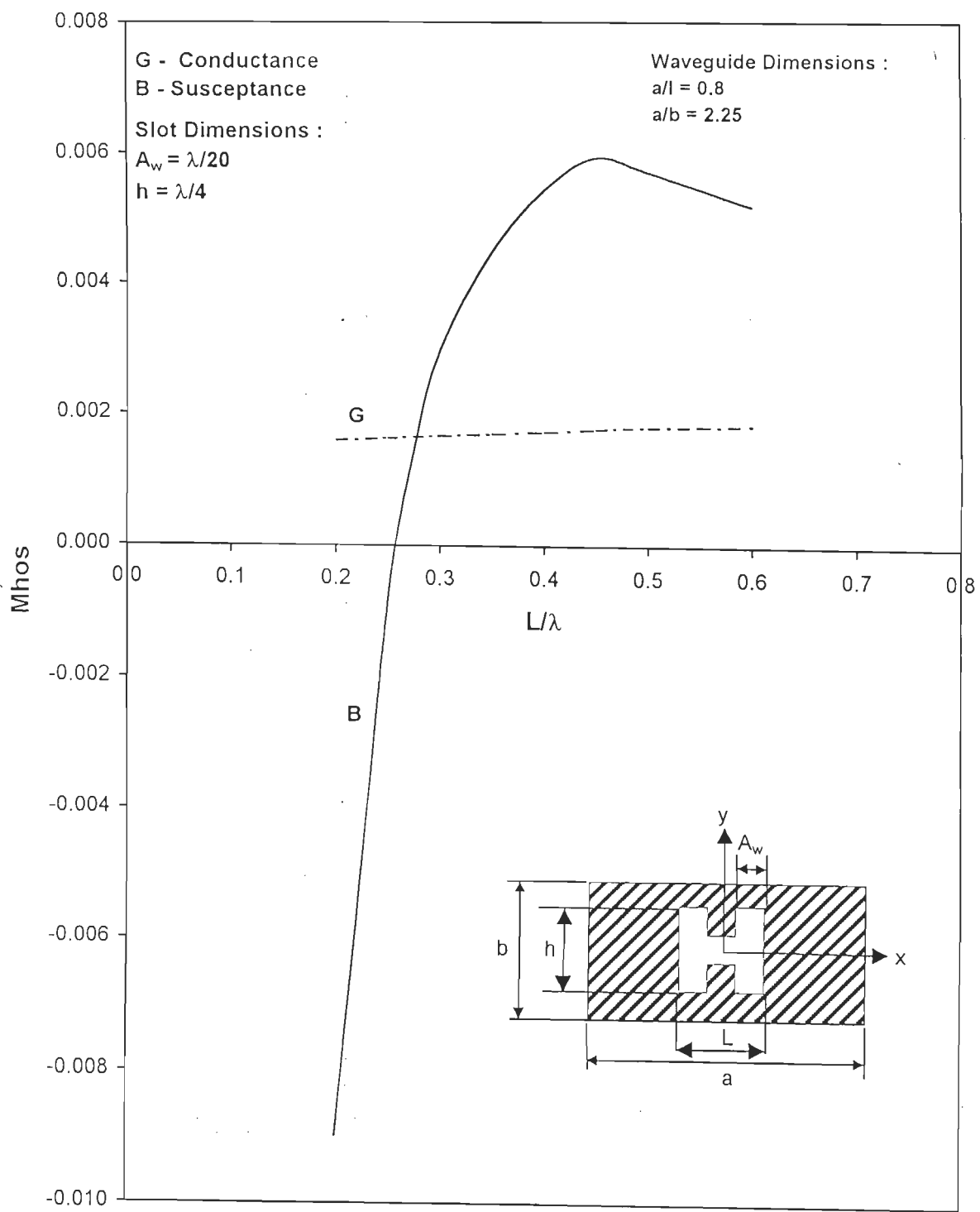
Fig. 4.26 : Equivqalent aperture admittance for H-shaped slots fed by
rectangular waveguide as a function of L/λ .

4.5-7 A Comparative Study of Antenna Power Gain Patterns for Various Aperture Shapes

We consider here a comparison of the antenna power gain patterns for apertures of various shapes. Two cases are considered. Small apertures having an area of $0.0325\lambda^2$ and relatively large apertures with an area of $0.1632\lambda^2$ each. Figs. 4.27 and 4.28 compare the E- and H-plane patterns for the smaller apertures of the same area but different shapes. It is seen that in Fig. 4.27, elliptical aperture has the highest power gain and the most directive H-plane pattern of the three shapes considered, namely, rectangular, elliptic and H. The E-plane pattern is more or less isotropic in the half space. Further, rectangular slot has a slightly higher power gain than H-shaped slot but both the apertures have nearly similar E- and H-plane patterns. In Fig. 4.28, patterns for circular, diamond and cross-shaped apertures have been shown. It is observed that the diamond-shaped aperture gives the highest power gain and the patterns for cross- and circular apertures are very nearly the same.

Figs. 4.29 and 4.30 compare the E- and H-plane patterns for the larger apertures of the same area but different shapes. It is seen that in Fig. 4.29, elliptic and diamond-shaped apertures have the same power gain. However, elliptic aperture has a more directive H-plane pattern while diamond-shaped aperture has a more directive E-plane pattern. In Fig. 4.30, patterns for rectangular-, cross-shaped and H-shaped slots have been shown. It is observed that cross-shaped slot has the highest power gain and H-shaped slot the lowest. Further, it is noted that all the three slots have similar H-plane patterns.
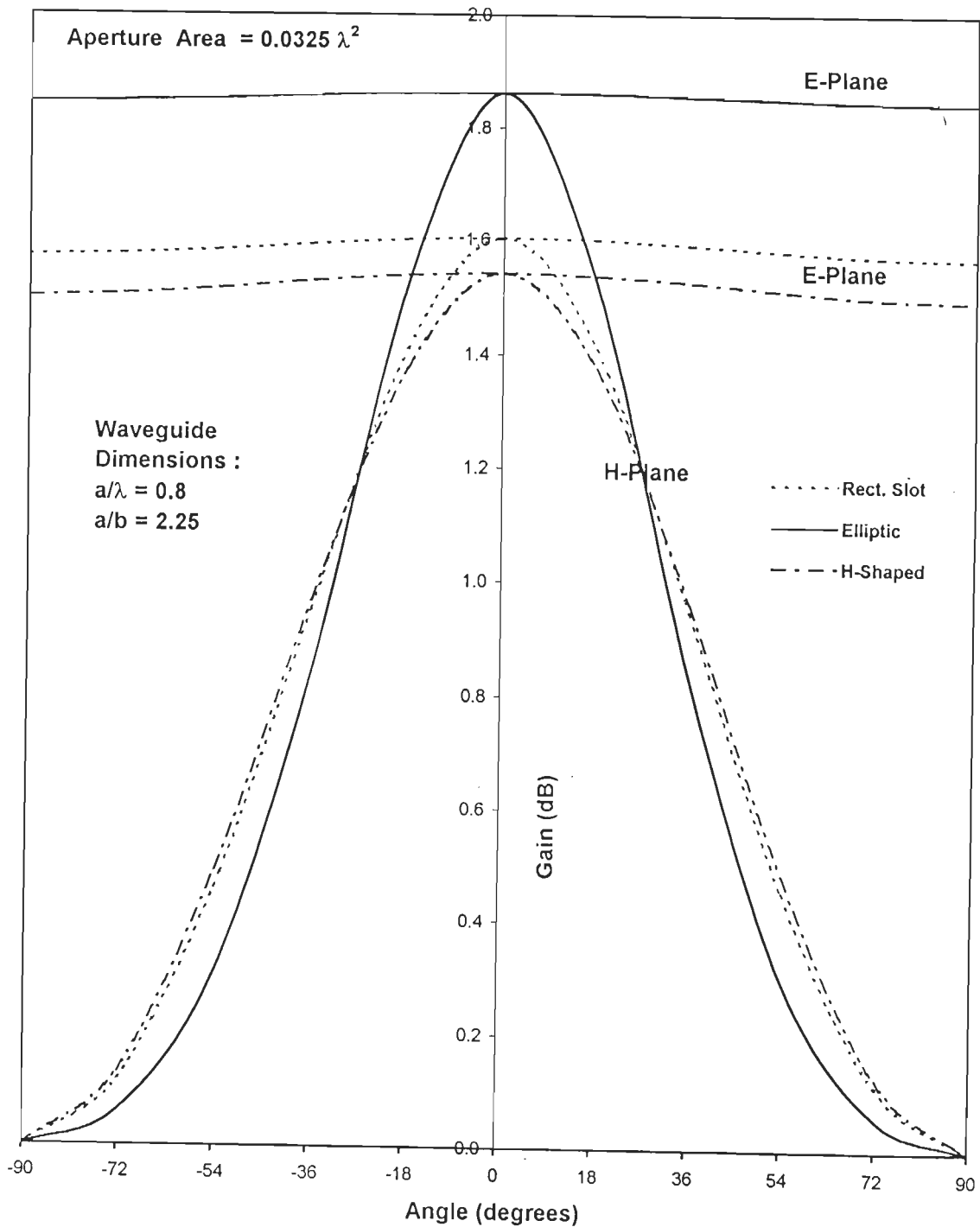
Fig. 4.27 : Power gain patterns for waveguide backed apertures of different shapes radiating into half space.

147
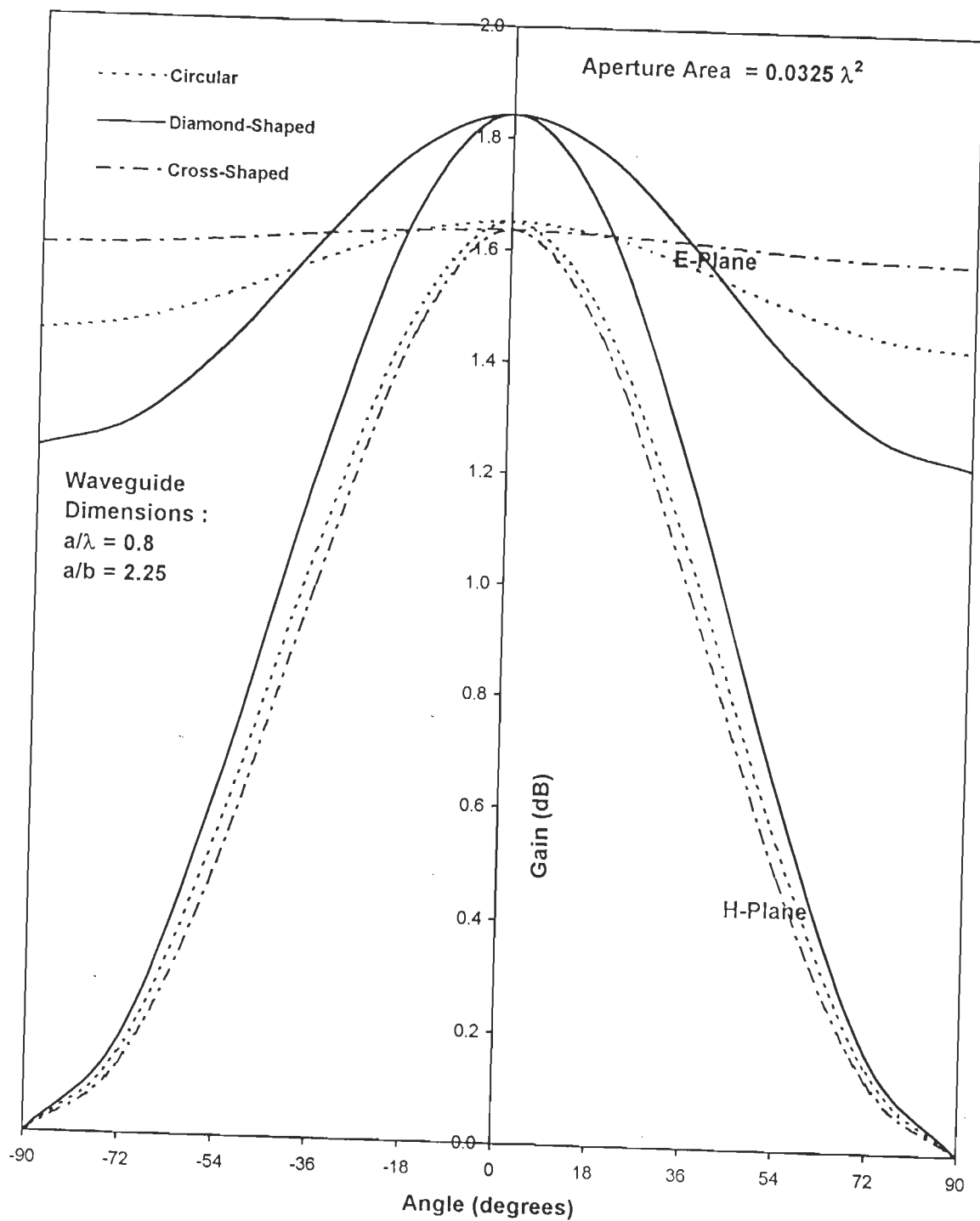
Fig. 4.28 : Power gain patterns for waveguide backed apertures of different shapes radiating into half space.

148
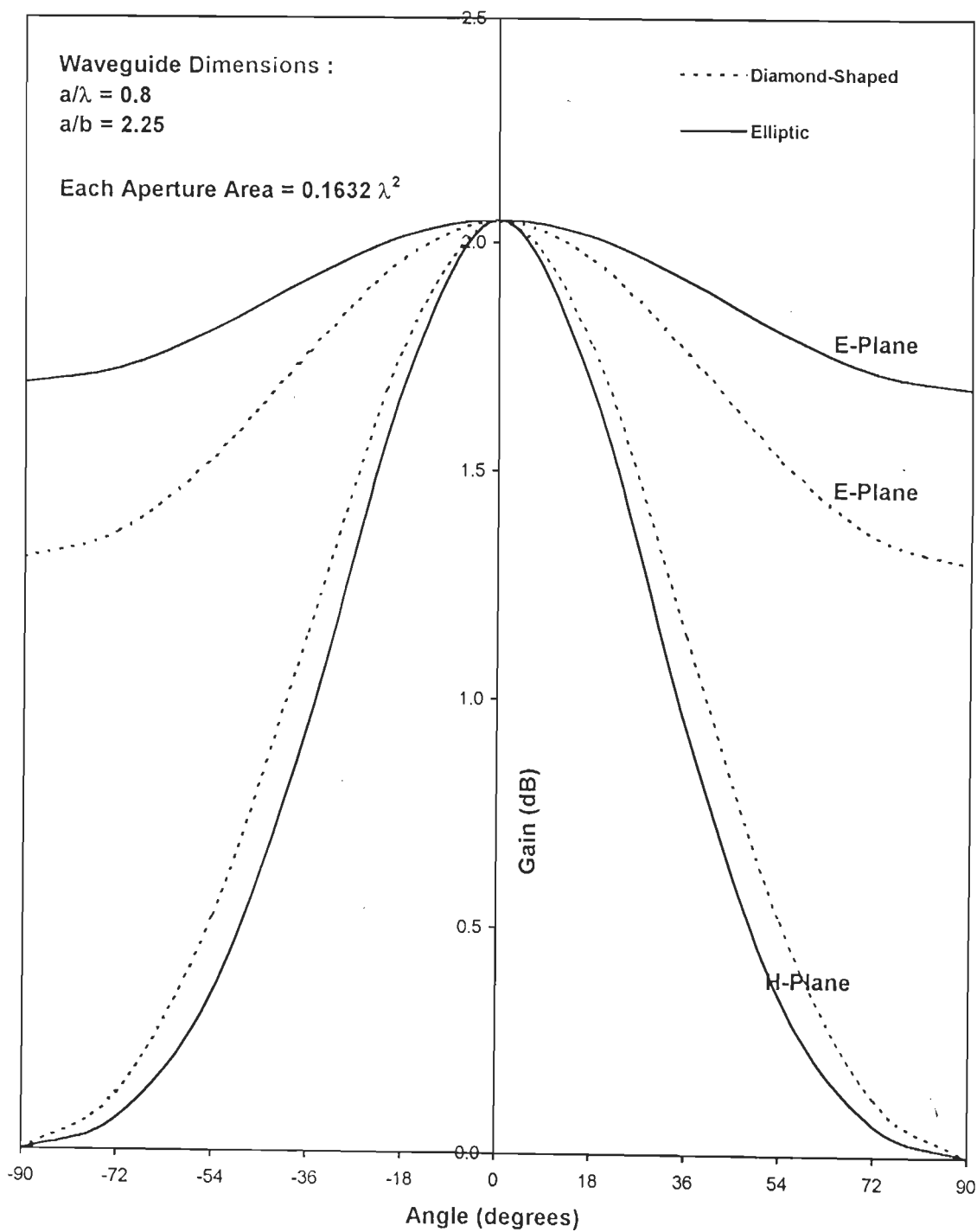
Fig. 4.29 : Power gain patterns for waveguide backed apertures of different shapes radiating into half space.
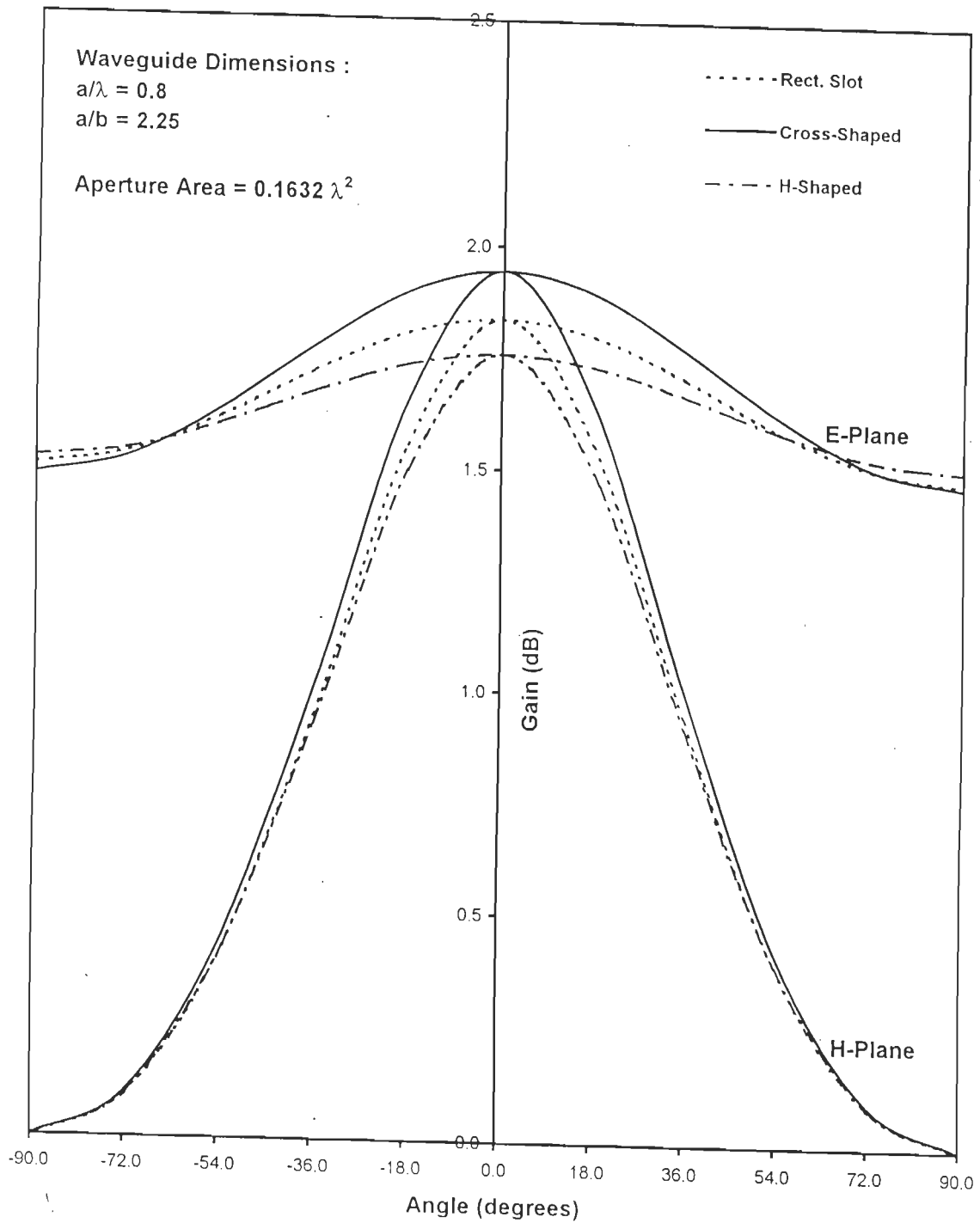
Fig. 4.30 : Power gain patterns for waveguide backed apertures of different shapes radiating into half space.

150

4.6 SUMMARY

In this chapter an extensive numerical study has been undertaken on waveguide-backed apertures of various shapes radiating into half space. The computer code has been validated by considering rectangular slots and square apertures for which data are available in literature. All the results have been tested for convergence by utilizing sufficient number of expansion functions.

Results have been presented for magnetic current distributions, power gain patterns and equivalent aperture admittance of various apertures. Finally, the radiation properties of various apertures have been compared.

Chapter - 5

APERTURES IN THE TRANSVERSE CROSS-SECTION OF A RECTANGULAR WAVEGUIDE

The analysis of diaphragms in waveguides is important because they can be used as directional couplers or as building blocks for microwave filters.

In this chapter, the problem of two uniform rectangular waveguides coupled via an arbitrary-shaped diaphragm in their transverse cross-section is considered. The problem is a special case of the general problem discussed in Chapter 2.

5.1 FORMULATION

Fig. 5.1 shows the problem under investigation and defines the coordinates and parameters used. The two waveguides are considered lossless and support only the dominant TE_{10} propagating mode. An electromagnetic source is assumed to be located in the region $z < 0$.

As discussed in Chapter 2, the equivalence theorem is first used to divide the problem into two separate regions, as illustrated in Fig. 5.2.

Since the two regions are identical, the operator equation in (2.2) reduces to

$$\overline{H}_t(\overline{M}) + \overline{H}_t^{io} = 0 \text{ over the aperture} \tag{5.1}$$

where $\overline{H}_t^{io}$ is given by eqn. (4.21), $\overline{H}_t(\overline{M})$ is the tangential component of the magnetic field due to $\overline{M}$ for region 'a' in eqn. (2.16) specialized to the waveguide region, as further explained in Sec. 4.2. From eqn. (4.1), the admittance matrix for either region can be written as

$$[Y] = [< W_i, H_t(\overline{M}_j) >]_{N \times N} \tag{5.2}$$
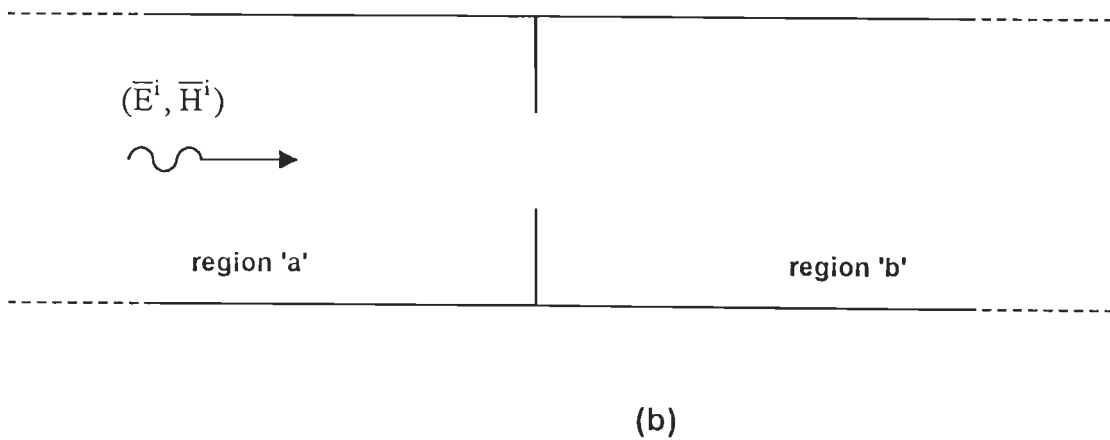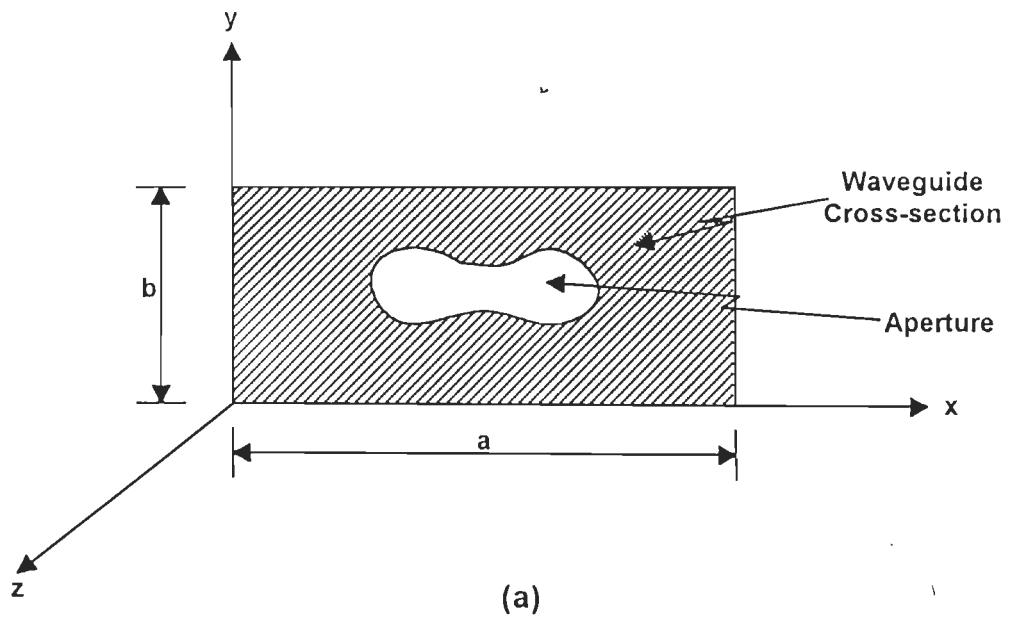
Fig. 5.1 : Original problem (a) cross-sectional view, showing diaphragm of irregular shape (b) lateral view showing coupling between two uniform waveguides
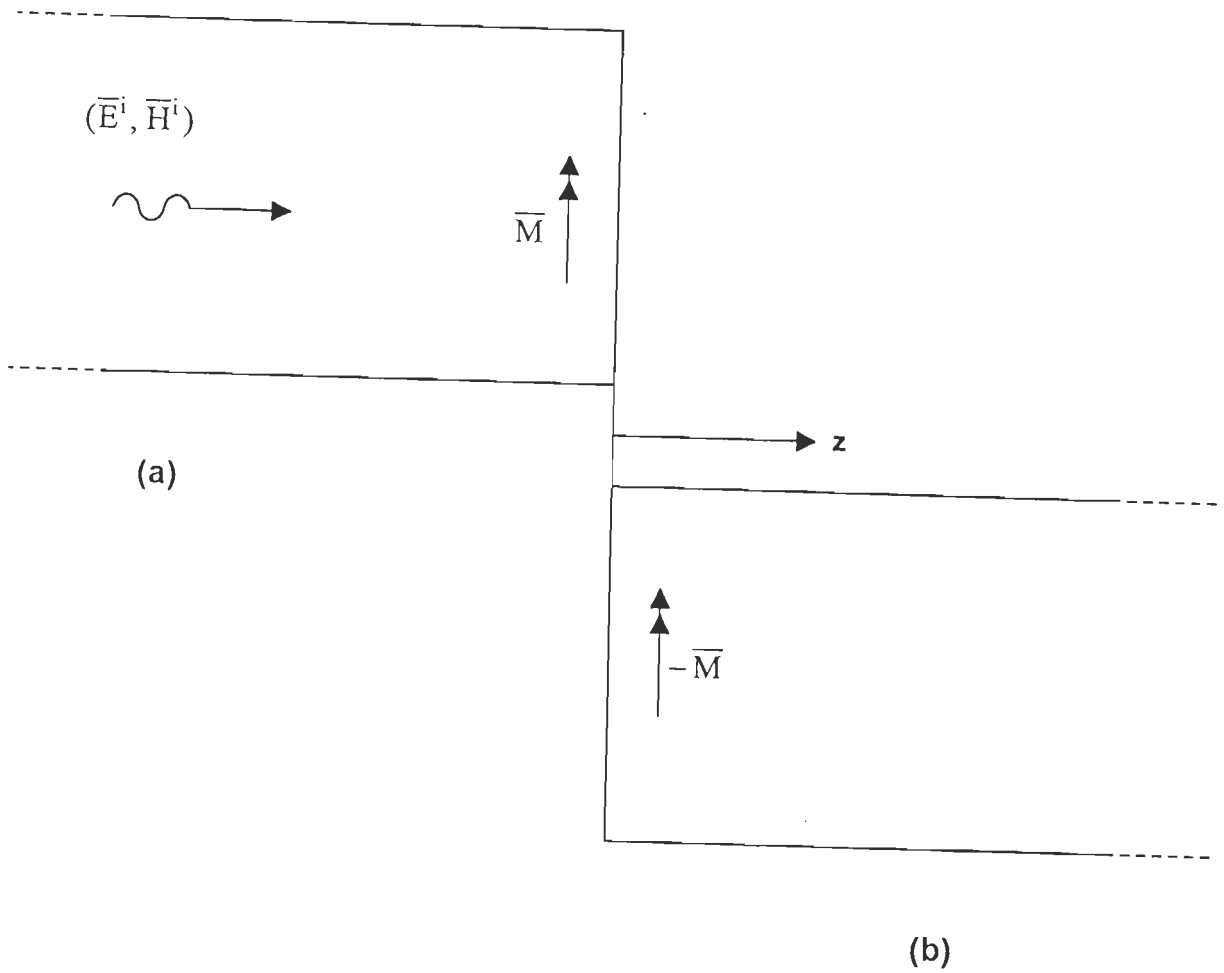
Fig. 5.2 : Equivalent problems (a) model valid in region z < 0, (b) model valid in region z > 0

and the excitation vector, according to eqn. (2.10) as

$$\bar{I}^i = [- < W_i, H_t^i >]_{Nx1} \tag{5.3}$$

Upon applying Galerkin method and centroid approximation to eqns. (5.2) and (5.3), an element of admittance matrix can be written as

$$Y_{mn} = -1_m \left\{ j\omega \left[\bar{F}_n(\bar{r}_m^{C+}) \bullet \frac{\bar{\rho}_m^{C+}}{2} + \bar{F}_n(\bar{r}_m^{C-}) \bullet \frac{\bar{\rho}_m^{C-}}{2} \right] + \phi_n\left(\bar{r}_m^{C-}\right) - \phi_n\left(\bar{r}_m^{C+}\right) \right\} \tag{5.4}$$

where $\bar{F}_n$ and ϕ_n are the electric vector and magnetic scalar potentials, respectively, given by eqns. (4.18) and (4.19), and an element of excitation

154

vector according to eqn. (4.26), after substituting eqn. (4.25) in eqn. (5.3), becomes

$$I_m^i = -2l_m \left\{ \overline{H}_t^{io} \left(\overline{r}_m^{C+} \right) \bullet \frac{\overline{\rho}_m^{C+}}{2} + \overline{H}_t^{io} \left(\overline{r}_m^{C-} \right) \bullet \frac{\overline{\rho}_m^{C-}}{2} \right\}$$ (5.5)

5.2 EQUIVALENT CIRCUIT AND SCATTERING PARAMETERS

The class of discontinuities considered here can be represented by normalized shunt susceptance, $j\overline{B}$, across a transmission line of unit characteristic admittance [26]. If Γ_o denotes the reflection coefficient of dominant TE_{10} mode, then from eqn. (4.36)

$$S_{11} = \frac{-j\overline{B}}{2+j\overline{B}} = \Gamma_o$$

or $$j\overline{B} = \frac{-2\Gamma_o}{1+\Gamma_o}$$ (5.6)

Γ_o is given by eqn. (4.33).

Thus, the waveguide junction can be characterized by scattering matrix S given by

$$S = \begin{bmatrix} \Gamma_o & 1+\Gamma_o \\ 1+\Gamma_o & \Gamma_o \end{bmatrix}$$ (5.7)

5.3 RESULTS AND DISCUSSION

In this study, the waveguide has been assumed to support only the dominant propagating mode and, so, the effect of discontinuity on only the TE_{10} mode has been considered.

Fig. 5.3 illustrates the geometry of typical inductive and capacitive diaphragms in a rectangular waveguide.
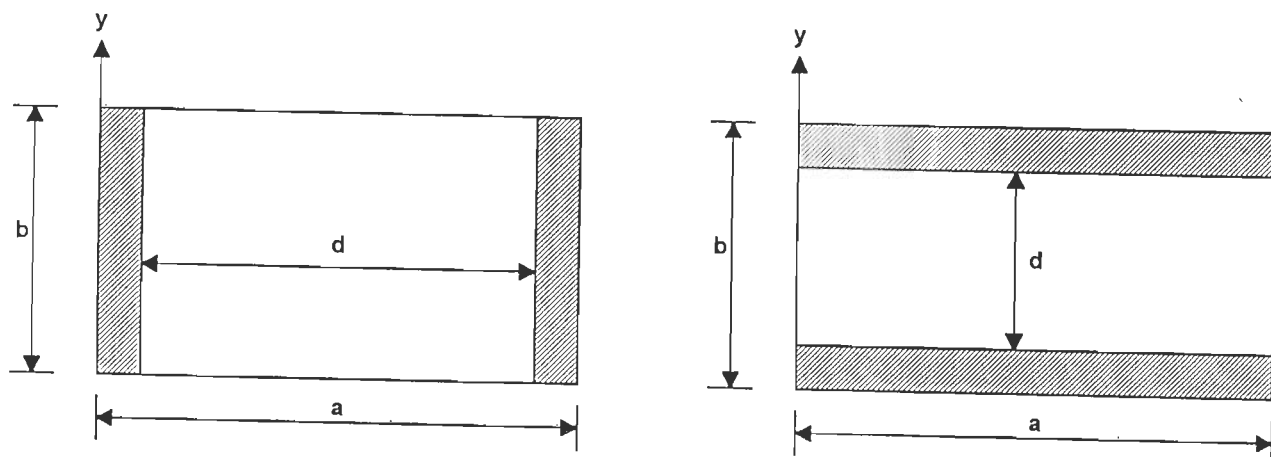
Fig. 5.3 : Diaphragm (a) inductive (b) capacitive

The evaluation of waveguide field involves doubly infinite summations r and s as in eqn. (4.8), which represent the variation of the field along x- and y-directions, respectively. This corresponds to inclusion of infinite number of TE and TM modes in the computation of electromagnetic field in a waveguide. However, in practice, the summations are truncated to only finite values of the indices r and s, i.e., $r = 0, 1, 2, ..., N_R$ and $s = 0, 1, 2, ..., N_S$, where N_R and N_S are so chosen that only further increase in their values does not result in any significant change in the value of matrix elements.

According to data available in the literature, notably by Lee et al [56], Mittra et al. [71] and De Smedt et al. [32], it was established that in the mode-matching and MOM solutions of apertures in waveguides, erroneous results are obtained unless one chooses a correct ratio of the number of expansion functions to the number of modes used to approximate the waveguide field. This ratio depends upon the dimension of the aperture in the direction normal to the direction of the electric field and the phenomenon is known as 'relative

156

convergence'. In particular, it has been shown for an inductive diaphragm [56], that

$$\frac{N_1}{p_1} \leq \frac{d}{a} \tag{5.8}$$

where N_1 = total number of expansion functions

$\quad$ p_1 = minimum value of N_R that satisfies eqn. (5.8)

$\quad$ a = waveguide broad-wall dimension

$\quad$ d = discontinuity size.

Eqn. (5.8) is valid for analyzing inductive diaphragms since the discontinuity is uniform along y-axis and varies only along the direction normal to the direction of the electric field and the electromagnetic wave incident in the dominant TE_{10} mode causes only TE_{m0} modes to be excited at z = 0. As such, eqn. (5.8) need only be satisfied along the x-axis to eliminate the problem of 'relative convergence'.

However, in order to analyse an arbitrary-shaped aperture, which may require two-dimensional discretization, both TE and TM modes should be included in the evaluation of the waveguide field. This observation was made by Sinha [100] regarding capacitive diaphragms in his analysis of multiple-strip discontinuity in a rectangular waveguide.

In fact, this study has established that in order to account for waveguide field in capacitive diaphragms, the two conditions that need to be met are :

$$\frac{N_1}{p_1} \leq \frac{d}{a} \tag{5.9}$$

$$\frac{p_2}{N_2} \leq 1 \tag{5.10}$$

where N_1 = total number of expansion functions

$\quad$ b = waveguide narrow-wall dimension

$\quad$ d = discontinuity size

p_1 = minimum value of N_S that satisfies eqn. (5.9)

N_2 = number of expansion function corresponding to the number of non-boundary edges in a single row in the x-direction.

p_2 = minimum value of N_R that establishes convergence of results.

We have further noted that it is only for the cases of inductive and capacitive diaphragms that N_1 in eqn. (5.8) and eqn. (5.9), respectively, must be the total number of expansion functions. For other aperture shapes, such as circular, elliptic and diamond, which may be located only in a limited central position of the waveguide cross-section, satisfying the following two conditions is sufficient to yield the correct results

$$\frac{N_1}{p_1} \leq \frac{d}{a} \tag{5.11}$$

$$\frac{p_2}{p_1} \leq 1 \tag{5.12}$$

where N_1 = number of expansion functions corresponding to the number of non-boundary edges along a single row in the x-direction.

p_1 = value of N_R that satisfies eqn. (5.11).

p_2 = minimum value of N_S that yields converged results.

5.3-1 Symmetrical Inductive Diaphragms

For symmetrical inductive diaphragms (inset of Fig. 5.5), four triangulation schemes have been considered, namely, single-row, double-row, triple-row and quadruple-row. Typical double- and quadruple-row triangulation schemes are shown in Fig. 3.3 and Fig. 3.4, respectively. Fig. 5.4 depicts typical single-row triangulation schemes comprising 39 non-boundary edges. In Fig. 5.4(a) the density of triangular patches is uniform. This type of triangulation scheme was found to give satisfactory results for smaller apertures upto

$d/a \le 0.6$. However, for larger apertures, the results obtained from this type of uniform triangulation were inaccurate. Therefore, for larger apertures the triangulation scheme shown in Fig. 5.4(b) was considered. In this scheme the patch density is less at the aperture centre and increases towards the ends. Thus, this scheme takes into account the edge effects more accurately. The scheme was found to give accurate results for larger apertures.

Table 5.1 lists the results for convergence test on shunt susceptance B/Y_0 of symmetrical inductive diaphragms as a function of the number of expansion functions with different number of rows in the triangulation scheme. The results were obtained using uniform and non-uniform triangulation schemes, and, for each discontinuity, where results based on both schemes were approximately the same only data based on uniform triangulation scheme is listed, otherwise data based on non-uniform discretization is given. For $0.65 \le d/a \le 0.95$, results based on non-uniform discretization were found to be in good agreement with the data in the literature [65].

As a whole, results obtained corresponding to different rows and number of expansion functions for a given discontinuity size were found to be in good agreement with one another and also with the data in the literature [65], [100]. These results confirm the validity of our computer code for analyzing both single- and multi-row triangulated diaphragms.

Fig. 5.5 shows normalized shunt susceptance versus d/a for $0.2 \le d/a \le 0.95$, where good agreement with published data is observed.

Fig. 5.6 shows equivalent surface magnetic current distribution M^x along the centre of the diaphragm for d/a = 0.25 and 0.6. It is seen that $|M^x|$ curves are symmetrical about the centre and the phase curves are constant. As expected, the larger the aperture, the larger the peak current.
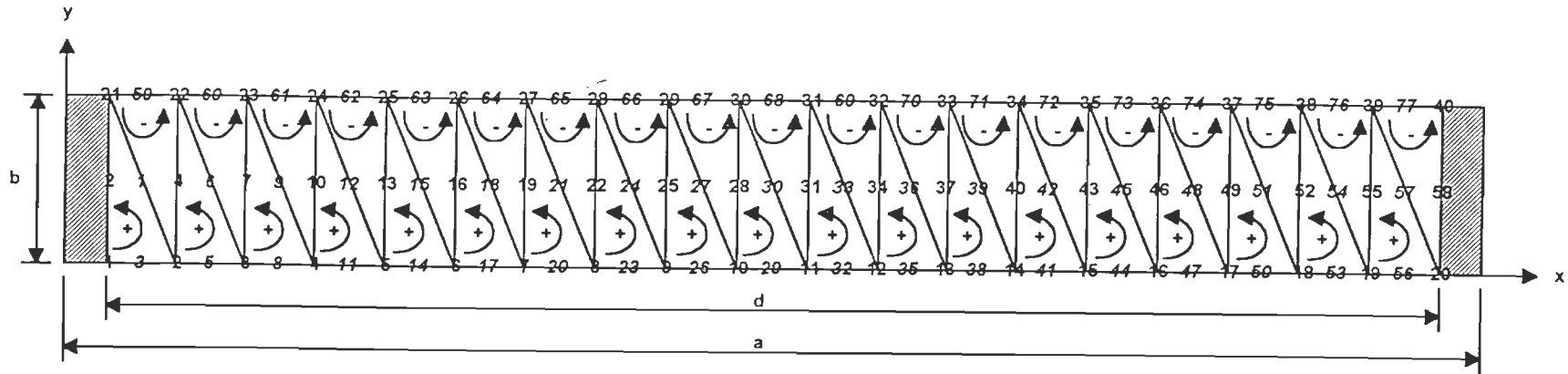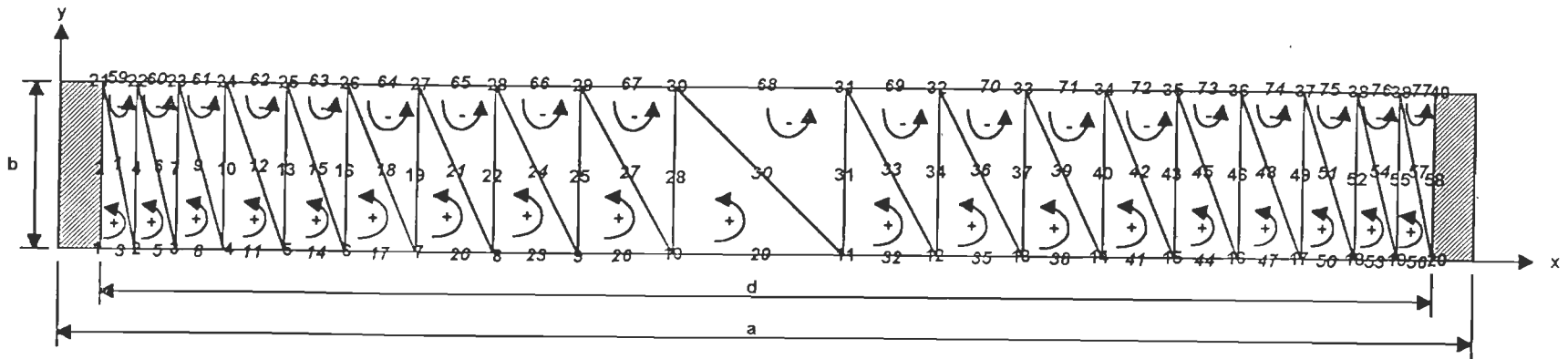
Fig. 5.4 : Symmetrical inductive diaphragm discretization using (a) uniform triangulation (b) non-uniform triangulation

160

Table - 5.1
Convergence Test on Shunt Susceptance of a Symmetrical Inductive Diaphragm in a Uniform Rectangular Waveguide

d/a	No. of Rows	No. of Expn. Functions	Modal Indices in eqn.(4.8)		Shunt Susceptance B/Y_o	
			r	s	This Method	Classical Method in [65]
0.4	1	7	18	0	-2.8393	-2.74
		11	28	0	-2.8363	
		15	38	0	-2.8350	
		23	58	0	-2.7895	
		27	68	0	-2.7779	
		39	98	0	-2.7330	
	2	18	18	1	-2.8281	
		23	23	1	-2.8277	
		28	28	1	-2.8272	
	3	21	13	2	-3.0471	
		29	18	2	-2.8335	
		45	28	2	-2.8320	
	4	29	13	3	-3.0510	
		40	18	3	-2.8354	
		62	28	3	-2.8335	
0.65	1	39	60	0	-0.55509	-0.5325
	1	49	75	0	-0.55347	
	2	78	48	3	-0.53720	
	3	93	35	5	-0.53680	
0.70	1	39	56	0	-0.39221	-0.37965
	1	49	70	0	-0.38823	
	2	78	44	3	-0.38035	
	3	93	33	5	-0.37890	
0.75	1	39	52	0	-0.267298	-0.25772
	1	49	62	0	-0.263220	
	2	78	41	3	-0.267110	
	3	93	31	5	-0.259392	
0.80	1	39	49	0	-0.17447	-0.162185
	1	49	61	0	-0.17339	
	2	78	39	3	-0.16480	
	3	93	29	5	-0.16132	
0.85	1	39	46	0	-0.09378	-0.09010
	1	49	58	0	-0.09557	
	2	78	36	3	-0.08995	
	3	93	27	5	-0.09211	
0.90	1	39	43	0	-0.045143	-0.03951
	1	49	54	0	-0.039111	
	2	78	34	3	-0.03077	
	3	93	26	5	-0.03071	
0.95	1	39	41	0	-0.013735	-0.00989
	1	49	52	0	-0.011326	
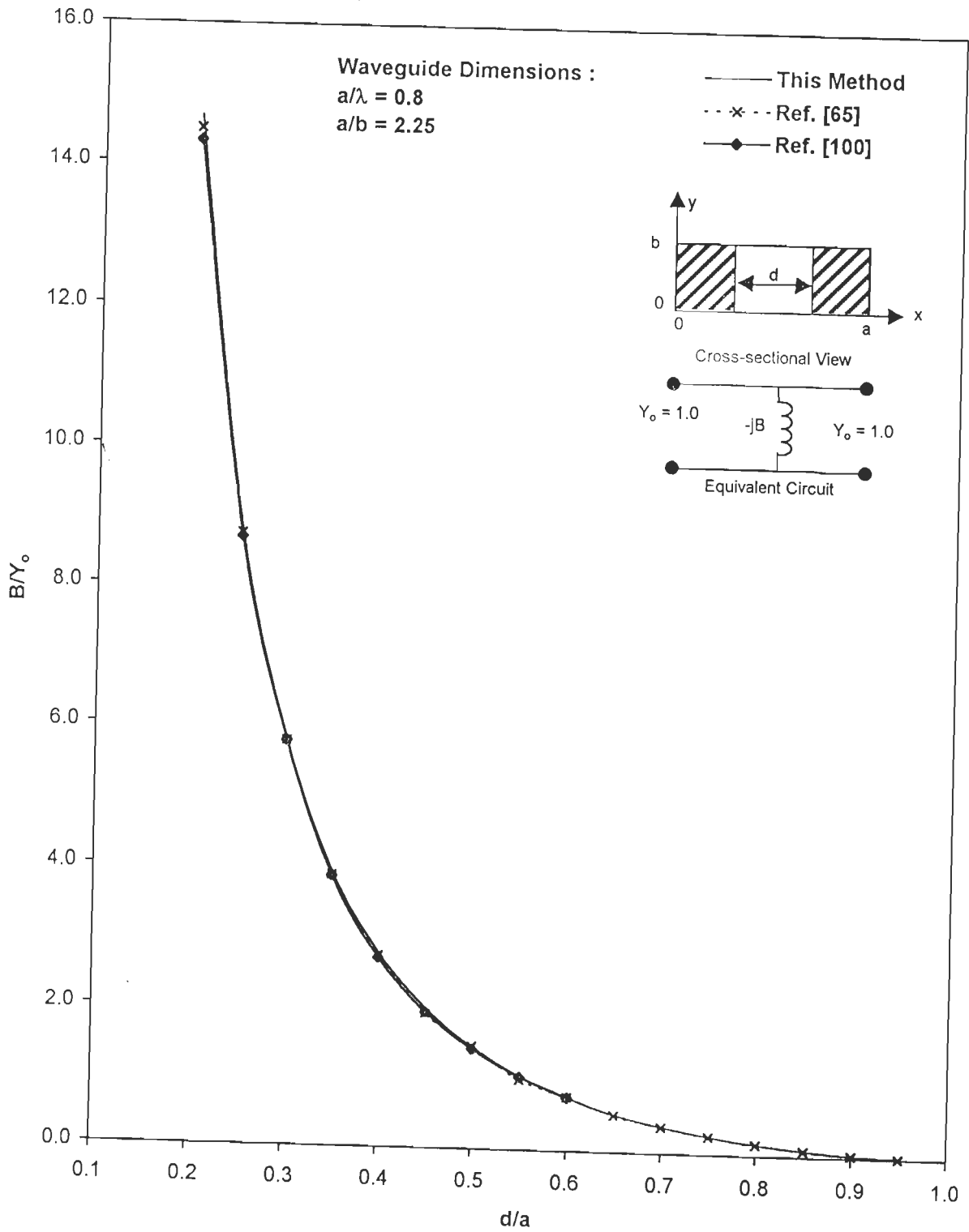
Fig. 5.5 :   Normalized susceptance B/Y₀ as a function of aperture
size for symmetrical inductive diaphragms
in uniform rectangular waveguides.

162

Fig. 5.6 : Equivalent surface magnetic current distributions M^x for symmetrical inductive diaphragms in uniform rectangular waveguides.

5.3-2 Symmetrical Capacitive Diaphragms

The geometrical parameters of a symmetrical capacitive diaphragm are shown in the inset of Fig. 5.9. Fig. 5.7 shows two triangulation schemes for capacitive diaphragm in which each discretized surface comprises 18 non-boundary edges. In Fig. 5.7(a) the diaphragm is partitioned into two rows in a direction perpendicular to diaphragm edges and in Fig. 5.7(b) it is partitioned into four rows.

A comparative study on convergence of results based on the two schemes was carried out and the results are listed in Table 5.2. It is seen that the rate of convergence of susceptance B/Y_o as a function of modal index r is much faster for the triangulation scheme of Fig. 5.7(b) than that for Fig. 5.7(a). In Fig. 5.7(b), r = 1 is sufficient to yield the required susceptance while in Fig. 5.7(a), r = 3 is required in order to obtain approximately the same value of susceptance. Increase of the rate of convergence for the triangulation scheme of Fig. 5.7(b) means fewer number of modes are required and consequently less computational burden since the number of expansion functions is the same in both schemes. It is also noted that as the size of the discontinuity increases, the discretization scheme in Fig. 5.7(b) yields results which are more closer to the data available in the literature [65], [100].

Having adopted the scheme shown in Fig. 5.7(b), we further considered the effect of uniform and non-uniform discretization on convergence of susceptance B/Y_o. For this purpose, the discretization schemes shown in Fig. 5.8 were considered. Table 5.3 summarizes the results of our investigation. It is noted that the results corresponding to uniform triangulation scheme agree with the published data only for $d/b \leq 0.7$. For $d/b \geq 0.7$, non uniform triangulation scheme yields results which are in good agreement with the data available in [65].

(a)

(b)
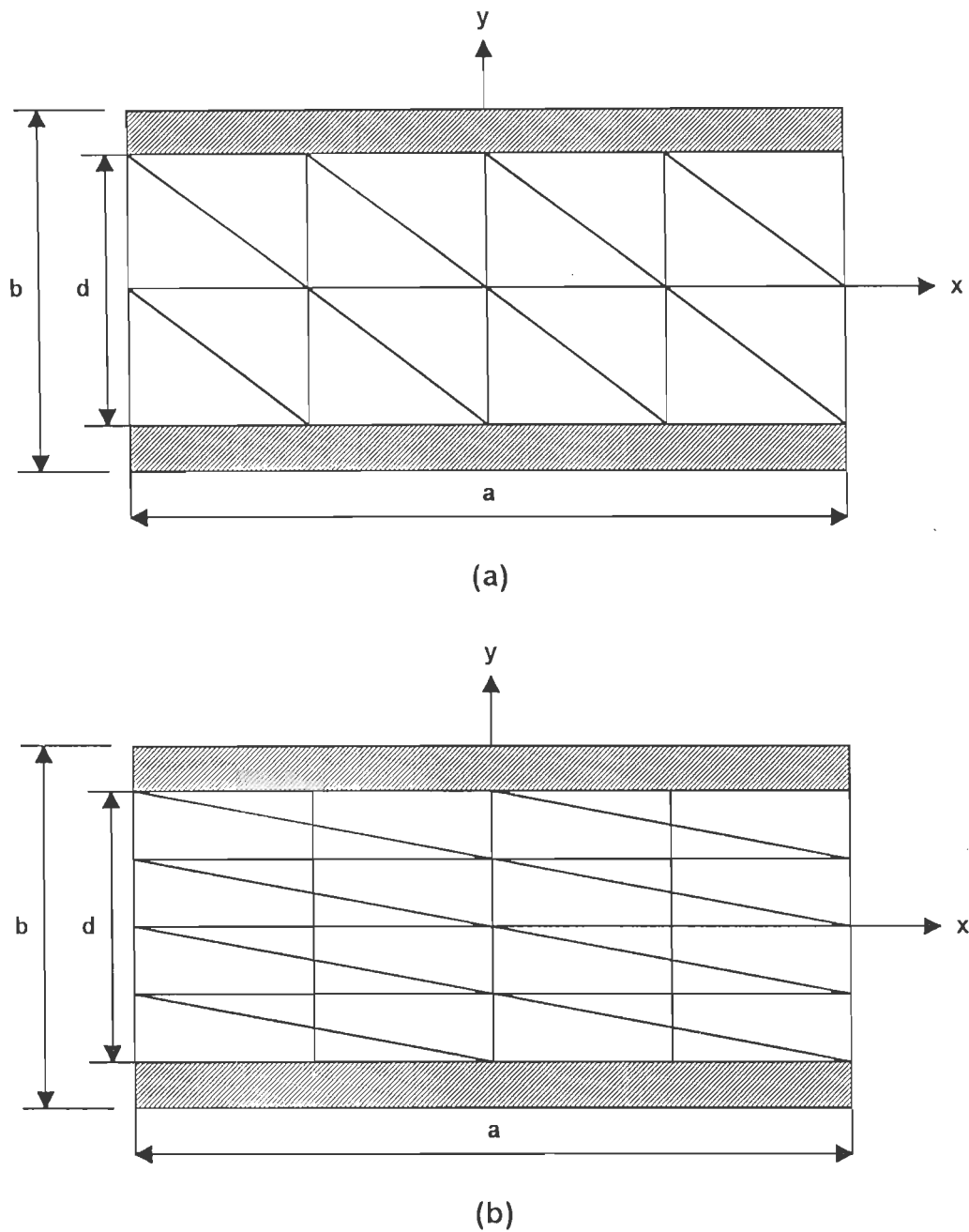
Fig. 5.7 : Two triangulation schemes for symmetrical capacitive diaphragm.

Fig. 5.9 shows normalized susceptance B/Y_o, based on results of Table 5.3, as a function of discontinuity size d/b. Excellent agreement between the results and data available in [65] is observed.
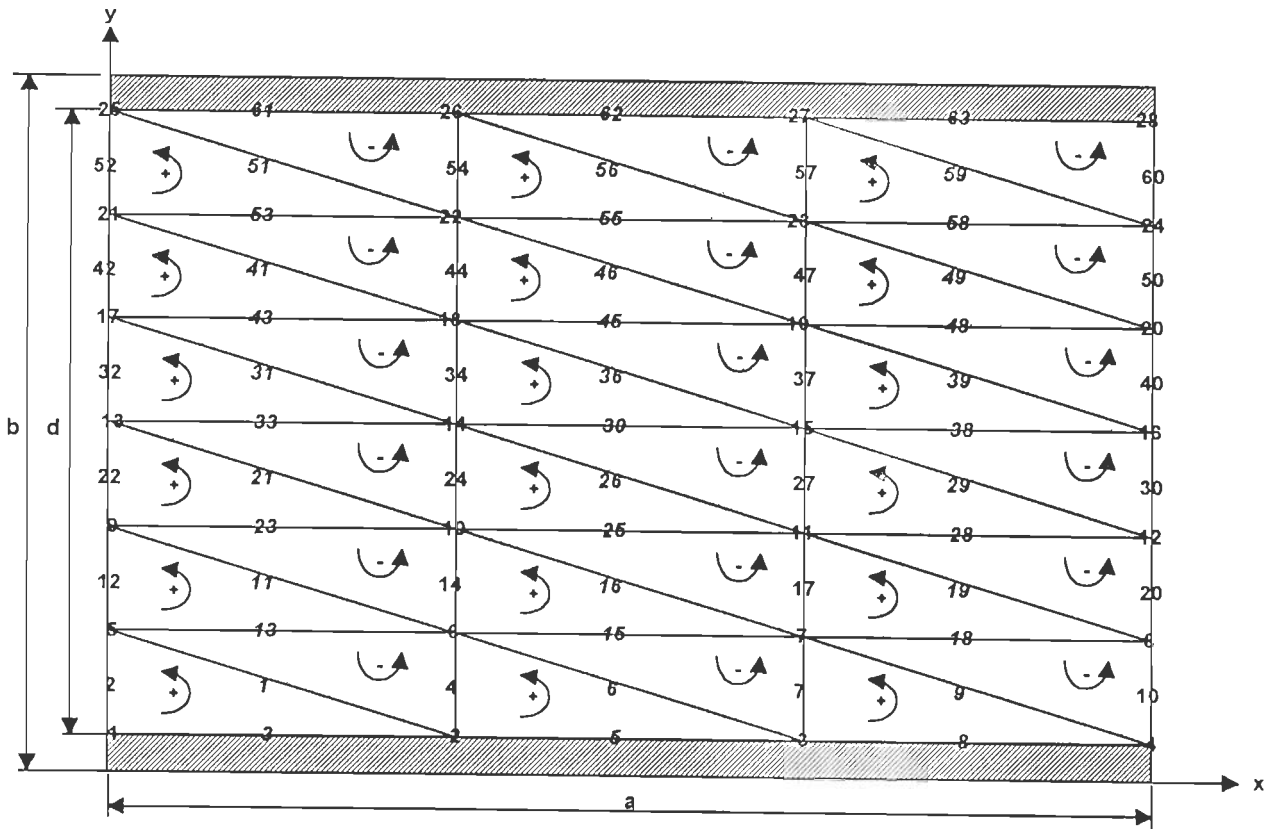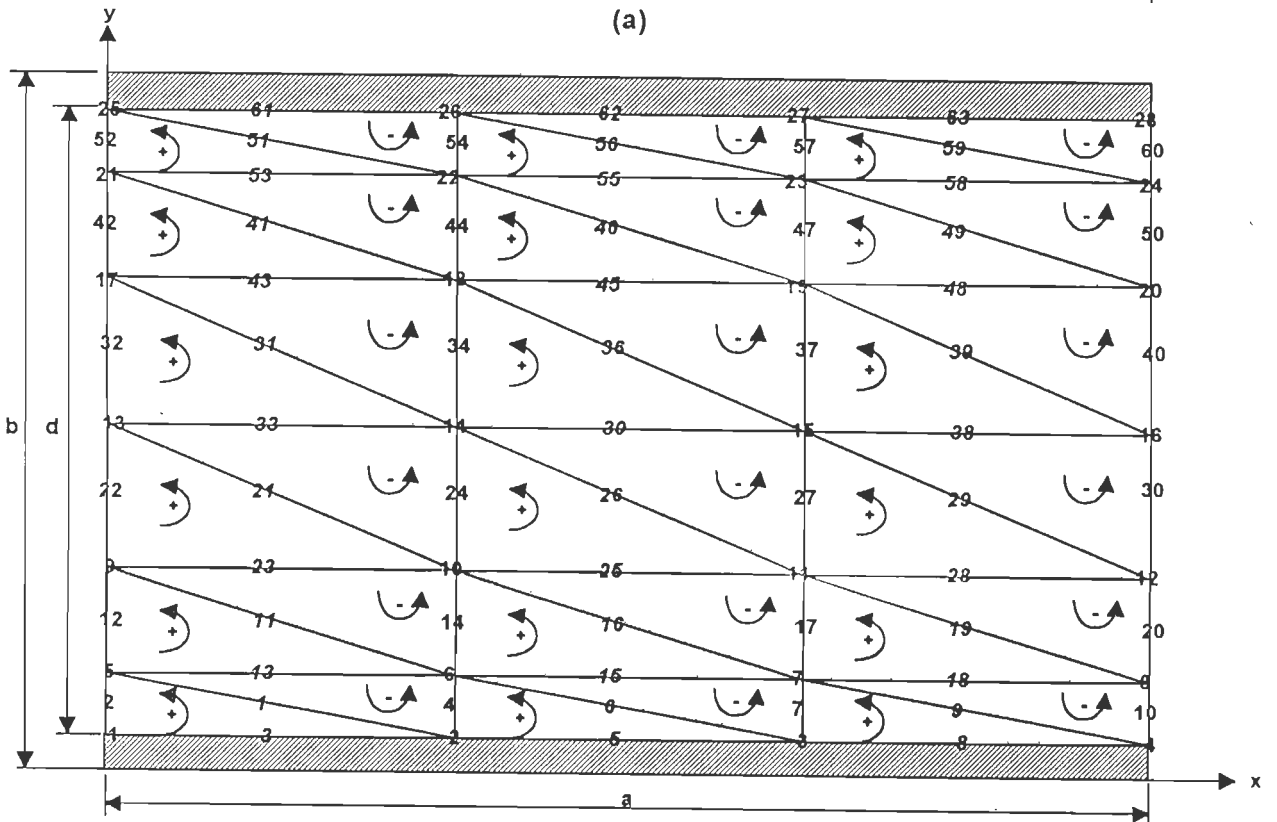
Fig. 5.8 : Symmetrical capacitive diaphragm discretization using
(a) uniform triangulation (b) non-uniform triangulation

166

Table - 5.2
Comparative Study of the Discretization Schemes of Figs. 5.7(a) and (b) on Capacitive Diaphragms

d/b	Modal Indices in eqn (4.8)		Susceptance B/Y_0 for Fig. 5.7(a)	Suscepatance B/Y_0 for Fig. 5.7(b)	Susceptance B/Y_0 Based on Method in [65]
	r	s			
0.15	1		1.126340	1.160609	
	2	120	1.165860	1.162150	1.1781
	3		1.173778	1.162340	
0.20	1		0.900500	0.9462218	
	2	90	0.933800	0.9623070	0.9525
	3		0.944049	0.9634770	
0.25	1		0.513980	0.78162	
	2	72	0.689200	0.78360	0.7799
	3		0.767304	0.78410	
0.30	1		0.75116	0.648977	
	2	60	0.66240	0.653120	0.6420
	3		0.62445	0.653360	
0.35	1		0.566700	0.53871	
	2	51	0.510900	0.54270	0.5270
	3		0.504813	0.54320	
0.40	1		0.44490	0.44570	
	2	45	0.42390	0.44720	0.4320
	3		0.40275	0.44810	
0.45	1		0.38690	0.36546	
	2	40	0.33720	0.36610	0.3543
	3		0.31626	0.36650	
0.50	1		0.2978	0.296171	
	2	36	0.2788	0.296201	0.2716
	3		0.2398	0.296222	

Table - 5.3
Summary of Convergence Test on Susceptance for Symmetrical Capacitive Diaphragms

d/b	No. Of Expn Functions	No. of Columns	Modal Indices in eqn. (4.8)		Capacitive Susceptance		Remarks on Discretization
			r	s	This Method	Classical Method [65]	
0.55	37	3	5	67	0.2251300		Uniform
	45	3	5	82	0.2245280	0.2225	
	61	3	5	111	0.2229000		
0.60	37	3	5	62	0.1742071		Uniform
	45	3	5	75	0.1720183	0.1720	
	61	3	5	102	0.1707970		
0.65	37	3	5	57	0.1346632		Uniform
	45	3	5	69	0.1303875	0.1293	
	61	3	5	94	0.1302260		
0.70	37	3	5	53	0.089085		Uniform
	45	3	5	64	0.088640	0.093299	
	61	3	5	87	0.088250		
0.75	37	3	5	49	0.0537050		Uniform
	45	3	5	60	0.0551863		
	61	3	5	81	0.0560120		
	77	3	5	102	0.0565670	0.06384	
	109	3	5	145	0.0708710		Non Uniform
	125	3	5	167	0.0690900		
	141	3	5	188	0.0677560		
	157	3	5	209	0.0667300		
0.80	37	3	5	46	0.0263300		Uniform
	45	3	5	56	0.0273900		
	61	3	5	76	0.0294700		
	77	3	5	96	0.0310700		
	93	3	5	116	0.0555900	0.04036	
	109	3	5	136	0.0466300		
	125	3	5	156	0.0451200		
	141	3	5	176	0.0433400		Non Uniform
	157	3	5	196	0.0433500		
0.85	45	3	5	53	0.0058840		Uniform
	61	3	5	72	0.0084440		
	77	3	5	91	0.0111899		
	93	3	5	109	0.0303169		
	109	3	5	128	0.0280340	0.022486	
	125	3	5	147	0.0267272		
	141	3	5	166	0.0255870		Non Uniform
	157	3	5	185	0.0232268		
	173	3	5	204	0.0232290		
0.90	61	3	5	68	0.0004098		Uniform
	77	3	5	86	0.0050040		
	93	3	5	103	0.0165640		
	109	3	5	121	0.0147910		
	125	3	5	139	0.0133656	0.009925	
	141	3	5	157	0.0123760		Non Uniform
	157	3	5	174	0.0104836		
	173	3	5	192	0.0099210		
0.95	93	3	5	98	0.0080400		Non Uniform
	109	3	5	115	0.0062530		
	125	3	5	132	0.0050800		
	141	3	5	148	0.0040940	0.002471	
	157	3	5	165	0.0020820		
	173	3	5	182	0.0012920		
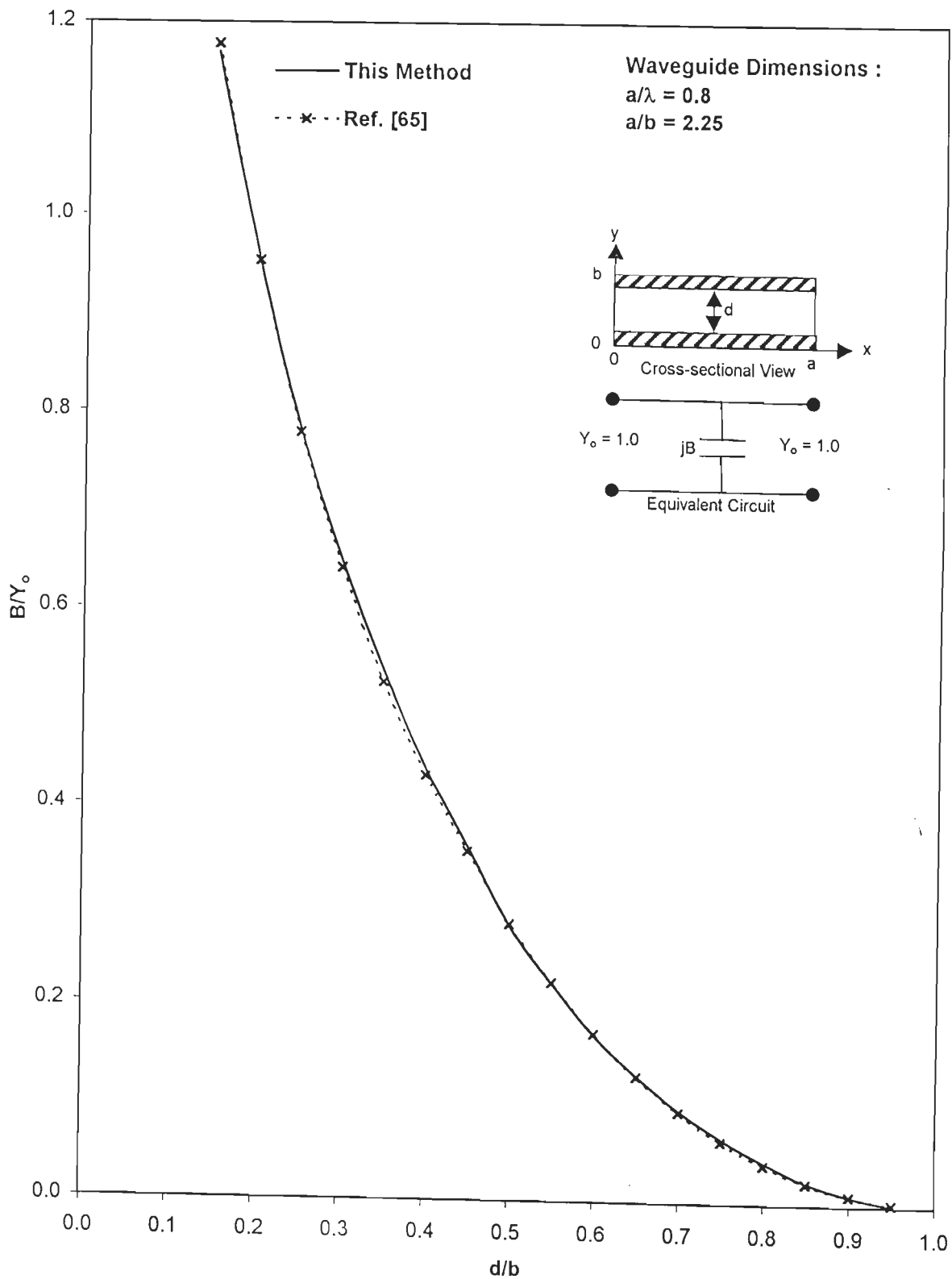
Fig. 5.9 :   Normalized susceptance B/Y$_o$ as a function of aperture size
for symmetrical capacitive diaphragms in
uniform rectangular waveguides.

169

Fig. 5.10 shows equivalent surface magnetic current M^x for $d/b = 0.2$ and 0.45. $|M^x|$ curves in Fig. 5.10(a) are seen to be symmetrical about the centre at which both have their peaks. Further, in both cases, the phase is constant. In Fig. 5.10(b), $|M^x|$ curves for $d/b = 0.2$ and 0.45 are similar in nature but their phase distributions are different.
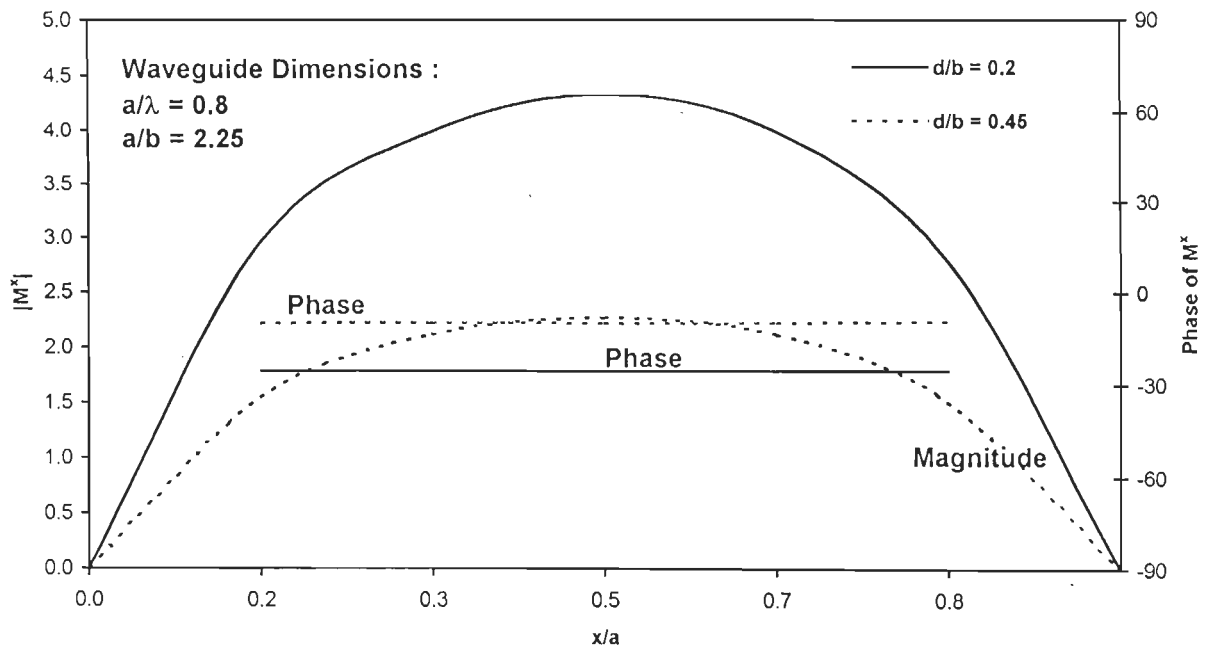
(a) y/b = 0.5
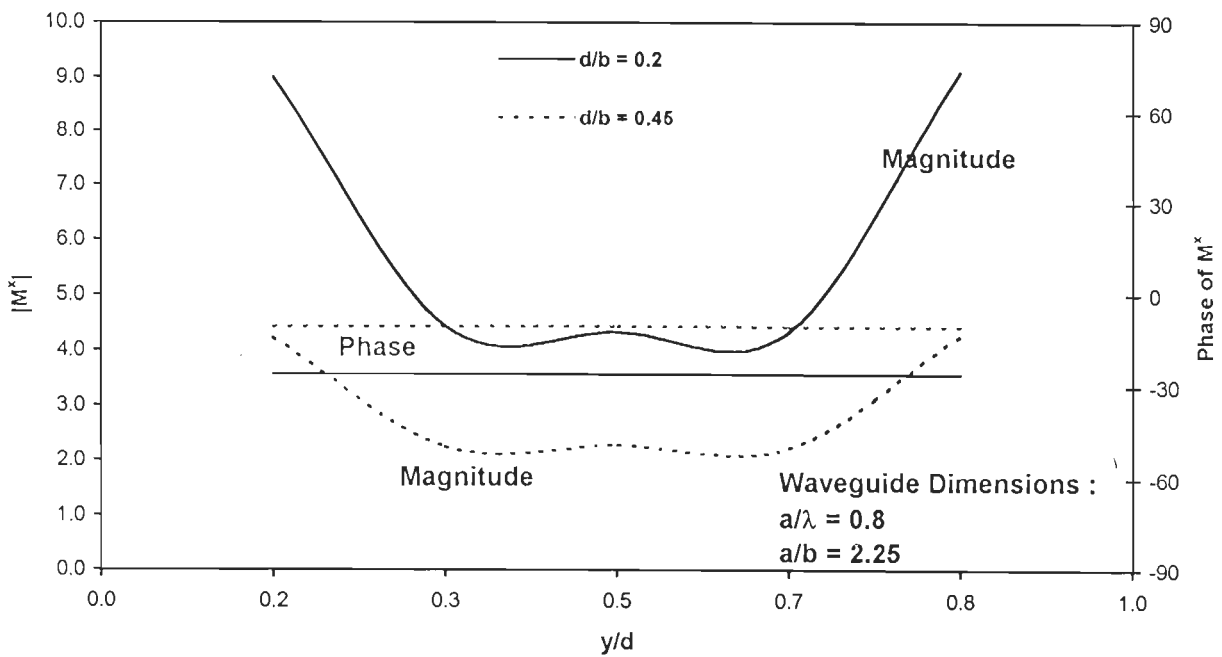
(b) x/a = 0.5

Fig. 5.10 : Equivalent surface magnetic current distributions
for symmetrical capacitive diaphragms
in uniform rectangular waveguides.

5.3-3 Centered Rectangular Diaphragm

In computing the susceptance of the rectangular diaphragm depicted in the inset of Fig. 5.11, we recognized that the aperture is situated only in a limited central region of the waveguide cross-section. Hence, based on the criteria developed in Sec. 5.2, it is only necessary to consider the number of non-boundary edges in the aperture discretization in a single row along the aperture axis in order to determine the modal indices r and s in Eqn. (4.8). For the present problem we used 45 expansion functions generated from a 3 x 6 row-column discretization of the aperture which resulted in 11 non-boundary edges on a single row along the aperture x-axis. Thus, according to Eqns. (5.11) and (5.12), $r = 33$ and $s = 5$ should yield converged results.

Fig. 5.11 compares our results for $r = 33$ and $s = 5$ with those obtained by Yang and Omar [113]. An excellent agreement is observed between the results, thus confirming the validity of criterion developed in section 5.2 for the selection of modal indices.
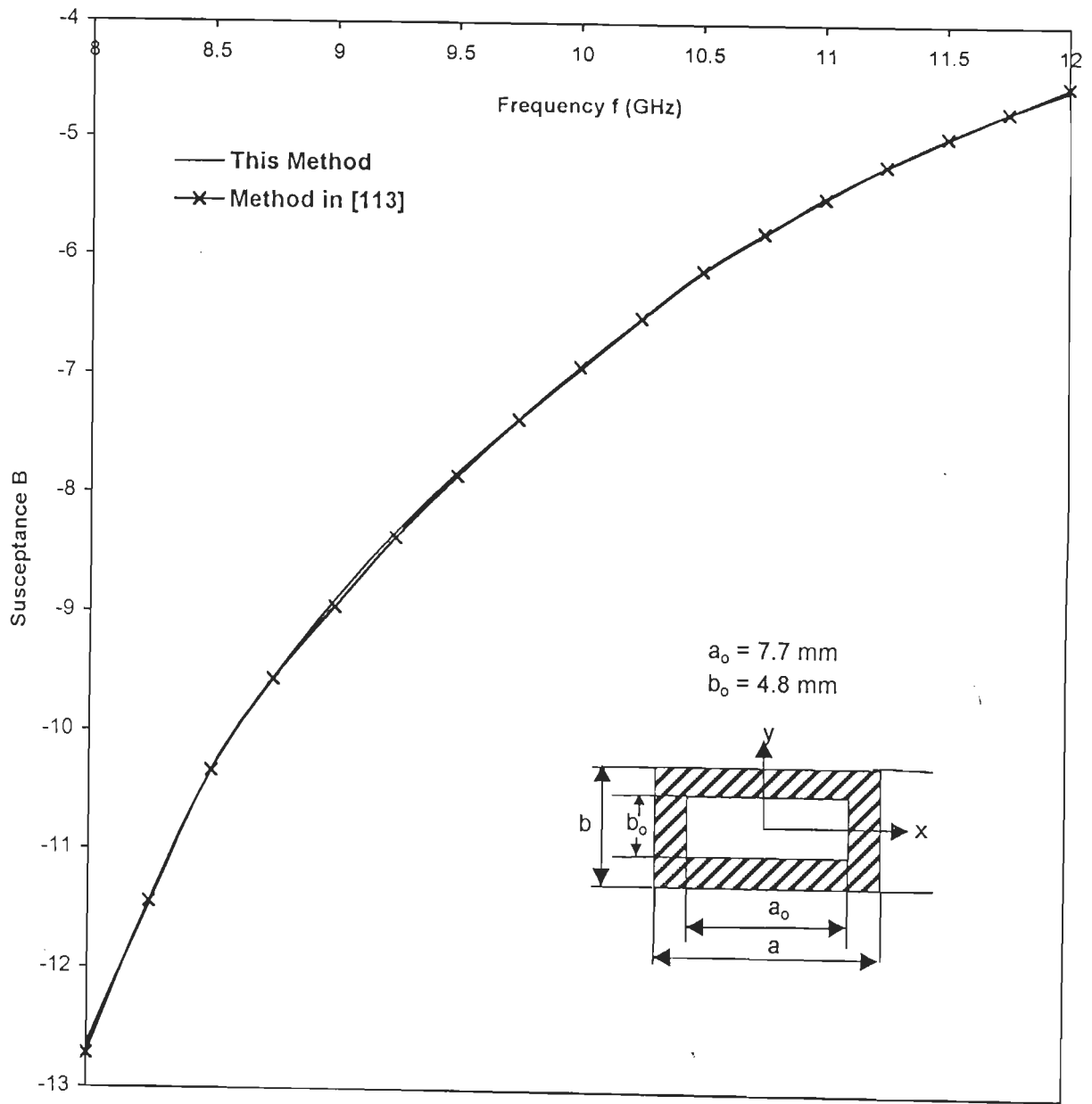
Fig. 5.11 : Normalized shunt susceptance as a function of frequency for a waveguide backed rectangular aperture

5.3-4 Centered Circular Diaphragms

Table 5.4 lists the values of B/Y_0 as a function of normalized diameter d/a in a uniform rectangular waveguide ($\lambda/a = 1.6$, $a/b = 2.25$). It is seen that our results converge closely to the data available in the literature [65].

Using the discretization scheme of Fig. 3.13 with 76 expansion functions, circular apertures in uniform rectangular waveguides of various dimensions were analyzed. Fig. 5.12 shows normalized susceptance B/Y_0 as a function of normalized diameter d/a for two different waveguides. The results for each waveguide are compared with the corresponding data in the literature and a good agreement is observed.

Fig. 5.13 shows equivalent surface magnetic current distributions corresponding to the circular aperture in waveguide with $\lambda/a = 1.25$ and $a/b = 2.25$. It is observed that for small aperture size ($d/a = 0.2$), the current distribution is fairly uniform along x with very small variations along y-direction. However, for bigger apertures ($d/a = 0.4$), the current exhibits large variation over the aperture.

Table - 5.4
Convergence Test Results for Thin, Centrally Located Circular Diaphragms in Uniform Rectangular Waveguide ($a/\lambda = 0.625$, $a/b = 2.25$)

d/a	Aperture Area (x 10^{-6} m^2)	Computed Area (x 10^{-6} m^2)	No. of Expn. Functions	Modal Indices in eqn. (4.8)		Computed Susceptance B/Y_o	Classical Method [65] B/Y_o
				r	s		
0.10	4.1043	4.1011	20	50	26	-616.64	-
		4.0639	48	90	38	-614.88	
		4.0687	76	110	36	-587.92	
		4.0689	128	150	54	-582.43	
0.15	9.2350	9.2240	20	33	16	-183.71	-
		9.3018	48	60	24	-176.11	
		9.2340	76	73	24	-171.51	
		9.2370	128	100	36	-169.92	
0.20	16.4170	16.5040	48	45	18	-73.85	-68.0
		16.4220	76	55	18	-70.80	
		16.418	128	75	26	-70.34	
0.25	25.6210	25.5970	48	36	14	-36.54	-34.0
		25.6370	76	44	14	-35.59	
		25.6280	128	60	24	-34.78	
0.30	36.9389	36.9390	48	30	12	-20.58	-18.75
		36.9390	76	37	10	-18.61	
		36.9370	128	50	14	-18.01	
0.35	50.2781	50.2420	48	26	10	-12.69	-11.35
		50.2860	76	31	28	-12.48	
		50.2730	128	43	18	-12.30	
0.40	65.6693	65.5920	48	23	6	-8.47	-7.5
		65.5960	76	28	8	-8.44	
		65.5720	128	38	14	-8.36	

Fig. 5.12 : Normalized susceptance B/Y_o as a function of aperture size for centered circular diaphragms in uniform rectangular waveguides
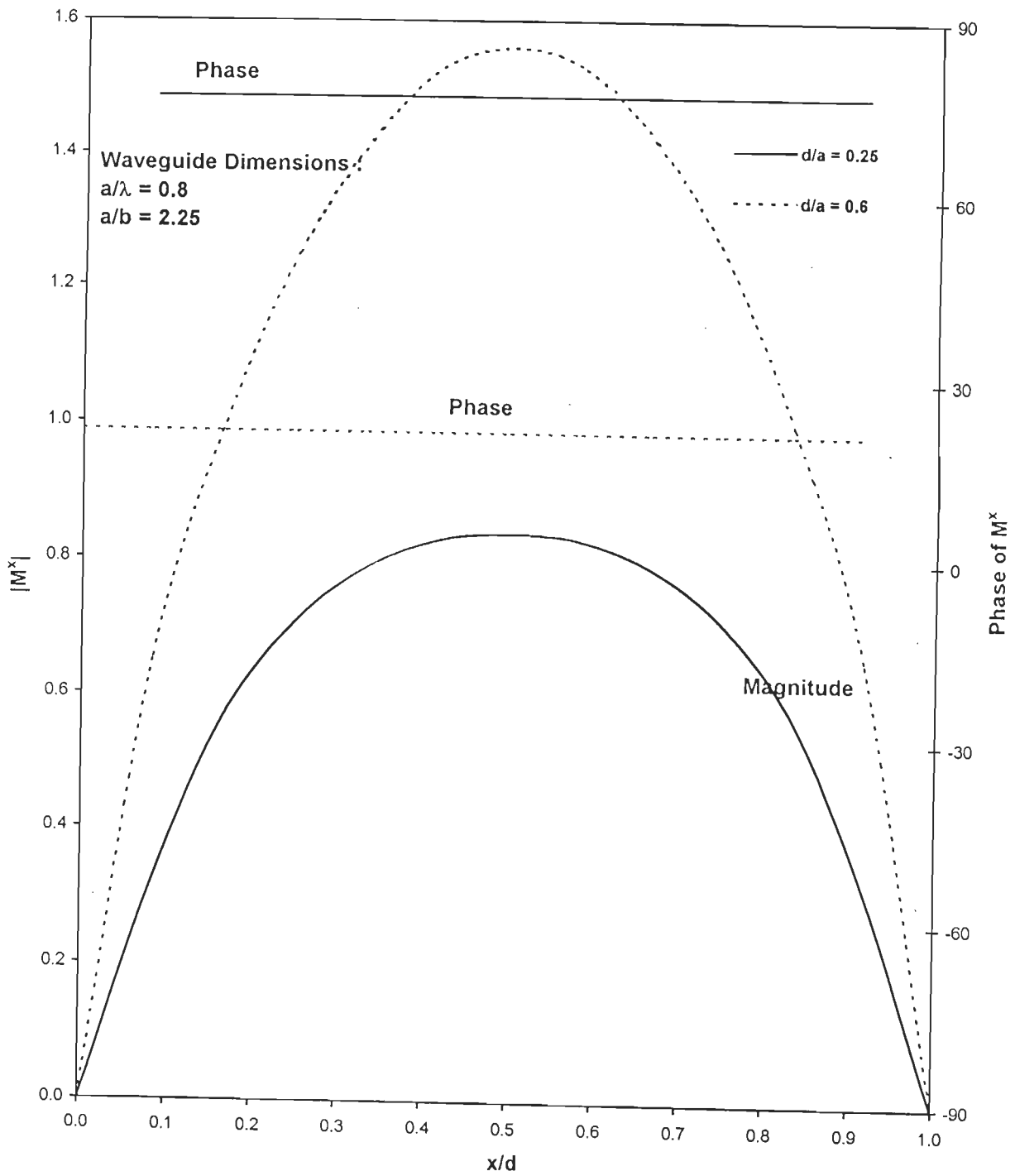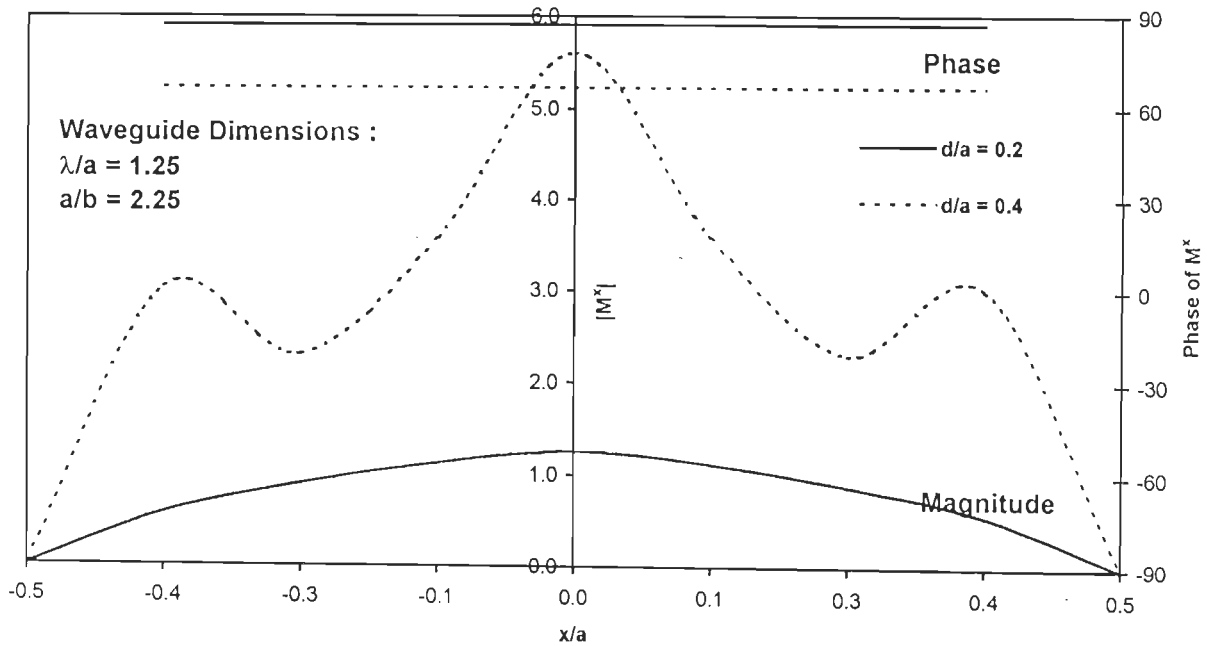
(a) y/d = -0.125
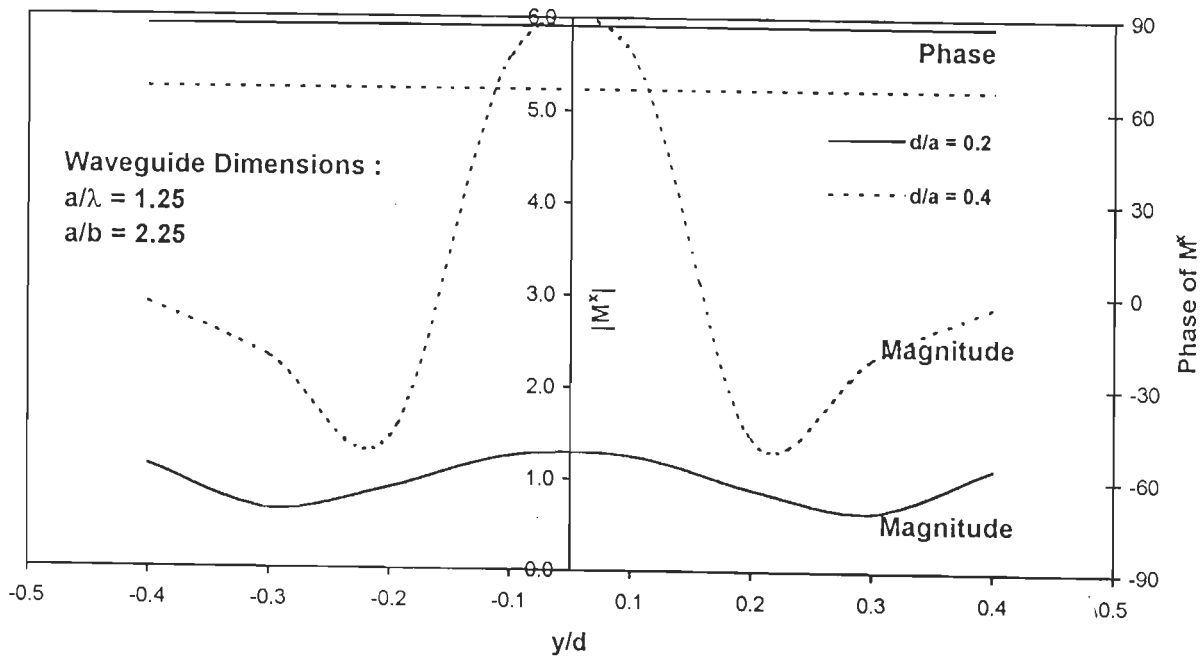
(b) x/a = 0.0

Fig. 5.13 : Equivalent surface magnetic current distributions for centered circular diaphragms in uniform rectangular waveguides.

5.3-5 Centered Elliptical Diaphragms

The geometrical parameters of elliptic apertures are shown in inset of Fig. 5.14.

Table 5.5 shows the results of convergence test on susceptance B/Y_o for various eccentricities e (according to eqn. (3.29)). The results converge closely to the data available in the literature [65], further underscoring the flexibility of our computer code and the validity of the modified criterion. The results that follow were based on the triangulation scheme similar to the one shown in Fig. 3.18 consisting of 76 interior edges. Fig. 5.14 shows normalized susceptance B/Y_o as a function of eccentricity e. A good agreement is obtained between these results and the data in [65].

Fig. 5.15 shows equivalent surface magnetic current distributions at $y/d_2 = -0.125$ and $x/d_1 = 0.0$ in (a) and (b), respectively, corresponding to e = 0.6 and e = 0.9. In Fig. 5.15(a), it is observed that in the larger diaphragm (e = 0.6), the current is maximum at the centre and falls gradually to zero at the aperture edges. However, the current distribution corresponding to e = 0.9 exhibits three peaks : one at the centre of the aperture and the higher peaks which are symmetrically located on either side of the centre. The phase distribution is, however, uniform for both cases.

Similarly, Fig. 5.15(b) shows that the distribution of M^x along the y-direction at the aperture centre exhibits entirely different behaviours for the two different values of e.

Table - 5.5
Convergence Study on Susceptance B/Y_0 for Various Eccentricities of Elliptic Apertures.

d_1/a	Eccentricity e	Actual Area x 10^{-5} m^2	Computed Area x 10^{-5} m^2	No. of Expn. Functions	Modal Indices in eqn. (4.8)		This Method B/Y_0	Method in [65] B/Y_0
					r	s		
0.2	0.2	1.60855	1.6080	20	25	6	-41.60	-37.20
			1.6045	48	45	12	-41.40	
			1.6051	76	55	24	-40.59	
	0.3	1.56610	1.5658	20	25	12	-43.40	-42.60
			1.5650	48	45	18	-41.20	
			1.5633	76	55	27	-41.16	
	0.4	1.50467	1.5042	20	25	12	-44.70	-44.66
			1.5046	48	45	20	-43.64	
			1.5047	76	55	24	-42.37	
	0.5	1.42179	1.4233	20	25	14	-46.83	-46.66
			1.4217	48	45	14	-46.73	
			1.4261	76	55	24	-46.41	
			1.4217	156	75	26	-46.20	
	0.6	1.31339	1.3131	48	45	14	-48.93	-50.20
			1.3127	76	55	30	-47.14	
			1.3142	156	75	38	-47.09	
	0.7	1.17243	1.1724	48	45	18	-53.51	-56.00
			1.1768	76	55	26	-51.02	
			1.1717	156	75	44	-51.03	
	0.8	0.98504	0.98503	48	45	30	-55.999	-63.70
			0.98519	76	55	42	-56.74	
			0.98501	156	75	52	-57.39	
	0.9	0.71562	0.71562	48	45	42	-66.01	-78.50
			0.71568	76	55	32	-70.47	
			0.71595	156	75	72	-70.55	
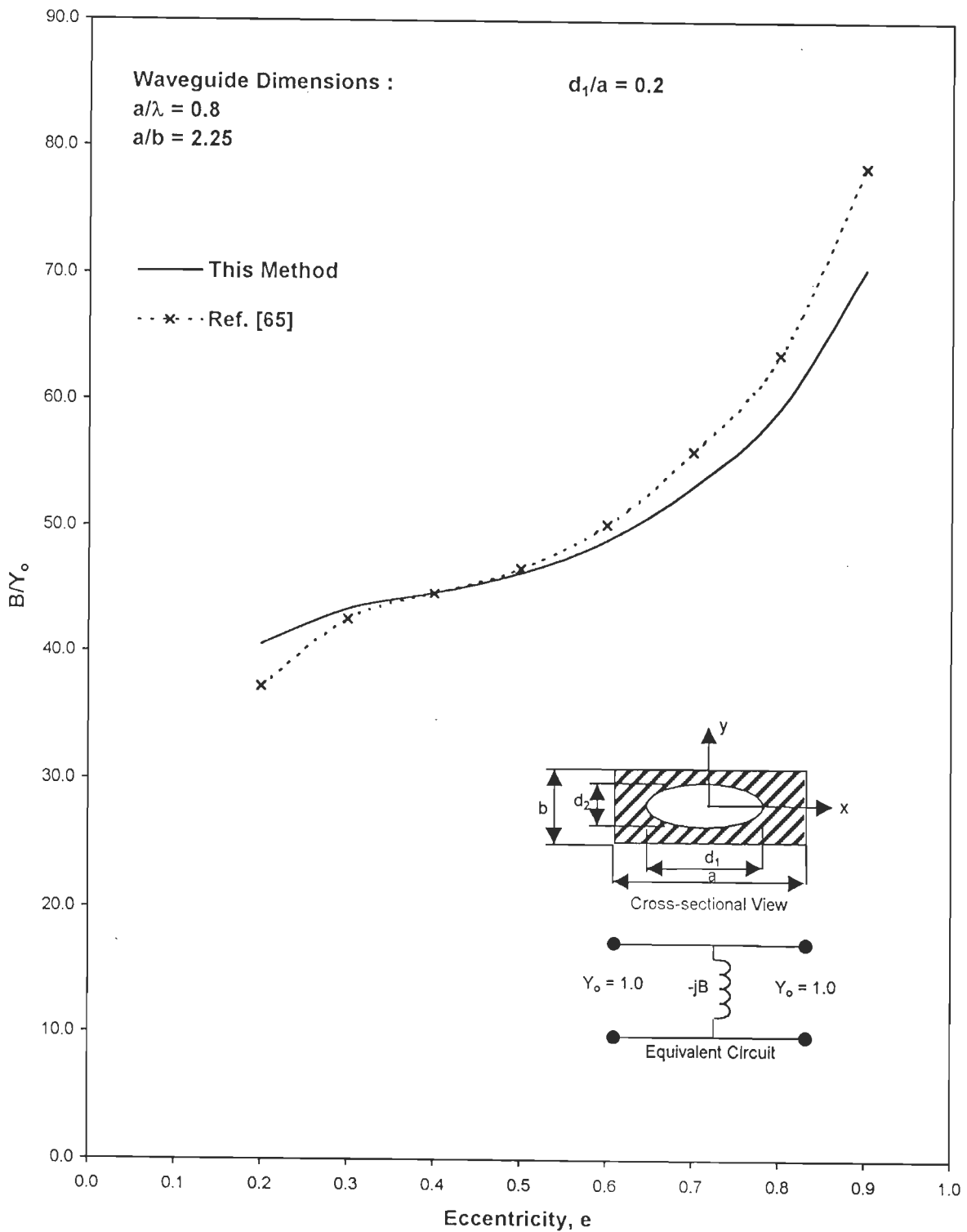
Fig. 5.14 : Normalized susceptance B/Y_o as a function of eccentricity for centered elliptical diaphragms in uniform rectangular waveguides.
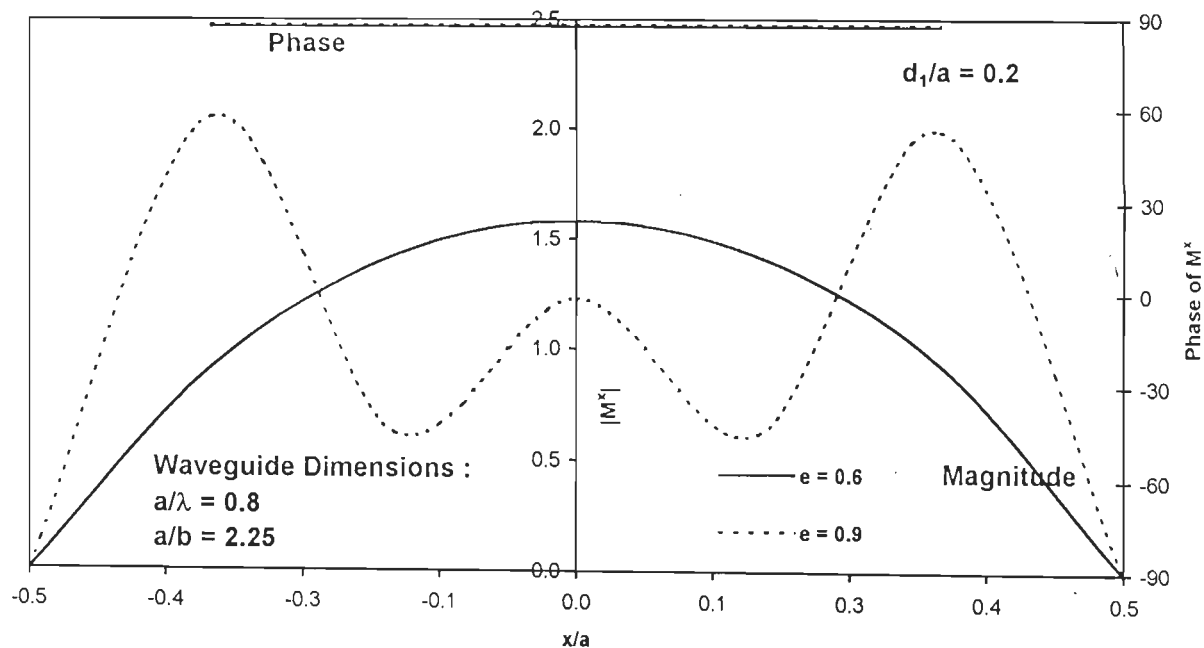
(a) $y/d_2 = -0.125$
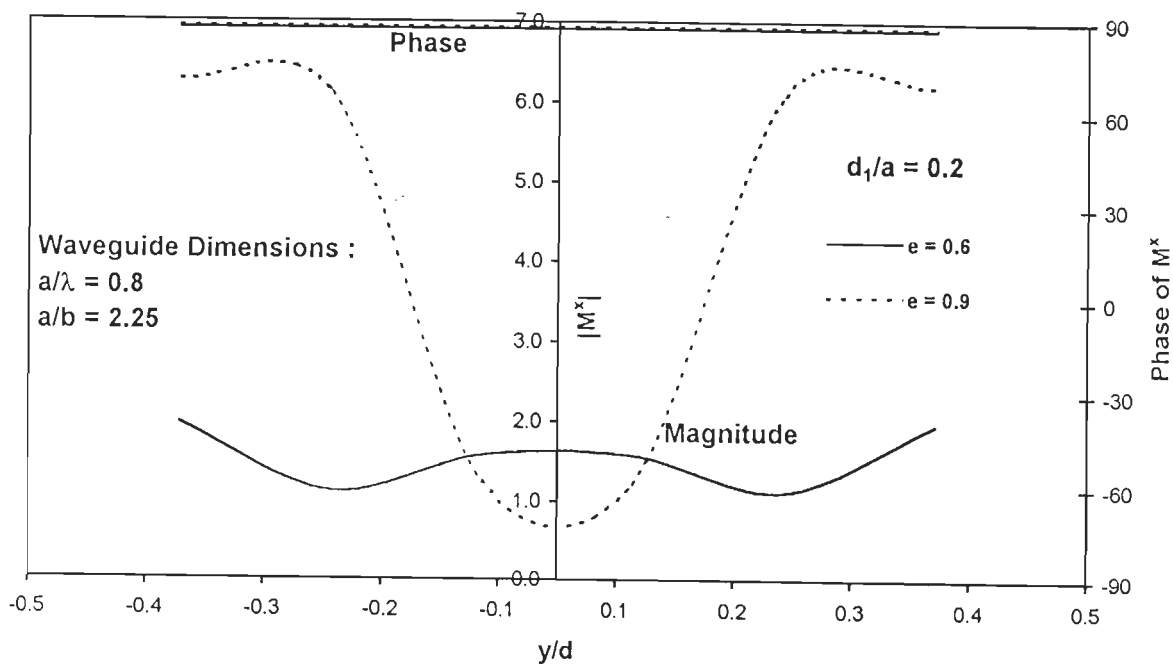
(b) $x/d_1 = 0.0$

Fig. 5.15 : Equivalent surface magnetic current distributions for centered elliptical diaphragms in uniform rectangular waveguides.

181

5.3-6 Centered Diamond-shaped Diaphragms

The inset in Fig. 5.16 shows the geometrical parameters of the aperture.

Results that follow were obtained using 88 expansion function based on the triangulation scheme in Fig. 3.25.

Fig. 5.16 shows susceptance B/Y_o as a function of discontinuity length L/λ. It is observed that for $0.2 \leq L/\lambda \leq 0.49$, the diaphragm exhibits inductive susceptance but becomes capacitive for $L/\lambda > 0.49$. Thus, the susceptance for diamond-shaped diaphragm exhibits a transition from inductive nature to capacitive.

Fig. 5.17 shows equivalent surface magnetic current distributions at $y/h = -0.125$ and $x/L = 0.0$, respectively, in Fig. 5.17(a) and (b) for $L/\lambda = 0.2$ and 0.6. It is seen that $|M^x|$ corresponding to $L/\lambda = 0.2$, in which the angle formed on the x-axis is obtuse, varies gradually from its peak value at the centre of the aperture and the phase distribution is uniform over the aperture. On the other hand, for $L/\lambda = 0.6$, in which the angle is acute, the current is largely confined to the region at the vicinity of the aperture centre. For $x/L > 0.2$, the current magnitude is nearly zero. In Fig. 5.17(b) which shows the distribution of M^x as a function of y, it is found that the curve for $L/\lambda = 0.2$ has a broader peak with a corresponding constant phase distribution. The distribution corresponding to $L/\lambda = 0.6$, on the other hand, exhibits a narrow peak and its corresponding phase is non-uniform.
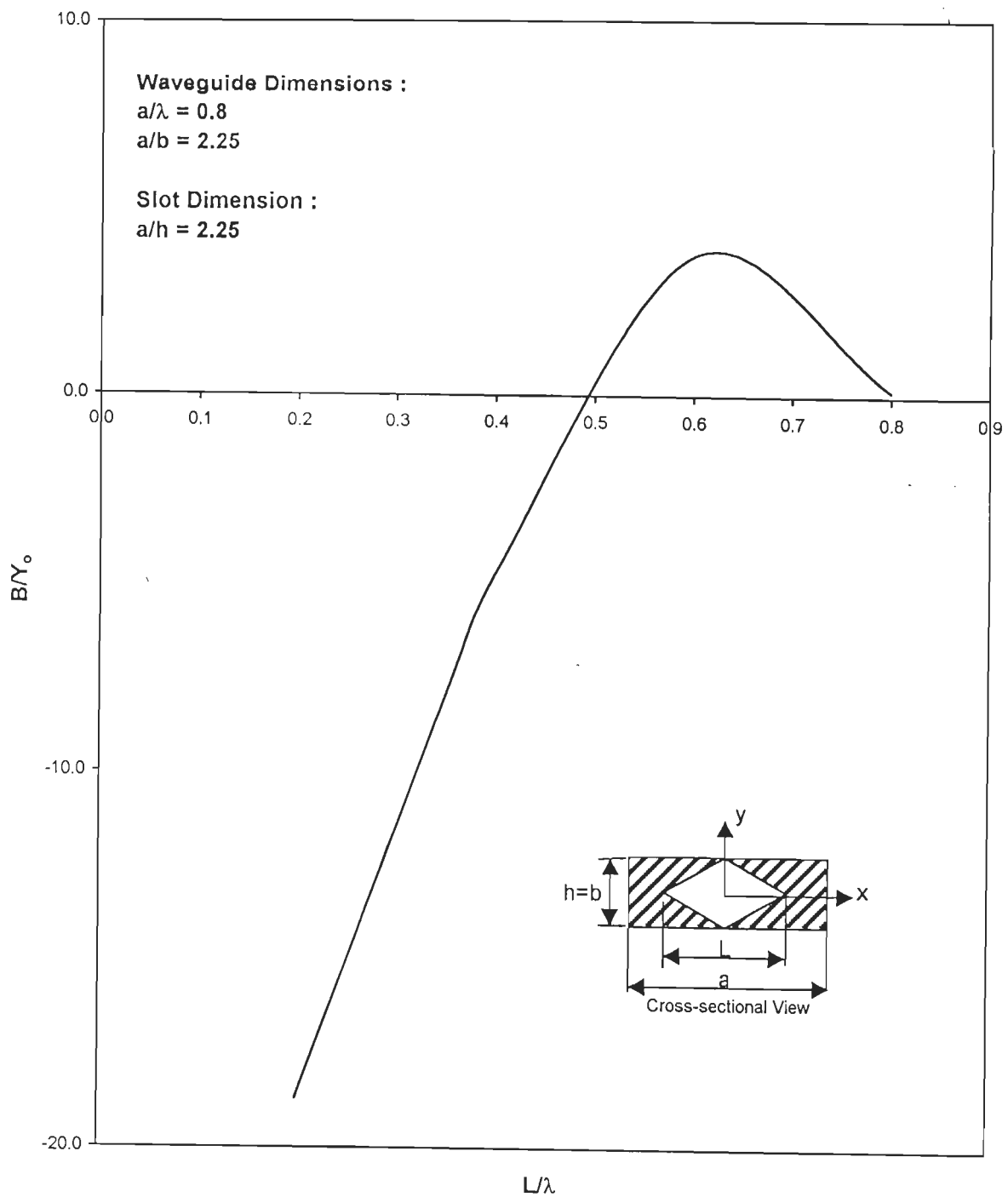
Fig. 5.16 : Normalized susceptance B/Y_o as a function of length L/λ for centered diamond-shaped diaphragms in uniform rectangular waveguides.
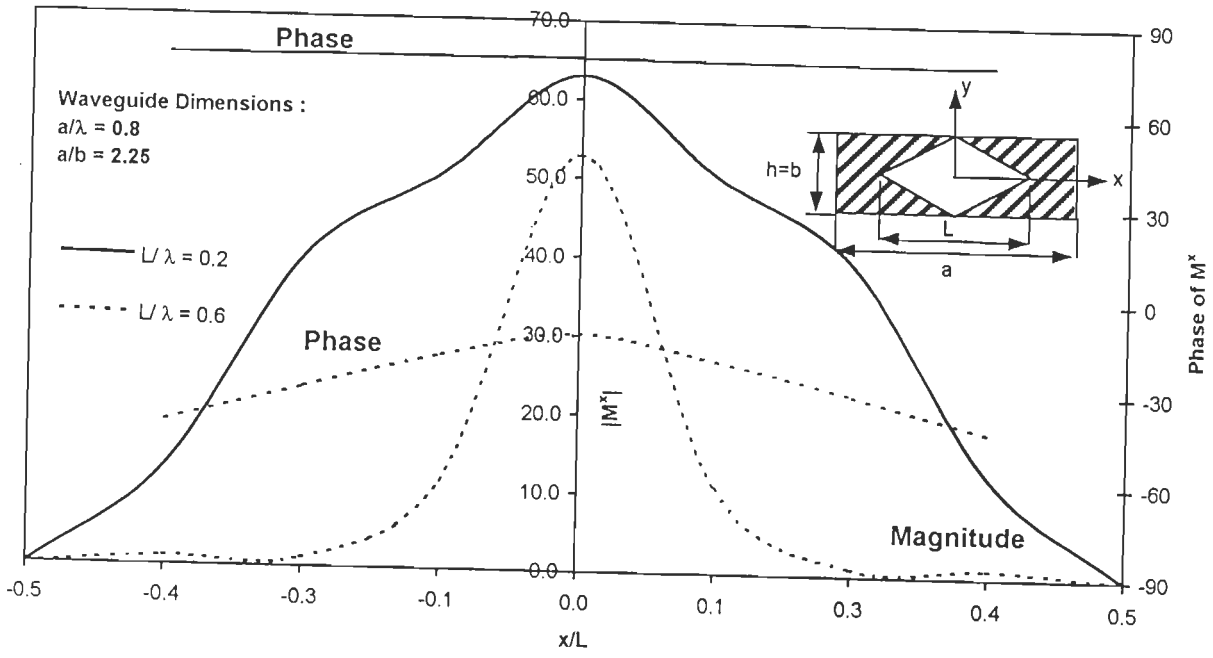
(a) y/h = -0.125
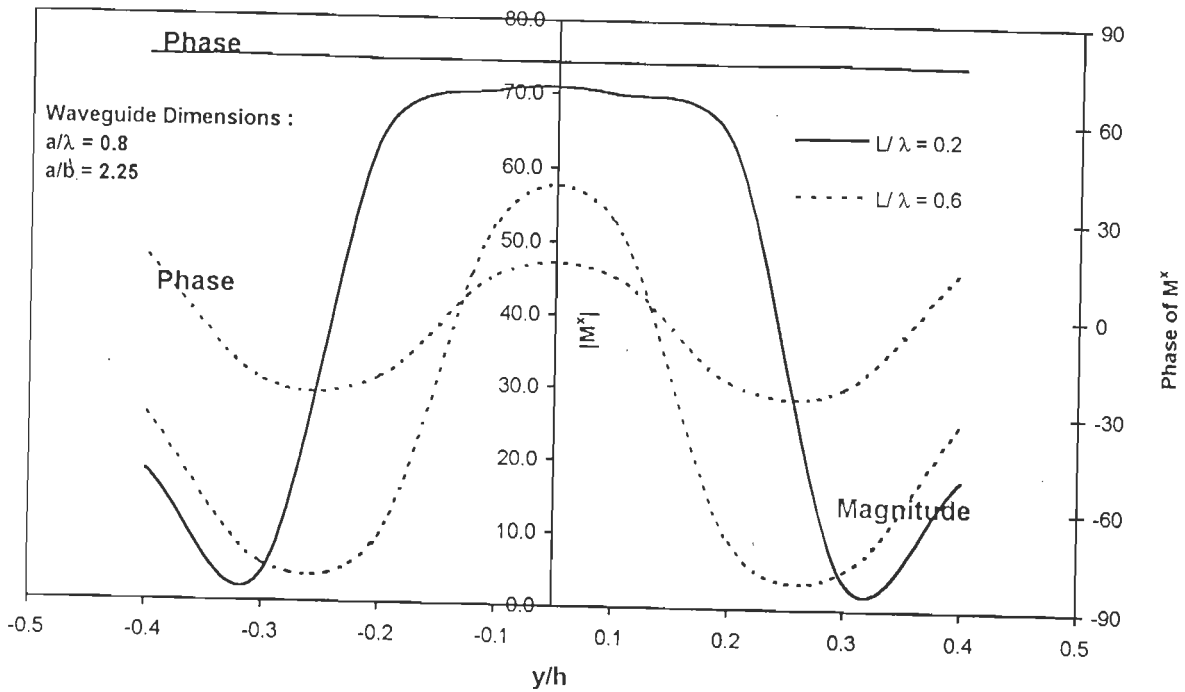
(b) x/L = 0.0

Fig. 5.17 : Equivalent surface magnetic current distributions for centered diamond-shaped diaphragms in Uniform Rectangular Waveguides.

184

5.3-7 Centered Cross-shaped Diaphragms

The geometrical parameters of the slot are shown in the inset of Fig. 5.18. The discretization scheme for the diaphragm is shown in Fig. 3.28 having 68 interior edges. In Fig. 5.18 shunt susceptance B/Y_o is shown as a function of slot length L/λ for fixed values of h and A_w. It is noted that B/Y_o increases sharply for $0.2 \le L/\lambda \le 0.3$ then decreases for $0.3 \le L/\lambda \le 0.44$ and thereafter increases again, changing from inductive nature to capacitive one for $L/\lambda > 0.44$. The reason for decrease in B/Y_o between $L/\lambda = 0.3$ and $L/\lambda = 0.44$ is postulated to be due to the slot experiencing resonance conditions at $L/\lambda = 0.3$ and at $L/\lambda = 0.44$.

The equivalent shunt susceptance curve shown in Fig. 5.18 has one similarity with that of diamond-shaped diaphragm shown in Fig. 5.16; both exhibit a transition from inductive susceptance to capacitive one.

Fig. 5.19 shows equivalent surface magnetic current distributions over the aperture. In Fig. 5.19(a) $|M^x|$ curves corresponding to $L/\lambda = 0.2$ and $L/\lambda = 0.4$ show minima at the slot centre, as expected. However, the curve corresponding to $L/\lambda = 0.3$ shows a maxima; a behaviour which our earlier results on these slots do not support. It is for this reason that we postulate that resonance must be occurring at this slot length. The phase curves corresponding to $L/\lambda = 0.2$ and $L/\lambda = 0.4$ are constant while that corresponding to $L/\lambda = 0.3$ is non-uniform, varying rapidly towards the slot ends. In Fig. 5.19(b), the current is maximum at the centre of the slots, as expected, based on the previous results of Fig. 4.22.
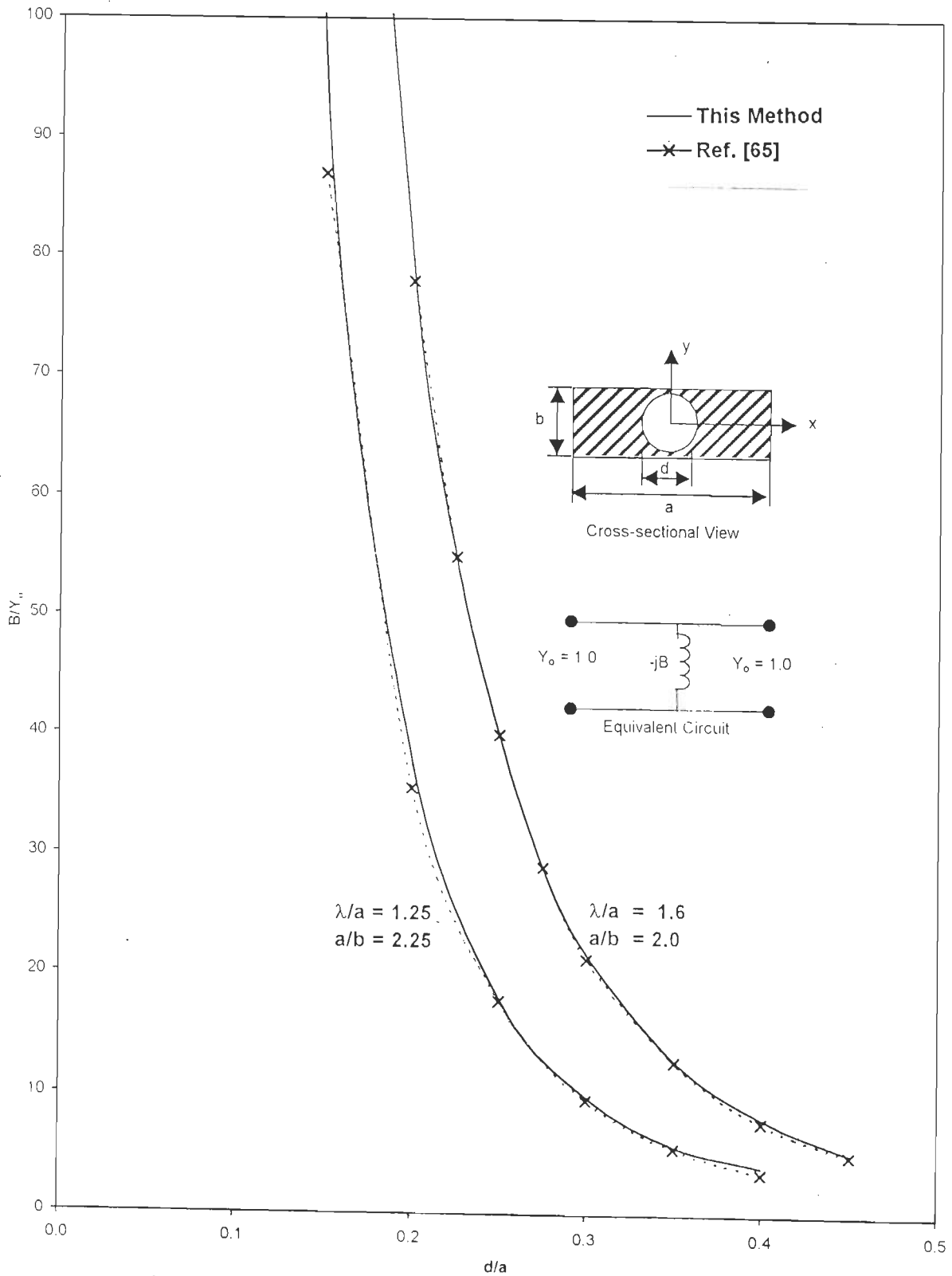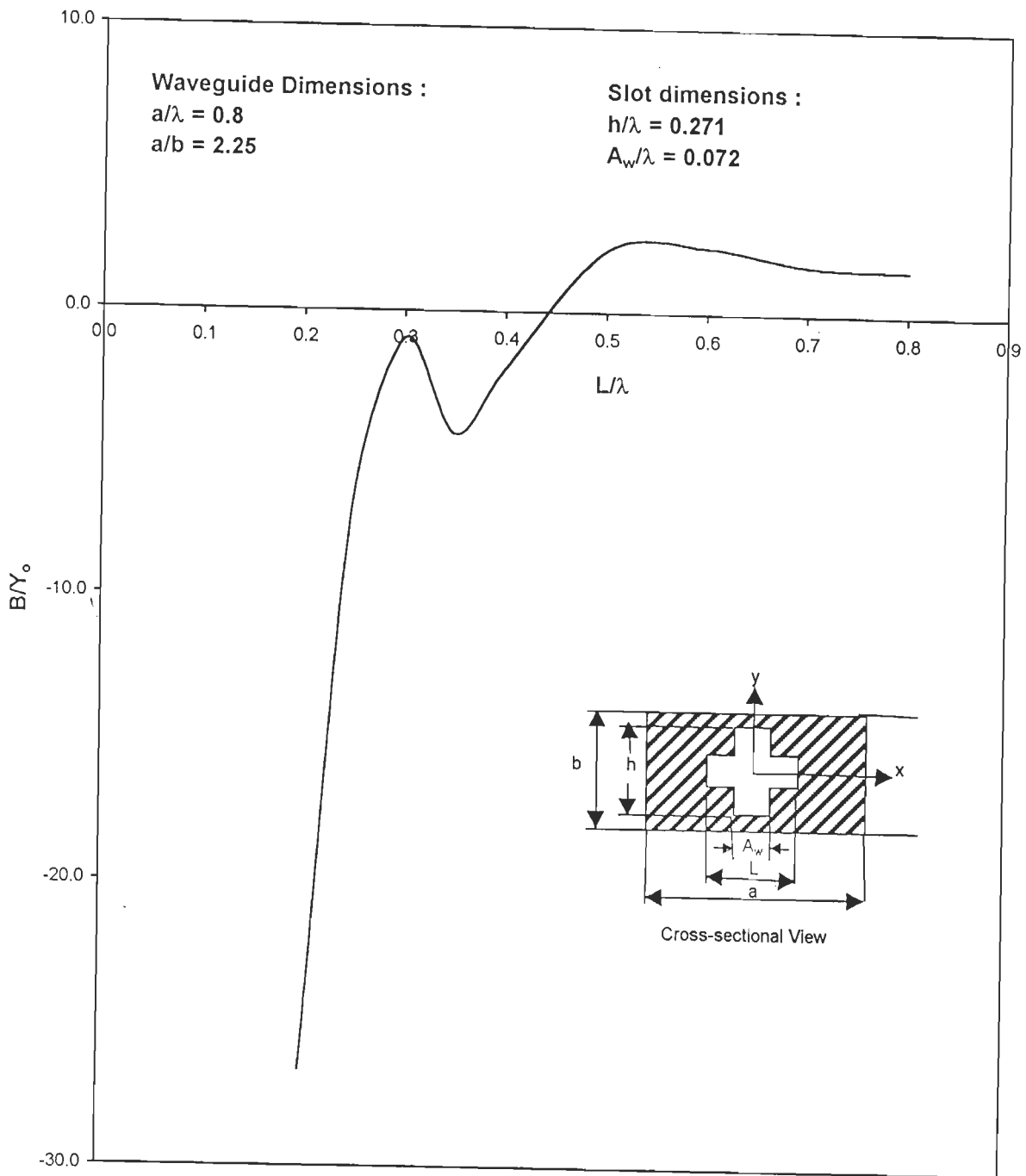
Fig. 5.18 : Normalized susceptance B/Y$_o$ as a function of length L
for centered cross-shaped diaphragms in
uniform rectangular waveguides.
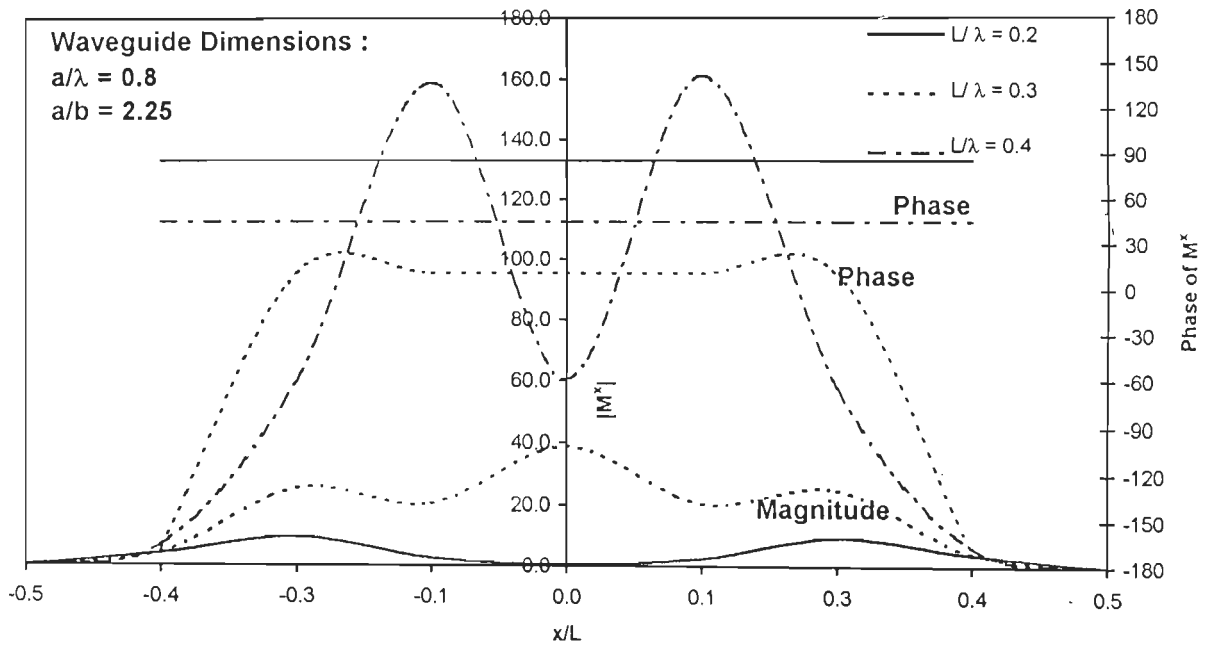
(a) y/h = -0.0125
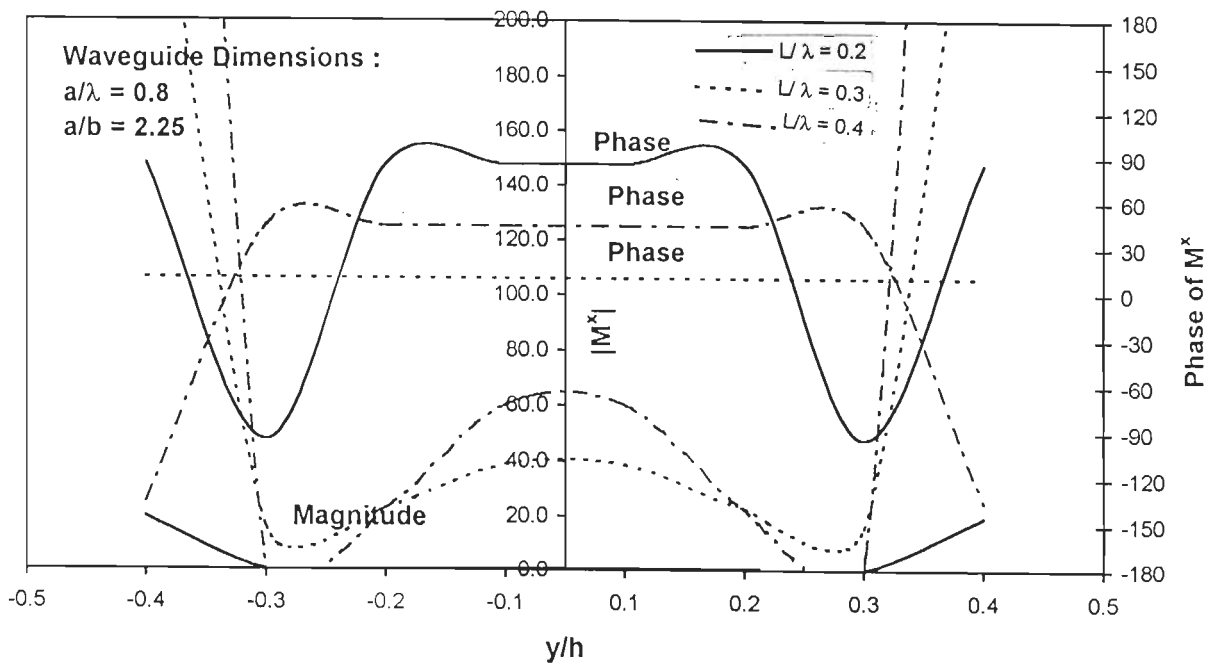
(b) x/L = 0.0

Fig. 5.19 : Equivalent surface magnetic current distributions for centered cross-shaped diaphragms in uniform rectangular waveguides.

187

5.4 SUMMARY

In this chapter, a numerical study on apertures of various shapes in the transverse cross-section of rectangular waveguides has been undertaken. A criterion for computing discontinuity solutions has been proposed and implemented using our computer program. The computer code has been validated by considering inductive, capacitive, circular and elliptical diaphragms. All results have been tested for convergence by using sufficient number of expansion functions.

Results have been presented for normalized shunt susceptance and magnetic current distribution of various diaphragms.

Chapter - 6

BROADWALL RADIATING SLOTS OF ARBITRARY SHAPE IN A RECTANGULAR WAVEGUIDE

Although there is substantial data available in the literature pertaining to waveguide broadwall slots, notably in [33], [50], [51], [63], [89], [102] and [108], the data are mostly given for rectangular slots. Data for slots and apertures of other shapes are lacking because PWS functions and rooftop functions, which are often used in the Moment Method analysis, are not flexible enough to deal with slots of arbitrary shape.

In this chapter, radiation characteristics of broadwall slots/apertures of arbitrary shape in a rectangular waveguide are investigated. The general formulation developed in Chapter 2 has been specialized to this problem.

In the subsequent sections, the waveguide matrices, electric vector and magnetic scalar potentials have been evaluated. Further, expressions for computing scattering parameters and radiated power have been derived and incorporated into our computer code. Although the formulation is completely general and can be used for analysing waveguide-to-waveguide coupling, waveguide-to-cavity coupling, etc., here only limited results for radiating slots have been presented and more detailed investigations are left for future workers.

6.1 FORMULATION

Fig. 6.1 illustrates the general problem of coupling between a rectangular waveguide and an arbitrary region via an arbitrary shaped aperture located in the broadwall. The waveguide walls have been assumed to be infinitesimally thin.

As described in the general formulation of Chapter 2, equivalence principle is used to divide the problem into two separate parts, as shown in Fig. 6.2.
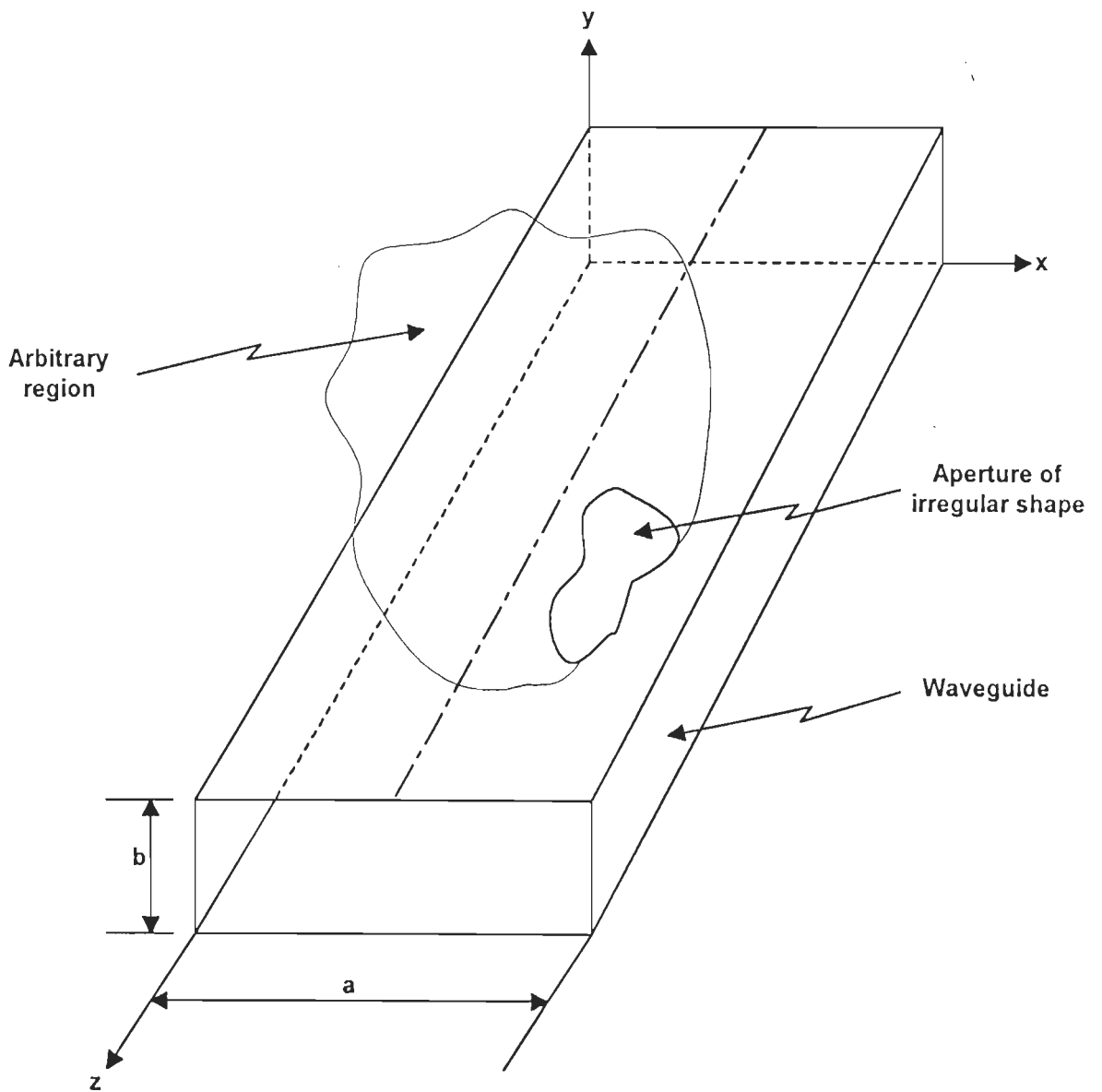
Fig. 6.1 : General problem of a rectangular waveguide coupling to an arbitrary region via an arbitrarily-shaped aperture in the broadwall.
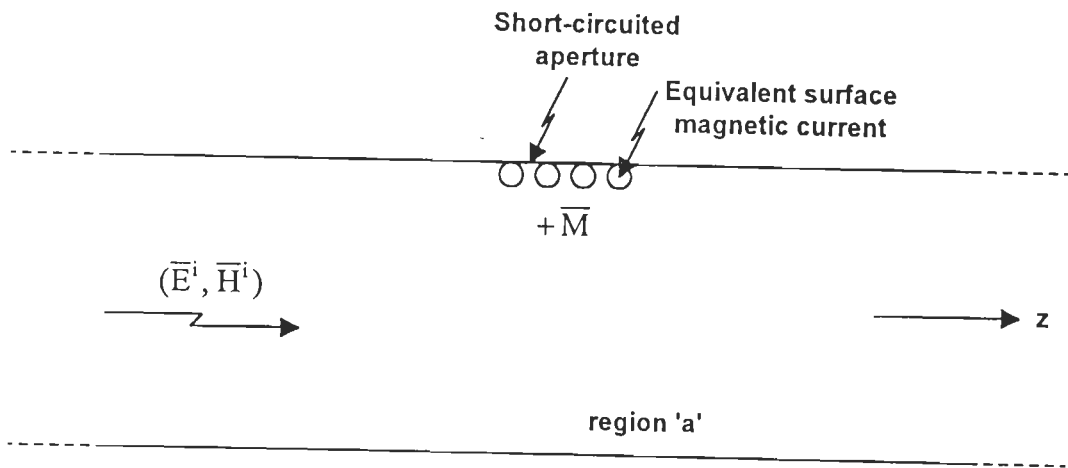
Short-circuited
aperture

Equivalent surface
magnetic current

$+\overline{M}$

$(\overline{E}^i, \overline{H}^i)$

z

region 'a'

(a) Equivalent problem valid for region 'a'

region 'b'

X X X X
$-\overline{M}$

Conducting
plane

(b) Equivalent problem valid for region 'b'

$-2\overline{M}$

X X X X X
X X X X X

Image
plane
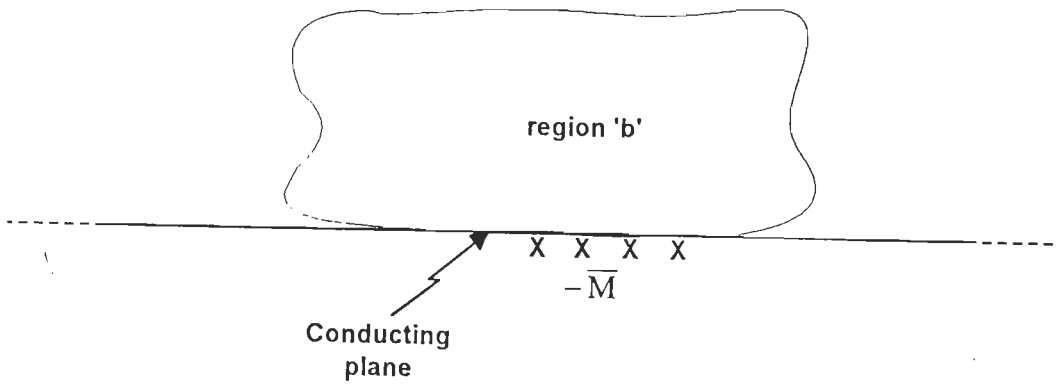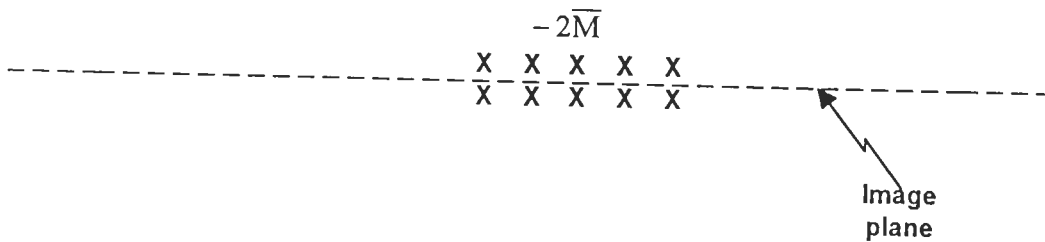
(c) Equivalent problem valid for region 'b',
when region 'b' is half-space

Fig. 6.2 : Equivalent models.

In Fig. 6.2(a), region 'a' is a uniform waveguide in which the total field is the superposition of the field due to the impressed sources $(\overline{E}^i, \overline{H}^i)$ and that due to equivalent surface magnetic current $\overline{M}$ over the aperture region. In region 'b' (Fig. 6.2(b)), which is arbitrary, the field is due to current $-\overline{M}$ over the aperture region, radiating in the presence of a continuous conductor. For the special case under consideration, where region 'b' is a half-space, image theory can be invoked and the equivalent problem for region 'b' reduces to the problem of a current $-2\overline{M}$ over the aperture region radiating in free space.

From eqns. (2.8) and (2.9), the aperture admittance matrices for region 'a' and region 'b' can be written as

$$[Y^a] = [Y^{wg}] = [<M_m, H_t^a(\overline{M}_n)>]_{N \times N} \tag{6.1}$$

$$[Y^b] = [Y^{hs}] = [<M_m, H_t^b(\overline{M}_n)>]_{N \times N} \tag{6.2}$$

and excitation vector $\vec{I}_m$ as

$$\vec{I}_m = [<M_m, -H_t^i>]_{N \times 1} \tag{6.3}$$

The elements of admittance matrices and excitation vector have been derived in Chapter 2 (eqns. (2.21) and (2.24), respectively) and are repeated here for the sake of completeness

$$Y_{mn}^{wg} = -l_m \left\{ j\omega \left[\overline{F}_n^a(\overline{r}_m^{c+}) \bullet \frac{\overline{\rho}_m^{c+}}{2} + \overline{F}_n^a(\overline{r}_m^{c-}) \bullet \frac{\overline{\rho}_m^{c-}}{2} \right] + \phi_n^a(\overline{r}_m^{c-}) - \phi_n^a(\overline{r}_m^{c+}) \right\} \tag{6.4}$$

$$Y_{mn}^{hs} = -2l_m \left\{ j\omega \left[\overline{F}_n^b(\overline{r}_m^{c+}) \bullet \frac{\overline{\rho}_m^{c+}}{2} + \overline{F}_n^b(\overline{r}_m^{c-}) \bullet \frac{\overline{\rho}_m^{c-}}{2} \right] + \phi_n^b(\overline{r}_m^{c-}) - \phi_n^b(\overline{r}_m^{c+}) \right\} \tag{6.5}$$

$$I_m^i = -l_m \left\{ \overline{H}_t^i(\overline{r}_m^{c+}) \bullet \frac{\overline{\rho}_m^{c+}}{2} + \overline{H}_t^i(\overline{r}_m^{c-}) \bullet \frac{\overline{\rho}_m^{c-}}{2} \right\} \tag{6.6}$$

Evaluation of the half-space admittance matrix eqn. (6.5), has already been carried out in subsections 2.4.1 and 2.4.2. In the next section, we discuss the evaluation of electric vector potential and magnetic scalar potential which are required in eqn. (6.4).

6.2 EVALUATION OF ELECTRIC VECTOR POTENTIAL AND MAGNETIC SCALAR POTENTIAL

Eqn. (2.16) gives the magnetic field $\overline{H}^a(\overline{M}_n)$ due to the nth expansion function at any point inside region 'a' in terms of $\overline{F}_n^a(\overline{r}')$ and $\phi_n^a(\overline{r}')$. Further, $\overline{F}_n^a(\overline{r}')$ and $\phi_n^a(\overline{r}')$ are given by Eqns. (2.22) and (2.23), respectively, as

$$\overline{F}_n^a(\overline{r}') = \varepsilon \iint_{T_n^\pm} \overline{\overline{G}}^a(\overline{r}|\overline{r}') \cdot \overline{M}_n(\overline{r}') ds' \tag{6.7}$$

$$\phi_n^a(\overline{r}') = \frac{-1}{j\omega\mu} \iint_{T_n^\pm} \left\{ \nabla \cdot \overline{\overline{G}}(\overline{r}|\overline{r}') \right\} \cdot \overline{M}_n(\overline{r}') ds' \tag{6.8}$$

However, the dyadic Green's function $\overline{\overline{G}}^a(\overline{r}|\overline{r}')$ is different from that used in Chapter 4. The relevant $\overline{\overline{G}}^a(\overline{r}|\overline{r}')$ has been derived by Rahmat-Samii [80] and can be written as

$$\overline{\overline{G}}^a(\overline{r}|\overline{r}') = \sum_{r=0}^{\infty} \sum_{s=0}^{\infty} \frac{\varepsilon_r \varepsilon_s}{2ab\gamma_{rs}} \exp\left[-\gamma_{rs}|z-z'|\right]$$

$$\times \left\{ \hat{x}\hat{x} \sin\left(\frac{r\pi x}{a}\right) \sin\left(\frac{r\pi x'}{a}\right) \cos\left(\frac{s\pi y}{b}\right) \cos\left(\frac{s\pi y'}{b}\right) \right.$$

$$+ \hat{y}\hat{y} \cos\left(\frac{r\pi x}{a}\right) \cos\left(\frac{r\pi x'}{a}\right) \sin\left(\frac{s\pi y}{b}\right) \sin\left(\frac{s\pi y'}{b}\right)$$

$$\left. + \hat{z}\hat{z} \cos\left(\frac{r\pi x}{a}\right) \cos\left(\frac{r\pi x'}{a}\right) \cos\left(\frac{s\pi y}{b}\right) \cos\left(\frac{s\pi y'}{b}\right) \right\} \tag{6.9}$$

where $\varepsilon_l = \begin{cases} 1, & p = 0 \\ 2, & p > 0 \end{cases}$ (6.10)

is the Neumann's number,

γ_{rs} is the propagation constant for the rs^{th} mode and is given by

$$\gamma_{rs} = \left(\frac{r\pi}{a}\right)^2 + \left(\frac{s\pi}{b}\right)^2 - k^2$$ (6.11)

where k has been given by eqn. (4.11).

Since at the plane of the aperture y = b, eqns. (6.7) and (6.8) become

$$F_{nx}^a(\bar{r}') = \frac{\pm\varepsilon}{2ab} \frac{1_n}{2A_n} \sum_{r=0}^{\infty} \sum_{s=0}^{\infty} \frac{\varepsilon_r \varepsilon_s}{\gamma_{rs}} \iint_{T_n^{\pm}} \exp\left[-\gamma_{rs}|z-z'|\right]$$

$$\times \left\{(x'-x_n)\sin\left(\frac{r\pi x}{a}\right)\sin\left(\frac{r\pi x'}{a}\right)\right\} dx'\,dz'$$ (6.12a)

$$F_{nz}^a(\bar{r}') = \frac{\pm\varepsilon}{2ab} \frac{1_n}{2A_n} \sum_{r=0}^{\infty} \sum_{s=0}^{\infty} \frac{\varepsilon_r \varepsilon_s}{\gamma_{rs}} \iint_{T_n^{\pm}} \exp\left[-\gamma_{rs}|z-z'|\right]$$

$$\times \left\{(z'-z_n)\cos\left(\frac{r\pi x}{a}\right)\cos\left(\frac{r\pi x'}{a}\right)\right\} dx'\,dz'$$ (6.12b)

$$\phi_n^a(\bar{r}') = \frac{\mp 1_n}{2A_n} \frac{1}{2j\omega\mu ab} \sum_{r=0}^{\infty} \sum_{s=0}^{\infty} \frac{\varepsilon_r \varepsilon_s}{\gamma_{rs}} \iint_{T_n^{\pm}} \nabla\bullet\exp\left[-\gamma_{rs}|z-z'|\right]$$

$$\times \left\{\hat{x}(x'-x_n)\sin\left(\frac{r\pi x}{a}\right)\sin\left(\frac{r\pi x'}{a}\right)\right.$$

$$\left. + \hat{z}(z'-z_n)\cos\left(\frac{r\pi x}{a}\right)\cos\left(\frac{r\pi x'}{a}\right)\right\} dx'dz'$$

$$\phi_n^a(\bar{r}') = \frac{\mp 1_n}{2A_n} \frac{1}{2j\omega\mu ab} \sum_{r=0}^{\infty} \sum_{s=0}^{\infty} \frac{\varepsilon_r \varepsilon_s}{\gamma_{rs}} \iint_{T_n^{\pm}} \left\{ e^{-\gamma_{rs}|z-z'|} \frac{r\pi}{a}(x'-x_n)\right.$$

$$\times \cos\left(\frac{r\pi x}{a}\right)\sin\left(\frac{r\pi x'}{a}\right)$$

$$\left. + (z'-z_n)\cos\left(\frac{r\pi x}{a}\right)\cos\left(\frac{r\pi x'}{a}\right)\begin{cases} -\gamma_{rs}e^{-\gamma_{rs}(z-z')}, & z > z' \\ \gamma_{rs}e^{\gamma_{rs}(z-z')}, & z < z' \end{cases}\right\} dx'dz'$$ (6.13)

194

As discussed in Chapter 2, we utilize Galerkin method and centroid approximation to evaluate the integrals in eqns. (6.12) and (6.13) for observation point in triangle p and source currents residing in triangle q.

Thus, according to eqns. (2.26) and (2.27), eqns. (6.12) and (6.13) can be written as :

$$F_{jx}^{pq} = \frac{\pm l_j}{2A_q} \frac{\varepsilon}{2ab} \sum_{r=0}^{\infty} \sum_{s=0}^{\infty} \iint_{A_q} \frac{\varepsilon_r \varepsilon_s}{\gamma_{rs}} \exp\left[-\gamma_{rs} | z_p - z'|\right]$$

$$\times \left\{ (x' - x_j) \sin\left(\frac{r\pi x_p}{a}\right) \sin\left(\frac{r\pi x'}{a}\right) \right\} dx'\, dz' \qquad (6.14a)$$

$$F_{jz}^{pq} = \frac{\pm \varepsilon}{2ab} \frac{l_j}{2A_q} \sum_{r=0}^{\infty} \sum_{s=0}^{\infty} \frac{\varepsilon_r \varepsilon_s}{\gamma_{rs}} \iint_{A_q} \exp\left[-\gamma_{rs} | z_p - z'|\right]$$

$$\times \left\{ (z' - z_j) \cos\left(\frac{r\pi x_p}{a}\right) \cos\left(\frac{r\pi x'}{a}\right) \right\} dx'\, dz' \qquad (6.14b)$$

$$\phi_j^{pq} = \frac{\mp l_j}{2A_q} \frac{1}{2j\omega\mu ab} \sum_{r=0}^{\infty} \sum_{s=0}^{\infty} \frac{\varepsilon_r \varepsilon_s}{\gamma_{rs}} \iint_{A_q} \left\{ e^{-\gamma_{rs}| z_p - z'|} \right.$$

$$\times \frac{r\pi}{a} (x' - x_j) \cos\left(\frac{r\pi x_p}{a}\right) \sin\left(\frac{r\pi x'}{a}\right)$$

$$+ (z' - z_j) \cos\left(\frac{r\pi x}{a}\right) \cos\left(\frac{r\pi x'}{a}\right) \left\{ \begin{array}{ll} -\gamma_{rs}\, e^{-\gamma_{rs}(z_p - z')} , & z_p > z' \\ \gamma_{rs}\, e^{\gamma_{rs}(z_p - z')} , & z_p < z' \end{array} \right\} \right\} dx'dz' \quad (6.15)$$

Integrals in eqns. (6.14) and (6.15) can be evaluated conveniently, after transformation into area coordinates. Thus, according to eqn. (2.60), $\overline{F}_j^{pq}$ and ϕ_j^{pq} can be expressed as :

$$F_{jx}^{pq} = \frac{\pm l_j}{2A_q} \frac{\varepsilon}{2ab} 2A_q \sum_{r=0}^{\infty} \sum_{s=0}^{\infty} \frac{\varepsilon_r \varepsilon_s}{\gamma_{rs}} \int_0^1 \int_0^{1-L_2} \exp\left[-\gamma_{rs}\left| (z_p - z_1) + (z_1 - z_2)L_2 + (z_1 - z_3)_{3|}\right]\right.$$

$$\times \left((x_1 - x_j) + (x_2 - x_1)L_2 + (x_3 - x_1)L_3 \right)$$

$$\times \sin\left(\frac{r\pi x_p}{a}\right) \sin\left(\frac{r\pi}{a}(x_1 + (x_2 - x_1)L_2 + (x_3 - x_1)L_3)\right) dL_2 dL_3 \qquad (6.16a)$$

$$F_{jz}^{pq} = \frac{\pm l_j}{2A_q} \frac{\varepsilon}{2ab} 2A_q \sum_{r=0}^{\infty} \sum_{s=0}^{\infty} \frac{\varepsilon_r \varepsilon_s}{\gamma_{rs}} \int_0^1 \int_0^{1-L_2} \exp\left[-\gamma_{rs}\left| (z_p - z_1) + (z_1 - z_2)L_2 + (z_1 - z_3)L_3\right|\right]$$

$$\times \left((z_1 - z_j) + (z_2 - z_1)L_2 + (z_3 - z_1)L_3 \right)$$

$$\times \cos\left(\frac{r\pi x_p}{a}\right) \cos\left(\frac{r\pi}{a}(x_1 + (x_2 - x_1)L_2 + (x_3 - x_1)L_3)\right) dL_2 dL_3 \qquad (6.16b)$$

$$\phi_j^{pq} = \frac{\mp l_j}{2A_q} \frac{2A_q}{2j\omega\mu ab} \sum_{r=0}^{\infty} \sum_{r=0}^{\infty} \frac{\varepsilon_r \varepsilon_s}{\gamma_{rs}} \int_0^1 \int_0^{1-L_2} \left\{ \exp\left[-\gamma_{rs}\left| (z_p - z_1) + (z_1 - z_2)L_2 + (z_1 - z_3)L_3\right|\right]\right.$$

$$\times \left(\frac{r\pi}{a}\right)\left((x_1 - x_j) + (x_2 - x_1)L_2 + (x_3 - x_1)L_3 \right)$$

$$\times \cos\left(\frac{r\pi x_p}{a}\right) \sin\left(\frac{r\pi}{a}(x_1 + (x_2 - x_1)L_2 + (x_3 - x_1)L_3)\right)$$

$$+ \left((z_1 - z_j) + (z_2 - z_1)L_2 + (z_3 - z_1)L_3 \right) \cos\left(\frac{r\pi x_p}{a}\right)$$

$$\times \cos\left(\frac{r\pi}{a}(x_1 + (x_2 - x_1)L_2 + (x_3 - x_1)L_3)\right)$$

$$\times \left\{ \begin{array}{ll} -\gamma_{rs}\, e^{-\gamma_{rs}((z_p - z_1) + (z_1 - z_2)L_2 + (z_1 - z_3)L_3)}, & z_p > z' \\ \gamma_{rs}\, e^{\gamma_{rs}((z_p - z_1) + (z_1 - z_2)L_2 + (z_1 - z_3)L_3)}, & z_p < z' \end{array} \right\} dL_2 dL_3 \qquad (6.17)$$

For seven point numerical integration, the equations reduce to

$$F_{jx}^{pq} = \frac{\pm l_j}{2A_q} \frac{\epsilon}{2ab} \sum_{r=0}^{\infty} \sum_{s=0}^{\infty} \frac{\epsilon_r \epsilon_s}{\gamma_{rs}} A_q \sum_{m=1}^{7} W(m) \left\{ e^{-\gamma_{rs}|(z_p - z_1) + (z_1 - z_2)L_{2m} + (z_1 - z_3)L_{3m}|} \right.$$

$$\times \left((x_1 - x_j) + (x_2 - x_1)L_{2m} + (x_3 - x_1)L_{3m} \right)$$

$$\left. \times \sin\left(\frac{r\pi x_p}{a}\right) \sin\left(\frac{r\pi}{a}(x_1 + (x_2 - x_1)L_{2m} + (x_3 - x_1)L_{3m})\right) \right\} \qquad (6.18a)$$

$$F_{jz}^{pq} = \frac{\pm l_j}{2A_q} \frac{\epsilon}{2ab} \sum_{r=0}^{\infty} \sum_{s=0}^{\infty} \frac{\epsilon_r \epsilon_s}{\gamma_{rs}} A_q \sum_{m=1}^{7} W(m) \left\{ e^{-\gamma_{rs}|(z_p - z_1) + (z_1 - z_2)L_{2m} + (z_1 - z_3)L_{3m}|} \right.$$

$$\times \left((z_1 - z_j) + (z_2 - z_1)L_{2m} + (z_3 - z_1)L_{3m} \right)$$

$$\left. \times \cos\left(\frac{r\pi x_p}{a}\right) \cos\left(\frac{r\pi}{a}(x_1 + (x_2 - x_1)L_{2m} + (x_3 - x_1)L_{3m})\right) \right\} \qquad (6.18b)$$

$$\phi_j^{pq} = \frac{\mp l_j}{2A_q} \frac{1}{2j\omega\mu ab} \sum_{r=0}^{\infty} \sum_{s=0}^{\infty} \frac{\epsilon_r \epsilon_s}{\gamma_{rs}} A_q \sum_{m=1}^{7} W(m) \left\{ e^{-\gamma_{rs}|(z_p - z_1) + (z_1 - z_2)L_{2m} + (z_1 - z_3)L_{3m}|} \right.$$

$$\times \left(\frac{r\pi}{a}\right)\left((x_1 - x_j) + (x_2 - x_1)L_{2m} + (x_3 - x_1)L_{3m} \right)$$

$$\times \cos\left(\frac{r\pi x_p}{a}\right) \sin\left(\frac{r\pi}{a}(x_1 + (x_2 - x_1)L_{2m} + (x_3 - x_1)L_{3m})\right)$$

$$+ \left((z_1 - z_j) + (z_2 - z_1)L_{2m} + (z_3 - z_1)L_{3m} \right)$$

$$\left. \times \cos\left(\frac{r\pi x_p}{a}\right) \cos\left(\frac{r\pi}{a}(x_1 + (x_2 - x_1)L_{2m} + (x_3 - x_1)L_{3m})\right) \right\}$$

$$\times \left\{ \begin{array}{ll} -\gamma_{rs}\, e^{-\gamma_{rs}((z_p - z_1) + (z_1 - z_2)L_{2m} + (z_1 - z_3)L_{3m})}, & z_p > z' \\ \gamma_{rs}\, e^{\gamma_{rs}((z_p - z_1) + (z_1 - z_2)L_{2m} + (z_1 - z_3)L_{3m})}, & z_p < z' \end{array} \right\} \qquad (6.19)$$

where m denotes the mth sampling point in the domain of T^q, $W(m)$ is the weighting factor for the mth sampling point, L_{2m} and L_{3m} are the values of L_2 and L_3 at the mth sampling point. $W(m)$, L_{2m} and L_{3m} are given in Table 2.1.

6.3 EVALUATION OF EXCITATION VECTOR

The excitation of the waveguide is assumed to be due to the dominant TE_{10} mode of unit amplitude produced by an electromagnetic source at $z = -\infty$. Therefore, the incident field components in region 'a' are

$$E_y^i = \sin\left(\frac{\pi x}{a}\right) e^{-j\beta_{10}z} \tag{6.20}$$

$$H_x^i = \frac{-\beta_{10}}{\omega\mu} \sin\left(\frac{\pi x}{a}\right) e^{-j\beta_{10}z} \tag{6.21}$$

$$H_z^i = \frac{-\pi}{j\omega\mu a} \cos\left(\frac{\pi x}{a}\right) e^{-j\beta_{10}z} \tag{6.22}$$

where $\beta_{10} = k\sqrt{1 - (f/f_c)^2}$ $\tag{6.23}$

and $k = \omega\sqrt{\mu\varepsilon}$ $\tag{6.24}$

Thus, eqn. (6.6) may now be written as

$$I_j^i = -1_j \left\{ H_x^i\left(\bar{r}_j^{c+}\right)\frac{\rho_{jx}^{c+}}{2} + H_x^i\left(\bar{r}_j^{c-}\right)\frac{\rho_{jx}^{c-}}{2} + H_z^i\left(\bar{r}_j^{c+}\right)\frac{\rho_{jz}^{c+}}{2} + H_z^i\left(\bar{r}_j^{c-}\right)\frac{\rho_{jz}^{c-}}{2} \right\} \tag{6.25}$$

where $\rho_{jx}^{c\pm} = \pm\left\{ \dfrac{x_j^{m+j+1} + x_j^{n+j+2}}{2} - \dfrac{x_j^j + x_j^{m+j+1} + x_j^{n+j+2}}{3} \right\}$ $\tag{6.26a}$

$\rho_{jz}^{c\pm} = \pm\left\{ \dfrac{z_j^{m+j+1} + z_j^{n+j+2}}{2} - \dfrac{z_j^j + z_j^{m+j+1} + z_j^{n+j+2}}{3} \right\}$ $\tag{6.26b}$

$j = 1, 2, 3$

where m and n are dummy variables such that

$$m = \begin{cases} 0, & j = 1, 2 \\ -3, & j = 3 \end{cases}$$

and $n = \begin{cases} 0, & j = 1 \\ -3, & j = 2, 3 \end{cases}$ $\tag{6.27}$

$H_x^i\left(\bar{r}_j^{c\pm}\right)$, $H_z^i\left(\bar{r}_j^{c\pm}\right)$ are the values of H_x^i and H_z^i, evaluated at the centroids of the triangles $T_j^{\pm}$ associated with the jth edge.

6.4 COMPUTATION OF SCATTERING PARAMETERS

Assuming that the aperture centre coincides with the $z = 0$ plane, we consider two reference planes T_1 and T_2 located, respectively, at $z_1 = -z$ and $z_2 = +z$, where z_1 and z_2 are an integral multiple of the guide wavelength. Once the scattering parameters are computed, the terminal planes can be shifted to the aperture centre without causing any change in the scattering parameter values.

Thus, the scattering parameter S_{11} pertaining to dominant TE_{10} mode is given by

$$S_{11} = \frac{E_t^a(\overline{M})|_{T_1}}{E_t^i|_{T_1}} \tag{6.28}$$

In terms of magnetic field components, S_{11} can be written as

$$S_{11} = -\frac{H_x^a(\overline{M})|_{T_1}}{H_x^i|_{T_1}} = -\frac{\sum_{n=1}^{N} V_n H_x^a(\overline{M}_n)|_{T_1}}{H_x^i|_{T_1}} \tag{6.29}$$

where H_x^i has been given by eqn. (6.21) and

$$H_x^a(\overline{M}_n) = -j\omega F_{nx}^a(\overline{r}) - \nabla\phi_n^a(\overline{r}) \tag{6.30}$$

From eqns. (6.12a) and (6.13), using the dominant term of Green's function leads to

$$F_{nx}^a(\overline{r}) = \frac{\pm\varepsilon}{2ab} \frac{I_n}{\gamma_{10}} \iint_{T_n^{\pm}} \exp\left[-\gamma_{10}|z - z'|\right]$$

$$\times \left\{ (x'-x_n)\sin\left(\frac{\pi x}{a}\right)\sin\left(\frac{\pi x'}{a}\right) \right\} dx'\, dz' \tag{6.31}$$

$$\phi_n^a(\overline{r}) = \mp\frac{I_n}{2A_n} \frac{1}{2j\omega\mu ab} \frac{2}{\gamma_{10}} \iint_{T_n^{\pm}} \left\{ \exp\left[-\gamma_{10}|z-z'|\right]\frac{\pi}{a}(x'-x_n)\cos\left(\frac{\pi x}{a}\right)\sin\left(\frac{\pi x'}{a}\right) \right\}$$

$$+(z'-z_n)\cos\left(\frac{\pi x}{a}\right)\cos\left(\frac{\pi x'}{a}\right)\begin{Bmatrix} -\gamma_{10}\, e^{-\gamma_{10}(z-z')}, & z > z' \\ \gamma_{10}\, e^{\gamma_{10}(z-z')}, & z < z' \end{Bmatrix} dx'dz' \qquad (6.32)$$

Following the procedure leading to eqn. (6.19), we can write

$$F_{jx}^a(\bar{r})\Big|_{z<z'} = \frac{\pm\varepsilon}{2ab}\frac{l_j}{2A_q}\frac{2}{\gamma_{10}}A_q\sum_{m=1}^{kk}W(m)\Big\{\exp\left(-\gamma_{10}\,|\,(z_1+(z_2-z_1)L_{2m}+(z_3-z_1)L_{3m}\,|\right)$$

$$\times\left((x_1-x_j)+(x_2-x_1)L_{2m}+(x_3-x_1)L_{3m}\right)$$

$$\times\sin\left(\frac{\pi x}{a}\right)\sin\left(\frac{\pi}{a}(x_1+(x_2-x_1)L_{2m}+(x_3-x_1)L_{3m})\right)\Big\}_{z<z'} \qquad (6.33)$$

$$\frac{\partial\phi_j^a(\bar{r})}{\partial x}\Bigg|_{z<z'} = \frac{1}{2j\omega\mu ab}\frac{\mp l_j}{2A_q}\frac{2}{\gamma_{10}}A_q\sum_{m=1}^{kk}W(m)\Big\{\exp(-\gamma_{10}|\,z_1+(z_2-z_1)L_{2m}+(z_3-z_1)L_{3m}\,|)$$

$$\times\left(\frac{-\pi^2}{a^2}\right)\left((x_1-x_j)+(x_2-x_1)L_{2m}+(x_3-x_1)L_{3m}\right)$$

$$\times\sin\left(\frac{\pi x}{a}\right)\sin\left(\frac{\pi}{a}\left(x_1+(x_2-x_1)L_{2m}+(x_3-x_1)L_{3m}\right)\right)$$

$$-\gamma_{10}\frac{\pi}{a}\left((z_1-z_j)+(z_2-z_1)L_{2m}+(z_3-z_1)L_{3m}\right)$$

$$\times\sin\left(\frac{\pi x}{a}\right)\cos\left(\frac{\pi}{a}(x_1+(x_2-x_1)L_{2m}+(x_3-x_1)L_{3m})\right)$$

$$\times\exp\left(-\gamma_{10}\,(z_1+(z_2-z_1)L_{2m}+(z_3-z_1)L_{3m})\right)\Big\}\ z<z' \qquad (6.34)$$

In a similar manner, transmission coefficient S_{21}, is given by

$$S_{21} = 1 + \frac{\displaystyle\sum_{n=1}^{N}V_n\,H_x^a(\overline{M}_n)\,|_{T_2}}{H_x^i\,|_{T_1}} \qquad (6.35)$$

where $H_x^a(\overline{M}_n)$ is given by eqn. (6.30) in which $F_{jx}^a(\bar{r})$ and $\dfrac{\partial\phi_j^a}{\partial x}(\bar{r})$ can be

written as

$$\left. F_{jx}^a(\bar{r}) \right|_{z>z'} = \frac{\pm\varepsilon}{2ab} \frac{l_j}{2A_q} \frac{2}{\gamma_{10}} A_q \sum_{m=1}^{kk} W(m) \left\{ \exp\left(-\gamma_{10} \mid (z_1 + (z_2 - z_1)L_{2m} + (z_3 - z_1)L_{3m} \mid\right)\right.$$

$$\times \left((x_1 - x_j) + (x_2 - x_1)L_{2m} + (x_3 - x_1)L_{3m}\right)$$

$$\left.\times \sin\left(\frac{\pi x}{a}\right) \sin\left(\frac{\pi}{a}(x_1 + (x_2 - x_1)L_{2m} + (x_3 - x_1)L_{3m})\right)\right\}_{z>z'} \qquad (6.36)$$

$$\left. \frac{\partial \phi_j^a(\bar{r})}{\partial x} \right|_{z>z'} = \frac{1}{2j\omega\mu ab} \frac{\mp l_j}{2A_q} \frac{2}{\gamma_{10}} A_q \sum_{m=1}^{kk} W(m) \left\{ \exp(-\gamma_{10} \mid z_1 + (z_2 - z_1)L_{2m} + (z_3 - z_1)L_{3m} \mid)\right.$$

$$\times \left(\frac{-\pi^2}{a^2}\right)\left((x_1 - x_j) + (x_2 - x_1)L_{2m} + (x_3 - x_1)L_{3m}\right)$$

$$\times \sin\left(\frac{\pi x}{a}\right) \sin\left(\frac{\pi}{a}\left(x_1 + (x_2 - x_1)L_{2m} + (x_3 - x_1)L_{3m}\right)\right)$$

$$+ \gamma_{10}\frac{\pi}{a}\left((z_1 - z_j) + (z_2 - z_1)L_{2m} + (z_3 - z_1)L_{3m}\right)$$

$$\times \sin\left(\frac{\pi x}{a}\right) \cos\left(\frac{\pi}{a}(x_1 + (x_2 - x_1)L_{2m} + (x_3 - x_1)L_{3m})\right)$$

$$\left.\times \exp\left(\gamma_{10}(z_1 + (z_2 - z_1)L_{2m} + (z_3 - z_1)L_{3m})\right)\right\}_{z>z'} \qquad (6.37)$$

Thus, power radiated, p_{rad}, is given by

$$p_{rad} = \left\{1 - \mid S_{11}\mid^2 - \mid S_{21}\mid^2\right\} \qquad (6.38)$$

6.5   RESULTS AND DISCUSSION

A computer program has been written based on the preceding formulation, which is capable of analysing broadwall slots/apertures of arbitrary shape in a rectangular waveguide radiating into half space. The code has been validated by using rectangular longitudinal slots and centrally-located transverse rectangular slots for which data are available in the literature [63]. The waveguide wall has been assumed to be infinitesimally thin. Convergence tests have been carried out to establish the correct results.

6.5-1 Offset Broadwall Longitudinal Rectangular Slot

Rectangular slot surface was triangulated as per the scheme shown in Fig. 3.3. The slot lies in the xz plane with its axis along the +z direction and is offset 2 mm from the centre of the broadwall. The slot width is 1.5 mm and its length is variable. Fig. 6.3 shows the power-radiated/power-incident ratio versus slot length. The results obtained are compared with those of Lyon and Sangster's data [63] and are seen to be in good agreement.

6.5-2 Centrally-located Broadwall Transverse Slot

Next, centrally-located transverse rectangular slot, based on the triangulation scheme depicted in Fig. 3.3, in the broadwall of a rectangular waveguide was considered. Fig. 6.4 shows power-radiated/power-incident ratio as a function of slot-length. Our results are in good agreement with those of Lyon and Sangster [63].

6.5-3 Centrally-located Circular Aperture

A circular aperture surface on the broadwall of a rectangular waveguide was triangulated as depicted in Fig. 3.13. About 76 expansion function were found to yield converged results. Fig. 6.5 shows power-radiated/power-incident ratio versus normalized diameter, d/a. It is noted that radiated power increases with the size of the aperture. However, at $d/a \cong 0.35$ aperture seems to be at resonance and any further increase in d/a beyond 0.35 results in a decrease in radiated power. As in the case of a rectangular slot, the size of the circular aperture that can be accommodated in the broadwall is limited by the waveguide broadwall dimension a.
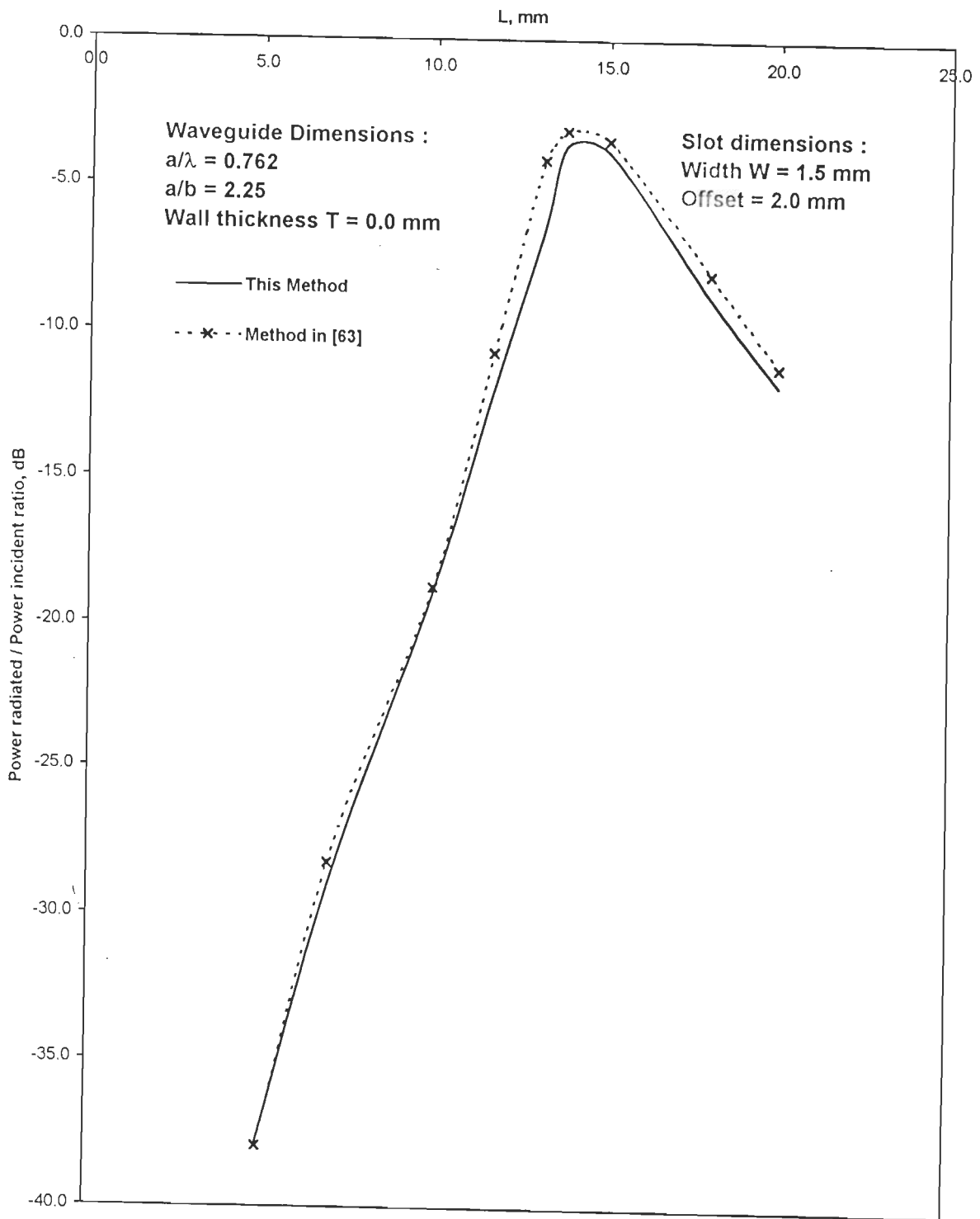
Fig. 6.3 : Power radiated/power incident against slot length for
infinitesimally thin longitudinal slot in WG 16.
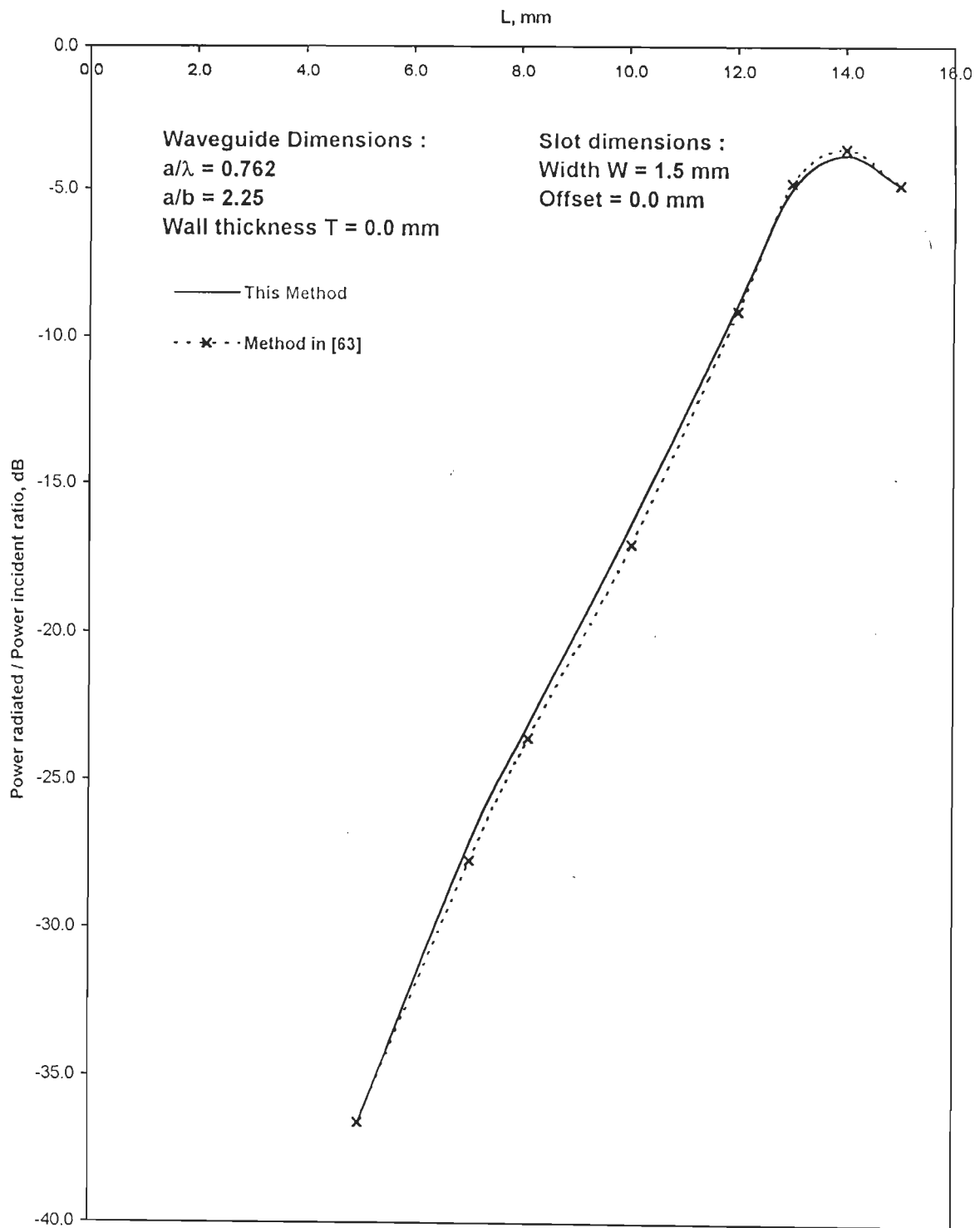
Fig. 6.4 : Power radiated/power incident against slot sength for infinitesimally thin centrally located transverse slot in WG16.
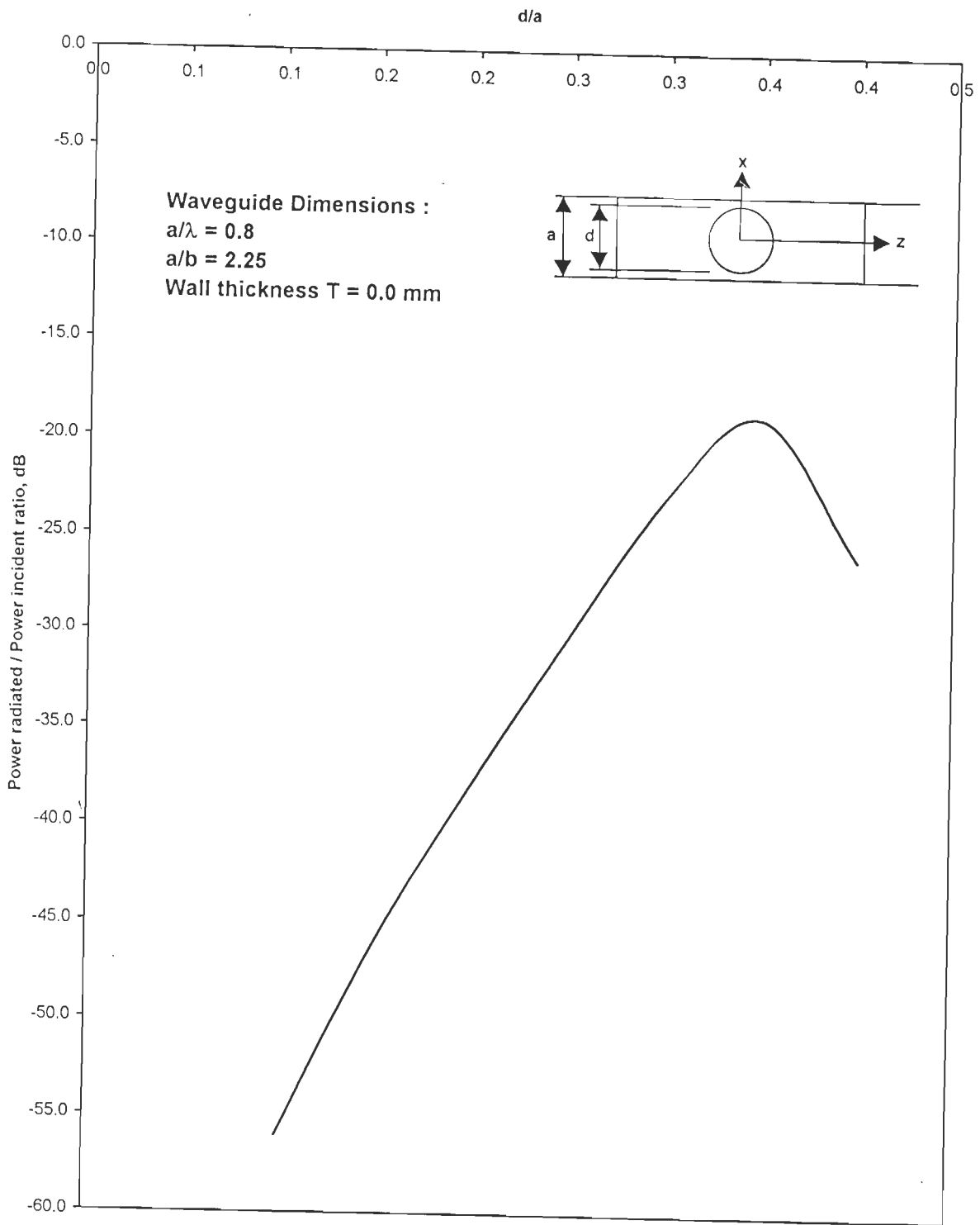
Fig. 6.5 : Centrally-located broad wall circular aperture power radiated/ power incident ratio against aperture diameter d/a.

6.5-4 Centrally-located Elliptical Aperture

Using a discretization scheme similar to that in Fig. 3.18, it was found that about 76 expansion functions yielded converged results for an elliptic aperture on the broadwall of a rectangular waveguide.

Fig. 6.6 shows power-radiated/power-incident ratio versus eccentricity e given in eqn. (3.29) for two orientations of the aperture. In Fig. 6.6(a), it is noted that reducing d_2 for a fixed value of d_1, results in a reduced radiated power. However, at e $=$ 0.5, the radiated power exhibits a peak, suggesting that resonance occurs at this value of e. Fig. 6.6(b), on the other hand, shows that power-radiated increases with decrease in d_2 for a fixed value of d_1.
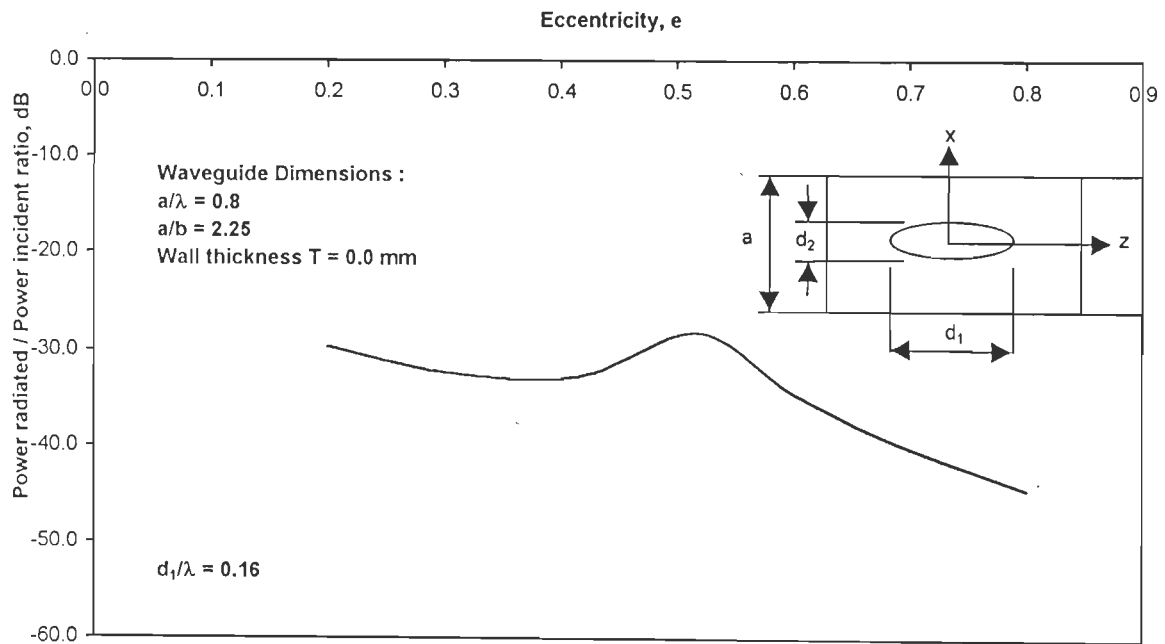
(a)
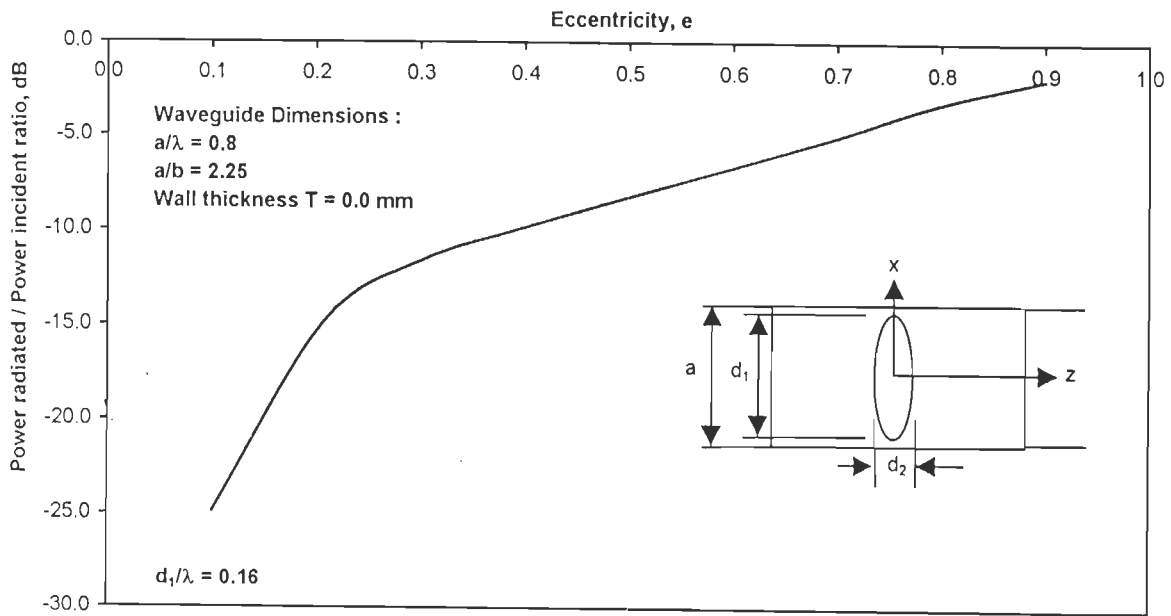
(b)

Fig. 6.6 : Centrally-located broad wall elliptical aperture power radiated/power incident ratio against eccentricity e.

6.6   SUMMARY

In this chapter, a numerical study has been undertaken on a limited number of broadwall apertures of various shapes radiating into half space. The computer code has been validated by considering transverse and longitudinal rectangular slots for which data are available in the literature. All the results have been tested for convergence by utilizing sufficient number of expansion functions.

Results have been presented for power-radiated by rectangular, circular, and elliptic apertures.

Chapter - 7
DISCUSSION AND CONCLUSIONS

In the preceding chapters, a comprehensive study has been carried out on apertures of arbitrary shapes in waveguides and conducting screens. The analysis has been based on a rigorous formulation exploiting an appropriate choice of computational technique and a flexible modelling scheme incorporating versatile basis functions. This strategy has culminated in writing a general efficient computer program. The program has been validated and tested on apertures of various shapes, amongst which rectangular, circular, elliptic, diamond, cross and H have been presented as representative examples of the diverse range of arbitrarily-shaped apertures.

In this chapter, a critical review of the analysis, results and their practical implications are presented. Finally, some of the areas which require further research have also been suggested.

7.1 THE ANALYSIS

The analysis is based on the "generalized network formulation" for aperture problems originally proposed by Harrington and Mautz [44]. The formulation is completely general in that two arbitrary open or closed regions coupled via an arbitrary-shaped aperture can be treated. However, for actual evaluation of the matrices, expansion and testing functions must be selected with particular care. In this dissertation, triangular patch modelling, with appropriately defined basis functions, has been utilized which is appropriate for modelling surfaces of arbitrary shape, since the shape of a triangle can easily conform to any geometry and the

density of the triangles can be increased in those regions of the aperture in which a higher resolution is desirable. The greatest advantage of the formulation and the scheme lies in the fact that the evaluation of the admittance matrix of a region involves only that region. This means that once the admittance matrix of a region is known, it can be combined with the admittance matrices of the other regions for various problems. This is to say that routines for computing admittance matrices of different regions may be written separately and can then be combined in a number of ways to obtain solutions for a wide category of problems.

The method of moments has a number of advantages over other methods. First it inherently takes into account the effect of higher order evanescent modes in waveguides. Further, unlike the other methods, which mostly deal only with the dominant mode incidence, this method can treat arbitrary incidence with equal ease. Also, the effect of finite wall thickness can easily be incorporated in the method, although in the present study only infinitesimally thin walls have been used.

First, a general formulation has been developed for solving the problem of an aperture of arbitrary shape coupling two arbitrary regions. Important aspects, such as choice of basis functions evaluation of matrices and excitation vector and efficient computation of integrals over observation and source triangles have been considered. Further, particular attention has been given in developing expressions which treat integrals with singular kernels, associated with Green's function of free space, and integrals with bounded kernels, for closed regions. Finally, equations for computing aperture near- and far- field parameters have been derived.

In Chapter 3, the study has addressed itself to the analysis of apertures of various shapes in an infinitesimally thin, perfectly conducting screen. The general formulation of Chapter 2 has been specialized to this problem. In this chapter, evaluation of admittance matrices has been based on dyadic Green's function of free

space. Expressions for evaluating various parameters, such as transmission coefficient and magnetic current distributions have been derived.

In Chapter 4, the problem of waveguide-fed apertures of arbitrary shape on a perfectly conducting ground plane radiating into half-space has been investigated. Dyadic Green's function of the electric vector potential pertaining to a waveguide short-circuited at one end, has been used in evaluating waveguide admittance matrix. Evaluation of equivalent aperture admittance has been based on the dominant TE_{10} mode incidence.

In Chapter 5, apertures of arbitrary shape in the waveguide cross-section have been analysed. The admittance matrices of uniform rectangular waveguides have been adopted from Chapter 4. The power of the formulation is amply demonstrated by the fact that no new admittance matrices are to be derived for solving this entirely new problem.

In Chapter 6, we have presented an analysis of radiating apertures of arbitrary shape in the broadwall of a rectangular waveguide. The guide wall has been assumed to be infinitesimally thin. For the waveguide region, dyadic Green's function of the vector potential pertaining to an infinite rectangular waveguide [80] has been utilized. Equations for determining scattering parameters have been derived using the dominant TE_{10} mode term of the dyadic Green's function. An expression for computing power radiated by the aperture based upon the reflection and transmission coefficients has been developed.

7.2   THE COMPUTER PROGRAM

An efficient computer program has been written in FORTRAN-77 based upon the expressions derived for the various problems. A modular approach has been used in writing the program to make it flexible and versatile. It has been

211

divided into a number of subprograms. In the process, separate subroutines for computing various admittance matrices and parameters have been written. These subroutines may be used in any number of permutations and combinations to solve various problems after slight modifications in the storage strategy of the matrices. The complete program itself is quite general and can analyse all the four problems in chapters three to six and, also the problem of waveguide to -cavity coupling which was validated but not explored further in this study.

The program listing is available with the author and Prof. S.N. Sinha, the Research Supervisor

7.3 THE NUMERICAL RESULTS

The computer program has first been validated for each class of problems considered, prior to generating data for any new problem. Extensive computations have been carried out for various aperture parameters. Convergence of results has been established for each problem by utilizing sufficient number of expansion functions, that is to say, including sufficient number of non-boundary edges to ensure accurate modelling of the physical surface of a particular aperture. Results have been presented in chapters three to six for typical aperture shapes, i.e., rectangular, circular, elliptic, diamond, cross and H, which may be considered diverse enough to simulate any possible physical aperture shape.

In Chapter 3, results have been given for apertures in an infinite conducting screen coupling two half spaces. Convergence results for transmission coefficient versus number of expansion functions have been presented for $\lambda/20$-wide rectangular slots, square apertures (of size $\lambda/4 \times \lambda/4$ and $\lambda/2 \times \lambda/2$) and circular apertures of various sizes. Further, surface magnetic current distributions and transmission cross-sections have been presented for all the six aperture shapes

alluded to above. Each aperture studied has exhibited unique near- and far-field characteristics. Finally, the results for comparative study on transmission cross-sections for apertures of different shapes with equal area have been given. Elliptic and diamond-shaped apertures and H-shaped slot have exhibited attractive transmission cross-sections.

Chapter 4 has presented results of a study on waveguide-backed apertures in a conducting plane. First, convergence study results for peak magnitude of surface magnetic current as a function of number of expansion functions for open-ended square waveguide has been given. Validation results have included surface magnetic current distributions and power gain patterns for $\lambda \times \lambda/10$ rectangular slot and open-ended rectangular and square waveguides radiating into half space. In addition, results for equivalent admittance seen by the dominant TE_{10} mode for open-ended rectangular and square-waveguides have also been given. Having validated the formulation and the computer program, new data have been presented for surface magnetic current distributions, equivalent aperture admittance seen by dominant TE_{10} mode and power gain patterns for circular, elliptical, diamond-shaped, cross-shaped and H-shaped apertures/slots radiating into half space. Finally, a comparative study on antenna power gains for relatively small apertures of different shapes with equal area and relatively large apertures of various shapes with equal area has been conducted. The results have shown that elliptic and diamond-shaped apertures have the highest power gains, among all the apertures studied. Further, elliptic aperture has a more directive H-plane pattern while diamond shaped aperture has a more directive E-plane pattern.

In Chapter 5, we have considered conducting diaphragms with apertures of various shapes in the cross-section of a uniform rectangular waveguide. First, the study has established a pair of criteria for eliminating the phenomenon of

213

"relative convergence" inherent in such aperture coupling problems. The pair of criteria has been applied to study convergence of normalized shunt susceptance for symmetrical inductive and capacitive diaphragms and centered - circular and elliptical apertures. Good to excellent agreement with published data have been obtained. Then, normalized Shunt susceptance results for diamond-shaped aperture and cross-shaped slot have also been presented. Further, a comparison of equivalent surface magnetic current distributions for symmetrical inductive and capacitive diaphragms and centered circular, elliptical, diamond shaped apertures and cross-shaped slot has been made. The major contribution in this chapter is the proposed pair of criteria which can be applied for the computation of parameters for waveguide apertures (discontinuities) of any size and shape.

In chapter 6, results for broadwall radiating slots/apertures of different shapes in a rectangular waveguide have been presented. Power radiated by offset longitudinal slots and centrally- located transverse slots have been presented for the validation of the formulation. Thereafter, power radiated by centrally-located circular and elliptical apertures for different orientations of the elliptic aperture has been given. The main contribution in this chapter is the updating of the general computer program such that it can analyse any radiating broadwall apertures/slots in a rectangular waveguide.

7.4   SCOPE FOR FUTURE WORK

The various apertures studied in this work have been assumed to be residing in an infinitesimally thin conducting screen or thin-walled rectangular waveguide. The case of apertures of arbitrary shape in a thick conducting screen and in a thick-walled rectangular waveguide were not considered due to lack of Green's function for the interior arbitrary region formed by apertures of arbitrary shape in such thick

walls. However, of practical interest are apertures in a thick conducting wall, both as a single radiating element or an array of radiating elements and those occurring in EMC/EMI problems. The scope for further research, therefore, lies in extending our present formulation to incorporate Finite Element Method, i.e., a hybrid MOM/FEM technique, whereby the FEM can be utilized to evaluate the fields in the interior cavity region, which is formed when the aperture surfaces in a thick wall are closed with perfect conductors, while the MOM formulation the fields on the surfaces of arbitrarily-shaped aperture. The technique can be used to analyse the apertures of various shapes studied in chapter 3 in a thick conducting screen and in chapters 4 to 6 in a thick-walled rectangular waveguide.

In addition, problems of electromagnetic radiation from apertures of various shapes in a metallic box (i.e., a shielded enclosure), inhomogeneously filled with a dielectric material, can be studied to establish various resonance and other parameters of interest. Such a problem is of practical importance as an example of EMC and EMI problem. Another area that can be explored is that of apertures occurring in printed circuits either due to cracks or deficiency in fabrication technique. Further, problem of apertures of various shapes coupling a microstripline to a microstrip-patch antenna and a waveguide to microstrip-patch antenna etc. can be investigated.

APPENDIX - A

Let the coordinates of observation point be denoted by (x_o, y_o). We denote by superscripts -, + respectively, the parameters related to the first and second nodes of a given side of T^q. The arclength variables t_i, increasing in the $\hat{t}_i$ direction from the value t_i^- at the 1st node to the final value $t_i^+ = t_i^- + l_i$ at the 2nd node, Fig A-1, has the projections at the endpoints of each side of T^q given by

$$t_1^- = \{\hat{x}(l_3 - x_o) - \hat{y}y_o\} \bullet \{(x_3 - l_3)\hat{x} + \hat{y}y_3\}/l_1$$

$$= [(l_3 - x_o)(x_3 - l_3) - y_o y_3]/l_1 \tag{A.1}$$

$$t_1^+ = \{\hat{x}(x_3 - x_o) + \hat{y}(y_3 - y_o)\} \bullet \{\hat{x}(x_3 - l_3) + \hat{y}(y_3 - 0)\}/l_1$$

$$= [(x_3 - x_o)(x_3 - l_3) + y_3(y_3 - y_o)]/l_1 \tag{A.2}$$

$$t_2^- = \{\hat{x}(x_3 - x_o) + \hat{y}(y_3 - y_o)\} \bullet \{\hat{x}(x_3 - 0) + \hat{y}(y_3 - 0)\}/l_2$$

$$= [x_3(x_3 - x_o) + y_3(y_3 - y_o)]/l_2 \tag{A.3}$$

$$t_2^+ = \{\hat{x}(-x_o) + \hat{y}(-y_o)\} \bullet \{-\hat{x}x_3 - \hat{y}y_3\}/l_2$$

$$= [x_o x_3 + y_o y_3]/l_2 \tag{A.4}$$

$$t_3^- = \{\hat{x}(-x_o) + \hat{y}(-y_o)\} \bullet \hat{x}(-l_3)/l_3$$

$$= x_o \tag{A.5}$$

$$t_3^+ = \{\hat{x}(l_3 - x_o) + \hat{y}(-y_o)\} \bullet [l_3 \hat{x}]/l_3$$

$$= (l_3 - x_o) \tag{A.6}$$

(A.1) to (A.6) can be written in compact form as

$$t_i^\pm = (\bar{p}_i - \bar{p}_o) \bullet (\bar{p}_{m+i-1} - \bar{p}_{n+i+1})/l_i \tag{A.7}$$

$$i = 1, 2, 3$$

where m and n are dummy variables such that

216

$$m = \begin{cases} 3, & i = 1 \\ 0, & i = 2,3 \end{cases}$$

$$\text{and} \quad n = \begin{cases} 0, & i = 1, 2 \\ -3, & i = 3 \end{cases}$$

Distances from observation point to segment end points at the vertices, Fig. A-2, are given as

$$s_1^- = \sqrt{(l_3 - x_o)^2 + y_o^2}$$

$$s_1^+ = \sqrt{(x_3 - x_o)^2 + (y_3 - y_o)^2}$$

$$s_2^- = s_1^+$$

$$s_2^+ = \sqrt{x_o^2 + y_o^2}$$

$$s_3^- = s_2^+$$

$$s_3^+ = s_1^-$$

Or in a more compact form $s_i^{\pm}$ can be written as

$$s_i^{\pm} = |\bar{p}_i - \bar{p}_o| \tag{A.8}$$

Perpendiculars p_i^o to the arc length l_i or their extension are given by

$$p_1^o = \{y_o(x_3 - l_3) + (l_3 - x_o)y_3\}/l_1 \tag{A.9}$$

$$p_2^o = |\{\hat{x}(x_3 - x_o) + \hat{y}(y_3 - y_o)\} \times \{\hat{x}x_3 + \hat{y}y_3\}|/l_2$$

$$= |\{y_3(x_3 - x_o) - x_3(y_3 - y_o)\}|/l_2$$

$$= (y_o x_3 - x_o y_3)/l_2 \tag{A.10}$$

$$p_3^o = |[\hat{x}(x_1 - x_o) + \hat{y}(y_1 - y_o)] \times [(l_3 - x_1)\hat{x} + \hat{y}(y_2 - y_1)]|/l_3$$

$$= \left| y_o \, l_3 \, / \, l_3 \right|$$

$$= y_o \qquad\qquad (A.11)$$

Or in a compact form, $p_i^{\,0}$ can be written as

$$p_i^{\,0} \;=\; |\,(\bar{p}_{n+i+1} - \bar{p}_o) \times (\bar{p}_{m+i-1} - \bar{p}_{n+i+1})\,| \,/\, l_i \qquad\qquad (A.12)$$
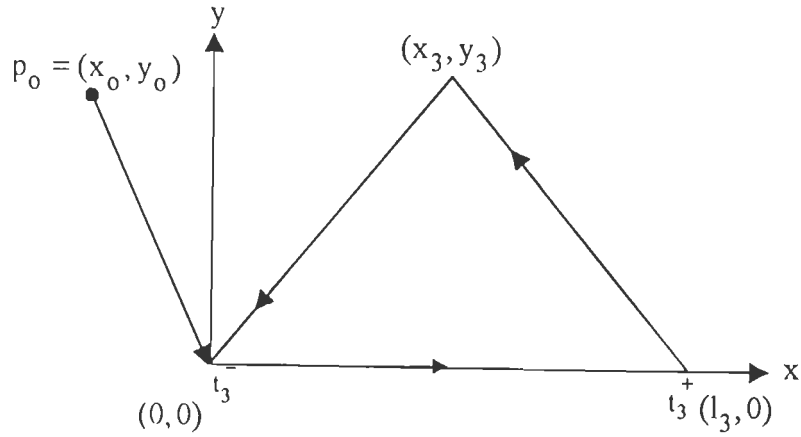
Fig. A-1
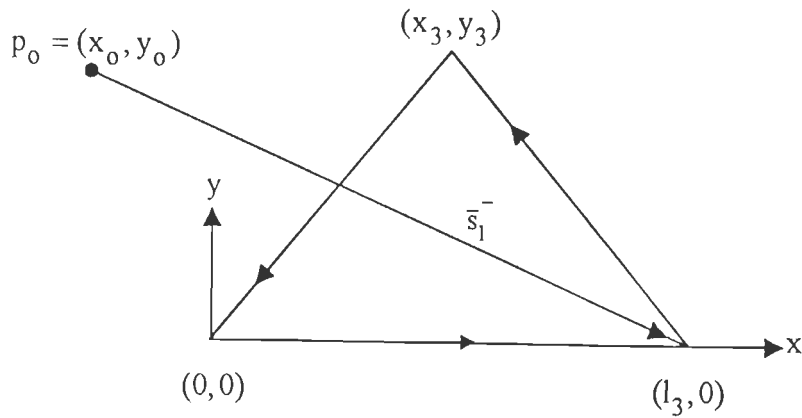
Fig. A-2

APPENDIX - B

Transformation from x-y plane to $L_2 - L_3$ (area coordinate) plane,

$0 \le L_2 \le 1, \ 0 \le L_3 \le 1$

where

$$\begin{bmatrix} x \\ y \end{bmatrix} = \begin{bmatrix} l_3 & x_3 \\ 0 & y_3 \end{bmatrix} \begin{bmatrix} L_2 \\ L_3 \end{bmatrix}$$

$x = l_3 L_2 + x_3 L_3$

$y = y_3 L_3$

Taking partial derivatives leads to

$$\frac{\partial x}{\partial L_2} = l_3, \qquad \frac{\partial x}{\partial L_3} = x_3$$

$$\frac{\partial y}{\partial L_2} = 0, \qquad \frac{\partial y}{\partial L_3} = y_3$$
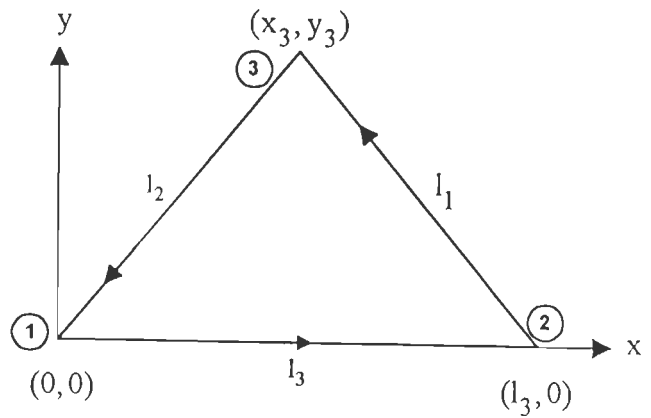
Fig. B-1

and the Jacobian of the transformation J is

$$J = \begin{vmatrix} \dfrac{\partial x}{dL_2} & \dfrac{\partial x}{dL_3} \\ \dfrac{\partial y}{dL_2} & \dfrac{\partial y}{dL_3} \end{vmatrix} = \begin{vmatrix} l_3 & x_3 \\ 0 & y_3 \end{vmatrix}$$

$$= l_3 y_3$$

For a triangle Fig. B-1,

The area $\Delta = \dfrac{1}{2} l_3 y_3$

i.e., $J = 2\Delta$

BIBLIOGRAPHY

[1] Aksun, M. I. and Mittra, R. : "Choices of expansion and testing functions for the method of moments applied to a class of electromagnetic problems," IEEE Trans. Microwave Theory Tech., Vol. 41,pp. 503-509, 1993.

[2] Ali, E., Kabalan, K.Y. and Assad, R.: "Characteristics mode formulation of multiple rectangular apertures in a conducting plane with a dielectric filled cavity," IEEE Trans. Electromag. Compat., Vol.40, 2, pp.89-93, 1998.

[3] Allessandri, F., Bartolucci, G. and Sorrentino, R.: "Admittance matrix formulation of waveguide discontinuity problems : Computer - aided design of branch guide couplers," IEEE Microwave Theory Tech., Vol.36, 394-403, 1988.

[4] Armstrong, M.E. and Alexopoulos, N.G.: "On the design of circularly polarized waveguide narrow wall linear arrays," IEEE Trans. Antennas Propagat., Annals, No.503, AP014, pp.244-250, 1975.

[5] Arndt, F., Koch, B., Orlok, H. J., Shroder, N. : "Field theory design of rectangular waveguide broadwall metal-insert slot couplers for millimeter wave applications," IEEE Trans Microwave Theory Tech., Vol. MTT-35, pp. 95-104, 1985.

[6] Auckland, D.T. and Harrington, R.F.: "Electromagnetic transmission through a filled slit in a conducting plane of finite thickness, TE case," IEEE Trans. Microwave Theory Tech., Vol.MTT-26, pp.499-505, 1978.

[7] Auda, H. and Harrington, R.F.: "Inductive posts and diaphragms of arbitrary shape and number in a rectangular waveguide," IEEE Trans. Microwave Theory Tech., Vol. MTT-32, pp. 606-613, 1984.

[8] Auda, H. and Harrington, R.F.: "A moment solution of waveguide junction problems," IEEE Trans. Microwave Theory Tech., Vol. MTT-31, pp. 515-520, 1983.

[9]   Bailey, M.C.: "Design of dielectric-covered resonant slots in a rectangular waveguide," IEEE Trans. Antennas Propagat., Vol.AP-15, pp. 594-598, 1967.

[10]   Baudrand, H., Tao, J. and Atechian, J. : "Study of radiating properties of open-ended rectangular guides," IEEE Trans. Antennas Propagat., Vol. 36, pp. 1071-1077, Aug. 1988.

[11]   Bethe, H.A. : "Theory of diffraction by small holes," Phys. Rev., Vol. 66, pp. 163-182, 1944.

[12]   Bornemann, J. and Vahldieck, R. : "Characterization of a class of waveguide discontinuities using a modified TE^x_{mn} mode approach," IEEE Trans. Microwave Theory Tech., Vol. MTT-38, pp. 1816-1822, Dec. 1990.

[13]   Bozzetti, M., Caorsi, F. and De Leo, R.: "Electromagnetic coupling between apertures and biological structures," Radio Sci., Vol.16, pp.1217-1222, 1981.

[14]   Butler, C.M. and Umashankar, K.R.: "Electromagnetic excitation of a wire through an aperture-perforated conducting screen," IEEE Trans. Antennas Propagat., Vol.AP-24, pp.456-462, 1976.

[15]   Butler, C.M. and Wilton, D.R.: "General analysis of narrow strips and slots," IEEE Trans. Antennas Propagat., Vol.AP-28, pp.42-48, 1980.

[16]   Butler, C.M., Courtney, C.C., Mannikko, P.D. and Silvestro, J.W.: "Flanged parallel-plate waveguide coupled to a conducting cylinder," IEE Proc. pt-H, Vol.138, pp.549-559, 1991.

[17]   Caorsi, S., Moreno, D. and Sidoti, F.: "Theoretical and numerical treatment of surface integrals involving free-space Green's function," IEEE Trans. Antennas Propagat., Vol.41, pp.1296-1301, 1993.

[18]   Cerri, G., De Leo, R. and Primiani, V.: "Theoretical and experimental evaluation of the electromagnetic radiation from apertures in shielded enclosures," IEEE Trans. Electromag. Compat., Vol. 34, pp.423-432, Nov.1992.

[19] Cheng, J., Dib, N. I. and Katehi, L. P. : "Theoretical modelling of cavity-backed patch antennas using a hybrid technique," IEEE Antennas Propagat., Vol. 43, pp. 1003-1013 , 1995.

[20] Chow, Y. L. and Wu, S. C. : "A moment method with mixed basis functions for scattering waveguide junctions," IEEE Trans. Microwave Theory Tech., Vol. MTT-21, pp. 333-340, 1973.

[21] Cohen, M., Crowley, T. and Levis, K.: "The aperture admittance of a retangular waveguide radiating into half-space," Airforce Cambridge Res. Lab., Tech. Rept. ac21114, S.R., Ohio State University, 1953.

[22] Cohn, S.B. : "Determination of aperture parameters by electrolytic tank measurements", Proc. IRE, Vol. 39, pp. 1416-1421, 1951.

[23] Cohn, S.B.: "Microwave coupling by large apertures," Proc. IRE, Vol.40, pp.696-699, 1952.

[24] Collin, R.E. and Zucker, F.J.: Antenna Theory, Vol.1, New York : McGraw-Hill, 1969.

[25] Collin, R.E.: Field Theory of Guided Waves, New York: McGraw-Hill, 1960.

[26] Collin, R. E.: Foundations for Microwave Engineering, McGraw Hill, Tokyo, 1966.

[27] Das, B.N. and Sanyal, G.S.: "Network parameters of a waveguide broadwall slot radiator," Proc. Inst. Elec. Eng. Vol.117, pp.41-44, 1970.

[28] Das, B.N. and Sarma, N.V.S.: "Analysis of E-H plane TEE junction using a variational formulation," IEEE Trans. Microwave Theory Tech., Vol.39, pp.1770-1773, 1991.

[29] Das, B.N. and Sinha, M.: "Impedance characteristics of series slots," Proc. Inst. Elec. Eng. Vol.121, pp.1360-1362, 1974.

[30] Das, B.N., Sarma, N.V.S. and Chakraborty, A.: "A rigorous variational formulation of an H plane slot-coupled TEE junction," IEEE Trans. Microwave Theory Tech., MTT. Vol.38, pp.93-95, 1990.

[31] Datta, A., Rajeek, A.M., Chakrabarty, A., and Das, B.N.: "S matrix of a broad wall coupler between dissimilar rectangular waveguides," IEEE Trans. Microwave Theory Tech., Vol.43, pp.56-62, 1995.

[32] De Smedt, R. and Denturck, B.: "Scattering matrix of junctions between rectangular waveguides," IEE, Proc. Pt. H, Vol.130, pp.183-190, 1983.

[33] Elliott, R.S.: "An improved design procedure for small arrays of shunt slots," IEEE Trans. Antennas Propagat., Vol.AP-31, pp.48-53, 1983.

[34] Elliott, R.S.: Antenna Theory and Design, Englewood, Cliffs, NJ., Prentice Hall, 1981.

[35] Fenn, A., Thiele, G.A. and Munk, B.A.: "Moment method analysis of finite rectangular waveguide phased arrays," IEEE Trans. Antennas Propagat., Vol. AP-30, pp.554-564, 1982.

[36] Finlayson, B.A. and Scriven, L.E. : "The method of weighted residuals-a review,"Appl. Mech. Rev., Vol.19, pp.735-748, 1966.

[37] Gedney, S. D. and Mittra, R.: "Electromagnetic transmission through inhomogeneously filled slots in a thick conducting plane – Arbitrary incidence," IEEE Trans. Electromag. Compat., Vol. 34, pp. 404-415, Nov. 1992.

[38] Gessel, G.A. and Ciric, I.R.: "Recurrence modal analysis for multiple waveguide discontinuities and its application to circular structures," IEEE Trans. Antennas Propagat. Vol. 41, pp.484-490, 1993.

[39] Graglia, R.D.: "On the numerical integration of the linear shape function or its gradient on a plane triangle," IEEE Trans. Antennas Propagat., Vol.41, pp.1448-1455, 1993.

[40] Hadidi, A. and Hamid. M.: "Aperture field and circuit parameters of cavity-backed slot radiator," Proc. Pt-H, Vol.136, pp.139-146, 1989.

[41] Hanyang, W. and Wei, W.: "Moment method analysis of feeding system in a slotted waveguide antenna," IEE Proc. Pt. H, Vol. 135, pp. 313-318, 1988.

[42] Harrington, R.F. : Field Computation by Moment Methods, New York : MacMillan, 1968.

[43] Harrington, R.F. and Auckland, D.T.: "Electromagnetic transmission through narrow slots in thick conducting screens,". IEEE Trans. Antennas Propagat., Vol.AP-28, no.5, pp.616-622, 1980.

[44] Harrington, R.F. and Mautz, J.R. : "A generalized network formulation for aperture problems," IEEE Trans. Antennas Propagat., Vol. AP-24, pp. 870-873, 1976.

[45] Harrington, R.F.: "Resonant behaviour of a small aperture backed by a conducting body," IEEE Trans. Antennas Propagat., Vol.AP-30, pp.205-212, 1982.

[46] Harrington, R.F.: Time-harmonic Electromagnetic Fields, New York : McGraw-Hill, 1961.

[47] Hirokawa, J., Arai, H. and Goto, N. : "Cavity-backed wide slot antenna," IEEE Proc. Pt-H, Vol. 136, pp. 29-33, 1989.

[48] Jin, J. and Volakis, J. L. : "Scattering and radiation analysis of three-dimensional cavity arrays via a hybrid fEM," Trans. Antennas Propagat., Vol. 41, pp. 1580-1586, 1993.

[49] Jordan, E.C. and Balmain, K.G. : Electromagnetic waves and radiating systems, New Delhi, Prentice-Hall, 1969.

[50] Joseffson, L.: "Transverse slot for array applications," IEEE Trans. Antennas and Propagat., Vol.AP-41, pp.845-850, 1993.

[51] Joseffson, L.G.: "Analysis of longitudinal slots in rectangular waveguides," IEEE Trans. Antennas Propagat., Vol. AP-35, pp.1351-1357, 1987.

[52] Joubert, J. and McNamara, D.: "Analysis of radiating slots in rectangular waveguide inhomogeneously loaded with a dielectric slab," IEEE Trans. Antennas Propagat., Vol.41, no.9, pp.1212-1221, 1993.

[53] Kabalan, K.Y., Harrington, R.F.: "Characteristic modes for slots in a conducting plane, TE case," IEEE Trans. Antennas Propagat., Vol. AP-35, pp. 162-168, 1987.

[54] Kabalan, K.Y., Ali, E. and Harrington, R.F. : "Characteristic mode analysis of a slot separating different media," IEEE Trans. Antennas Propagat., Vol. AP-38, pp. 476-481, 1990.

[55] Katehi, P.B.: "Dielectric-covered waveguide longitudinal slots with finite wall thickness," IEEE Trans. Antennas Propagat., Vol.38, pp.1039-1045, 1990.

[56] Lee, S.W., Jones, W.R. and Campbell, J.J.: "Convergence of numerical solutions of iris-type discontinuity problems," IEEE Trans. Microwave Theory Tech., Vol. MTT-19, pp.528-536, June 1971.

[57] Leong, M.S., Kooi, P.S. and Chandra : "Radiation from a flanged parallel-plate waveguide : solution by moment method with inclusion of edge condition," IEE Proc. Pt.H, Vol.135, pp.249-255, 1988.

[58] Leong, M.S., Kooi, P.S., Chandra and Yeo, T.S.: "Theoretical and experimental investigations of two-dimensional waveguide-excited short back fire antenna structure", IEE Proc., Pt.H, Vol.136, pp.263-268, 1989.

[59] Leviatan, Y., Li, P. G., Adams, A. T. and Perini, J. : "Single-post inductive obstacle in rectangular waveguide," IEEE Trans. Microwave Theory Tech., Vol. MTT-31, pp. 806-811, Oct. 1983.

[60] Levy, R.: "Analysis and Synthesis of waveguide multiaperture directional couplers," Trans. Microwave Theory Tech., Vol.MTT-16, No.12, pp.995-1006, 1968.

[61] Lewin, L. : "Some observations on waveguide coupling through medium sized slots," Proc. Inst. Elec. Eng., Vol.107c, pp.171-178, 1960.

[62] Luebbers, R.J. and Munk, B.A. : "Analysis of thick rectangular waveguide windows with finite conductivity," IEEE Trans. Microwave Theory Tech., Vol. MTT-21, pp. 461-468, 1973.

[63] Lyon, R.W. and Sangster, A.J.: "Efficient moment method analysis of radiating slots in a thick walled rectangular waveguide," IEE Proc. pt-H, Vol.128, 4, pp.197-205, 1981.

[64] Mailloux, R.J.: "On the use of metallized cavities in printed slot arrays with dielectric substrates", IEEE Trans. Antennas Propagat., Vol.AP-35, pp.477-487, 1987.

[65] Marcuvitz, N., ed., Waveguide Handbook, New York, McGraw-Hill, 1951.

[66] Mastermann, P. H. and Claricoats, P. J. B. : "Computer field matching solution of waveguide transverse discontinuities," Proc. Inst. Elect. Eng., Vol. 118, pp. 51-63, 1971.

[67] Mautz, J.R. and Harington, R.F.: "Electromagnetic transmission through a rectangular aperture in a perfectly conducting plane," Tech. Rept. TR-76-1, Electrical and Computer Engg. Deptt., Syracuse Univ., New York, 13210, 1976.

[68] Mautz, J.R. and Harrington, R.F.: "Transmission from a rectangular waveguide into half space through a rectangular aperture," Airforce Cambridge Res. Lab, Tech. Rept., TR-76-5, Contract F 19628-73-C-0047, 1976.

[69] Mazzarella, G. and Panariello, G.: "On the evaluation of mutual coupling between slots", IEEE Trans. Antennas Propagat. Vol. AP-35, pp.1289-1293, 1987.

[70]   McDonald, N.A.: "Electric and magnetic coupling through small apertures in shield walls of any thickness," IEEE Trans. Microwave Theory Tech., Vol.MTT-20, pp.689-695, 1972.

[71]   Mittra, R., Itoh, T. and Li, T.: "Analytical and numerical studies of the relative convergence phenomenon arising in solution of an integral equation by moment method," IEEE Trans. Microwave Theory Tech., Vol. MTT-20, pp.96-104, Feb. 1972.

[72]   Mongiardo, M. and Rozzi, T. : "Singular integral equation analysis of flange-mounted rectangular waveguide radiators," IEEE Trans. Antennas Propagat., Vol. 41, pp. 556-565, May 1992.

[73]   Montgomery, J.C.G., Dicke, R. H. and Purcel, E.M. : Principle of microwave circuits, Radiation Lab. Series, McGraw-Hill, New York, 1948.

[74]   Naiheng, Y. and Harrington, R.F.: "Electromagnetic coupling to an infinite wire through a slot in a conducting plane," IEEE Trans. Antennas Propagat., Vol.AP-31, pp.310-316, 1983.

[75]   Oliner, A.A.: "The impedance properties of narrow radiating slots in the broad face of rectangular waveguide, Pt. I-theory, Pt. II-Comparison with Measurement," IRE Trans., AP-5, pp.4-20, 1957.

[76]   Omar, A. S. and Schünemann, K. : "Transmission matrix representation of finline discontinuities," IEEE Trans. Microwave Theory Tech., Vol. MTT-33, pp. 765-770, Sep. 1985.

[77]   Park, P.K., Stern, G.J. and Eliott, R.S.: "An improved technique for the evaluation of transverse slot discontinuities in rectangular waveguide," IEEE Trans. Antennas Propagat, Vol.31, pp.148-154, 1983.

[78]   Patzelt, H. and Arndt, F.: "Double-plane steps in rectangular waveguides and their applications for Transformers, irises and filters," IEEE Trans. Microwave Theory Tech. Vol.MTT-30, pp.771-776, 1982.

[79] Pozar, D. M. : Microwave Engineering, 2nd Ed., John Wiley & Sons, New York, 1998.

[80] Rahmat-Samii, Y.: "On the question of Computation of the Dyadic Green's function at the source region in waveguide and cavities," IEEE Trans. Microwave Theory Tech., Vol. MTT-23, pp.762-765, 1975.

[81] Ramo, S., Whinnery, J.R. and Van Duzer, T. : Fields and waves in communication electronics, 2nd ed., New York, John Wiley & Sons., Inc., 1984.

[82] Rao, S.M., Wilton, D.R. and Glisson, A.W.: "Electromagnetic scattering by surfaces of arbitrary shape," IEEE Trans. Antennas Propagat., Vol. AP-30, pp.409-418, 1982.

[83] Rengarajan, S.R.: "Higher order mode coupling effects in feeding waveguide of a planar slot array," IEEE Trans. Microwave Theory Tech., Vol.39, pp.1219-1223, 1991.

[84] Rozzi, T.E.: "Equivalent network for interacting thick inductive irises," IEEE Microwave theory Tech., Vol.MTT-20, pp.323-330, 1972.

[85] Rozzi, T.E.: "The variational treatment of thick interacting inductive irises," IEEE Microwave theory Tech., Vol.MTT-21, pp.82-88, 1973.

[86] Rozzi, T.E. and Mecklenbrauker, W.F.G.: "Wideband network modelling of interacting inductive irises and steps," IEEE Trans. Microwave Theory Tech., Vol.MTT-23, pp.235-245, 1975.

[87] Rozzi, T.E.: "A new approach to the network modelling of capacitive irises and steps in waveguide," Int. J. Circuit Theory Appl., 3, pp.339-354, 1975.

[88] Safavi-Naini, R. and MacPhie, R.H.: "On solving waveguide junction scattering problems by the conservation of complex power technique," IEEE Trans. Microwave Theory Tech., Vol. MTT-29, pp.337-343, 1981.

[89]   Sangster, A.J. and McCormick, A.H.I.: "Moment method applied to round-ended slots," IEE Proc.Pt-H, Vol.134, no.3, pp.310-314, 1987.

[90]   Sangster, A.J. and Wang, H.: "Moment method analysis of a horizontally polarized omnidirectional slot array antenna," Proc. Inst. Elec. Eng. Pt.H., Vol.142, pp. 1-6, 1995.

[91]   Sangster, A.J.: "Slot coupling between uniform rectangular waveguide," IEEE Trans. Microwave Theory Tech., Vol.MTT-27, pp.705-707, 1979.

[92]   Sarkar, T.K., Costa, Chin-Lin, I., Harrington, R.F.: "Electromagnetic transmission through mesh covered apertures and arrays of apertures in a conducting screen," IEEE Trans. Antenna Propagat., Vol. AP-32, pp. 908-913, 1984.

[93]   Satyanarayama, D. and Chakraborty, A.: "Analysis of wide inclined slot coupled narrow wall coupler between dissimilar rectangular waveguides," IEEE Trans. Microwave Theory Tech., Vol.42, pp.914-917, 1994.

[94]   Savov, S.V. and Hristov, H.D.: "Cavity-backed slot array analysis," IEEE Proc. Pt. H, Vol.134, pp.260-264, 1987.

[95]   Schaller, G.: "On the imaging of hot spots using correlation radiometers and a circular aperture," IEEE Trans. Microwave Theory Tech., Vol.37,pp. 1210, 1989.

[96]   Scharstein, R.W.: "Mutual coupling in a slotted phased array, infinite in E-plane and finite in H-plane," IEEE Trans. Antennas Propagat., Vol. 38, pp.1186-1190, 1990.

[97]   Sinha, S.N., Mehra, D.K. and Agarwal, R.P.: "Radiation from a waveguide backed aperture in an infinite ground-plane in the presence of a thin conducting plate," IEEE Trans. Antennas Propagat. Vol.AP-34, pp. 539-545, 1986.

[98] Sinha, S.N.: "A generalized network formulation for a class of waveguide coupling problems", IEE Proc. Pt-H, Vol.134, pp.502-508, 1987.

[99] Sinha, S.N.: "A generalized network formulation for transverse discontinuites in a rectangular waveguide," Journ. Electromag. Waves Appl., Vol.4, pp.771-787, 1990.

[100] Sinha, S.N.: "Analysis of multiple-strip discontinuity in a rectangular waveguide," IEEE Trans. Microwave Theory Tech. Vol. MTT-34, pp.696-700, 1986.

[101] Sphicopoulos, T.: "C-slot : a practical solution for phased arrays of radiating slots located on the narrow side of rectangular waveguides," IEE Proc. pt-H, Vol.129, pp.49-55, 1982.

[102] Stegen, R.J. : "Longitudinal shunt slot characteristics", Hughes Tech. Memo 261, Hughes Aircraft Co., Culver City, CA, 1951.

[103] Stern, G.T. and Elliott, R.S.: "Resonant length of longitudinal slots and validity of circuit representation : Theory and experiment," IEEE Trans. Antennas Propagat., Vol.22, pp.1264-1271, 1985.

[104] Stevenson, A.F. : "Theory of slots in rectangular waveguide, " J. Appl. Phys., 19, pp. 24-38, 1948.

[105] VanBlaricum, G.F., Jr, and Mittra, R.: "A modified residue-calculus technique for solving a class of boundary value problems-Part I : Waveguide discontinuities," IEEE Microwave Theory Tech. Vol. MTT-17, 302-309, 1969.

[106] Verma, S.K. : "A moment solution for thick dielectric-filled windows in waveguides," M.E. Dissertation, University of Roorkee, 1987.

[107] Vu Khac, T.: "Solutions for some waveguide discontinuities by the method of moments," IEEE Trans. Microwave Theory Tech., Vol.MTT-20, pp.416-418, 1972.

[108] Vu Khac, T. and Carson, C.T. : "Impedance properties of a longitudinal slot antenna in broadface of a rectangular waveguide," IEEE Trans. Antennas Propagat., pp. 708-710, 1973.

[109] Wexler, A.: "Solution of waveguide discontinuites by modal analysis," IEEE Trans. Microwave Theory Tech., MTT-15, 508-517, 1967.

[110] Wilton, D.R., Rao, S.M., Glisson, A.W., Al-Bundak, O.M. and Butler, C.M.: "Potential integrals for uniform and linear source distributions on polygonal and polyhedral domains," IEEE Trans. Antennas Propagat., Vol.41, pp.276-281, 1984.

[111] Wilton, D.R.: Review of Current Status and Trends in the Use of Integral Equations in Computational Electromagnetics, Electromag. 12 : 287-341, Hemisphere Publ. Corp. 1992.

[112] Wu, S.C. and Chow, Y. L. : "An application of the moment method to waveguide scattering problems," IEEE Trans. Microwave Theory Tech., Vol.MTT-20, pp. 744-749, 1972.

[113] Yang, R. and Omar, A. S. : "Investigation of multiple rectangular aperture irises in rectangular waveguide using TE^x_{mn}-modes," IEEE Trans. Microwave Theory Tech., Vol. MTT-41, pp. 1369-1374, Aug. 1993.

[114] Yee, H.Y.: "The design of large waveguide arrays of shunt slots," IEEE Trans. Antennas Propagat. Vol. AP-40, pp.775-781, 1992.

[115] Yeganeh, S.H. and Bitcher, C.: "Theoretical and experimental studies of cavity-backed slot antenna excited by a narrow strip," IEEE Trans Antennas Propagat., Vol.41, pp.236-241, 1993.

[116] Zienkiewicz, O.C.: The Finite Element Method, 3rd Ed., New York, McGraw Hill, 1977.

RESEARCH PAPERS OUT OF THE PRESENT WORK

1.   Konditi, D.B.O. and Sinha, S. N. : "Radiation from an arbitrary-shaped aperture fed via a rectangular waveguide," APSYM-98, Proc. National Symposium on Antennas Propagat., pp. 201-206, Cochin, India, 15-16 Dec., 1998.

2.   Sinha, S.N. and Konditi, D.B.O. : "Analysis of arbitrary-shaped apertures in waveguides," Accepted for presentation at AP-2000 Millennium Conference on Antennas and Propagation, Davos, Switzerland, Due on 9-14 April, 2000.